Improving the Advanced Virgo+ calibration with the photon calibrator for the 04 run

Paul Lagabbe

UNIVERSITÉ SAVOIE MONT BLANC

THÈSE

Pour obtenir le grade de

DOCTEUR DE L'UNIVERSITÉ SAVOIE MONT BLANC

Spécialité : **Physique Subatomique et Astroparticules**

Arrêté ministériel : 25 Mai 2016

Présentée par

Paul Lagabbe

Thèse dirigée par **Loïc Rolland**

préparée au sein du
Laboratoire d'Annecy de Physique des Particules
dans **l'École Doctorale de physique de Grenoble**

Improving the Advanced Virgo+ calibration with the photon calibrator for the 04 run

Thèse soutenue publiquement le **10 octobre 2023,**
devant le jury composé de :

Dr. Benoît Mours
Directeur de recherche, IPHC Strasbourg, Rapporteur
Dr. Myriam Zerrad
Ingénieure de recherche, Institut Fresnel de Marseille, Rapportrice
Pr. Richard Taillet
Professeur des universités, LAPTH Annecy, Examinateur
Dr. Dominique Boutigny
Directeur de recherche, LAPP Annecy, Examinateur
Dr. Gael Obein
Maître de conférences, CNAM/LNE Saint-Denis, Examinateur
Dr. Loïc Rolland
Directeur de recherche, LAPP Annecy, Directeur de thèse

Contents

Introduction

Gravitational waves are perturbations of the space-time metric propagating at the speed of light. They were predicted as a consequence of the theory of General Relativity in 1916 by Albert Einstein. Gravitational waves are induced by the acceleration of massive bodies. Waves whose amplitude is large enough to be detected on earth come from astrophysical sources. To date, the only gravitational waves detected came from the coalescences of binary systems of compact objects. Those binary systems can be splitted into three categories: Binary Black Holes (BBH), Binary Neutron Stars (BNS) and Neutron Star - Black Hole (NSBH).
The first gravitational waves event was detected on September 14, 2015 (GW150914) by the two LIGO detectors, during an observing run which has been named "O1". The joint observation run of the different detectors are designated by "O1, O2, etc", and the detectors are upgraded between the observation runs in order to improve their sensitivity. The Virgo detector started observing the gravitational waves in August 2017, during the O2 observation run, and KAGRA joined the collaboration on February 25, 2020 during O3. My thesis started in October 2020, after the O3 run, during the improvement period of Advanced Virgo+ phase I, in prevision of the O4 run.
The LIGO, Virgo and KAGRA detectors are ground-base kilometer-scale Michelson interferometers. They use the laser interferometry to measure the length variations between free test masses induced by gravitational waves signals, in the frequency range from ten hertz to a few kilohertz. The search for gravitational waves is done using the reconstructed detector strain signal, called $h(t)$, continuously produced by each detector when observing. The strain signal $h(t)$ is also used during the commissioning to provide a sensitivity curve to monitor ans study the impacts of detector tunings and look for the noise sources. The main difficulty of the reconstruction is to estimate properly the displacement of the different mirrors induced by their actuators. The estimation of the mirror motion has to be absolute. So the actuators have to be calibrated absolutely. Another crucial parameter calibrated is the effect of the mirror motions on the output power of the interferometer. The response of the interferometer to a mirror displacement is called the "optical response" of the interferometer, and it is also needed to reconstruct the strain signal. The upgrades of the detectors done between the observation run has improved their sensitivity, which allows them to detect more gravitational waves events, with a higher SNR. In order not to limit the precision of the data analysis, the precision of the calibration have to be improved so that the uncertainty value on the reconstructed strain signal $h(t)$ is of the order of a few %.
During the O3 run, the main reference for the interferometer calibration was the photon calibrator. The photon calibrator is a mirror actuator which induces a motion to the end mirrors by pushing it with the radiation pressure of an auxiliary laser. The designed Virgo sensitivity for the O4 run is improved, so a more precise calibration of the interferometer is required. My work consisted in improving the design of the photon calibrator in prevision of the O4 run, and using it to calibrate the interferometer.
Chapter 1 introduces the concept of gravitational waves, their different sources, their effect on a Michelson interferometer. The current and future gravitational wave detectors are also presented.
The European detector Advanced Virgo+ is presented in chapter 2 in the configuration planned to be used for the O4 run. The working principle of the detector is explained, and the nominal models of the optical responses and of the mirror actuators responses needed in the reconstruction of the strain signal $h(t)$ are defined. A brief description of the different noise sources is also provided.
The frequency responses of the mirror actuators of the detector have to be calibrated. The three calibration methods used to calibrate the actuators during the O3 run are presented in chapter 3. Two of these methods require a reference actuator, the photon calibrator (PCal) and the newtonian calibrator (NCal), and the third method, called Free Swinging Michelson, uses the wavelength of the interferometer laser as reference for the actuator calibration. The PCal was used as the main reference for the calibration during O3.
The reconstruction of the strain signal $h(t)$ is described in chapter 4. The reconstruction algorithm of

$h(t)$ uses the models of the actuator responses and of the interferometer optical responses. A frequency dependant bias in the reconstructed signal is measured and corrected, and some of the interferometer noise sources are subtracted from the reconstructed signal.
In chapter 5, the improvements of the photon calibrator that we have done during my PhD in prevision of the O4 run are detailed. Improvements have been done in the PCal optical layout, new power sensors have been designed and the control loop of the laser has been improved in order to improve the precision of the calibration and lower the power noise of the PCal.
The laser power calibration of the PCal requires a power measurement standards which is calibrated with respect to national institutes of metrology. The calibration and the characterization of the power standards used for the calibration in power of the PCal sensors are described in chapter 6. The new intercalibration strategy between LIGO, Virgo and KAGRA is also explained.
Chapter 7 describes the calibration in power of the PCal power sensors, and the measurement of the mechanical response of the PCal in order to estimate the mirror displacement induced by the PCal and the uncertainty budget on the displacement.
The calibration of the mirror actuators of the interferometer with respect to the photon calibrator is explained in chapter 8. The new models of the actuator responses measured in 2023 are compared with the nominal models and with the responses measured during the O3 run.
The new actuator response models are used to measure the optical response of the interferometer to a mirror displacement as shown in chapter 9. And the model of the optical response defined in chapter 2 are fitted to the measurement. The actuators response models and the optical response models are used in the $h(t)$ reconstruction algorithm presented in chapter 4.
Chapter 10 deals with future prospects to improve the calibration of Advanced Virgo+ towards O5, and the expected improvements of the photon calibrator.

Chapter 1

Gravitational waves detection

Contents

1.1 Gravitational waves

Gravitational waves are a consequence of the General relativity [4] predicted by Albert Einstein in 1916. In the theory of the General relativity, gravitation is seen as the deformation of the four dimensions space-time caused massive objects. Einstein equation bounds the space-time deformation to the mass-energy distribution.

1.1.1 General relativity

Gravitational waves are the propagation of a space-time perturbation. The approximation of the weak gravitational field is used. So the metric of the space time is written as $\boldsymbol{\eta} + \boldsymbol{h}$ where $\boldsymbol{\eta}$ is the Minkowsky's metric tensor which represent a flat space-time, and $\boldsymbol{h}$ is the space-time perturbation.

The coordinates (ct, x, y, z) has been chosen so as the gravitational wave propagates along the z axis. In the absence of mass and energy, the solution $\boldsymbol{h}$ to the Einstein equation can be described as a combination of monochromatic plane waves propagating at the speed of light c. The frequency of the wave is f:

$$\boldsymbol{h}(t, z) = ||\boldsymbol{h}|| \cdot Re\left\{e^{-i2\pi f(t-z/c)}\right\} \tag{1.1}$$

The amplitude tensor of the gravitational wave can be written using only two degrees of freedom h_+ and $h_\times$, which represent the polarization states of the wave. The polarization states are turned by 45° with respect to each other.

$$||\boldsymbol{h}|| = \begin{pmatrix} 0 & 0 & 0 & 0 \\ 0 & h_+ & h_\times & 0 \\ 0 & h_\times & -h_+ & 0 \\ 0 & 0 & 0 & 0 \end{pmatrix} \tag{1.2}$$

Figure 1.1 shows the effects of the two polarizations of a gravitational wave on a circle of test masses located in a plan perpendicular to the axis of propagation of the gravitational wave.

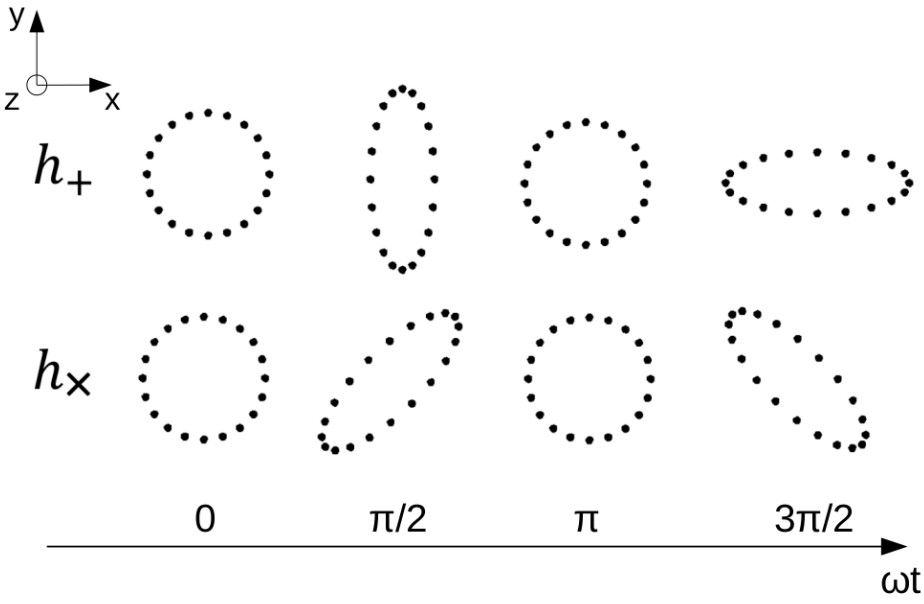

Figure 1.1: Effect of the + and × polarizations of a gravitational wave propagating along the z axis, on a circle of masses located on the plan (x, y)

In a three dimension space $(\hat{x}, \hat{y}, \hat{z})$, a gravitational wave propagating along the z axis. The amplitude of the space distortion due to the gravitational wave is represented by the following tensor:

$$\boldsymbol{h} = \begin{pmatrix} h_+ & h_\times & 0 \\ h_\times & -h_+ & 0 \\ 0 & 0 & 0 \end{pmatrix} \tag{1.3}$$

The polarization of the gravitational wave depend on the choice of the x and y axis. We assume that the gravitational wave is polarized along a vector $\vec{p}$ orthogonal to the propagation axis z. The vector $\vec{p}$ makes an angle ψ with the x axis. The amplitude tensor of the gravitational wave is written as:

$$\boldsymbol{h}' = R_z(\psi)^{-1} \cdot \boldsymbol{h} \cdot R_z(\psi) = \begin{pmatrix} h'_+ & h'_\times & 0 \\ h'_\times & -h'_+ & 0 \\ 0 & 0 & 0 \end{pmatrix} \tag{1.4}$$

With $R_z\psi$ the rotation matrix along the z axis by the angle ψ and with:

$$h'_+ = h_+ \cos(2\psi) - h_\times \sin(2\psi) \tag{1.5}$$
$$h'_\times = h_+ \sin(2\psi) + h_\times \cos(2\psi) \tag{1.6}$$

Therefore, a gravitational wave polarized along $\vec{p}$ with an amplitude matrix h is equivalent to a gravitational polarized along $\hat{x}$ with an amplitude matrix h'. Without losses of generality, one can assume that the gravitational wave is polarized along the x axis.

One can notice that a rotation by an angle $\psi = 45°$ exchanges the amplitudes of the polarization h_+ and $h_\times$. A rotation by an angle $\psi = 90°$ changes the sign of the polarization amplitudes. And a rotation by $\psi = 180°$ doesn't change the polarization amplitudes.

1.1.2 Effect of a gravitational wave on the detector

Let $\mathcal{B}_{ITF} = (A, \hat{i}, \hat{j}, \hat{k})$ be an orthonormal base centered on an Michelson interferometer. The arms of the interferometer are along the vectors $\hat{i}$ and $\hat{j}$. We consider a gravitational wave propagating along the vector $\vec{k}_{GW}$, which is defined in the spherical coordinates with the angles (θ, ϕ), as illustrated in figure 1.2. The gravitational waves travel at the speed of light c, so the wavelength of a gravitational waves at the frequency below 5 kHz is above 60 km. The length of the detector arms is 3 km, thus one can assume that the gravitational wave amplitude doesn't vary with the position around the detector.

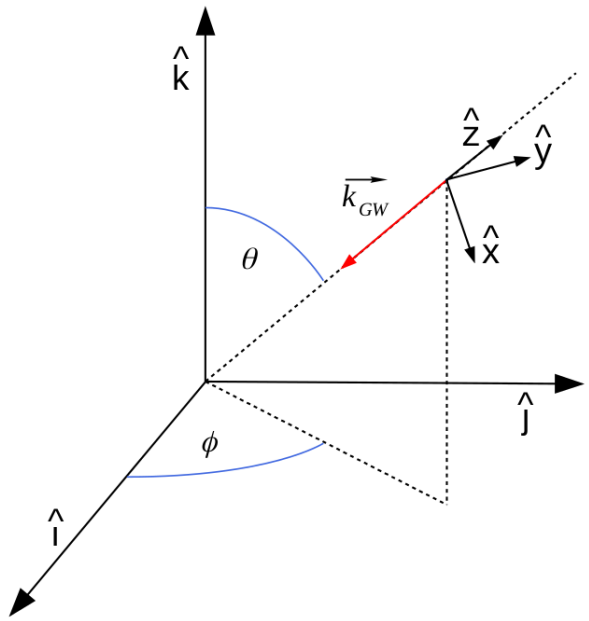

Figure 1.2: System of coordinate that represents the interferometer.
The arms of the interferometer are along the vectors $\hat{i}$ and $\hat{j}$, and the gravitational wave propagates along the vector $\vec{k}_{GW}$.

Let's define the base $\mathcal{B}_{GW} = (\hat{x}, \hat{y}, \hat{z})$ associated to the gravitational wave, where $\hat{z}$ is the opposite of $\vec{k}_{GW}$ and $\hat{x}$ and $\hat{y}$ are defined as in figure 1.2. Thus, the gravitational wave propagates along the $\hat{z}$ axis. As seen in the previous section, the polarization orientation can be chosen anywhere on the $(\hat{x}, \hat{y})$ plan. Without looses of generality, one can choose a wave polarized along the $\hat{x}$ axis. Therefore, the amplitude of the wave is described with the tensor $\boldsymbol{h}$ written in the base $\mathcal{B}_{GW}$ as:

$$\boldsymbol{h} = \begin{pmatrix} h_+ & h_\times & 0 \\ h_\times & -h_+ & 0 \\ 0 & 0 & 0 \end{pmatrix} \tag{1.7}$$

The base change matrix from the base $\mathcal{B}_{GW}$ to the base $\mathcal{B}_{ITF}$ is written as:

$$\begin{pmatrix} \hat{i} \\ \hat{j} \\ \hat{k} \end{pmatrix} = \begin{pmatrix} \cos(\theta)\cos(\phi) & -\sin(\theta) & \sin(\theta)\cos(\phi) \\ \cos(\theta)\cos(\phi) & \cos(\phi) & \sin(\theta)\sin(\phi) \\ -\sin(\theta) & 0 & \cos(\phi) \end{pmatrix} \cdot \begin{pmatrix} \hat{x} \\ \hat{y} \\ \hat{z} \end{pmatrix} \tag{1.8}$$

The length of the arms of the interferometer at rest is L_0. So in the base $\mathcal{B}_{GW}$, the vectors from the center of the interferometer to the edges of the arms are written as:

$$\vec{L}_N = L_0 \cdot \hat{i} = L_0 \cdot \begin{pmatrix} \cos(\theta)\cos(\phi) \\ -\sin(\theta) \\ \sin(\theta)\cos(\phi) \end{pmatrix} \tag{1.9}$$

$$\vec{L}_W = L_0 \cdot \hat{j} = L_0 \cdot \begin{pmatrix} \cos(\theta)\cos(\phi) \\ \cos(\phi) \\ \sin(\theta)\sin(\phi) \end{pmatrix} \tag{1.10}$$

We assume that the edges of each arms of the interferometer are free falling test masses. Thus, the arms $\vec{L}_N$ and $\vec{L}_W$ of distorted respectively by $\overrightarrow{\delta L}_N = \frac{1}{2}\mathbf{h}\cdot\vec{L}_N$ and $\overrightarrow{\delta L}_W = \frac{1}{2}\mathbf{h}\cdot\vec{L}_W$ due to the gravitational wave.

The interferometer is sensitive to the differential arm length variation $\Delta L = \delta L_N - \delta L_W$. The variation of the arm length due to the gravitational wave is the arm distortion $\overrightarrow{\delta L}_N$ (respectively $\overrightarrow{\delta L}_W$) along the axis $\hat{i}$ (respectively $\hat{j}$) of the arm, so it is equal to the scalar product of the distortion by the axis. Thus, an important quantity to consider is the detector strain $h = \frac{\Delta L}{L_0}$ which is the differential arm length variation normalized by the arm length at rest. It is written as:

$$h = \frac{1}{L_0} \cdot \left(\hat{i}^T \cdot \overrightarrow{\delta L}_N - \hat{j}^T \cdot \overrightarrow{\delta L}_W \right) = \frac{1}{2} \cdot \left(\hat{i}^T \cdot (\mathbf{h} \cdot \hat{i}) - \hat{j}^T \cdot (\mathbf{h} \cdot \hat{j}) \right) \tag{1.11}$$

The interferometer strain is function of the two polarizations of the gravitational wave h_+ and $h_\times$ and the propagation direction in relation to the detector.

$$h = -\frac{1}{2}(1 + \cos(\theta)^2)\cos(2\phi) \cdot h_+ - \cos(\theta)\sin(2\phi) \cdot h_\times = F_+(\theta, \phi) \cdot h_+ + F_\times(\theta, \phi) \cdot h_\times \tag{1.12}$$

$F_+(\theta, \phi)$ and $F_\times(\theta, \phi)$ are respectively the antenna response of the interferometer to a + polarized gravitational wave and × polarized gravitational wave. The pattern of the antenna responses are shown in the figure 1.3. One can notice that the response is not isotropic. The antenna response is maximum when if the gravitational wave propagates perpendicularly to the detector plan, and null when the gravitational wave propagates along the diagonal between the $\hat{i}$ and the $\hat{j}$ axis. Therefore, a network of detectors with different orientations is needed to cover the sky map.

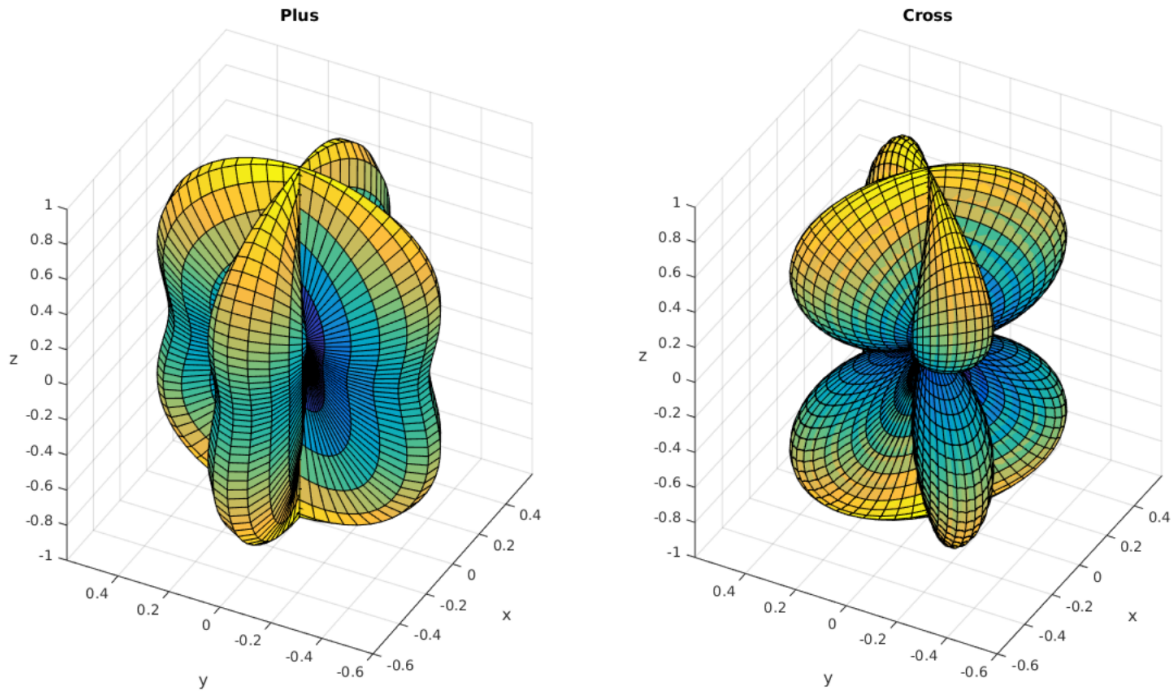

Figure 1.3: Patterns of the antenna responses of the interferometer to a + polarized gravitational wave on the left, and to × polarized gravitational wave on the right.

1.1.3 Detected gravitational waves sources

The acceleration of massive objects produces gravitational waves, to be observable from the Earth, the accelerated objects need to be massive enough. Typically, the gravitational waves observed during O3 come from the Compact object Binary system Coalescence (CBC). Since the first gravitational wave detection in 2015, 94 events have been observed at the end of the O3 run in March 2020, a catalog has been published [22]. The CBC can be divided into three categories:

- **Binary Black Holes (BBH):** This is the most common CBC event, and also the first gravitational wave event to be detected. The first detection was done by the LIGO detectors in September 14, 2015 (GW150914). Since then, 90 BBH merger events have been detected.
- **Binary Neutron Stars (BNS):** Since neutron stars are less massive than black holes, gravitational waves produces by BNS merger are fainter than BBH. Thus, the first BNS event detected was GW170817 during the O2 run. A second BNS event has been detected during O3, GW190425. Gravitational wave signals emitted by BNS merger last longer in the frequency detection bandwidth of the detector than signal emitted by BBH merger.
- **Neutron Star - Black Hole (NSBH):** The merger between a neutron star and a black hole has been detected for the first time during O3 during the event GW200105. A second event GW200115 has been detected since.

The gravitational wave signal emitted by a CBC can be split in three phases illustrated in figure 1.4:

1. Inspiral: The two compact objects are rotating around each other and the distance between them diminishes due to the energy lost with the gravitational wave emission.
2. Merger: The two compact objects merge
3. Ringdown: The gravitational wave produced by the relaxation of the resulting black hole.

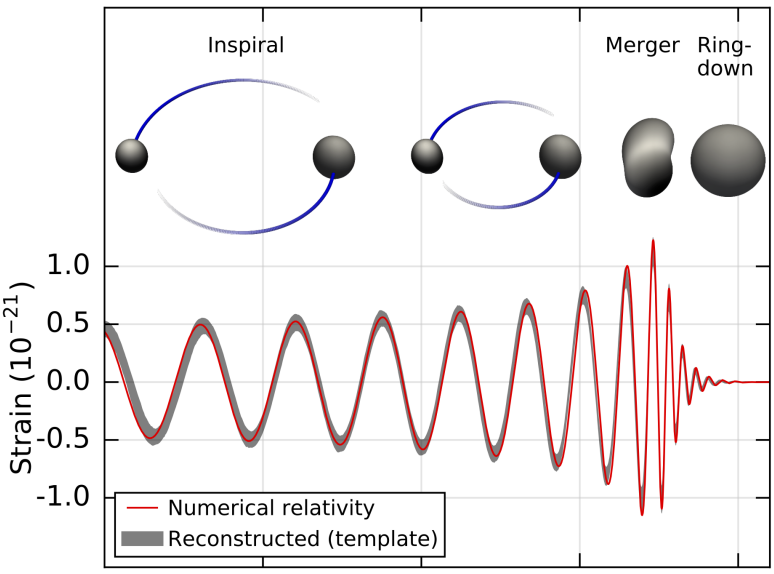

Figure 1.4: Typical shape of a gravitational wave signal emitted by a CBC, with the illustrated three phases of the coalescence.
Source: https://www.ligo.org/science/Publication-GW150914CBC/index.php

The shape of the gravitational wave signal depend on parameters such as the masses of the compact objects, the inclination of the binary system in relation to Earth or the distance of the system. These parameters are estimated from the gravitational wave signal. Starting from the O2 run, a trigger alarm system has been setup in order to detect gravitational waves event quickly enough to be able to alert electromagnetic telescopes and send them the location of the gravitational waves source. For the O4 run, we expect to automatize the trigger alert system to reduce its latency and improve the localisation of the gravitational wave source.

1.1.4 Other sources

There are other gravitational waves signals too faint to be observed with the current detectors, or with a frequency out of the observation bandwidth. These sources can be divided into three categories.

The burst signals are unmodeled short signals. Supernovae are expected to produce such signals. Since the knowledge on the supernovae evolution are limited, the resulting gravitational wave signal cannot be modeled. An other source of gravitational wave burst comes from the magnetars which are neutron-stars with a strong magnetic fields. This kind of neutron stars are prone to star-quakes which produces strong γ-ray and X-ray flares. These γ-ray flares are expected to have a gravitational wave counterpart. [21]

The continuous wave signals are monochromatic signal with a quasi-constant amplitude. The expected continuous signal sources are fast rotating neutron stars with an asymmetric mass distribution. The estimated number of neutron stars in the Milky-Way is of the order of 10^8, including ~ 1000 pulsars. The order of magnitude of the amplitude of such signal is $h \sim 10^{-25}$. [7]

The stochastic background is a combination of the different sources whose signals are non coherent, and too faint to be individually detectable. [25]

1.2 Current gravitational waves detector network

There are currently four gravitational waves detectors, two in the USA belonging to the LIGO collaboration, Virgo in Italy, and KaGra in Japan. A fifth detector is being constructed in India. Figure 1.5 shows the current and future gravitational waves detector observing in the frequency range from 10 Hz to 2 kHz.

Figure 1.5: Map of the gravitational wave detectors.

The different gravitational wave detector compensate the "blind spots" in their antenna response of each other. If an event is located in the blind spot of one of the detector, it can be seen by the others. The network is able to estimate the location of a gravitational wave source by triangulation. Working in a network also allows us to discriminate more effectively the gravitational waves event and non-stationary noises. Indeed, a trigger seen by several detectors at the same time is more likely to be a gravitational wave event than an trigger seen by only one detector.

1.2.1 Virgo

Virgo is the European gravitational waves detector located near Pisa in Italy. Its construction started in 1996, and it starts observing in June 2017 during the O2 run, jointly with the LIGO interferometers. The current design of the Virgo detector is named Advanced Virgo+ (AdV+) phase I, it has been developed for the O4 run. The phase II of AdV+ will be developed after O4, in preparation for O5. AdV+ is a Michelson Interferometer with 3 km long Fabry-Perot cavities on each arms, power and signal recycled. The main improvements of the detector done in preparation of O4 and the installation of the signal recycling mirror and the frequency dependent squeezing, and the increase of the laser input power. The expected detection range of the detector during O4 is 100 Mpc.

1.2.2 LIGO

Laser Interferometer Gravitational-Wave Observatory (LIGO) is the American collaboration for detecting gravitational waves. It has two detectors, one is located in Hanford in Washington state, the other is located in Livingston in Louisiana state. The detector started the first observation run O1 in 2015 and did their first detection in September of this year, which triggered the Nobel Price in Physics in 2017. Both detector are Michelson Interferometer with 4 km long Fabry-Perot cavities on each arms, power and signal recycled. The signal recycling mirror was already installed on both detector during O3, the main improvement of the detector in preparation of O4 is the frequency dependent squeezing.

1.2.3 KAGRA

Kamioka Gravitational Wave Detector (KAGRA) is the Japanese underground detector located inside the Kamioka mines. It is an interferometer with 3 km long Fabry-Perot cavities. It differs from the other detector by using cryogenic mirror to reduce the thermal noise. It has join LIGO and Virgo in the network in February 2020 in the end of O3.

1.2.4 LIGO-India

LIGO-India is a detector with the same design than LIGO-Hanford and and LIGO-Livingston, in construction in India. It is foreseen to start observing at the begin of O5.

1.2.5 GEO600

Is 600 meter long interferometer located near Hanover (Germany), built by a UK-Germany collaboration. It is also a dual recycled Michelson interferometer with Fabry-Perot cavities. It is used as a research and development facility for the others interferometer. It also keep observing the gravitational waves while the others detectors are in their improvement and commissioning phase.

1.3 Future detector projects

While the current gravitational waves detectors are being improved, a new generation of detectors is being designed. The sensitivity of the next detectors will be greater than the current one, and will observe gravitational waves in different frequency bandwidth. The next generation of detectors will enable us to test general relativity next to the event horizon of the black holes, probe the inside of the neutron stars and study supernovae. In this section is given an overview of the future gravitational wave projects.

1.3.1 Einstein Telescope

Einstein Telescope is the European next generation detector, funded by the INFN in Italy, the CNRS in France and the Nikhef in Netherlands. Like the current detectors, Einstein Telescope is based on the laser interferometer. It consists in an underground equilateral triangle of 10 km side. Each pair of sides contains two interferometers, one to detect low frequency gravitational waves, one for the high frequency gravitational waves, for a total of 6 interferometers. The thermal noise will be reduced using cryogenic mirrors. ET will probe the same frequencies than the current detectors, but its bandwidth is wider and the sensitivity of ET is designed to be 10 times higher. The detector is designed to probe the gravitational waves during the dark age era of the universe (redshift $z > 20$) before the birth of the first stars, and test general relativity at the horizons of the black holes. The construction of the detector should start in 2028, and the observations should start in 2035. [13]

1.3.2 Cosmic Explorer

Cosmic Explorer is the American gravitational waves detector project. It consists in two L-shaped facilities, one with 40 km long arms, the other with 20 km long arms. It is designed with the same technologies that has been developed for the LIGO interferometers. It is designed to probe the same frequencies than Einstein Telescope, but its bandwidth is narrower, and with the better sensitivity. The science goals of

Cosmic explorer are the same as Einstein telescope. [14]

1.3.3 Laser Interferometer Space Antenna

LISA is the space gravitational waves detector, designed by a collaboration between the NASA and ESA. It consists in three satellites orbiting around the sun, behind the earth, forming an equilateral triangle of 2.5 millions of kilometers side, around the Lagrange point L1. LISA is designed to observe gravitational waves in the frequency bandwidth [0.1 mHz, 100 mHz]. The LISA science goals are to monitor the compact binary objects signal far before their coalescence, observe the evolution of massive black hole binaries across ages and probes the dynamics of the stars orbiting around the galactic centers. [15] A proof of concept mission, named LISA-pathfinder [12] has been launched in December 2015. The final version eLISA, is planned to be lauched in 2032.

1.3.4 Pulsar Timing Array

The spin period of the pulsar is known to be highly stable, in particular, the millisecond pulsars have the most stable periods. However, ultra-low frequency gravitational waves [10^{-10} Hz, 10^{-6} Hz] can change the times of arrivals of pulses. Thus, correlations between the times of arrival of pulses from different pulsar highlight a gravitational wave. The observed millisecond pulsars are monitored using radio-telescopes such as MeerKat or SKA. PTA is expected to detect supermassive black holes binary system, and cosmic strings [20].

Chapter 2

Advanced Virgo+ detector

Contents

Introduction

Advanced Virgo+ (AdV+) is the European gravitational waves detector, located near Pisa in Tuscany, Italy. It is designed to detect gravitational waves in the frequency bandwidth [10 Hz, 5 kHz]. The detector consists in a Michelson interferometer, with 3 km long Fabry-Pérot cavities in the arms, and power and signal recycling cavities.

Figure 2.1: Aerial view of the Advanced Virgo+ interferometer.

In this section, an overview of the opto-mechanical configuration of the interferometer and its working principle is given. The different optical cavities are described, as well as the mirror actuation system which maintains the cavities at their working point. Finally, an overview of the different noise sources that limit the sensitivity of the interferometer is given.

2.1 Working principle of Advanced Virgo+

As seen in section 1, gravitational waves make the distance between two falling test mass vary. The variation of the arm length is proportional to the length of the arms at rest. AdV+ is based on the Michelson interferometer. The mirrors Beam-Splitter (BS), North-End (NE) and West-End (WE) form the simple Michelson interferometer. The mirrors of the interferometer are suspended to a pendulum and are in vacuum, in order to insulate them from external noises. A Michelson interferometer converts the variations of the difference between the arm lengths into a power to be measured with a photodetector. Thus, the longer the arms of the interferometer, the strongest the signal.

However, the amplitude of the arm length variation are too tiny to be detected by a simple Michelson interferometer. To increase the effective length of the arms, and so amplify the GW signal, two mirrors has been installed at the beginning of each arms: North-Input (NI) and West-Input (WI). Thus, each arm forms a Fabry-Perot optical cavity. Which increase the optical gain by a factor $\sim$300.

At its working point, the interferometer is close to a dark fringe at its output. Thus, most of the laser power injected in the interferometer is sent back to the injection bench. Thus, a mirror has been placed at the input port of the interferometer, and send the reflected laser back in the interferometer. Which amplify the power at the photodetector and so the gravitational wave signal by a factor $\sim$40. This mirror is named Power-Recycling (PR). It forms with the input mirror the power recycling cavity.

A new mirror has been added after the O3 run at the asymmetric port of interferometer and form the Signal Recycling cavity (SR). This cavity lowers the effective arm cavity finesse and so broadens

the detector frequency bandwidth. The locations of the mirrors of the interferometer are shown on the scheme on figure 2.2.

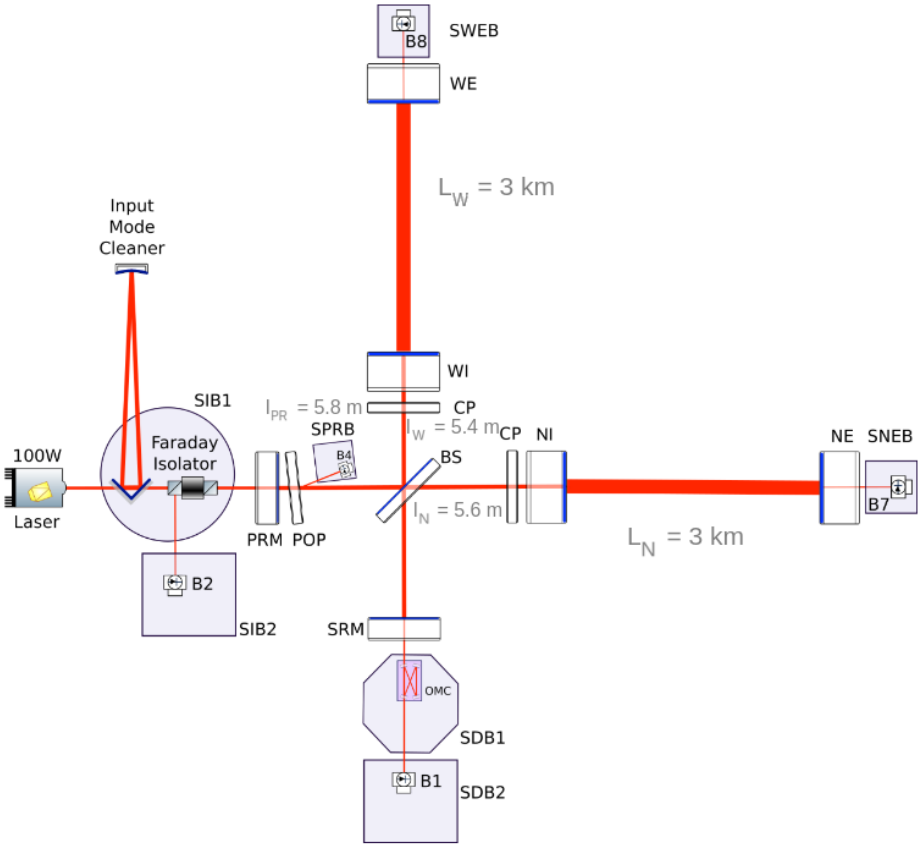

Figure 2.2: Scheme of the interferometer, with the length of each cavities and the position of each photodiodes.

The reflection and transmission rates of each mirrors, as well as other characteristics are given in the following table 2.1:

Mirror	NE	WE	NI	WI	BS	PR	SR
Power transmission	4.4 ppm	4.3 ppm	1.377%	1.375%	50.12%	4.835%	39.6%
Power reflection	99.9996%	99.9996%	98.623%	98.625%	49.88%	95.145%	60.4%
Amplitude transmission	0.210%	0.207%	11.735%	11.726%	70.795%	21.989%	62.929%
Amplitude reflection	99.9998%	99.9998%	99.309%	99.310%	70.625%	97.552%	77.717%
Diameter [mm]	350.36	350.33	350.36	350.37	550.33	350.36	350.31
Thickness [mm]	200.41	200.31	200.26	200.31	65.5	100.30	100.42
Mass [kg]	42.30	42.30	42.30	42.30	34.2	21.15	21.15

Table 2.1: Main characteristics of the interferometer mirrors.

2.1.1 The Michelson principle

A Michelson interferometer is a L-shaped interferometer with a 50% reflection 50% transmission beam splitter at its center and 100% reflection mirrors at the edges of each arm. A laser source hits the beam splitter which separates the beam in two. The reflected and transmitted beams go into each arm, are reflected by mirrors located at each end of the arm, and interfere on the beam splitter. The interference pattern can be observed by a photodetector located at the output port of the interferometer. A principle

diagram of the Michelson interferometer is shown in figure 2.3.

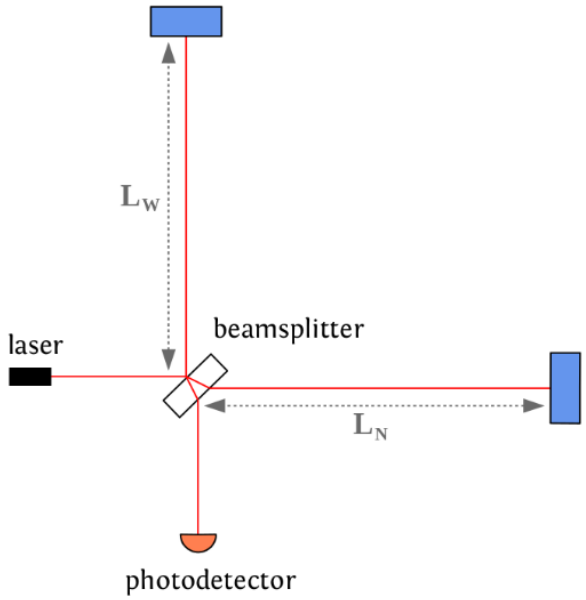

Figure 2.3: Scheme of a simple Michelson interferometer.

The electromagnetic field (EM field) is assumed to be a plane wave $E(\vec{x},t) = A \cdot e^{ik(z-ct)}$. By convention, the BS mirror is at $z = 0$, the time dependant term e^{-ikct} is present in every formula and will not be expressed. Each mirror has a high reflectivity surface and a anti-reflect surface. As shown in figure 2.4, when the EM field is reflected by a mirror with a reflectivity r, if the incident field E_i is coming from the high reflectivity surface, the reflected field has an opposite sign $E_r = -r.E_i$. If the incident field is coming from the anti-reflect surface, the reflected field has the same sign $E_r = r.E_i$ then the incident field.

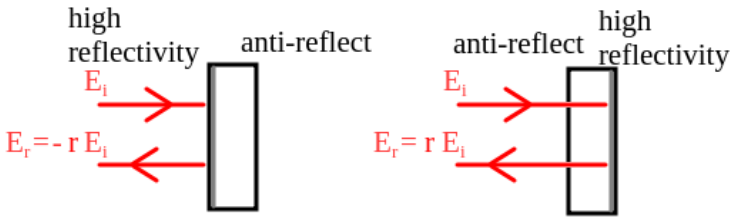

Figure 2.4: Sign of the field reflected by a mirror.

Let's $E_{in}(t)$ be the EM field at the input port of the interferometer. We suppose that the amplitude A_{in} of the input field is constant. Thus the input field is written as:

$$E_{in}(t) = A_{in} \tag{2.1}$$

After being splitted, the EM fields are written as:

$$E_{W,1}(t) = -A_{in} \cdot r_{BS} \tag{2.2}$$
$$E_{N,1}(t) = A_{in} \cdot t_{BS} \tag{2.3}$$

After a round trip across each arm, the EM fields are written as:

$$E_{W,2}(t) = A_{in} \cdot r_{BS} r_{WE} \cdot e^{i\Psi_W(t)} = A_{in} \cdot r_{BS} r_{WE} \cdot e^{ik \cdot 2L_W(t)} \tag{2.4}$$
$$E_{N,2}(t) = -A_{in} \cdot t_{BS} r_{NE} \cdot e^{i\Psi_N(t)} = -A_{in} \cdot t_{BS} r_{NE} \cdot e^{ik \cdot 2L_N(t)} \tag{2.5}$$

Where $\Psi_W(t) = k \cdot 2L_W(t)$ and $\Psi_N(t) = k \cdot 2L_N(t)$ are the phases of the reflected fields at the beam-splitter, and with $k = \frac{2\pi}{\lambda}$ the wave-number. Therefore, the transmitted EM field of the Michelson interferometer E_t is written as:

$$E_t(t) = r_{BS}E_{N,2}(t) + t_{BS}E_{W,2}(t) = E_{in}r_{BS}t_{BS} \cdot \left(-r_{NE}e^{i\Psi_N(t)} + r_{WE}e^{i\Psi_W(t)}\right) \tag{2.6}$$

And the reflected field $E_r(t)$ is written as:

$$E_r(t) = t_{BS}E_{N,2}(t) - r_{BS}E_{W,2}(t) = -E_{in} \cdot \left(t_{BS}^2 r_{NE}e^{i\Psi_N(t)} + r_{BS}^2 r_{WE}e^{i\Psi_W(t)}\right) \tag{2.7}$$

Let $P_{in} = A_{in}^2$ be the input power of the interferometer. Therefore, the power seen by the photodetector can be written as:

$$P_{out} = |E_t(t)|^2 = \frac{P_{max}}{2} \cdot [1 - C \cdot \cos(\Psi_W(t) - \Psi_N(t))] \tag{2.8}$$

Where $P_{max} = 2P_{in} \cdot (r_{BS}t_{BS})^2 \cdot (r_{WE}^2 + r_{NE}^2)$ is the maximum output power, and $C = 2\frac{r_{WE}r_{NE}}{r_{WE}^2+r_{NE}^2}$ is the contrast of the interferometer. The value of the contrast is $C = 1$ within $\pm 10^{-14}$, and the value of P_{max} is P_{in} within a relative error of 10 ppm. So the approximations $C = 1$ and $P_{max} = P_{in}$ will be used. As we can notice in formula (2.8), the power at the output is function of the phase shift between the two beams of the two arms $\Delta\Psi = \Psi_W(t) - \Psi_N(t)$.

In practice, when the interferometer is at rest, the output signal is almost in a dark fringe. If the interferometer was in dark fringe, the phase shift between the two reflected fields would be $\Delta\Psi = \Psi_W(t) - \Psi_N(t) \equiv 0[2\pi]$. A phase offset $\Delta\Psi_{DO} = 0.1$ mrad, also named "DARM-offset", is added to the differential arm length. Thus, the phase shift is written as:

$$\Delta\Psi \equiv \Delta\Psi_{DO} \ \ [2\pi] \tag{2.9}$$

And the power seen by the photodetector is:

$$P_{out} = \frac{P_{in}}{2} \cdot [1 - \cos(\Delta\Psi_{DO})] \tag{2.10}$$

When a gravitational wave passes through the interferometer, it makes the differential arm length vary by $d\Psi_{GW}$. It is assumed that $\delta\Psi_{GW} << \Delta\Psi_{DO} << \pi$, the second order Taylor's development of the output power gives us:

$$P_{out} = \frac{P_{in}}{2} \cdot \frac{1}{2}(\Delta\Psi_{DO} + d\Psi_{GW})^2 \sim \frac{P_{in}}{2} \cdot \left(\frac{1}{2}\Delta\Psi_{DO}^2 + \Delta\Psi_{DO} \cdot d\Psi_{GW}\right) = P_{out}^{(0)} + dP_{GW} \tag{2.11}$$

Thus the variation of the output power dP_{GW} due to the gravitational wave written as:

$$dP_{GW} = \frac{P_{in}}{2} \cdot \Delta\Psi_{DO} \cdot d\Psi_{GW} \tag{2.12}$$

The arms of AdV+ are 3 km long L_0, so the amplitude variation of the arm length due to a gravitational waves is $\delta L_{GW} = L_0 \cdot h \sim 10^{-19}$ m, the wave length of the laser is $\lambda = 1064$ nm and the input power of the interferometer is $P_{in} = 25$ W. The order of magnitude of the DARM offset is 0.1 mrad. Thus, in the case of a simple Michelson, the output power variation due to the gravitational wave is bounded by $dP_{GW}^{max} = 14 \times 10^{-15}\ W$, which is far below what a photodiode can detect. To amplify the gravitational wave signal, one can increase P_{in} the input power of the interferometer, or the DARM offset $\Delta\Psi_{DO}$. However, the output power is limited by the photodiodes at the output beam B1 of the interferometer. The other solution is to amplify $D\Psi_{GW}$ the phase shift between the two reflected beam.

2.1.2 Working principle of a Fabry-Perot cavity

To amplify the gravitational wave effect on the interferometer, Fabry-Perot cavities has been installed on the interferometer arms. A cavity is an optical resonator which amplifies the signal of the laser EM field, and thus, the sensitivity of the interferometer. The optical cavities of AdV+ are:

- **The Fabry-Perot arm cavities:** They are 3 km long cavities located in each arm of the interferometer. They are made with the end mirror and the input mirror of each arm. The laser beam travels back and forth across the arm cavity, which amplifies the phase offset due to a mirror displacement, which increase the sensitivity of Virgo.
- **The power recycling cavity:** It is made with the two input mirrors, NI and WI, the BS mirror and the PR mirror. The length of the cavity is $l_{PRCL} = l_{PR} + \frac{1}{2}(l_N + l_W)$. The PR cavity is set at the resonance for the reflected beam, so that it increases the input power on the BS mirror.
- **The signal recycling cavity:** It is made with the two input mirrors, NI and WI, the BS mirror and the newly installed SR mirror. The length of the cavity is $l_{SRCL} = l_{SR} + \frac{1}{2}(l_N + l_W)$. The SR cavity lowers the effective arm cavity finesse and broadens the detection frequency range of the interferometer.

A Fabry-Perot cavity consists in two mirrors M_1 and M_2, facing each other separated by a distance L. The transmission and reflection coefficients of the mirrors are t_1, t_2, r_1 and r_2. A scheme of a Fabry-Perot cavity is given in figure 2.5.

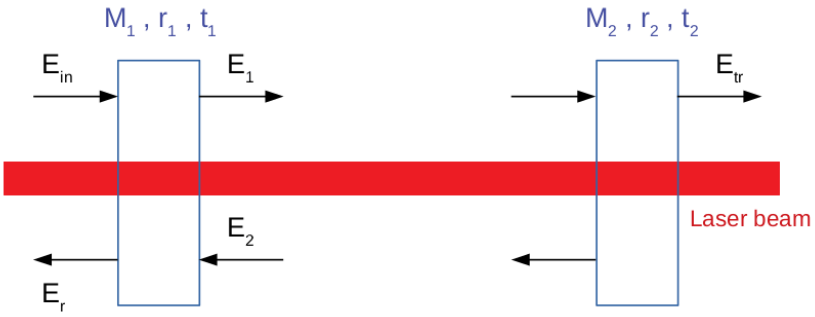

Figure 2.5: Scheme of a Fabry-Perot cavity.

The duration of a trip across the cavity is $\tau_{FP} = L/c$, where L is the length of the cavity and c is the speed of light. Let $k = \frac{2\pi}{\lambda}$ be the wave-number of the laser beam. We assume that the length of the cavity varies by δL so the EM fields associated with the laser light are:

- E_{in} the input EM field
- $E_r(t) = r_1 \cdot E_{in} + t_1 \cdot E_2(t)$ the reflected EM field
- $E_1(t) = t_1 \cdot E_{in} - r_1 \cdot E_2(t)$ the internal EM field going onward
- $E_2(t) = -r_2 \cdot E_1(t - 2\tau_{FP}) \cdot e^{i2k(L+\delta L(t))}$ the internal EM field going backward
- $E_t(t) = t_2 \cdot E_1(t - \tau_{FP}) \cdot e^{ik(L+\delta L(t))}$ the transmitted field

At each round trip across the cavity, the phase of the field is shifted by $2kL$. In the case the propagation time of the field in the cavity is neglected, one can express the internal field E_1 as functions of E_{in} by combining the expressions of the different EM fields:

$$E_1 = \frac{t_1}{1 - r_1 r_2 \cdot e^{i2kL}} E_{in} \tag{2.13}$$

So the power inside the cavity can be written as a function of the input laser power:

$$P_1 = |E_1|^2 = \frac{t_1^2}{1 - 2 \cdot r_1 r_2 \cdot \cos(2kL) + (r_1 r_2)^2} P_{in} = \frac{\left(\frac{t_1}{1 - r_1 r_2}\right)^2}{1 + \left(\frac{2\mathcal{F}}{\pi}\right)^2 \cdot \sin^2(kL)} P_{in} \tag{2.14}$$

The term $\mathcal{F} = \frac{\pi\sqrt{r_1 r_2}}{1 - r_1 r_2}$ represents the finesse of the cavity. Equation (2.14) shows that P_1 is maximized when the cavity length is a multiple of a half-wavelength $L = N\frac{\lambda}{2}$ with $N \in \mathbb{N}$, the cavity is at its resonant state. In the following, it is assumed that the cavity is at its resonance state, (i.e. $e^{i2kL} = 1$).

2.1.3 Response of the arm cavities

The arm cavities are 3 km long Fabry-Perot cavities located on each arm of AdV+. The west arm cavity is composed by the mirrors WI and WE mirrors, and the north arm cavity is composed by the NI and NE mirrors. These cavity amplify the gravitational wave signal of the interferometer by increasing the phase shift between the reflected EM fields of each arms.

The M_1 mirror is either WI are NI, its reflection and transmission rates is called r_I, the M_2 mirror is the end mirror with a reflection rate r_E and a transmission rate t_E. Since the cavities are 3 km long, the propagation time of the EM field in through cavity τ_{FP} is no longer neglected. It is assumed that the length of the cavity varies by δL from its resonant point. Thus, the field $E_r(t)$ reflected by the cavity is written as:

$$E_r(t) = E_{in} \cdot (r_I - r_E \cdot (r_I^2 + t_I^2) \cdot e^{i2k\delta L}) + r_I r_E \cdot e^{i2k\delta L} \cdot E_r(t - 2\tau_{FP}) \tag{2.15}$$

Let's write the reflected field as $E_r(t) = A_r \cdot e^{i\Psi_r(t)}$ with A_r the amplitude and $\Psi_r(t)$ the phase of the EM field. The phase of the field varies with the length of the cavity. The arm length variations due to the gravitational waves are tiny compare to the wavelength of the laser $\delta L << \lambda$. So the phase shift of the EM field is also tiny $\Psi_r << 2\pi$. Thus, the first order Taylor's expansion of equation (2.15) in $k\delta L(t)$ and $\Psi_r(t)$ gives us:

$$A_r(1+i\Psi_r(t)) = E_{in} \cdot (r_I - r_E \cdot (r_I^2 + t_I^2) \cdot (1 + i2k\delta L)) + r_I r_E \cdot (1 + i2k\delta L) \cdot A_r \cdot (1 + i\Psi_r(t - 2\tau_{FP})) \tag{2.16}$$

The term $(r_I^2 + t_I^2)$ is written as $1 - L_I$ where L_I is the losses of the input mirror, with $L_I = 60$ ppm [23]. The 0^{th} order term of the Taylor expansion is the constant state of reflected state. It gives the amplitude of the reflected field A_r as function of the injected field E_{in}.

$$A_r = \frac{r_I - r_E \cdot (1 - L_I)}{1 - r_I r_E} \cdot E_{in} = -r_{FP}^0 \cdot E_{in} \tag{2.17}$$

With $r_{FP}^0 = 0.991$ the reflectivity of the Fabry-Perot cavity at the resonant point.

The 1^{st} order terms gives us the phase equation:

$$\Psi_r(t) - r_I r_E \cdot \Psi_r(t - 2\tau_{FP}) = \left(\frac{r_E r_I^2 - r_E \cdot (1 - L_I)}{r_I - r_E \cdot (1 - L_I)} \right) \cdot 2k\delta L(t) \tag{2.18}$$

The Fourier transform of equation (2.18) gives:

$$\Psi_r(f) - r_I r_E \cdot e^{-i4\pi\tau_{FP} f} \cdot \Psi_r(f) = \left(\frac{r_E r_I^2 - r_E \cdot (1 - L_I)}{r_I - r_E \cdot (1 - L_I)} \right) \cdot 2k\delta L(f) \tag{2.19}$$

Therefore, the phase of the EM field reflected by the arm cavities is function of the arm length variation:

$$\Psi_r(f) = g_0 \cdot O^{FP}(f) \cdot 2k\delta L(f) \tag{2.20}$$

Where g_0 is the cavity amplification factor and $O^{FP}(f)$ is the normalized transfer function from a mirror displacement δL to the phase variation Ψ_r, also called the response of the Fabry-Perot cavity. Their expressions are:

$$g_0 = \frac{r_I}{r_E \cdot (1 - L_I) - r_I} + \frac{1}{1 - r_I r_E} \tag{2.21}$$

$$O^{FP}(f) = \frac{1 - r_I r_E}{1 - r_I r_E e^{-i4\pi f \tau_{FP}}} \tag{2.22}$$

The term g_0 is the amplification gain of the gravitational wave signal due to the arm cavity, its value is 289.7 on NE and 289.5 on WE. The transfer function $O^{FP}(f)$ is periodic over a spectral range of $\delta f_{FSR} = \frac{1}{2\tau_{FP}}$. At low frequency $f << \delta f_{FSR}$, the transfer function can be approximated with a simple pole function with a resonant frequency $f_p = \frac{1 - r_I r_E}{4\pi\tau_{FP} r_I r_E}$. The values of the pole frequencies are $f_p \sim 55$ Hz on both arm, however, this value will change due to the coupling with the other cavities.

$$O^{FP} \approx \frac{1}{1 + i\frac{4\pi \cdot \tau_{FP} \cdot r_I r_E}{1 - r_I r_E} \cdot f} = \frac{1}{1 + i\frac{f}{f_p}} \tag{2.23}$$

Figure 2.6 shows the optical response of a Fabry-Perot cavity and the simple pole approximation.

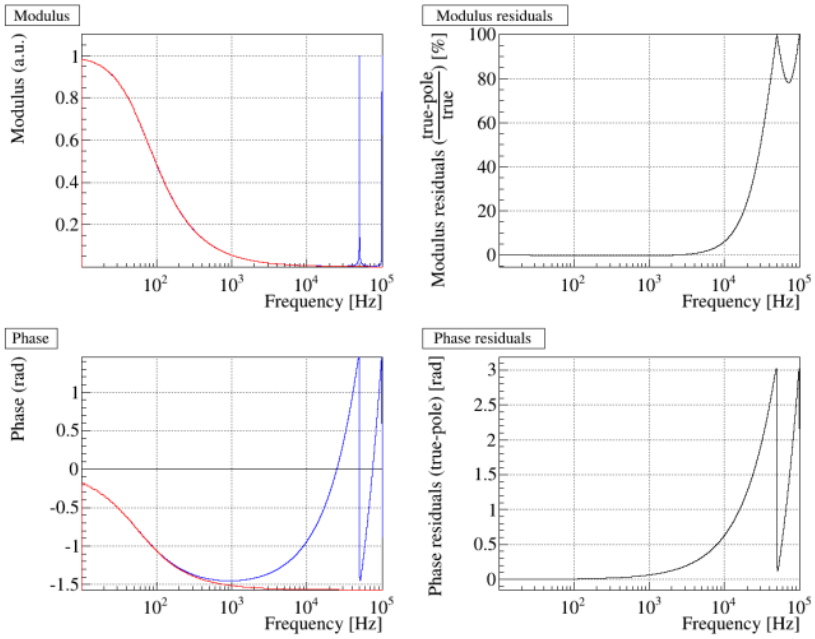

Figure 2.6: Left: optical response of a Fabry-Perot cavity and of its simple pole approximation . Right: residual between the true optical response of a Fabry-Perot cavity and its approximation

The error between the true response and its approximation is -0.28 % on the modulus at 1 kHz, and the error on the phase up to 10 kHz can be modeled as a simple delay $\phi = -2\pi f \tau_p$ with $\tau_p = -10$ µs. Thus the response of the cavity can be approximated with:

$$O^{FP}(f) = \frac{1}{1 + i\frac{f}{f_p}} \cdot \exp(-i2\pi\tau_p f) \tag{2.24}$$

If the end mirror moves by dL_E toward the end of the arm, the resulting phase shift is seen with the delay of τ_{FP} due to the propagation of the field in the arm cavity. And if the input mirror moves by dL_I, the length of the cavity is reduced. Thus, the phase shift due to the displacements dL_E and dL_I of the mirror is expressed by:

$$d\Psi_r(f) = g_0 \cdot O^{FP}(f) \cdot 2k \cdot (e^{-i2\pi\tau_{FP} f} \cdot dL_E(f) - dL_I(f)) \tag{2.25}$$

The Fabry-Perot cavity can be modeled as a simple mirror with a complex reflectivity r_{FP} written as:

$$r_{FP} = r^0_{FP} \cdot e^{i \cdot d\Psi_r(f)} \tag{2.26}$$

This model is used to modeled the behaviour of the Michelson interferometer with Fabry-Perot cavities in the arms.

2.1.4 Michelson interferometer with arm cavities

The Michelson interferometer with Fabry-Perot cavities arms can be modeled with a simple Michelson interferometer whose end mirrors have complex reflectivities r_N and r_W written as:

$$r_N = r^0_{FP} \cdot e^{id\Psi_{r,N}(f)} \tag{2.27}$$

$$r_W = r^0_{FP} \cdot e^{id\Psi_{r,W}(f)} \tag{2.28}$$

With $r^0_{FP} = \frac{r_E - r_I}{1 - r_I r_E}$ the reflectivity of the Fabry-Perot cavity at its resonant point. The length of the arms of the Michelson are called l_N and l_W. We assume that the BS mirror divide the laser beam into two beams with the same power $r_{BS} = t_{BS} = \frac{1}{\sqrt{2}}$. The field transmitted by the Michelson is written as:

$$E_t(f) = -E_{in} r^0_{FP} \frac{1}{2} \cdot \left(e^{i2kl_N + id\Psi_{r,N}(f)} - e^{i2kl_W + id\Psi_{r,W}(f)} \right) = -E_{in} r^0_{FP} \frac{1}{2} \cdot \left(e^{i\Psi_N(f)} - e^{i\Psi_W(f)} \right) \quad (2.29)$$

The terms $\Psi_N(f) = 2kl_N + d\Psi_{r,N}(f)$ and $\Psi_W(f) = 2kl_W + d\Psi_{r,W}(f)$ represent the phase of the field coming respectively from the north arm and the west arm at the BS mirrors. When the interferometer is at rest, the lengths of the small Michelson arms are tuned at the DARM-offset, so $2k \cdot (l_N - l_W) \equiv \Delta\Psi_{DO}\ [2\pi]$. The phase of the fields varies by $d\Psi_N(f)$ and $d\Psi_W(f)$ from the resting point. These terms can be written as function of the displacement of the mirrors with the following formula:

$$d\Psi_N(f) = 2k \cdot (g_0 \cdot O^{FP}(f) \cdot e^{-i2\pi\tau_{FP} f} \cdot dL_{NE} + (1 - g_0 \cdot O^{FP}(f)) \cdot dL_{NI}) \quad (2.30)$$

$$d\Psi_W(f) = 2k \cdot (g_0 \cdot O^{FP}(f) \cdot e^{-i2\pi\tau_{FP} f} \cdot dL_{WE} + (1 - g_0 \cdot O^{FP}(f)) \cdot dL_{WI}) \quad (2.31)$$

In conclusion, the variation output power of the interferometer $dP_{out}(f)$ can be expressed as function of the phase shift between the field coming from each arm $d\Psi(f)$ using equation (2.12):

$$dP_{out}(f) = \frac{P_{in}}{2} \cdot \Delta\Psi_{DO} \cdot (d\Psi_N(f) - d\Psi_W(f)) = \frac{P_{in}}{2} \cdot \Delta\Psi_{DO} \cdot d\Psi(f) \quad (2.32)$$

With:

$$\begin{aligned} \Delta\Psi(f) = 2k \cdot (& g_0 \cdot O^{FP}(f) \cdot e^{-i2\pi\tau_{FP} f} \cdot dL_{NE} \\ & + (1 - g_0 \cdot O^{FP}(f)) \cdot dL_{NI} \\ & - g_0 \cdot O^{FP}(f) \cdot e^{-i2\pi\tau_{FP} f} \cdot dL_{WE} \\ & - (1 - g_0 \cdot O^{FP}(f)) \cdot dL_{WI}) \end{aligned}$$

The optical responses of the interferometer $O_m(f)$ are the power variation at the output port of the interferometer as function of the displacement of the mirror m. The optical responses of the mirrors NE, WE, NI and WI are written as:

$$O_{NE}(f) = P_{in} \cdot \Delta\Psi_{DO} \cdot k \cdot g_0 \cdot O^{FP}(f) \cdot e^{-i2\pi\tau_{FP} f} \quad (2.33)$$

$$O_{WE}(f) = -P_{in} \cdot \Delta\Psi_{DO} \cdot k \cdot g_0 \cdot O^{FP}(f) \cdot e^{-i2\pi\tau_{FP} f} \quad (2.34)$$

$$O_{NI}(f) = P_{in} \cdot \Delta\Psi_{DO} \cdot k \cdot (1 - g_0 \cdot O^{FP}(f)) \quad (2.35)$$

$$O_{WI}(f) = -P_{in} \cdot \Delta\Psi_{DO} \cdot k \cdot (1 - g_0 \cdot O^{FP}(f)) \quad (2.36)$$

The frequency responses are displayed in figure 2.7. The optical response of the input mirror is the same as the optical response of the end mirror, but the gain is slightly lower due to the coupling with the Michelson. In both optical response, a pole at ∼55 Hz is visible. The response of the end mirror is also delayed by 10 µs with respect to the response of the input mirror due to the propagation of the EM field in the arm.

2.1.5 Optical response of the BS mirror

To compute the optical response of the interferometer to the displacement of BS mirror, one has to assume that the Fabry-Perot are at their resonant point, and that the positions of the arm mirrors are fixes. The length of the cavity L is a multiple of the half wavelength, $L \equiv 0[\frac{\lambda}{2}]$. If the BS mirror moves, the phase $\Psi_{in}(t)$ of the EM field E_{in} entering the Fabry-Perot cavity varies. With these conditions, the EM field reflected by the cavity $E_r(t)$, and the internal fields going onward $E_1(t)$ and backward $E_2(t)$ can be written as:

$$E_r(t) = r_I \cdot E_{in}(t) + t_I \cdot E_2(t) \quad (2.37)$$

$$E_1(t) = t_I \cdot E_{in}(t) - r_I \cdot E_2(t) \quad (2.38)$$

$$E_2(t) = -r_E \cdot E_1(t - 2\tau_{FP}) \quad (2.39)$$

By combining these equations, the reflected field can be expressed as function of the incident field E_{in} with the equation:

$$E_r(t) = r_I \cdot E_{in}(t) - r_E \cdot (r_I^2 + t_I^2) \cdot E_{in}(t - 2\tau_{FP}) + r_E r_I \cdot E_r(t - 2\tau_{FP}) \tag{2.40}$$

The term $(r_I^2+t_I^2)$ is written as $1-L_I$ where L_I is the losses of the input mirror, with $L_I = 60$ ppm [23]. Let's write the reflected field as $E_r(t) = A_r \cdot e^{i\Psi_r(t)}$ and the incident field as $E_{in}(t) = A_{in} \cdot e^{i\Psi_{in}(t)}$, and expand the equation (2.40) to the first order in Ψ. The 0^{th} order terms satisfy the equation:

$$A_r = \frac{r_I - r_E \cdot (1 - L_I)}{1 - r_I r_E} \cdot A_{in} \tag{2.41}$$

And the 1^{st} order terms satisfy:

$$A_r \cdot i\Psi_r(t) = A_{in} \cdot (r_I \cdot i\Psi_{in}(t) - r_E \cdot (1 - L_I) \cdot i\Psi_{in}(t - 2\tau_{FP})) + r_I r_E \cdot A_r \cdot i\Psi_r(t - 2\tau_{FP}) \tag{2.42}$$

Combining the equations (2.41) and (2.42) gives us the phase of the reflected field Ψ_r as function of the phase of the incident field Ψ_{in}.

$$\Psi_r(t) = \frac{1 - r_I r_E}{r_I - r_E \cdot (1 - L_I)} \cdot (r_I \cdot \Psi_{in}(t) - r_E \cdot (1 - L_I) \cdot \Psi_{in}(t - 2\tau_{FP})) + r_I r_E \cdot \Psi_r(t - 2\tau_{FP}) \tag{2.43}$$

The Fourier transform of equation (2.43) gives us the response of the Fabry-Perot cavity to a phase shift of the input field:

$$\Psi_r(f) = \Psi_{in}(f) \cdot \frac{1 - r_I r_E}{r_I - r_E \cdot (1 - L_I)} \cdot \frac{r_I - r_E \cdot (1 - L_I) \cdot e^{-i4\pi\tau_{FP} f}}{1 - r_I r_E \cdot e^{-i4\pi\tau_{FP} f}} = \Psi_{in}(f) \cdot \Phi^{FP}(f) \tag{2.44}$$

The frequency response of the cavity $\Phi^{FP}(f)$ to a phase shift of the input field $\Psi_{in}(f)$ can be approximated at low frequency $4\pi\tau_{FP} f << 2\pi$ with:

$$\Phi^{FP}(f) \sim \frac{1 - i\frac{f}{f'_z}}{1 + i\frac{f}{f_p}} \tag{2.45}$$

With $f_p = \frac{1-r_I r_E}{4\pi\tau_{FP} r_I r_E}$ and $f'_z = \frac{r_E \cdot (1-L_I) - r_I}{4\pi\tau_{FP} r_E \cdot (1-L_I)}$. The value of f_p is the same as the pole frequency of west arm cavity. If the BS mirror moves by $dL_{BS}(f)$, the phase of the field entering the cavity is shifted by $\Psi_{in} = k \cdot dL_{BS}(f)$ and the phase of the field reflected by the cavity is shifted by $\Psi_r = \Phi(f) \cdot k \cdot dL_{BS}$. The phase of the reflected field at the BS mirror is also shifted by $k \cdot dL_{BS}$ due to the variation of the distance between BS and WI. Using equation (2.12), the power variation of the interferometer due to the movement of BS is written as function of the displacement of BS:

$$dP_{out}(f) = \frac{P_{in}}{2} \cdot \Delta\Psi_{DO} \cdot (\Phi^{FP}(f) + 1) \cdot k \cdot dL_{BS} \tag{2.46}$$

The term $\Phi^{FP}(f) + 1$ can be written as:

$$\Phi^{FP}(f) + 1 = 2 \cdot \frac{1 - i\frac{f}{f_z}}{1 + i\frac{f}{f_p}} \tag{2.47}$$

The value of f_z is $f_z = \frac{-2}{1/f_p - 1/f'_z} = 6.9$ kHz, however, the low frequency approximation $4\pi\tau_{FP} f << 2\pi$ is not valid at this frequency. Thus, the optical response of the interferometer to a displacement of the BS mirror can be written as:

$$O_{BS}(f) = \frac{P_{in}}{2} \cdot \Delta\Psi_{DO} \cdot (\Phi^{FP}(f) + 1) \cdot k \tag{2.48}$$

In the bandwidth [1 Hz, 10 kHz] the frequency response of the BS mirror is similar to the frequency response of the input mirror, buy with a gain ∼300 times lower, because the response of BS is not amplified by the arm cavities. The frequency response is shown in figure 2.7.

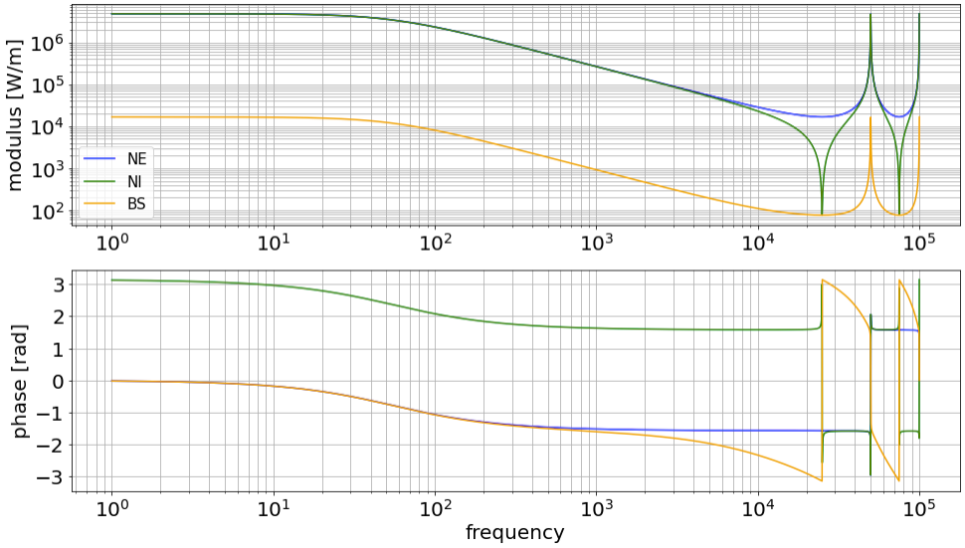

Figure 2.7: Simulation of the optical responses of the NE, NI and BS mirrors in the frequency bandwidth [1 Hz, 100 kHz].

2.1.6 Power recycling cavity

The PR mirror sends back the power reflected by the interferometer, to the injection system, to the interferometer. Its reflection and transmission coefficients are r_{PR} and t_{PR}. It forms an optical cavity with the Michelson interferometer, which increase the laser power on the BS, and so the sensitivity of the interferometer. This cavity is called "power recycling cavity", and it is schematized in figure 2.8.

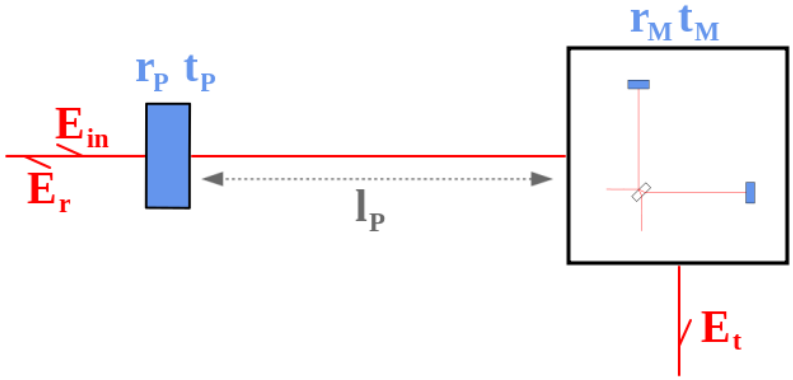

Figure 2.8: Scheme of the PR cavity made of the Michelson interferometer modelized as a simple mirror, and of the PR mirror.

The Michelson interferometer is modeled as a mirror with a complex reflection rate r_M, whose value can be computed using equation (2.7), assuming that $r_{BS} = t_{BS} = \frac{1}{\sqrt{2}}$, and that the interferometer is at the DARM offset $\cos(k(l_N - l_W)) = \cos(\Delta\Psi_{DO}) \sim 1$.

$$r_M = r_{FP}^0 e^{ik(l_N+l_W)} \cdot e^{\frac{i}{2}(d\Psi_{r,N}+d\Psi_{r,W})} \tag{2.49}$$

Thus the PR cavity can be modeled with a Fabry-Perot cavity, where the mirror M_1 is the PR mirror, and M_2 is the mirror model of the Michelson, and the length of the cavity l_P is the distance between the PR and BS mirrors. Since $l_P \sim 4.9$ m, the propagation time of the field across the cavity is neglected. The power of the cavity amplifies the gravitational wave signal by increasing the maximum power at the input of the interferometer. The coupling between the arm cavities and the PR cavity is neglected, so the reflection rate of the Michelson is approximated by $r_M \sim r_{FP}^0 e^{ik(l_N+l_W)}$. Using equation (2.13), the

EM field inside the power recycling cavity is expressed by:

$$E_1 = \frac{t_{PR}E_{in}}{1 - r_{PR}r_M e^{i2kl_p}} \sim \frac{t_{PR}E_{in}}{1 - r_{PR}r^0_{FP}e^{ik(2l_p+l_N+l_W)}} \tag{2.50}$$

And so the power inside the cavity is.

$$P_1 = |E_1|^2 = \frac{\left(\frac{t_{PR}}{1-r_{PR}r^0_M}\right)^2}{1 + \left(\frac{2\mathcal{F}_P}{\pi}\right)^2 \cdot \sin^2(kl_p + \frac{1}{2}k(l_N + l_W))} P_{in} \tag{2.51}$$

The resonant point of the cavity is reached when the cavity length $l_{PRCL} = l_p + \frac{1}{2}(l_N + l_W)$ satisfies $kl_{PRCL} \equiv 0\ [\pi]$. Now it is assumed that the length of the PR cavity varies by dl_P around the resonant point. Because of the PR cavity, the laser power at the beam splitter is amplified by $G_p = \left(\frac{t_{PR}}{1-r_{PR}r^0_{FP}}\right)^2 = 43$. The term $\mathcal{F}_P = \frac{\pi\sqrt{r_{PR}r^0_{FP}}}{1-r_{PR}r^0_{FP}}$ is called the finesse of the PR cavity. So the power transmitted by the cavity $P_{t,PR} = P_1 \cdot |t_M|^2$ is:

$$P_{t,PR} = \frac{G_P t_M^2}{1 + \left(\frac{2\mathcal{F}_P}{\pi}\right)^2 \cdot \sin^2(dl_P)} P_{in} \tag{2.52}$$

If the other mirrors are at the resting point, the second order Taylor's development of the formula (2.51) in dl_P is:

$$P_t(dl_P) \sim t_M^2 G_P \cdot \left(1 - \left(\frac{2\mathcal{F}_p}{\pi} \cdot k \cdot dl_P\right)^2\right) \cdot P_{in} \tag{2.53}$$

In conclusion, the output power of the interferometer doesn't depend on the PR mirror movement. This results is relevant only if the mirrors are perfectly aligned and at their resting position. In reality, if the position of the mirrors change a bit, a term representing the coupling between the PR cavity and the arm cavities appears, and the optical response of the PR mirror is no longer null and varies with the alignment of the mirrors. The PR cavity thus improved the sensitivity of Virgo by a factor 43. This value is computed using only the losses of the input mirrors $L_I = 60$ ppm. In reality, the losses of the BS and PR mirrors as well as the losses of the correction plates (CP) have to be taken into account in the model. Which lower the gain of the PR cavity to ∼37.

2.1.7 Signal recycling cavity

After the O3 run, the SR mirror has been placed at the asymmetric port of the Michelson interferometer at a distance l_s, and form the signal recycling cavity (SR cavity) with the input mirrors of the interferometer. The length of the SR cavity can be tuned to increase the sensitivity of the interferometer or expand its bandwidth.

The EM field inside the arm cavities sees the input mirror as an equivalent mirror with a complex reflectivity rate. The values of the equivalent reflectivity of the input mirrors r'_I can be written as function of the reflectivity of the SR mirror r_{SR} and of the input mirrors r_{NI} and r_{WI}, and of the length of the SR cavity $l_{SRCL} = l_s + \frac{1}{2}l_+$.

$$r'_I = \frac{r_I + r_{SR} \cdot (1 - L_I) \cdot e^{i2kl_{SRCL}}}{1 + r_I r_{SR} \cdot e^{i2kl_{SRCL}}} \tag{2.54}$$

Thus, the new optical responses of the arm cavities can be obtained by replacing r_I by r'_I in the equations (2.21) and (2.22) of the gain g_0 and response O^{FP} of the arm cavity. The signal recycling changes the pole frequency of the cavity by replacing r_I by r'_I in the formula of the pole frequency $f_p = \frac{1-r'_I r_E}{4\pi\tau_{FP}r'_I r_E}$.

In practice, the SR cavity is tuned so the carrier laser is anti-resonant in the cavity. So the cavity length satisfies $kl_{SRCL} \equiv \frac{\pi}{2}[\pi]$. The values of the equivalent reflectivity of the input mirrors are $r'_{NI} = 94.630\%$

and $r'_{WI} = 94.636\%$. Thus the value of the new pole frequencies are 451 Hz on NE and NI and 443 Hz on WE, WI and BS. The zero frequency of the optical response of the BS mirror is 15.7 kHz.

2.1.8 Control of the longitudinal position of the mirror

In order to keep the interferometer at its working point, the length of the cavities is controlled, and so the longitudinal position of the mirrors. The angular position of the mirror is also controlled, but we will focus only on their longitudinal positions, assuming that the mirrors are perfectly aligned. In practice, the signals which are controlled are the degrees of freedoms which are combination of the different cavity lengths. The different controlled degrees of freedom are:

- $DARM = L_N - L_W$ is the differential arm length of the arm cavities.
- $CARM = L_N + L_W$ is the common arm length of the arm cavities.
- $MICH = l_N - l_W$ is the differential arm length of the small Michelson interferometer made with the input mirrors.
- $PRCL = l_{PR} + \frac{1}{2}(l_n + l_w)$ is the power recycling cavity length.
- $SRCL = l_{SR} + \frac{1}{2}(l_n + l_w)$ is the signal recycling cavity length.
- $SSFS$ is the second stage frequency stabilization of the laser frequency.

To monitor the longitudinal position of the different mirrors, some sidebands are generated by modulating the phase of the laser. Some of these sidebands are resonant in some cavities and anti-resonant in the others. The frequency of the sideband is close to the frequency of the carrier beam, so they interfere. The interference pattern is seen by the different photodiodes, in the "RF" channel, sampled at 400 MHz. This signal is then demodulated to produce the in-phase and the quadrature signals.

The list of the sidebands are the following:

- Carrier
- 6 MHz sideband
- 8 MHz sideband
- 56 MHz sideband

2.2 Detector description

The Advanced Virgo+ detector is a dual recycled Michelson Interferometer. The optical layout of the detector is schematized in figure 2.2.

The detector is made of the laser source, the input mode cleaner cavity, the different suspended mirrors, the output mode cleaner cavity, the different optical benches with photodiodes monitoring the position of the mirrors.

2.2.1 Laser source

The laser of AdV+ is a Nd:YAG laser with a wavelength of 1064 ± 0.1 nm. The laser source is designed to deliver a maximum power of 130 W. During the O4 run, the average power at the laser source is $\sim$50 W, which corresponds to 25 W at the entrance of the interferometer and to $\sim$200 kW stored in the arms of the interferometer. The laser is frequency modulated in order to create the sidebands used to keep the cavities at their working point.

2.2.2 Suspension system

The mirror is suspended to the marionette, which is suspended to a serie of mechanical passive filters named the "super-attenuator". The resonant frequency of these filters is below 1 Hz. Thus the seismic noise is lowered in the frequency band of interest. A drawing of the super-attenuator is shown in figure 2.9.

- The longitudinal displacements of the mirror are attenuated by the filters by a factor $\left(\frac{f_r}{f}\right)^{2N}$. There are $N = 7$ filters (from filter 0 to the mirror), so the reduction factor of the seismic noise is $\left(\frac{f_r}{f}\right)^{14}$ for frequencies above 10 Hz.
- The vertical displacements are attenuated by mechanical springs above their resonant frequency.
- The rotation of the mirror is attenuated by the high moment of inertia of the mechanical attenuators. Also, the suspension wires between each filter are located as close as possible to their center of mass.

The set consisting of the mirror and the marionette is named the "payload". The payload is suspended to the last stage filter F7. The position of the marionette and the mirror can be controlled thanks to electromagnetic actuators which are described in section 2.3.

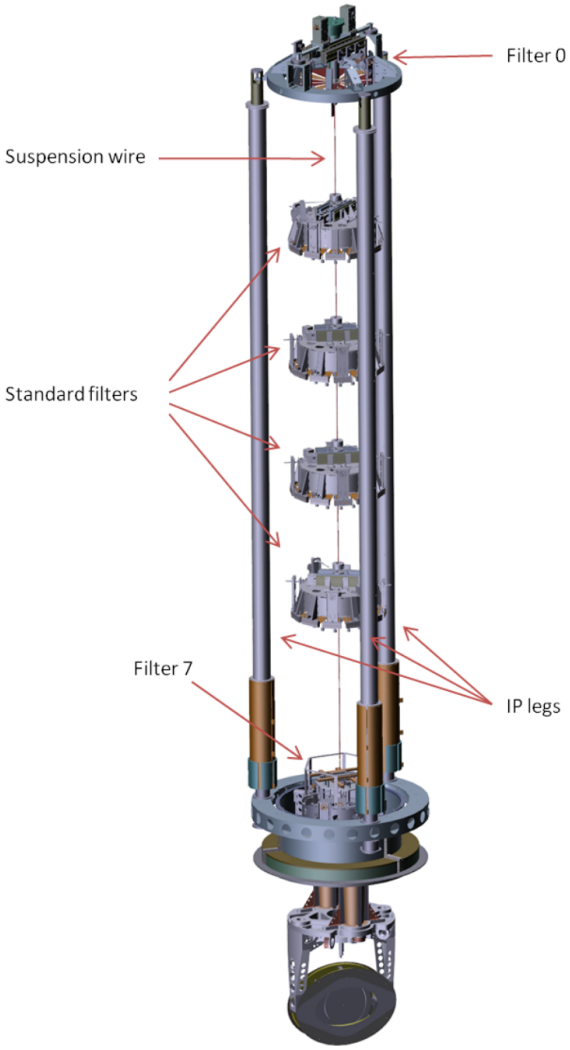

Figure 2.9: Sketch of the super-attenuator of Virgo.
It is composed of a series of filters suspended to each other. The payload is suspended to the last filter. It is composed of the marionette and the mirror.
source: Advanced Virgo+ design report [2]

The super-attenuator is suspended to the "filter 0" which is supported by 6 m long legs. The legs act as an active filter that isolates the suspension system from the seismic noise with a second order low-pass filter.

2.2.3 Input mode cleaner cavity

The laser source is not isolated from the seismic noise as are the mirrors. So the seismic noise induces variations in the laser beam position and changes the alignment the laser source with the interferometer, which produces beam jitters.

Only the TEM_{00} is sensitive to the gravitational waves. The higher order modes only produce frequency noise in the gravitational wave signal. In order to mitigate beam jitter, the input laser beam passes through the input mode cleaner cavity (IMC). This cavity is 150 m long, it consists in three mirrors under vacuum, arranged in a triangular configuration. Two of them are mounted on the suspended bench SIB1.

2.2.4 Output mode cleaner cavity

The laser beam can be decomposed into Transverse Electro-Magnetic (TEM) modes. A perfectly gaussian beam contains only the mode TEM_{00}. Only the TEM_{00} is sensitive to the gravitational waves. The higher orders only produce frequency noise in the gravitational wave signal. The optical defaults of the interferometer produce high order TEM modes that pollute the laser beam. Since only the TEM_{00} mode is observed by the detection system, the other modes have to be mitigated with the output mode cleaner (OMC). The sidebands of the laser are also rejected by the OMC, since the gravitational wave signal is contained only in the carrier signal. The OMC is a silicate block a few cm long. The length of the OMC is controlled in temperature with a Peltier cell and a piezo-controller, in order to keep the carrier at resonance.

2.2.5 Squeezing system

The interferometer sensitivity is limited by the radiation pressure noise of the laser at low frequency, and by the shot noise at high frequency. During O3 run, a frequency independent squeezing system was installed on the detector, which reduced the shot noise, and increased the sensitivity at high frequency. However, it also increased the laser pressure noise at low frequency.

The frequency depend squeezing system has been installed next to the detection system, after the O3 run. It squeezes the vacuum states of the light injected by the dark port of the interferometer in a way that the radiation pressure is reduced at low frequency and the shot noise is reduced at high frequency.

2.3 Mirror electromagnetic actuators

The longitudinal positions of the mirrors are controlled in order to maintain the different cavities at their resonant point. To control their position, electromagnetic actuators has been installed on the mirrors and marionettes of all the mirrors of the interferometers.

2.3.1 Description of the actuators

The electromagnetic (EM) actuators consist in pairs of coils attached to an actuation cage and magnets glued on the mirrors. To control the longitudinal position of each mirror, there are 4 pairs of coil-magnets on the mirror and 2 pairs on the marionette. A sketch of the mirror with its actuation cage is given in figure 2.10.

Each coil of the EM actuator is driven by a coil driver. All the coil drivers of the marionette receive the same signal from a digital signal processor (DSP) dedicated to the marionette. In the same way, the coil drivers of the mirror receive the signal from a DSP of the mirror. The input signals of the DSPs come from a real-time PC (RTPC).

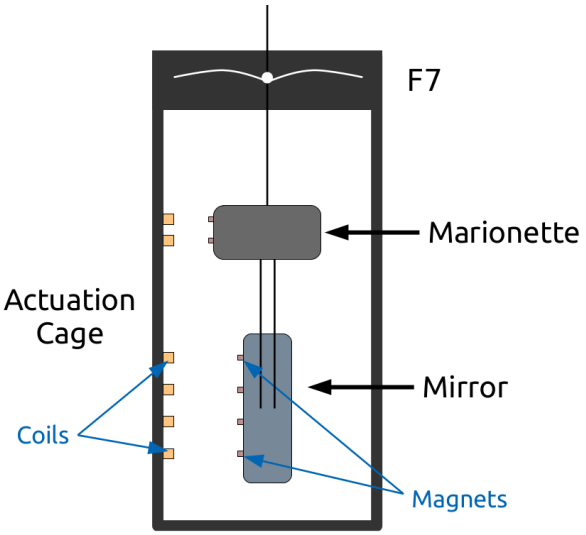

Figure 2.10: Sketch of the EM actuator of a mirror with its actuation cage. The mirror is suspended to the marionette which is suspended to a series of filters not shown in this figure.

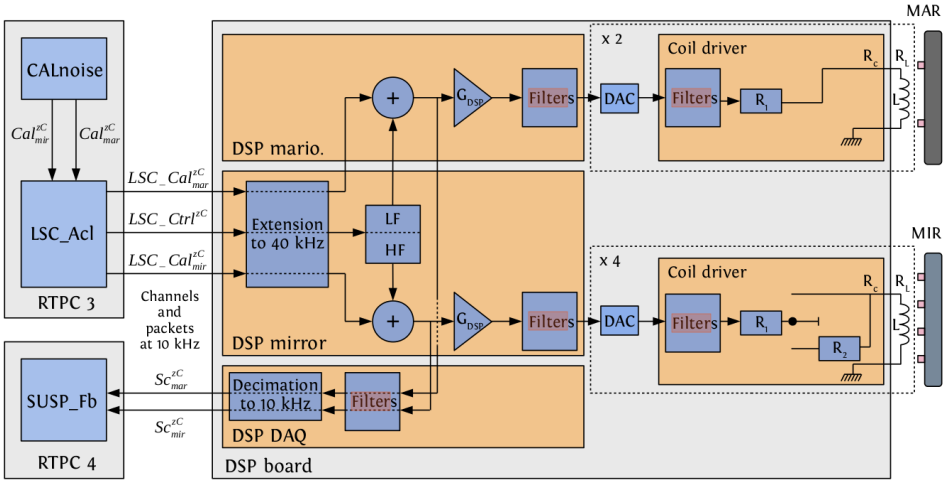

Figure 2.11: Electronic chain of the EM actuators that control the position of the mirror and the marionette.

Figure 2.11 shows the electronic chain from the command signal to the actuator. The command signal of the coil drivers is computed from a control signal LSC_Ctrl and calibration signals $LSC\_Cal_{mir/mar}$. The control signal is computed from the error signals of the different degrees of freedom. The calibration signals are digitally generated by an online process named $CALnoise$. The low frequency band $f < 30\ Hz$ of LSC_Ctrl is sent to the DSP of the marionette with the calibration signal LSC_Cal_{mar}, then these two signals are sum. The result is the signal of the marionette actuator Sc_{mar}. The high frequency band $f > 30\ Hz$ is summed with the LSC_Cal_{mir}, the result is the signal of the mirror actuator Sc_{mir}. The signals are shaped by the DSP digital filter, converted into an analog voltage signal and sent to the coil drivers. The coil drivers are composed of an analog filter, and the coil itself which acts as a RL circuit, where L is the coil inductance and R the total series resistance. The filter and the values of L and R depend of the configuration of the coil driver.

The coils drivers have different configurations with different dynamics and noise level. The configurations with the highest dynamics also have the highest noise level. The different configurations of the coil drivers are used sequentially at the different steps of the lock of the interferometer to its nominal configuration. The configurations of the coil drivers are listed below:

- **High Power (HP):** This configuration has the highest dynamic, but also the highest noise level. It is used at the first steps of the lock acquisition of the interferometer to bring roughly the mirrors at their working point.
- **Low Noise (LN) / Low Noise 1 (LN1) / Low Noise 2 (LN2):** These configurations varies from one mirror to another. These configurations have a noise level lower than the HP configuration, but has a lower dynamic. They are used at different steps of the lock acquisition and to keep the interferometer locked.
- **Open:** The mirrors are not controlled but the the noise level of this configuration is the lowest.

The values of the coil inductance L and resistance R associated to each actuator configuration is given in table 2.3.

2.3.2 Response of the electromagnetic actuators

The frequency response of the EM actuator A_{EM} in [m/V] is composed by the frequency response of the electronic part A^{elec} in [N/V] and the mechanical response of the mirror $A^{mech}_{mir/mar}$ in [m/N].

The mechanical response $A^{mech}_{mir/mar}$ of the EM actuator in [m/N] is the mirror displacement as function of the force applied on it, or on the marionette. Since the calibration of the detector is done above 10 Hz, we do not consider a realistic model of the actuator but an approximation valid above 10 Hz. Thus, the mechanical responses of the actuators are modeled with simple pendulum approximation.

The mirror is suspended to the marionette, with wires of l_{mir} long. Thus the response of the mirror to a force applied on it is modeled as the response of a simple pendulum with a resonant frequency $f_p = \frac{1}{2\pi}\sqrt{\frac{g}{l_{mir}}}$ and a quality factor $Q_p = 1000$. The normalized mechanical response is:

$$A^{mech}_{mir}(f) \propto \frac{1}{1 + \frac{i}{Q_p}\frac{f}{f_p} - \left(\frac{f}{f_p}\right)^2} \tag{2.55}$$

The marionette is suspended to the last filter level F7. So the response of the mirror to a force applied on the marionette is the product of two simple pendulums. Thus the mechanical response is modeled with a double pendulum response, with a resonant frequency $f_p = \frac{1}{2\pi}\sqrt{\frac{g}{l_{mir}}}$ and a quality factor $Q_p = 1000$:

$$A^{mech}_{mar}(f) \propto \frac{1}{\left(1 + \frac{i}{Q_p}\frac{f}{f_p} - \left(\frac{f}{f_p}\right)^2\right)^2} = \left(A^{mech}_{mir}(f)\right)^2 \tag{2.56}$$

Because the approximations used above are valid only for the frequencies above 10 Hz, the gains of the mechanical responses (G^{mech}_{mir} and G^{mech}_{mar}) cannot be estimated precisely using the standard formula of the pendulum gain:

$$G^{mech}_{mir/mar} = \frac{l_{mir}}{M_{mir/mar} \cdot g} \tag{2.57}$$

However, the modulus response at 100 Hz of the mechanical response of the mirror EM actuator can be estimated using the high frequency approximation $f >> f_p$ of formula (2.55):

$$A^{mech}_{mir}(f) \sim \frac{-1}{(2\pi f)^2 \cdot M_{mir}} \tag{2.58}$$

Thus, the theoretical value of the gain of the mirror actuator response at 100 Hz is given in table 2.2.

The frequency response of the electronic part A^{elec} in [N/V] is the force applied on the mirror by the EM actuator as a function of the input voltage of the actuator. The EM actuator consists in a RL circuit, so its response is given by a simple pole:

$$A_{RL}(f) \propto \frac{1}{1 + i\frac{f}{f_{elec}}} \tag{2.59}$$

mir	l_{mir}[m]	M_{mir}[kg]	f_p[Hz]	$A^{mech}_{mir}(f = 100\ Hz)$[m/N]
NI, WI	0.7	42.3	0.6	6.0e-8
PR	0.7	21.2	0.6	1.2e-7
SR	0.7	21.2	0.6	1.2e-7
BS	0.7	41.7	0.6	6.1e-8
NE, WE	0.7	42.3	0.6	6.0e-8
mar	l_{mar}[m]	M_{mar}[kg]	f_p[Hz]	$A^{mech}_{mar}(f > 10\ Hz)$[m/N]
BS	1.2	59.5	0.46	$\propto f^{-4}$
NE, WE	1.125	100	0.47	$\propto f^{-4}$

Table 2.2: Values of the parameters of the mechanic response ($l_{mir/mar}$, $M_{mir/mar}$), with the associated pole frequency and the gain at 100 Hz

Where $f_{elec} = \frac{R}{2\pi L}$. The gain of the electronic response G^{elec} is the product of the gain of the DSP G^{DSP}, the gain of the coils R^{-1}, the number of coil in the actuator N_{coil} and the coupling between the coil and the magnet α. Thus:

$$A^{elec}(f) = \frac{G^{elec}}{1 + i\frac{f}{f_{elec}}} e^{-i2\pi f \tau_{elec}} \qquad \text{with} \quad G^{elec} = G^{DSP} \cdot R^{-1} \cdot N_{coil} \cdot \alpha \tag{2.60}$$

The values of the inductance L and the total resistance R of the coil driver depend on the EM actuator and its configuration, but a digital gain G^{DSP} is applied in the DPS, so that the overall response (in N/V) does not depend on the actuator configuration. However, the frequency response changes since the pole frequency f_{elec} varies. The DSP process adds a delay τ_{elec} to the frequency response. The values of the electronic parameters and the associated gain and resonant frequency are given in table 2.3.

mir	configuration	G_{DSP}	R[Ω]	L[mH]	N_{coil}	α[N/A]	f_{elec}[Hz]	G^{elec}[N/V]
NI	Open HP	1	∞ 21.3	15	4	0.0017	∞ 226.0	0 3.19e-4
WI	Open HP	2	∞ 21.3	15	2	0.0017	∞ 226.0	0 3.19e-4
PR	Open HP	1	∞ 21.3	15	4	0.0025	∞ 226.0	0 4.69e-4
SR	Open HP	1	∞ 21.3	15	4	0.0017	∞ 226.0	0 3.19e-4
BS	HP LN	0.61 4.88	28.6 218.5	15	4	0.0025	303.5 2621.8	2.13e-4 2.23e-4
NE, WE	LN1 LN2	8 162	218.6 4418.5	15	4	0.0017	2319.4 49201.2	2.49e-4 2.49e-4
mar	configuration	G_{DSP}	R[Ω]	L[mH]	N_{coil}	α[N/A]	f_{elec}[Hz]	G^{elec}[N/V]
BS	Open LN	1	∞ 21.3	19	2	0.038	∞ 178.4	0 3.57e-3
NE, WE	LN	4	55.5	37	2	0.061	238.7	8.79e-3

Table 2.3: Values of the parameters of the electronic response (G_{DSP}, R, L, N_{coils}, α) associated to each actuator configuration, with the associated electronic gain and pole frequency.

Thus, the amplitude of the mirror actuator response at 100 Hz $A_{mir}(f = 100\ Hz)$ can be estimated from the values of the mechanical and electronic gains. The values of the responses are given in table 2.4. However, these estimations are limited by the precision of the parameters which is within a few %. The frequency response if the actuators in m/V are measured during the calibration of Virgo as describes in chapter 8.

mir	configuration	$A_{mir}(f = 100\ Hz)$[m/V]
NI, WI	HP	1.75e-11
PR	HP	5.15e-11
SR	HP	3.50e-11
BS	LN	1.35e-11
NE, WE	LN2	1.49e-11

Table 2.4: Estimation of the amplitude actuator response at 100 Hz, when the interferometer is at its working points.
The HP configuration of the input mirrors (NI and WI) actuator is used for the calibration of PR and SR mirrors.

2.4 Noise sources

The noises limiting the most the sensitivity of the AdV+ are described in [2]. Figure 2.12 shows the expected contribution of each noise sources of AdV+ for O4 design, and a comparison with the O3 sensitivity.

2.4.1 Quantum noise

The quantum noise is divided into two effects: radiation pressure and the shot noise.

The radiation pressure noise is due to a displacement of the mirrors due to the reflection of photons on the mirrors. The photon noise, which is flat in frequency, produces a noise on the mirror position. Because of the mirror suspension system, the mirror displacement signal is attenuated in $\propto f^{-2}$ in frequency above $\sim$1 Hz. Thus, the radiation pressure noise is visible mainly at low frequency. The power noise is proportional to the square root of the laser power, so the radiation pressure increase when the laser power increase.

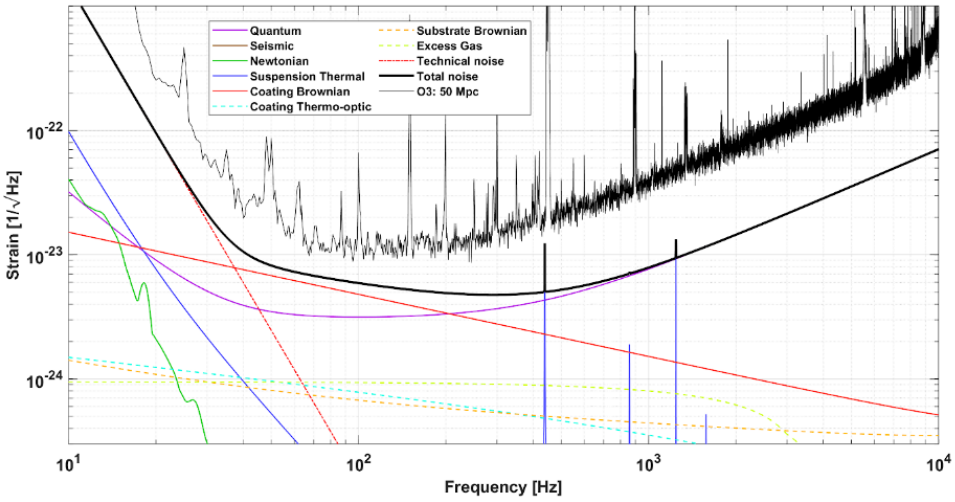

Figure 2.12: Noise level measured during the O3 run, and expected sensitivity for O4 with its different fundamental noise contributions.

The shot noise is due to the uncertainty on the measurement of the number of photon with a sensor. The shot noise seen by the photodiodes of B1 is flat in frequency. However, the optical response of the interferometer can be seen as a simple pole at ∼440 Hz. So the shot noise in the interferometer strain is flat in frequency below 440 Hz, and the increase in f^1 above. Thus, it is effective mainly in high frequency (above 200 Hz). The shot noise can be lowered by increasing the laser power, but it would increase the radiation pressure noise.

During the O3 run, the squeezing system was frequency independent. It reduced the shot noise on the photodiodes so the quantum noise was reduced at high frequency but it increasing the radiation pressure noise at low frequency. The frequency dependent squeezing installed for the O4 run has been built to reduces both the radiation pressure noise at low frequency and the shot noise at high frequency.

2.4.2 Seismic and newtonian noises

Seismic noise comes from the transmission of the seismic waves to the mirror through the suspension system of the interferometer, its effects on the sensitivity are damped by the suspension system of Virgo.

The newtonian noise comes from the local variations of the gravity field around the interferometer directly coupled with the mirror and inducing motion. The gravity field variations are caused by variation of the surrounding air pressure, or by local modification of the ground density due to seismic waves or to building deformation [19]. The newtonian noise was not corrected during O3 because the effect was considered as negligible. For the O4 run, seismic sensors has been placed in the end and central buildings in order to monitor seismic waves and cancel both the seismic noise and the newtonian noise resulting from these waves.

2.4.3 Thermal noise

Thermal noise is induced by either the thermal vibration of the mirror coating or the vibration of the suspension wires due to the thermal dissipation.

The mirror coating Brownian noise is the thermal vibration of the mirror surface. It limits the sensitivity of AdV+ between ∼50 and ∼300 Hz. The effect of the thermal noise is mitigated by using larger laser beam, so that the vibrations of the mirror are averaged over a larger surface. During the O3 and O4 run, the diameter of the beam is 5 cm on the NE, WE, NI and WI mirrors. During the O5 run, larger mirrors (55 cm in diameter) will be installed, and the beam will be enlarged to a diameter of 20 cm on the NE and WE mirrors.

The suspension thermal noise results from the thermal agitation of the suspension wires coupling with the longitudinal displacement of the mirror. The vibration modes of the suspension wires, also called "violin modes", are resonant at a specific frequency around 400 Hz. This noise is dominant at low frequency (up to 20 Hz) and at the resonant frequency of the violin modes.

2.4.4 Noise due to the excess gas

The air pressure in the vacuum chamber is $\sim 10^{-7}$ Pa. The movement of residual air induces fluctuations of the refraction index, which induces a residual noise.

2.4.5 Technical noises

The noise sources listed above are the fundamental noises. The others types of noise, comes from technical sources. These technical noise are hunted down during the commissioning periods and mitigated if possible. The noise level of each technical noise source is required to be lower than ∼10 % of the best design sensitivity over the whole frequency range. A few examples will be given in the list below:

- The control system that keep the interferometer locked induce some electronic and mechanical noise that may limit the sensitivity. The noise of the control system can come from the actuators, the DACs or the different sensors that monitor the interferometer state.
- The scattered light of the end optical benches (SNEB and SWEB) contributes to the sensitivity of the interferometer by entering the Fabry-Perot cavities and contributing to radiation pressure of the laser on the mirror by modulating the laser power in the cavities.
- The electromagnetic contamination coming from the mains supply of the different systems which can be seen at 50 Hz and at the harmonics.

Conclusion

At the end of the year 2022, we encountered difficulties to keep the recycling cavities locked. When a stble lock was achieved at the beginning of 2023, the noise hunting was started, a an excess noise has been found around 500 Hz and at low frequency. The noise 500 Hz was assumed to be a thermal noise from WI and the low frequency contribution was assumed to be a thermal noise due to a default observed on the NE mirror. Two of the four magnets of the WI mirror has been removed, which reduce the 500 Hz. In June 2023, the sensitivity of AdV+ was ∼25 Mpc, which is far below the ∼100 Mpc expected for the O4 run. So it has been decided to replace the NE mirror, and the interferometer is still recovering at the beginning of July 2023.

Thus, Virgo did not joined the O4 run that started in May 24, by LIGO with the sensitivity around 140 Mpc. The KAGRA detector also start observing with LIGO with a sensitivity of ∼1 Mpc for one month, then it will stop in order to be improved.

Chapter 3

Interferometer calibration during O3

Contents

Introduction

The strain signal $h(t)$ defined in chapter 1 is reconstructed with an algorithm. This algorithm uses reconstruct the strain signal from the interferometer output signal and the actuator command signal, using models of the optical responses of the interferometer and of the actuator responses. In practice, the optical responses and the actuator response are measured, and the models are fitted to these measurements.

To measure the responses, the effect of a gravitational wave on the interferometer is simulated by moving the mirrors of the interferometer by a known motion, and see the effect on the interferometer signals. This procedure is called the calibration of the interferometer. In this section, three independent methods to give a known motion to a mirror will be described. Two of these methods consist in an external actuator used as a reference for the calibration, the Photon Calibrator and the Newtonian Calibrator. The Photon Calibrator pushes the mirrors using the radiation pressure of an auxiliary laser. The Newtonian Calibrator uses the gravitation field produced by rotating masses placed near the mirror to move the mirror. The third method consists in calibrating the mirror displacement with respect to the wavelength of the laser, this method is called the Free swinging Michelson.

These three independent methods have been used to calibrate the interferometer during the O3 run, and they are still used during O4. The photon calibrator is used as reference for the calibration while the others confirm the calibration done with the Photon calibrator.

3.1 Photon calibrator

The Photon Calibrator (PCal) is an external mirror actuator that pushes the mirror with the radiation pressure of a laser. It is used as the main reference for the calibration of the interferometer. This section explains the working principle of the Photon Calibrator. The state of the PCal during O3 run is described in details in [8].

3.1.1 Working principle

The photon calibrator uses an auxiliary laser to push the mirror thanks to its the radiation pressure. The displacement of the end mirror ΔL is computed from the power variations of the laser beam reflected by the end mirror P_{ref}, and a model of the mechanical response of the mirror.

As shown in figure 3.1, the laser beam hit the end mirror with an angle of incidence $\theta = 18.5°$. If the laser beam reflected by the end mirror has a power P_{ref}, the laser push the end mirror with a force F. In the frequency space, the equation that link the force applied on the end mirror by the laser, and the power of the laser is:

$$\Delta F(f) = \frac{2.\cos(\theta)}{c} \Delta P_{ref}(f) \tag{3.1}$$

The mechanical response is the displacement response ΔL of the mirror to a force excitation ΔF. Since the mirrors are suspended, the mechanical response of the end mirror is first modeled by the mechanical response of a damped oscillator, with a gain G_0, a resonance frequency f_p and quality factor Q_p.

$$H_{pend}(f) = \frac{\Delta L_{pend}(f)}{F(f)} = \frac{G_0}{1 + \frac{j}{Q_p}\frac{f}{f_p} - \left(\frac{f}{f_p}\right)^2} \tag{3.2}$$

The end mirror has a mass of $M = 42.3$ kg, it is suspended with $l_p = 0.7$ m long monolithic wires. Thus, the static gain is $G_0 = \frac{l}{M.g} = 1.69 \times 10^{-3}$ kg^{-1}s^2 and the resonance frequency is $f_p = \frac{1}{2\pi}\sqrt{\frac{g}{l}} = 0.6$ Hz. The quality factor of the pendulum is $Q_p = 1000$.

If we combine the equations 3.1 and 3.2, we can write the displacement of the mirror due to a variation of the PCal laser power as:

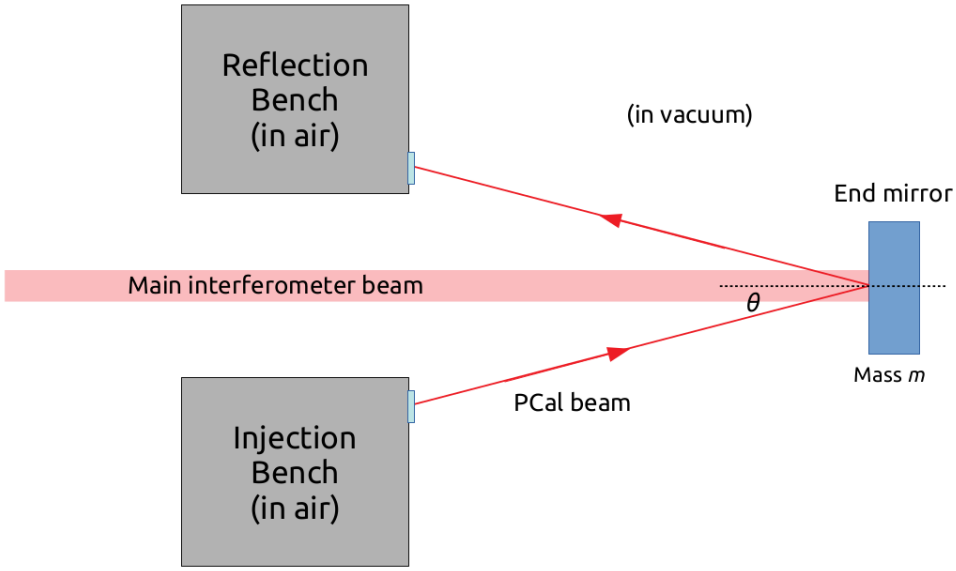

Figure 3.1: Drawing of the PCal principle. The force given to the end mirror depends on the power of the beam, and the angle of incidence of the beam on the mirror.

$$\Delta L_{pend}(f) = \frac{G_0}{1 + \frac{j}{Q_p}\frac{f}{f_p} - \left(\frac{f}{f_p}\right)^2} \frac{2.\cos(\theta)}{c} \times \Delta P_{ref}(f) \tag{3.3}$$

The emitted laser power $P(t)$ is modulated with an amplitude P_m, at a frequency f, around a mean power P_0.

$$P(t) = P_0 + P_m \sin(2\pi f t) = P_0 + \Delta P(t) \tag{3.4}$$

The frequency of the modulation is in the bandwidth $f \in [10\text{ Hz}, 10\text{ kHz}]$. Thus, the high frequency approximation $f \gg f_p$ of the pendulum can be done. Equation 3.3 can be written as:

$$\Delta L_{pend}(f) = \frac{-G_p f_p^2}{f^2} \frac{2.\cos(\theta)}{c} \times \Delta P_{ref}(f) = \frac{-2.\cos(\theta)}{Mc(2\pi f)^2} \Delta P_{ref}(f) \tag{3.5}$$

In addition of the pendulum response, the deformation of the high reflected mirror surface of the mirror due to the laser power are also modeled. This deformation is seen by the ITF as a variation of the length of the arms. The deformations of the surface are decomposed into a sum of internal modes of the mirror. Thus total displacement of the mirror is the sum of the simple pendulum with all the internal models. In practice, the laser beam hit the center of the mirror, which excite only the drum modes. The expression of the mechanical response of these modes $H_{drum,tot}$ can be expressed as a sum of responses of damped harmonic oscillators $H_{drum,i}$.

$$H_{drum,tot}(f) = \sum_i H_{drum,i}(f) = \sum_i \frac{G_{d,i}}{1 + \frac{j}{Q_{d,i}}\frac{f}{f_{d,i}} - \left(\frac{f}{f_{d,i}}\right)^2} \tag{3.6}$$

Thus, the model of the displacement of the mirror due to the PCal ΔL_{PCal} is written as

$$\Delta L_{PCal}(f) = \Delta L_{pend}(f) + \sum_i \Delta L_{drum,i}(f) = \left(H_{pend}(f) + \sum_i H_{drum,i}(f) \right) \times F(f) \tag{3.7}$$

The list of the drum modes taken into account during the calibration of O3 interferometer is given in table 3.1.

In practice, the calibration of the ITF with the PCal is done in the bandwidth $[10\text{ Hz}, 4\text{ kHz}]$. Only the first resonant mode was taken into account in the model of the mirror mechanical response. The contribution of the other drum modes are neglected. Thus, equation (3.6) becomes:

Resonant frequency [Hz]	Amplitude [h/W]	Quality factor
7812.8	$(4.24 \pm 0.06) \times 10^{-23}$	10^6
10120	$(9.28 \pm 3.28) \times 10^{-23}$	10^6
12905	$(-1.45 \pm 0.85) \times 10^{-22}$	10^5
-	$(3.08 \pm 0.54) \times 10^{-22}$	-

Table 3.1: List of the drum modes exited by the PCal laser on WE, with their resonant frequencies, amplitudes and quality factors. The resonant frequencies and quality factor are estimated with simulations of the mirror deformations. The last mode is modeled with only a simple gain.

$$\Delta L_{PCal}(f) = \Delta L_{pend}(f) + \Delta L_{drum}(f) = \left(\frac{-1}{M(2\pi f)^2} + \frac{G_d}{1 + \frac{j}{Q_d}\frac{f}{f_d} - \left(\frac{f}{f_d}\right)^2} \right) \times \frac{2.\cos(\theta)}{c} \times P_{ref}(f) \quad (3.8)$$

Since the pendulum and the drum mode have the same gain value at a frequency around $f_n = 2050$ Hz and opposite phases, there is a notch in the frequency response of the mirror around frequency f_n, as shown in figure 3.2. The values of the resonant frequency of the drum mode f_d and the frequency of the notch f_n will be measured, and the gain of the drum mode G_d is computed from the notch frequency.

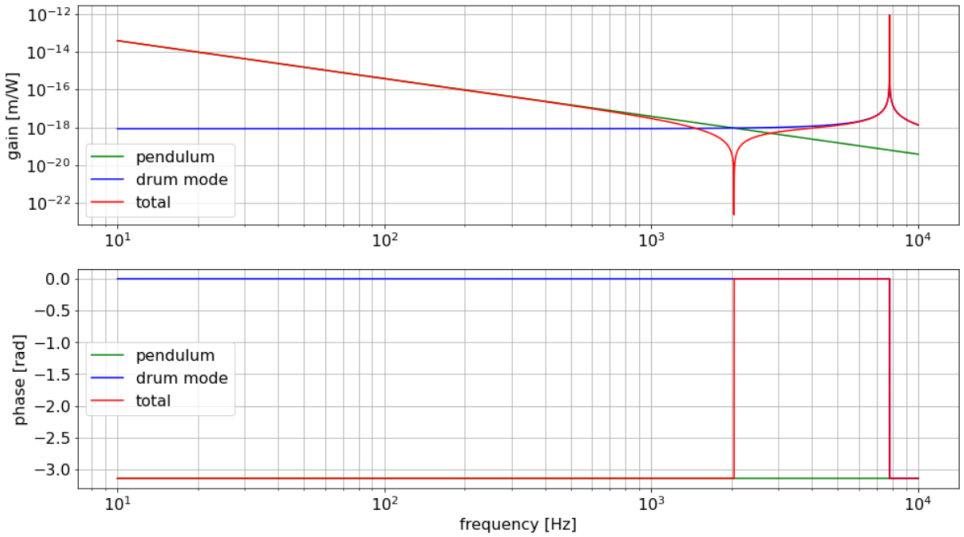

Figure 3.2: Gain and phase of the model of the mechanical response of the pendulum, the drum mode and the total model of mechanical response of the mirror.

3.1.2 Calibration of the PCal for the O3 run (2019-2020)

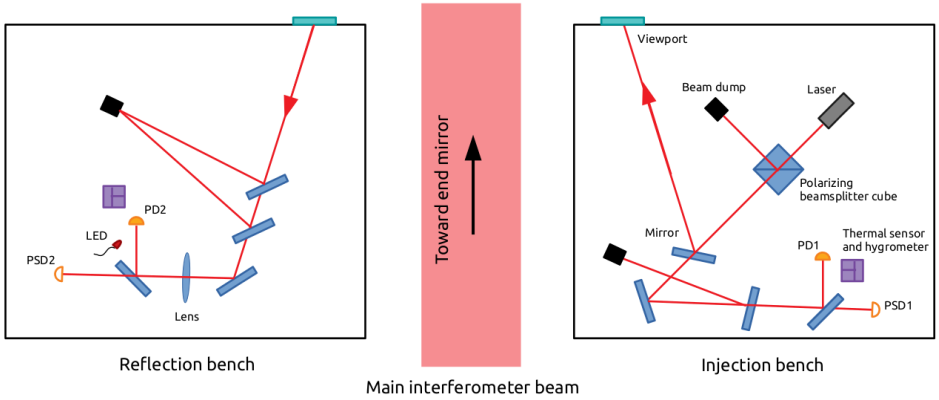

Figure 3.3: Optical scheme of the photon calibrator used during O3 run. The design contains two silicon photodiodes, one on each bench, 90% reflection 10% transmission beam splitters (Thorlabs BSX11), a polarizing cube (Thorlabs PBS203) and two PSD for the beam position measurement.

The PCal optical design installed during O3 run is shown in the figure 3.3. The power of the beam reflected by the end mirror P_{ref} is estimated by two photodiodes named "PD1" and "PD2", one on each bench of the PCal. ΔL_{PCal} the displacement of the end mirror due to the PCal is estimated from the outputs of these two photodiodes. Therefore, the photodiodes require an absolute power calibration.

During the O3 run, the calibration of the photodiodes was done using integrating spheres as standards. The Gold Standard (GS) was the common standard for Virgo and LIGO. From the GS, we calibrated two integrating spheres dedicated to the Virgo PCal calibration: The Working Standard Virgo (WSV) and the Virgo Integrating Sphere (VIS). GS and WSV were integrating spheres made by LabSphere with an InGaAs photodiode, VIS was a commercial sphere made by Newport. GS was calibrated absolutely by the National Institute of Sciences and Technologies (NIST). And VIS and WSV were calibrated with respect to GS. WSV was kept at LAPP in order to be used as reference for the Virgo calibration in power. VIS was sent to the Virgo site and used to calibrate the photodiodes of the PCal. A scheme of the power calibration chain from NIST to the PCal photodiode is shown in figure 3.4.

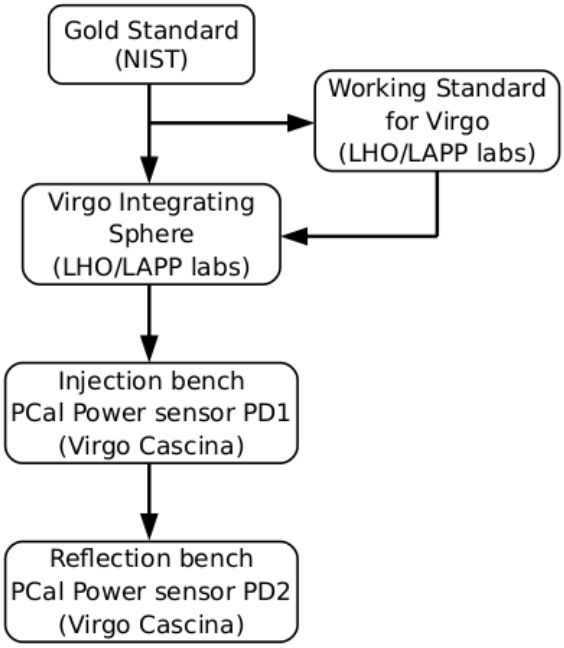

Figure 3.4: Scheme of the O3 intercalibration procedure.

3.1.3 PCal calibration uncertainty

Every parameters in equation (3.1) contribute to the total uncertainty on the mirror displacement estimation due to the PCal. The uncertainty sources on the calibration of the PCal are, the power calibration of the photodiodes, the geometry of the PCal, and the stability of the calibration throug time. The main contribution to the total uncertainty comes from the power calibration of the photodiodes.

The Gold standard is the reference for the power calibration for Virgo and LIGO. It has been calibrated in power by NIST. The uncertainty on the GS calibration was 0.32 %. The uncertainty on the calibration transfer from the GS to the VIS is 0.65 % [8]. The response of VIS is stable within an uncertainty of 1 %, and the uncertainty on the photodiodes calibration with respect to VIS is 0.04 %. Thus, the total uncertainty on the photodiode power calibration is 1.24 %.

All the parameters of the mechanical response of the mirror from equation (3.2), can be source of uncertainty. These parameters are called geometrical parameters, they consist in the angle of incidence θ of the laser beam on the end mirror and the mass of the mirror M. The uncertainty on the cosine of the angle of incidence of the beam on mirror θ is 0.12 %. The mass of the mirror in known with an uncertainty of 0.17 % [8]. The total uncertainty on the mirror response due to the geometrical parameters is 0.21 %.

The calibration of the PCal has been done at the beginning of the O3 run, the total uncertainty on the mirror displacement ΔL_{PCal}, due the PCal calibration was equal to 1.34 %. However, the uncertainty doesn't take into account the variation of the PCal calibration with time during the O3 run.

3.1.4 Stability of the PCal calibration during the observing run O3

The calibration of the PCal photodiodes has been monitored during the observing run O3. Two sinusoidal signals were added to the power command of the laser of each PCal. The frequencies of the signals are $f_{PCal,NE} = 63.5$ Hz on NE and $f_{PCal,WE} = 60.5$ Hz on WE. The signals $h_{PCal,i} = \frac{\Delta L_{PCal,i}}{L_0}$ where $i \in \{NE, WE\}$ are computed from the output signal of the PCal photodiodes. In parallel, the reconstructed strain signal h_{rec} is computed, and serve as a reference for PCal signal monitoring.

The transfer functions from $h_{PCal,i}$ to h_{rec} are computed at the corresponding frequency $f_{PCal,i}$, and

the evolution of the values of the transfer functions $\frac{h_{rec}}{h_{PCal,i}}(f_{PCal,i})(t)$ is monitored through the O3 run. A variation of the $\frac{h_{rec}}{h_{PCal,i}}$ is due either to a variation of the interferometer calibration or a variation of the PCal photodiode calibration. However, the two signals $\frac{h_{rec}}{h_{PCal,NE}}$ and $\frac{h_{rec}}{h_{PCal,WE}}$ from the two PCal are not correlated, thus $h_{rec}(f_{PCal,i})$ is considered as constant and only the signals $h_{PCal,i}(f_{PCal,i})(t)$ vary with time.

Therefore, the signals $\frac{h_{rec}}{h_{PCal,i}}(f_{PCal,i})(t)$ were used to monitor the calibration of the PCal photodiode during the O3 run. The distribution of these signals during the observing runs O3a and O3b are shown in figure 3.5.

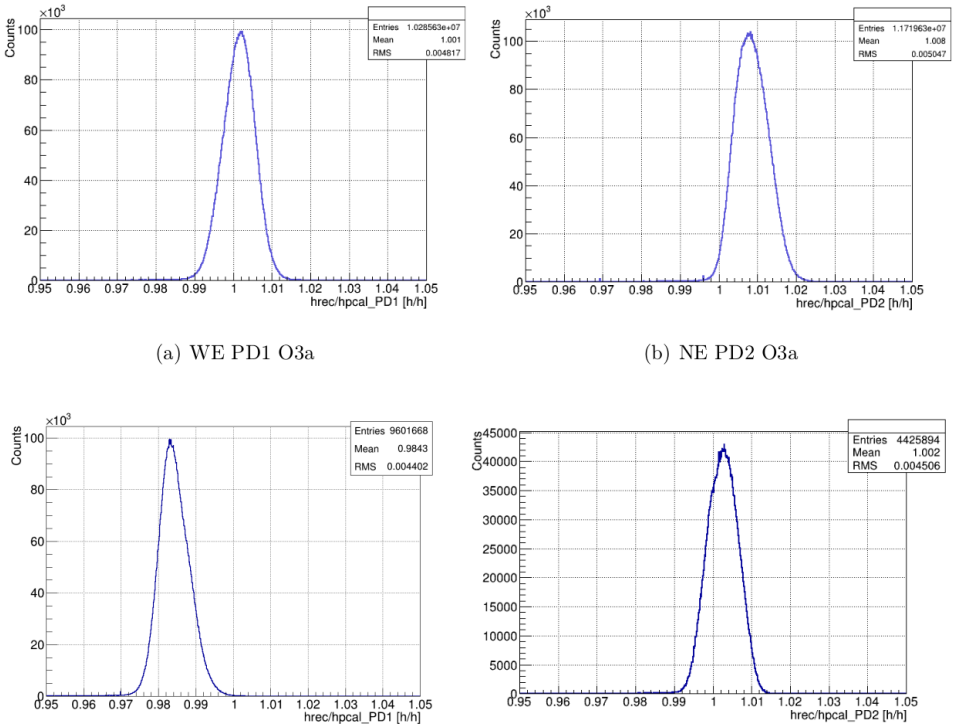

(a) WE PD1 O3a

(b) NE PD2 O3a

(c) WE PD1 O3b

(d) NE PD2 O3b

Figure 3.5: Distributions of the signals $\frac{h_{rec}}{h_{PCal,i}}(f_{PCal,i})(t)$ on NE and on WE. On NE $h_{PCal,NE}$ is computed from the output signal of PD2 photodiode. On WE, $h_{PCal,WE}$ is computed from PD1 photodiode. Source [8]

The standard deviation of the the distribution of the $\frac{h_{rec}}{h_{PCal,NE}}(f_{PCal,NE})(t)$ was 0.5 % during O3a run and 0.6 % during O3b run. And the standard deviation of the $\frac{h_{rec}}{h_{PCal,WE}}(f_{PCal,WE})(t)$ was 0.5 % during O3a run and 1.2 % during O3b run. The total uncertainty on the mirror displacement during the O3 run is summarized in table 3.2.

Parameters	1σ uncertainty O3a		1σ uncertainty O3b	
	NE	WE	NE	WE
Power calibration	1.24 %	1.24 %	1.24 %	1.24 %
Geometrical parameters	0.21 %	0.21 %	0.21 %	0.21 %
Calibration stability	0.5 %	0.5 %	0.6 %	1.2 %
Total	1.36 %	1.36 %	1.40 %	1.74 %

Table 3.2: Uncertainty budget of the photon calibrators below 1 kHz

During the O3 run, it has been noticed that the ratio between photodiodes outputs $\frac{P_{PD1}}{P_{PD2}}$ was correlated with the relative air humidity measured on the PCal bench. An example of a distribution of the

ratio as a function of the air humidity is shown in figure 3.6.

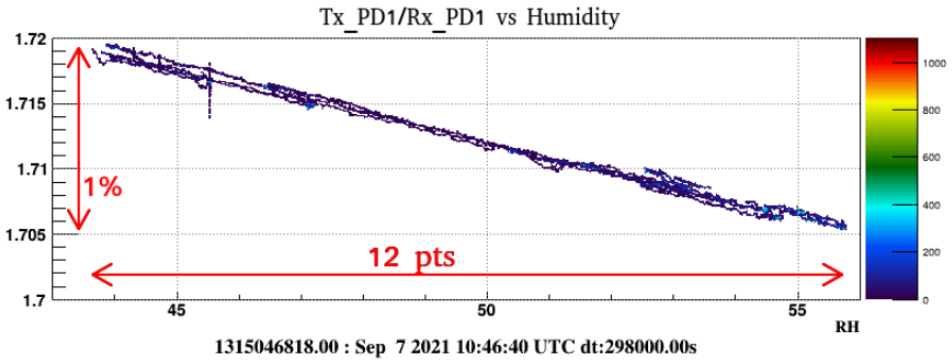

Figure 3.6: Ratio between the photodiodes outputs on NE PCal as function of the air humidity rate. A variation of the air humidity rate by 12 points makes $\frac{P_{PD1}}{P_{PD2}}$ vary by 1 %.

The signals $\frac{h_{rec}}{h_{PCal,i}}$ is computed from the photodiodes outputs. Thus, they are also correlated with the measured air humidity rate, as shown in figures 3.7. [8] The outputs signals of both photodiodes on both PCals are correlated with the air humidity.

Thus, the variation of the air humidity rate is suspected to be the main cause of the variation of the PCal calibration. The main hypothesis is that the air humidity is absorbed by the coating of the BSX11 beam splitter installed on the PCal benches affect their reflection and transmission rates. So the PCal optical setup has been changed for O4 run as described in section 5.

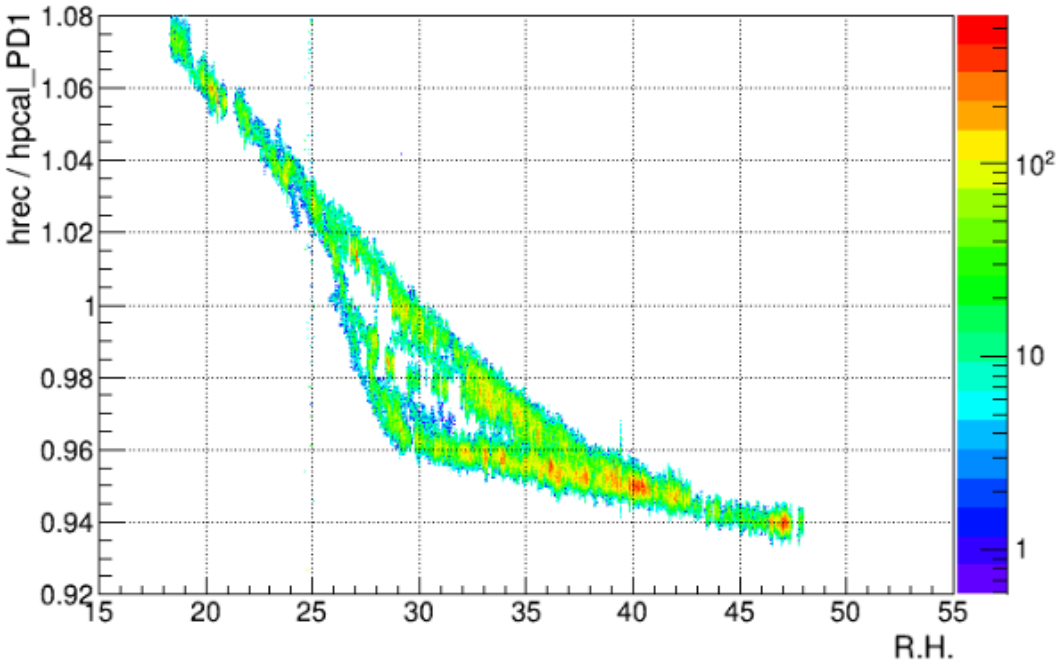

Figure 3.7: Distribution of $\frac{h_{rec}}{h_{PCal,PD1}}$ on NE, with as a function of the relative air humidity (R.H.) on the PCal bench. The distribution is is done over all the O3b run.
Source [8]

3.2 Newtonian calibrator

During O3 run, an other external actuator has been installed, the Newtonian Calibrator (NCal). The NCal has been tested for the first time after the O2 run, and has been used during O3 to cross-check the calibration with the PCal. The working principle of the NCal is detailed in [5].

3.2.1 Working principle

The NCal consists in a rotor with two rotating masses m_1 and m_2 which produce a local variations of the gravitational field around the mirror. We assume that the masses are point-like and located at a distance r from the rotor, which is located at a distance d from the end mirror, which is also point like. A scheme of the NCal is given in figure 3.8

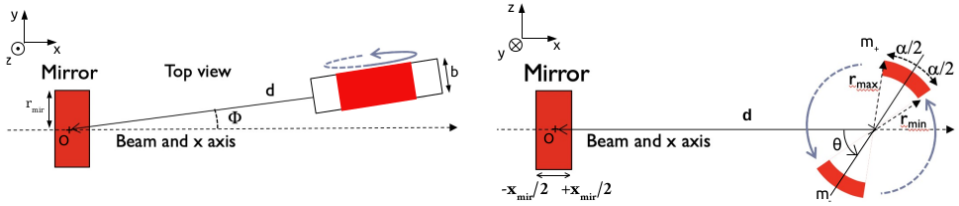

Figure 3.8: Scheme of the NCal principle. The NCal makes the mirror move along the x axis which is the laser axis. The z axis is the vertical axis.
Left: View from the top
Right: View from the side

Let d be the distance between the mirror and the center of the rotor, Φ the angle between the optical axis and the rotor axis and r the distance between the rotation axis of the rotor and the center of mass. In a referential centered in the mirror, the position of the m_1 mass is located at the position $\vec{x}_1$.

$$\vec{x}_1 = \begin{pmatrix} x_1 \\ y_1 \\ z_1 \end{pmatrix} = \begin{pmatrix} \cos(\Phi) \times [d + r.\cos(\theta)] \\ \sin(\Phi) \times [d + r.\cos(\theta)] \\ r.\sin(\theta) \end{pmatrix} \tag{3.9}$$

The gravitational potential created by the mass at the mirror position can be written as:

$$U(\vec{x}_1) = -\frac{G.m_1.M}{D(\vec{x}_1)} \tag{3.10}$$

Where $D(\vec{x}_1)$ is the distance between the mirror and the mass. With $\epsilon = \frac{r}{d}$, $D(\vec{x}_1)$ can be written as:

$$D(\vec{x}_1) = d \times \sqrt{1 + 2\epsilon.\cos(\theta) + \epsilon^2} \tag{3.11}$$

The gravitational force applied by the mass on the mirror along the x axis is:

$$F_x(\vec{x}_1) = \vec{\nabla} U(\vec{x}).\hat{e}_x = G.m.M.\frac{x_1}{D(\vec{x}_1)^3} = \frac{G.m.M}{d^2}\frac{(1 + \epsilon.\cos(\theta)) \cdot \cos(\Phi)}{(1 + 2\epsilon.\cos(\theta) + \epsilon^2)^{3/2}} \tag{3.12}$$

With $\epsilon << 1$, one can compute the second order of Taylor's development of formula (3.12).

$$F_x(\vec{x}_1) \sim \frac{G.m.M}{d^2} \times \cos(\Phi) \times \left(1 - 2\epsilon.\cos(\theta) - \frac{3}{2}\epsilon^2 + \frac{9}{2}\cos^2(\theta)\epsilon^2\right) \tag{3.13}$$

In the same way, the force applied by m_2 on the mirror can be written as:

$$F_x(\vec{x}_2) \sim \frac{G.m.M}{d^2} \times \cos(\Phi) \times \left(1 + 2\epsilon.\cos(\theta) - \frac{3}{2}\epsilon^2 + \frac{9}{2}\cos^2(\theta)\epsilon^2\right) \tag{3.14}$$

Thus, the total force applied on the mirror by the NCal is

$$F_x = \frac{G.m.M}{d^2} \times \cos(\Phi) \times \left(2 - 3\epsilon^2 + 9\cos^2(\theta)\epsilon^2\right) = \frac{G.m.M}{d^2} \times \cos(\Phi) \times \left(2 + \frac{3}{2}\epsilon^2 + \frac{9}{2}\cos(2\theta)\epsilon^2\right) \quad (3.15)$$

Let f_r be the rotation frequency of the rotor. Then, the phase of the rotor becomes $\theta = 2\pi f_r.t$. The term in $\cos(2\theta)$ in equation (3.15) shows that the frequency of the force signal of the mirror is twice the rotation frequency of the rotor. If we consider only the varying terms of equation (3.15), and compute its Fourier transform, we get the amplitude of the force signal:

$$F_x(2f_r) = \frac{9}{2}\frac{G.m.M.r^2}{d^4}\cos(\Phi) \quad (3.16)$$

The amplitude of the mirror displacement can computed by using the pendulum model in formula (3.5).

$$\Delta L_{NCal}(2f_r) = \frac{F_x(f)}{M(2\pi f)^2} = \frac{9}{2}\frac{G.m.r^2}{d^4.(2\pi f_r)^2} \cdot \cos(\Phi) \quad (3.17)$$

3.2.2 Status of the NCal during O3

During the O3 run, two NCal rotors have been installed near the NE mirror. These rotors are named Near NCal and Far NCal, and they are identical.

The calibration of the NCal consists in measuring the geometrical parameters of the NCal, which are the d distance between the mirror and the center of the rotor, Φ the angle between the optical axis and the rotor axis and r the distance between the rotation axis of the rotor, and the center of mass. [5] The values and their uncertainties are given in table 3.3.

parameter	value
d_{near}	1.2667 m ± 6.4 mm
d_{far}	1.9467 m ± 6.4 mm
Φ	0.6056 rad ± 5 mrad
r	95 mm ± 1.3 mm
m	4.837 kg ± 8 g

Table 3.3: Values of the geometrical parameters measured during the O3 run.

During O3, calibrations lines have been injected with the NCal and PCal in order to monitor the reconstructed strain signal of AdV+, $h_{NCal}(f) = \frac{\Delta L_{NCal}(f)}{L_0}$ is the amplitude of the injected line at the frequency f. The ratio between h_{NCal} and h_{rec} is computed at frequencies between 10 Hz and 200 Hz.

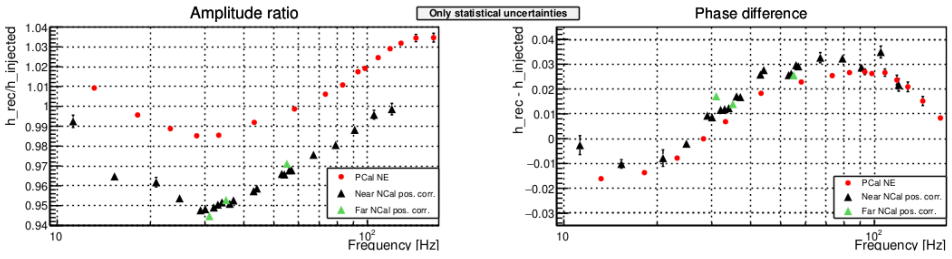

Figure 3.9: $\frac{h_{rec}}{h_{NCal}}$ as function of the frequency, injected with the Near NCal and the Far NCal. With comparison with $\frac{h_{rec}}{h_{PCal}}$

Figure 3.9 shows the measured ratio between $\frac{h_{rec}}{h_{injected}}$, with lines injected with PCal and NCal. We can see that there were a bias of 3 % on the modulus between the PCal and the two NCals. The phases of $\frac{h_{rec}}{h_{PCal}}$ and $\frac{h_{rec}}{h_{NCal}}$ corresponded to each other. The 3 % bias between the PCal and the NCal has to be reduced for the O4 run.

3.3 Free swinging Michelson

The free swinging Michelson (FreeMich) calibration method has been used as reference for the ITF calibration until the O2 run. And it was still used to cross check the calibration with the photon calibrator during O3 run. The FreeMich method consists in calibrating the NI and WI mirror electromagnetic actuators (in m/V) with respect to the wavelength of the ITF laser, using the Michelson principle. And then, the calibration is transferred from the input mirrors to the end mirror actuators. The method is detailed in [16] and [11]

3.3.1 Calibration of NI, WI and BS mirror actuators

In order to calibrate the electromagnetic actuators of the NI, WI and BS mirrors, the ITF is put in the Free swinging Michelson mode. The NE, WE and PR mirror are misaligned with the main laser beam. The output beam of the laser is observed by B1p photodiodes. The photodiode signals used to reconstruct the mirror displacement signal ΔL_i are the continuous signal P_{DC} and the in-phase demodulated signal P_{AC} at 6 MHz of the B1p photodiodes. [16]

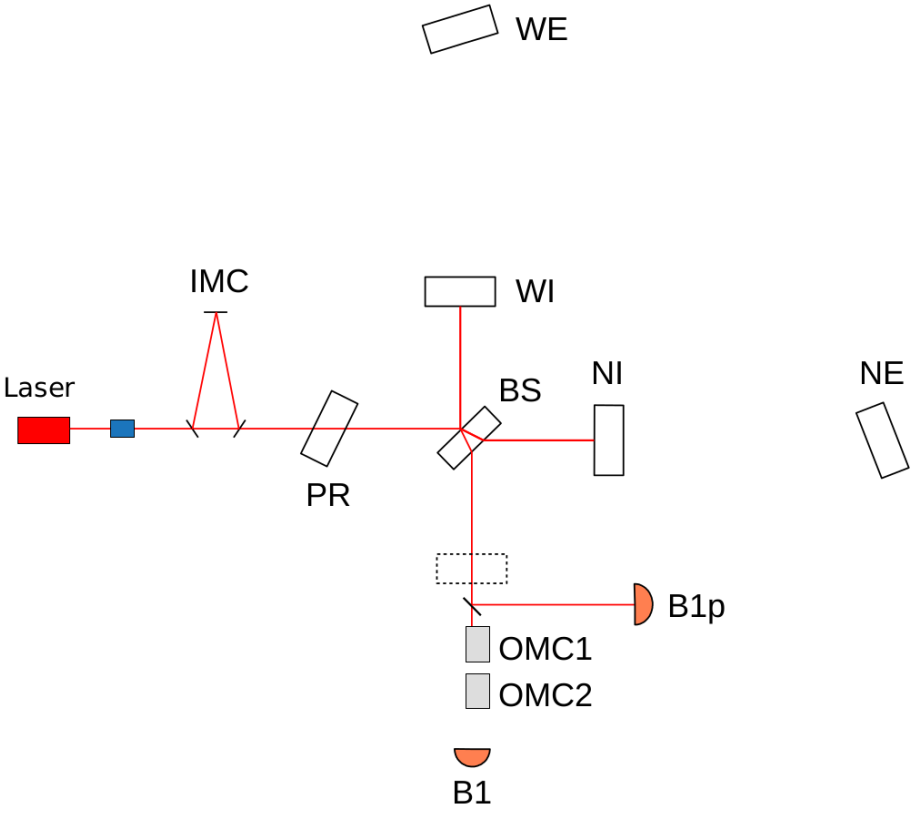

Figure 3.10: Scheme of the interferometer in free swinging Michelson mode

In a simple Michelson ITF, the phase between the two interfering beams is written as a function of the differential arm length ΔL:

$$\Delta\Phi = \frac{4\pi\Delta L}{\lambda} \tag{3.18}$$

The continuous signal and the in-phase demodulated signal are function of the phase between the two beams.

$$P_{DC} = P_0 \times (1 - \alpha.\cos(\Delta\Phi)) \tag{3.19a}$$
$$P_{AC} = P_1 \times \sin(\Delta\Phi) \tag{3.19b}$$

We can see in equation 3.19 that the signal in the (P_{DC}, P_{AC}) plane follow an ellipse. An example of such an ellipse is given in figure 3.11. The center and width of this ellipse is fitted, in order to center and normalize the ellipse. Therefore, the angle between the P_{DC} axis and the point (P_{DC}, P_{AC}) is equal to $\Delta\Phi$, and the differential arm length ΔL signal can be reconstructed from $\Delta\Phi$ and equation 3.18.

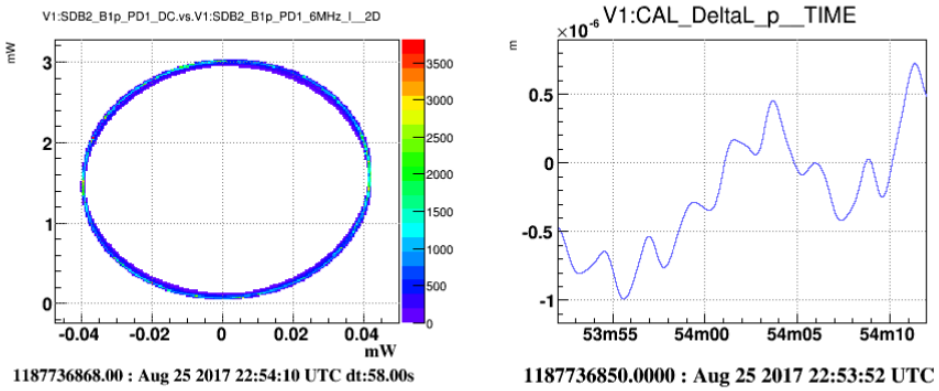

Figure 3.11: Left: P_{AC} as function of P_{DC} while a signal is injected on the mirror command. Right: Reconstructed ΔL signal

While the ITF is in Free Swinging Michelson mode, a sinusoidal command ΔV_i is sent to the mirror $i \in \{NI, WI, BS\}$ at frequency f in the bandwidth [10 Hz, 1 kHz]. The transfer function from the command to the reconstructed differential arm length is computed. This transfer function is the response of the electromagnetic actuator of the mirror i.

3.3.2 Calibration transfer from Input mirror to the other mirrors

The actuators of the end mirrors and PR mirror were calibrated with respect to the input mirrors and BS mirror actuators. The calibration of the end mirrors consists in comparing the effect of the end mirrors displacement on the interferometer output, with the effect of the input mirrors. The output signal is the $DARM$ signal, which is computed from the output signal of the B1 photodiodes. With the interferometer fully locked, the end mirrors are moved by a sinusoidal signal at a frequency f, the excitation signal of the end mirror is named CAL_{end}. The transfer function from the excitation to the output signal of the interferometer is computed $\left(\frac{DARM}{CAL_{end}}\right)(f)$. Then, a sinusoidal signal at the same frequency is sent to the input mirror, and the transfer function from the excitation to the output signal is computed $\left(\frac{DARM}{CAL_{input}}\right)(f)$. The responses of the actuators of the end mirrors are written as follow:

$$A_{end}(f) = A_{input}(f) \times \left(\frac{DARM}{CAL_{end}}\right)(f) \times \left(\frac{CAL_{input}}{DARM}\right)(f) \times \frac{O_{input}(f)}{O_{end}(f)} \tag{3.20}$$

Where O_{end} is the optical response of the interferometer to an end mirror displacement and O_{input} is the optical response to an input mirror displacement. As seen in section 2.1, the optical response of the interferometer to the end mirror displacement are approximately the same as the optical response to the input mirror displacement but the end mirror responses are delayed by $\tau_{FP} = 10$ µs due to the light

propagation in the arm cavity $\frac{O_{input}(f)}{O_{end}(f)} \sim -e^{i2\pi\tau_{FP}f}$.

Because the optical response to the PR mirror displacement is not comparable with the optical response to an input mirror displacement, the PR mirror actuator cannot be calibrated with the interferometer locked. Thus, the interferometer is set in a special configuration where only the PR cavity is locked while the rest of the interferometer is unlocked. The length of the PR cavity $PRCL$ is monitored with the output signal of the B4 photodiodes. The PR mirror actuator is calibrated with respect to the actuator of the WI mirror. The method to calibrate the PR mirror is similar to the method used to calibrate the end mirrors. The response of the PR mirror actuator is written as:

$$A_{PR}(f) = A_{WI}(f) \times \left(\frac{PRCL}{CAL_{PR}}\right)(f) \times \left(\frac{CAL_{WI}}{PRCL}\right)(f) \tag{3.21}$$

3.3.3 Comparison with the PCal calibration

The FreeMich is a calibration method which is independent from the PCal. This method has been used to cross-check the PCal calibration during O3 run. Thus, the motion signal of the mirror reconstructed with the FreeMich method $\Delta L^{FreeMich}$ and with the PCal ΔL^{PCal} are compared. Figure 3.12 shows the transfer function from an actuator model computed with the PCal, A^{PCal}, to the model computed with the FreeMich $A^{FreeMich}$ [11]. This transfer function is equal to the transfer function from ΔL^{PCal} to $\Delta L^{FreeMich}$.

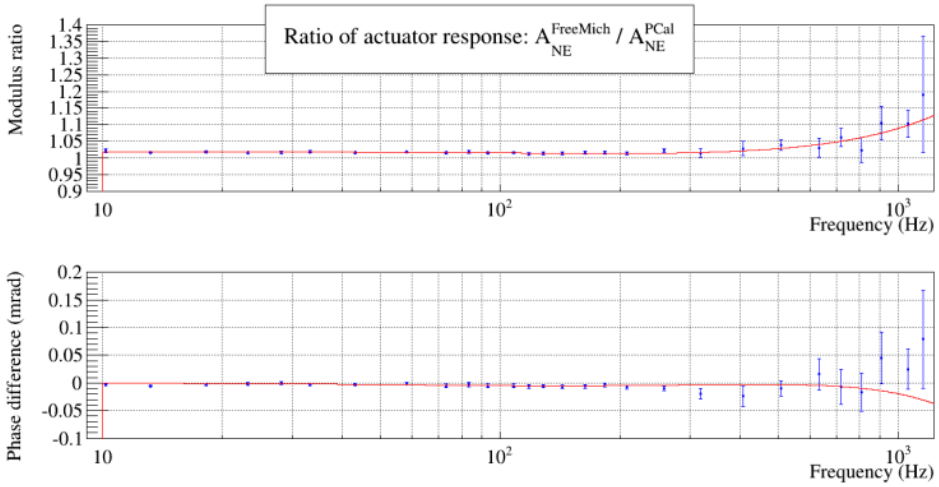

Figure 3.12: Transfer function from the actuator model computed with the PCal A^{PCal} to the model computed with the FreeMich, $A^{FreeMich}$. These models represent the actuator of the NE mirror, and have been measured during the O3 run.
Source: [11]

In the frequency bandwidth [10 Hz, 2 kHz], the modulus is biased by ∼3 %, and flat within 0.7 %. The phase difference between both techniques is lower than 12 mrad. The differences between the two models were compatible with the uncertainties estimated from both methods during O3. When the input mirrors are calibrated, the order of magnitude of the displacement is the same as the wavelength of the laser $\lambda = 1064$ nm. Whereas the order of magnitude of the input mirror displacement when the end mirrors actuator are calibrated is 10^{-15} m. The calibration gain (in m/V) of the actuator may not be the same between these two amplitudes, which may be the cause of the bias between the PCal and the Free Swinging Michelson. Therefore, the Free Michelson is not used as a reference method for calibrating the interferometer after O2.

Chapter 4

Interferometer strain signal reconstruction

Contents

Introduction

The strain signal $h(t)$ of the detector is reconstructed from the output power signal of the interferometer and the excitation signal of the mirrors actuators, using models of the optical responses of the interferometer and models of the electronic actuators. In this chapter, the algorithm that computes the strain signal is described.

4.1 Reconstruction principle

4.1.1 $h(t)$ reconstruction formula

The gravitational wave signal is contained in the strain signal of the interferometer $h(t)$ which is defined as following:

$$h(t) = \frac{L_N(t) - L_W(t)}{L_0} \tag{4.1}$$

Where L_N and L_W are respectively the North and the West Fabry-Perot cavity length, and $L_0 =$ 3000 m is the nominal length of the cavities. $h(t)$ is proportional to the differential arm length signal (DARM) defined in section 2.1. The DARM signal is estimated with the power of the (B1) beam, also named the error signal $\mathcal{E}$. However, the DARM control loop attenuates the DARM signal, and so the gravitational wave signal. In addition, the control loops of the other optical cavities such as CARM, PRCL, SRCL and MICH produce some noise on the strain signal. Therefore, the control signal of all mirror actuators must be taken into account in the reconstruction of the strain signal.

In the frequency domain, the error signal $\mathcal{E}(f)$ can be written as:

$$\mathcal{E}(f) = S(f)\left[\sum_i O_i(f).(\Delta L_{mir,i}(f) + \Delta L_{mar,i}(f)) + O_{ITF}(f).L_0.h(f)\right] \tag{4.2}$$

Where $S(f)$ is the sensing function of the photodiodes of the detection system, $O_i(f)$ is the optical response of the interferometer in [W/m] to a displacement of the i mirror, ($i \in \{NE, WE, NI, WI, BS, PR, SR\}$), $O_{ITF}(f)$ is the optical response of the interferometer to a gravitational wave, and it is the mean of the optical responses of NE and WE, $O_{ITF}(f) = (O_{NE}(f) + O_{WE}(f))/2$, $\Delta L_{mir,i}$ is the displacement of the i mirror caused by the EM actuators on the mirror, and $\Delta L_{mar,i}$ is the mirror displacement caused by the actuator on the marionetta.

The strain signal $h(f)$ is deduced from the previous equation:

$$h(f) = \frac{1}{O_{ITF}(f).L_0}\left[\frac{\mathcal{E}(f)}{S(f)} - \sum_i O_i(f).(\Delta L_{mir,i}(f) + \Delta L_{mar,i}(f))\right] \tag{4.3}$$

The mirror displacements $\Delta L_{mir,i}$ and $\Delta L_{mar,i}$ are estimated from the control signals $Sc_{mir,i}$ and $Sc_{mar,i}$ of the EM actuators and the calibrated actuator responses $A_{mir,i}$ and $A_{mar,i}$. Thus the strain signal is written as:

$$h(f) = \frac{1}{O_{ITF}(f).L_0}\left[\frac{\mathcal{E}(f)}{S(f)} - \sum_i O_i(f).(A_{mir,i}(f).Sc_{mir,i}(f) + A_{mar,i}(f).Sc_{mar,i}(f))\right] \tag{4.4}$$

In equation (4.4), $Sc_{mir,i}(f)$, $Sc_{mar,i}(f)$ and $\mathcal{E}(f)$ are the Fourier transform of measured signals, and $S(f)$, $O_i(f)$, $O_{ITF}(f)$, $A_{mir,i}(f)$ and $A_{mar,i}(f)$ are the optical responses and actuators response measured and modeled. The reconstruction algorithm is based on this equation (4.4). To reconstruct the strain signal, the fft of the error signal $\mathcal{E}$ is computed, and the contribution of the sensing of the B1 photodiodes $S(f)$ is compensated. Then, the contribution of each mirror displacement to the error signal is computed from the control signal $Sc(f)$, and subtracted from the error signal. The result is named P_{raw}, and the optical response of the interferometer $O_{ITF}(f)$ is compensated to compute the raw strain signal h_{raw}. A diagram of the reconstruction algorithm is given in figure 4.1.

All the control signals $Sc_{level,i}$ are sampled at 10 kHz, and the error signal $\mathcal{E}$ is sampled at 20 kHz. The reconstruction of h is done in the frequency domain. The Fourier transforms of the signals are computed using the Fast Fourier Transform (FFT) over Hann windows of 8 s duration, overlapping over 4 s.

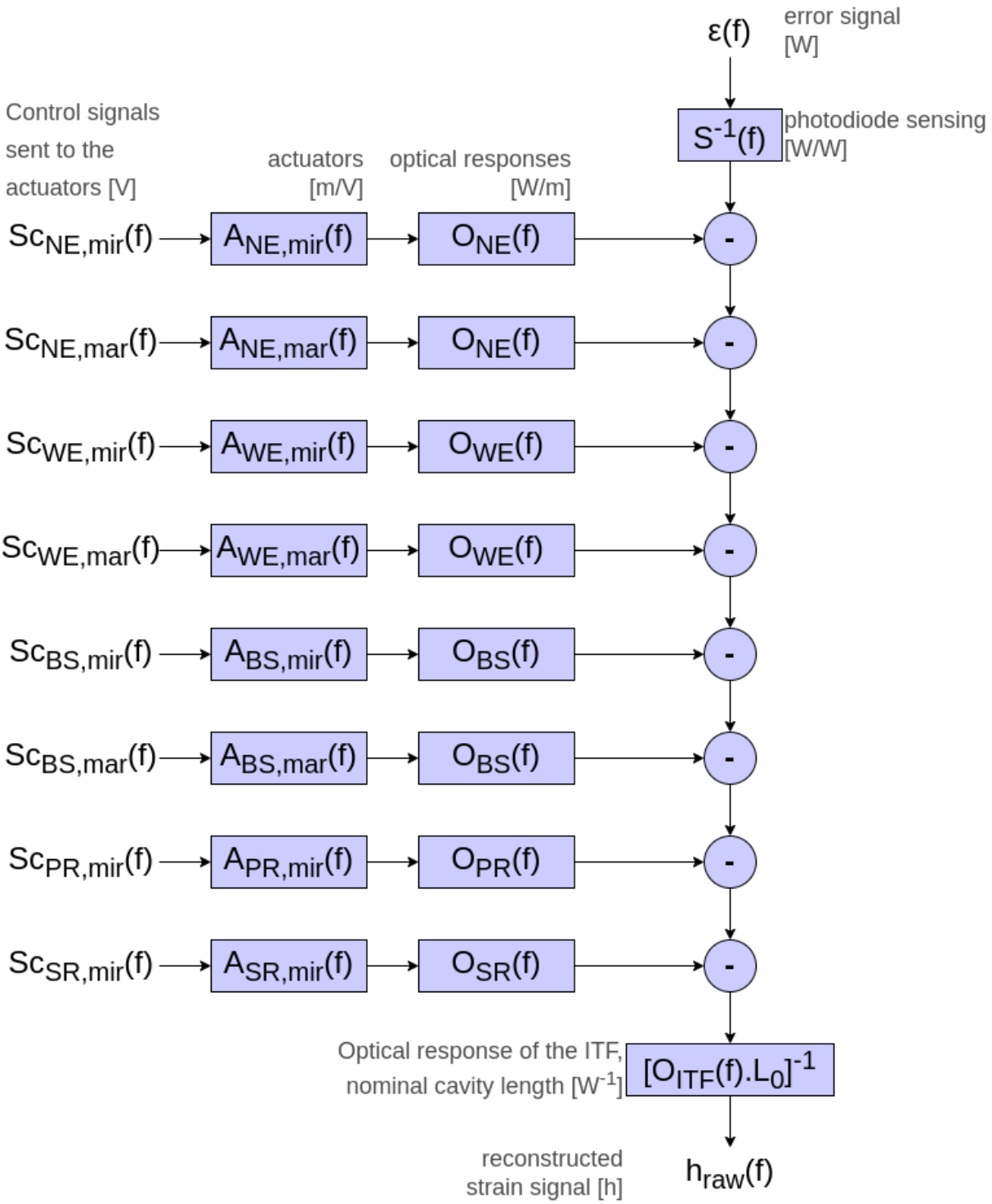

Figure 4.1: Detailed block diagram of the reconstruction showing the reconstruction of the raw strain signal.

4.1.2 Main components of the reconstruction pipeline

The raw reconstructed strain signal h_{raw} may be biased, and contains some interferometer noises which reduce the sensitivity of the interferometer. So this raw signal has to be improved. The full scheme of the strain signal reconstruction is given in figure 4.2.

The bias $H_{corr}(f)$ between $h_{raw}(f)$ and a reference signal is computed in order to correct the strain signal. The correction signal is called $H_{corr}^{-1}(f)$, it is applied on the reconstructed strain signal $h(f)$.

The unbiased strain signal h_{unbias} still contains the lines injected by the photon and newtonian calibrators. However, the mirror displacements ΔL_{cal} caused by both calibrators is known, so the calibration lines can be subtracted. The contribution of the calibration signal to the error signal is subtracted from the raw power signal P_{raw}. The resulting power signal is called P_{clean}, and the strain signal computed from this power signal is called h_{clean}.

Some of the noise sources contained in the strain signal are monitored. The transfer function $TF_i(f)$ from the noise channel $\omega_{noise}(f)$ to the power signal P_{clean} is computed and the contribution of the noise channel to the power signal is subtracted. The resulting power signal is called P_{rec} and the strain signal computed from it is called h_{rec}.

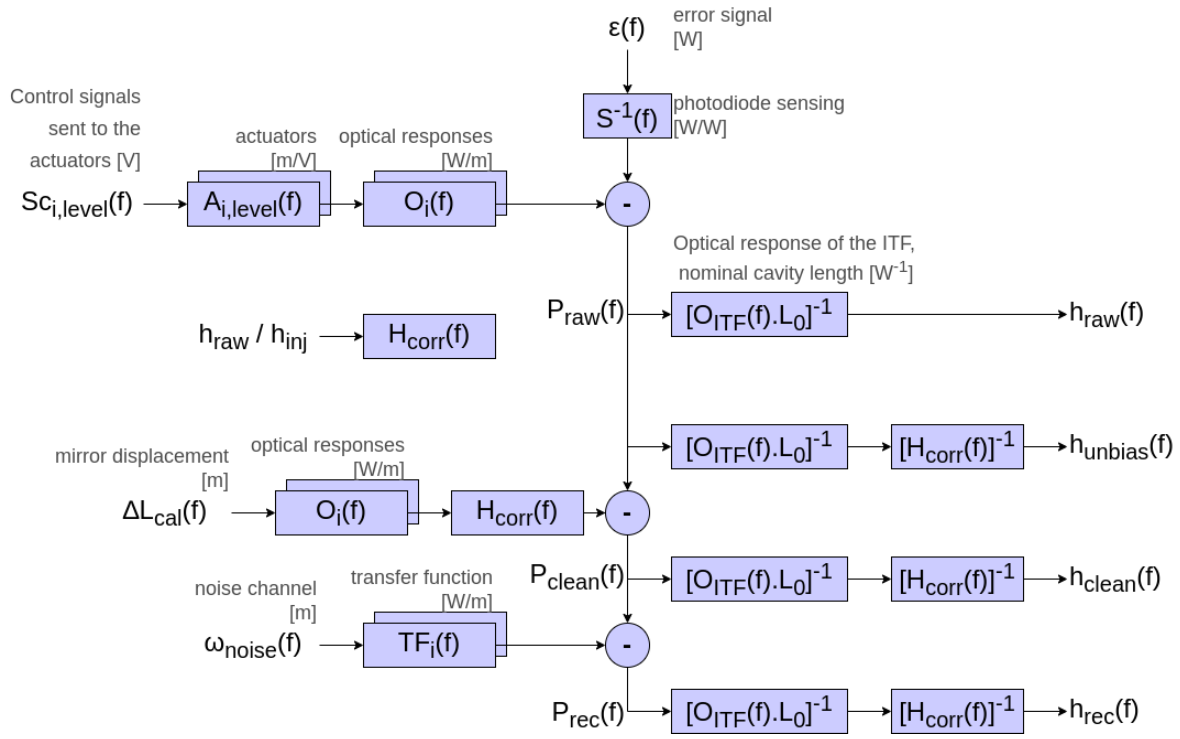

Figure 4.2: Simplified block diagram of the total reconstruction pipeline.

The reconstruction algorithm needs models of the optical responses of the interferometer and models of the responses of the actuators. All these models have been defined in chapter 2, the value of their parameters are determined by fitting the response measurements. The method for measuring the actuator response and the optical responses will be described in chapters 8 and 9.

4.1.3 Monitoring the optical responses of the interferometer

As seen in chapter 2, the optical responses of the detector to the displacement of the mirrors NE, WE, NI, WI and BS are modeled with a simple pole response.

$$O_{FP}(f) = \frac{G_p}{1 + i\frac{f}{f_p}} \cdot \exp(-i2\pi\tau_p f) \tag{4.5}$$

However, the resonant frequency and the gain of the optical cavity may vary with time, due, for instance, to the variations of the interferometer alignment. Thus, the values of these parameters have to be monitored, in order to adjust the optical response models used in the reconstruction pipeline.

A permanent sinusoidal hardware injection is done on the mirrors WE, NE and BS respectively at the frequencies 356.5 Hz, 357.5 Hz and 356.0 Hz. These frequencies are close to the expected value of the resonant pole of the optical response at ∼440 Hz. At the injected frequencies f_i (with $i \in \{NE, WE, BS\}$), we consider that the error signal variations $\mathcal{E}(f_i)$, at the frequency f_i are caused only by the corresponding mirror displacement:

$$\mathcal{E}(f_i) = S(f_i) \sum_k O_k(f_i) A_k(f_i) Sc_k(f_i) \tag{4.6}$$

With $A_k(f_i)$ the response of the actuator of the k mirror, and $Sc_k(f_i)$ its control signal, and $O_k(f_i) = \frac{G_k(f_i)}{1+i\frac{f_i}{f_{p,k}}}$ is the complex unknown. In practice, the computed unknown is $X_k = \frac{O_k(f_i)}{O_{ref}(f_i)}$, where $O_{k,ref}(f_i)$ is the reference optical response to the displacement of the mirror k. $O_{k,ref}$ is a first order pole with a gain $G_{ref} = 1$, and a resonant frequency $f_{p,ref} = 400\ Hz$. Thus:

$$\frac{\mathcal{E}(f_i)}{S(f_i) \cdot O_{ref}(f_i)} = \sum_k A_k(f_i) \cdot Sc_k(f_i) \cdot X_k(f_i) \tag{4.7}$$

The complex solution $X_k(f_i)$ of the equation system can be written in terms of gains $|X_k(f_i)|$ and phase $Arg[X_k(f_i)]$, from which the resonant frequencies $f_{p,k}$ and the gains G_k of the optical response can be computed.

The phase $\phi(f)$ of a first order pole with a resonant frequency f_p is:

$$\phi(f) = -\arctan\left(\frac{f}{f_p}\right) \tag{4.8}$$

Thus, the resonant frequency $f_{p,k}$ of the optical response $O_k(f_i)$ can be written as:

$$f_{p,k} = \frac{f_i}{\tan(-Arg[O_k(f_i)])} = \frac{f_i}{\tan\left(\arctan\left(\frac{f_i}{f_{p,ref}}\right) - Arg[X_k(f_i)]\right)} \tag{4.9}$$

And then the gain G_k of the optical response can be computed directly from the modulus of the solution and the resonant frequency.

$$G_k = G_{ref} \cdot |X_k(f_i)| \cdot \sqrt{\frac{1 + \left(\frac{f_i}{f_{p,k}}\right)^2}{1 + \left(\frac{f_i}{f_{p,ref}}\right)^2}} \tag{4.10}$$

Every 4 s, the reconstruction algorithm computes the solution of the complex system 4.7, and so the resonant frequencies and gains of the optical responses $O_k(f_i)$. The medians over 20 values (80 s) of the gain and of the resonant frequency are computed. The median values of the gain and resonant frequency are used to compute the model of the optical response used to reconstruct the strain signal h_{rec}.

4.2 Verification and correction of the h_{raw} signal

Even if the optical responses and the actuator responses of the interferometer are monitored, there may be some differences between the physical responses and the model used to reconstruct the strain signal. Thus, the raw reconstructed signal h_{raw} may be biased. To monitor the bias of h_{raw}, this signal has to be compared to a reference signal. A known motion is given to the end mirrors by using the EM actuators, the PCal or the NCal. This motion serves as a reference for h_{raw} bias monitoring. This action is named Hardware Injection. In this section, the method to compute and to correct the bias is explained.

4.2.1 Hardware injections

To verify the reconstructed strain signal h_{raw}, a known signal is injected with the EM actuator $h_{inj,i}$, the photon calibrator $h_{PCal,i}$ or the newtonian calibrator h_{NCal}, of the mirror $i \in \{NE, WE\}$. The injected signal is compared to the reconstructed detector strain signal h_{raw}. The injected signal can either be a sinusoidal signal or a broadband noise injected by the EM actuator or the PCal. The NCal can only inject sinusoidal lines.

The injected signal $h_{inj,i}$ is equal to the ratio between the mirror displacement $\Delta L_{mir,i}$ and the nominal cavity length L_0:

$$h_{inj,i}(f) = \frac{\Delta L_{mir,i}(f)}{L_0} \tag{4.11}$$

$$h_{PCal,i}(f) = \frac{\Delta L_{PCal,i}(f)}{L_0} \tag{4.12}$$

$$h_{NCal}(f) = \frac{\Delta L_{NCal}(f)}{L_0} \tag{4.13}$$

The mirror displacement caused by the PCal and the NCal, $\Delta L_{PCal,i}$ and $\Delta L_{NCal,i}$ are computed with a method described in sections 3.1 and 3.2. The mirror displacement caused by the EM is computed with the control signal of the actuator and the model of the actuator.

$$\Delta L_{mir,i}(f) = A_{mir,i}(f) \times Sc_{mir,i}(f) \tag{4.14}$$

What interests us is the ratio between the reconstructed signal and the injected signal, $\frac{h_{raw}(f)}{h_{inj}(f)}$ and $\frac{h_{raw}(f)}{h_{PCal}(f)}$. If the reconstruction of h is done properly, this ratio is equal to 1. Any deviation to 1 indicates a bias in the reconstruction. Which can be due to a difference bias on the model of the actuator responses or a bias on the model of the optical responses.

There are two kinds of the hardware injections:

- **The permanent injections** are 14 lines sent by the EM actuators or the PCal on the end mirrors. They are used to monitor the stability of the calibration, and to estimate the time variations of the bias of the raw reconstructed signal. The permanent injection done with the electromagnetic actuator are done after the signal Sc is computed. The frequencies of the lines injected by each actuator is given in table 4.1

Frequency [Hz]	Actuator
34.5	NE PCal
36.5	WE PCal
37.5	NE EM
56.5	WE EM
60.5	WE PCal
63.5	NE PCal
77.5	NE EM
106.5	WE EM
107.5	NE EM
137.5	NE EM
206.5	WE EM
355.5	WE PCal
359.5	NE PCal
406.5	WE EM

Table 4.1: Frequencies of the permanent lines injected by the actuators or the PCal on the end mirror

- **The weekly injections** are 28 lines, or a broadband noise, between 10 Hz and 2 kHz, injected during a dedicated shift once a week. These signals are injected successively by each actuator of the

end mirror, EM actuator, PCal and NCal. Each injection last for ∼2 min. The weekly injections are added to the DARM loop before the Sc signal is computed, so they are visible in the Sc signal. The weekly injections are used to estimate more precisely the frequency dependence of the bias and to provide a frequency-dependent uncertainty on the reconstructed h.

4.2.2 Frequency dependant bias

At the beginning of the O4 run for Virgo, the frequency dependant bias $H_{corr}(f)$ of the raw reconstructed signal will be computed. The bias is corrected after computing the reconstructed strain signal h_{raw} by multiplying the result by the inverse bias $[H_{corr}(f)]^{-1}$. The corrected bias is the same during all the run. The resulting signal is called $h_{unbias}(f)$.

A residual bias on h_{unbias} is computed using the weekly injection. Every week, the transfer function $\frac{h_{unbias}}{h_{inj,i}}(f_{inj})$ is computed at every injected lines. The transfer functions are used to compute a frequency and time dependant residual bias $b(f,t)$ on h_{unbias}, which gives the uncertainty on the reconstructed signal.

4.3 Lines and noise subtraction

The PCal and NCal are independent from the rest of the interferometer, thus the reconstruction algorithm considers the mirror motion given by the calibrators as an external motion. Therefore, the lines injected by the PCal and NCal are still visible in the corrected strain signal h_{unbias}. Since the permanent lines of the electromagnetic actuators are added to the DARM loop after the signal Sc is computed, they are still visible in the reconstructed signal and have to be subtracted too.

4.3.1 Calibration lines subtraction

The contribution of the PCal to the power signal P_{raw} is given by the signal $\Delta P_{PCal,i} = O_i(f)\Delta L_{PCal,i}$. In the same way, the contribution of the NCal is given by $\Delta P_{NCal} = O_{NE}(f)\Delta L_{NCal}$. The mirror displacement caused by the PCal $\Delta L_{PCal,i}$ or the NCal ΔL_{NCal} is computed from the models of the calibrators defined in chapter 3. The contributions are then subtracted from P_{raw}, the resulting signal is called P_{clean}. The unbiased strain signals computed from the power signals P_{raw} and P_{clean} are called respectively h_{unbias} and h_{clean}. Figure 4.3 shows the amplitude spectral densities of h_{unbias} and of h_{clean} before and after the subtraction.

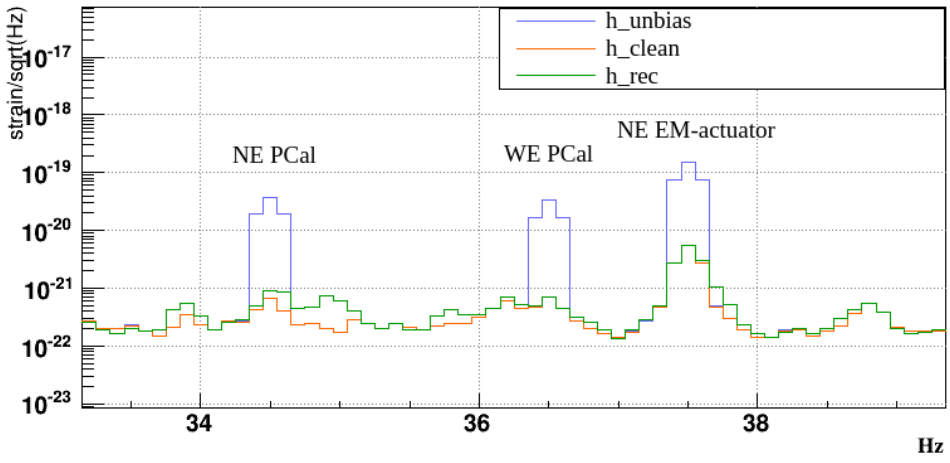

Figure 4.3: Amplitude spectral densities of the h_{unbias}, h_{clean} and h_{rec}, in the bandwidth [33 Hz, 39 Hz]. The frequency resolution is 0.1 Hz.

4.3.2 Noise channel subtraction

Even if the contributions of the different actuators and calibrators to the reconstructed signal are subtracted, some noise channels are coherent with h_{unbias}. The list of the witness channel for the O4 run is not defined yet. The witness channels used during O3 are:

- LSC_MICH
- SIB2_B2_8MHz_I
- SDB2_B1s1_PD1_Blended
- SNEB_B7_DC
- SWEB_B8_DC

When the coherence between one of these noise channels ω_i and P_{clean} at the frequency f is above 0.04, the transfer function from the noise channel to the reconstructed signal $TF\left[\frac{P_{clean}}{\omega_i}\right](f)$ is computed at the frequency f. The transfer function is the mean of 60 transfer functions computed over Hann windows of 8 s duration, overlapping over 4 s. Then, the fft of the noise channel $\omega_i(f)$ is computed, and multiplied by the transfer function $TF\left[\frac{P_{clean}}{\omega_i}\right](f)$. The result is the contribution of the noise channel to P_{clean}. Then, this contribution is subtracted from P_{clean}.

However, if at least two noise channels are coherent with h_{unbias}, and between each other, the subtraction of the two noise channels may subtract a noise twice. Thus, the noise channels are decorrelated thanks to a method described in [10]. Let $V(f)$ be the vector of the transfer functions from the noise channels to the raw reconstructed power signal P_{clean}.

$$V_k(f) = TF\left[\frac{P_{clean}}{\omega_k}\right](f) \tag{4.15}$$

And let $\Omega(f)$ be the vector of noise channels $\omega_i(f)$. For each frequency where the coherences between the channels are above 0.04, the matrix $T(f)$ of transfer functions between all channels is computed. Each element $T_{ij}(f)$ of this matrix is the transfer function between the noise witness channels ω_i and ω_j, at the frequency f.

$$T_{ij}(f) = TF\left[\frac{\omega_j}{\omega_i}\right](f) \tag{4.16}$$

Then, $T(f)$ in diagonalized by applying the base change matrix $B(f)$. The diagonal matrix equivalent to $T(f)$ is called $D(f)$. The base change matrix is specific to each frequency, so they are indexed by the frequency.

$$D(f) = B(f) \cdot T(f) \cdot B^T(f) \tag{4.17}$$

The vectors $V(f)$ and $\Omega(f)$, written in the new base, are called $V'(f)$ and $\Omega'(f)$.

$$V'(f) = B(f) \cdot V(f) \tag{4.18}$$
$$\Omega'(f) = B(f) \cdot \Omega(f) \tag{4.19}$$

Thus, at each frequency f the contribution of the channel $\omega'_i(f)$ to the raw reconstructed power signal P_{clean} is computed with the transfer function $V'_i(f)$, and it is subtracted from the power signal P_{clean}, the resulting power signal is called P_{rec}. The final strain signal h_{rec} is computed from P_{rec} by compensating the optical response of the interferometer $O_{ITF}(f)$, and the bias $H_{corr}(f)$.

Conclusion

The reconstruction algorithm has been modified for the O4 run in order to used independent optical response for each mirror. So the optical responses of each mirror has to be estimated. The optical responses of NE, WE and BS are already modeled in chapter 2. However, the optical responses of PR and SR mirror need to be be estimated and modeled. The new reconstruction algorithm also correct the bias, which requires a good estimation of the actuator responses. The calibration of the optical responses and actuator response of each mirror is done using the photon calibrator. In July 2023, the O4 run has not started yet for the interferometer Virgo, and the response of the actuators and the optical responses are not measured precisely.

The following chapters discuss the calibration of the PCal actuators and their use to calibrate the electromagnetic actuators, and the optical responses of each mirror of Virgo.

Chapter 5

PCal upgrades in prevision of O4

Contents

Introduction

During the O3 run, the PCals were already installed in front of the NE and WE mirrors. They were used as reference for the calibration of the interferometer. The design sensitivity of AdV+ has been improved for the O4 run, so to detect the gravitational waves signal with a higher SNR. Thus a more precise calibration of the interferometer is required. In addition, since the laser power noise of the PCal may limit the Virgo sensitivity, so the PCal noise level had to be reduced.

To satisfy these new constraints, the PCal design has been improved during my PhD. This chapter presents the new optical layout of the PCal with its optical and electronic components. The new control loop designed to reduce the laser power noise is also presented. The calibration of the PCal actuators is presented later, in the following two chapters.

5.1 Optical layout

As shown in section 3.1, the calibration of the PCal during O3 varied in time because of a correlation between the air humidity and the PCal response. This correlation was a large contribution to the calibration uncertainty, and had to be reduced for the O4 run. In addition, the constrain on the laser power noise has become stronger for the O4 run. Thus, the PCal design has been improved to satisfy these constraints.

5.1.1 Optical scheme

A scheme of the PCal optical setup is given in figure 5.2, and pictures are given in figure 5.1. The photon calibrator consists in two squared optical benches of 40 cm each. The PCal benches are installed on both sides of the vacuum tube. The optical benches are :

- The injection bench which produces the PCal laser beam and sends it to the center of the NE or WE mirrors.
- The reflection bench which measures the power of the reflected laser beam in order to estimate the end mirror displacement induced by the PCal actuator.

Each end mirror is in a vacuum chamber whereas the PCal optical benches are on air, out of the vacuum chamber. Thus, the PCal laser beam passes through two viewports, one at the exit of the injection bench , the second at the entrance of the reflection bench.

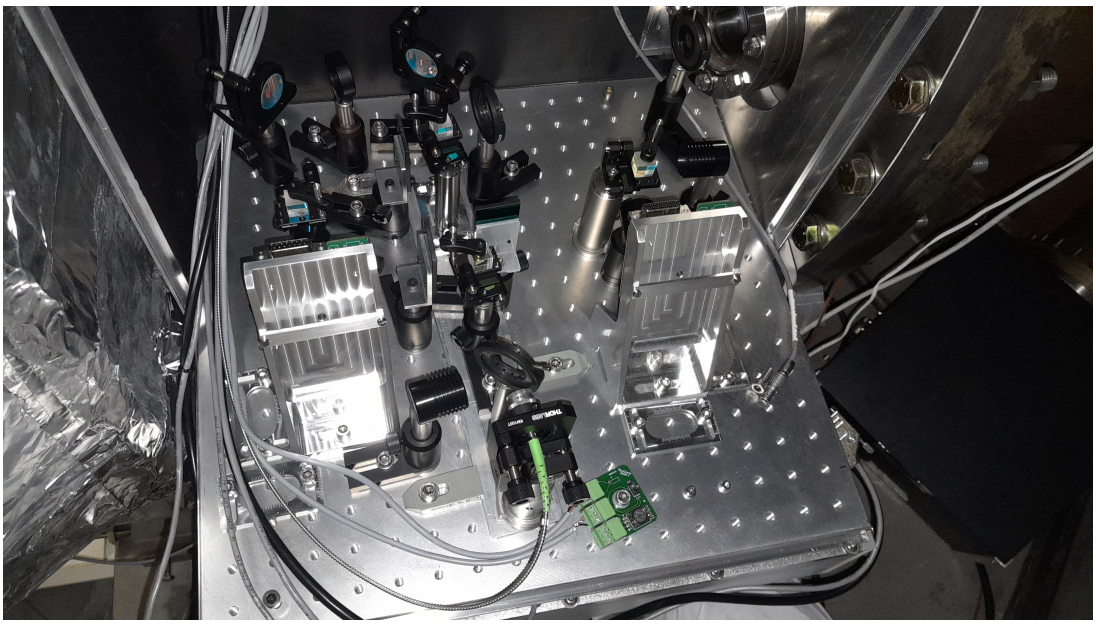

(a) Injection bench

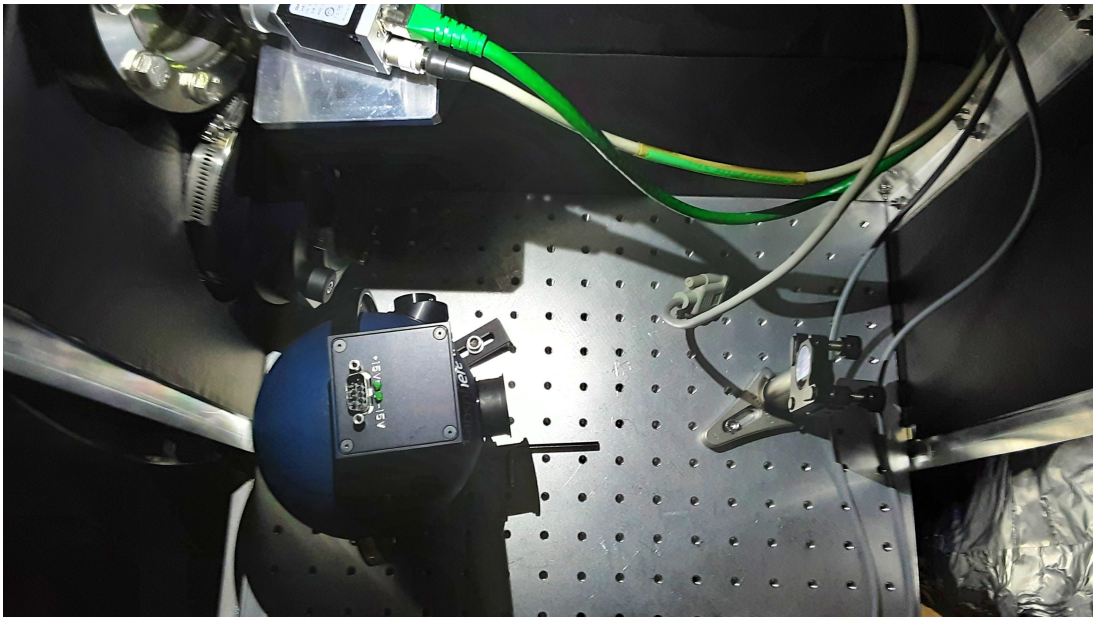

(b) Reflection bench

Figure 5.1: Pictures of the photon calibrator on WE, taken in September 2022.

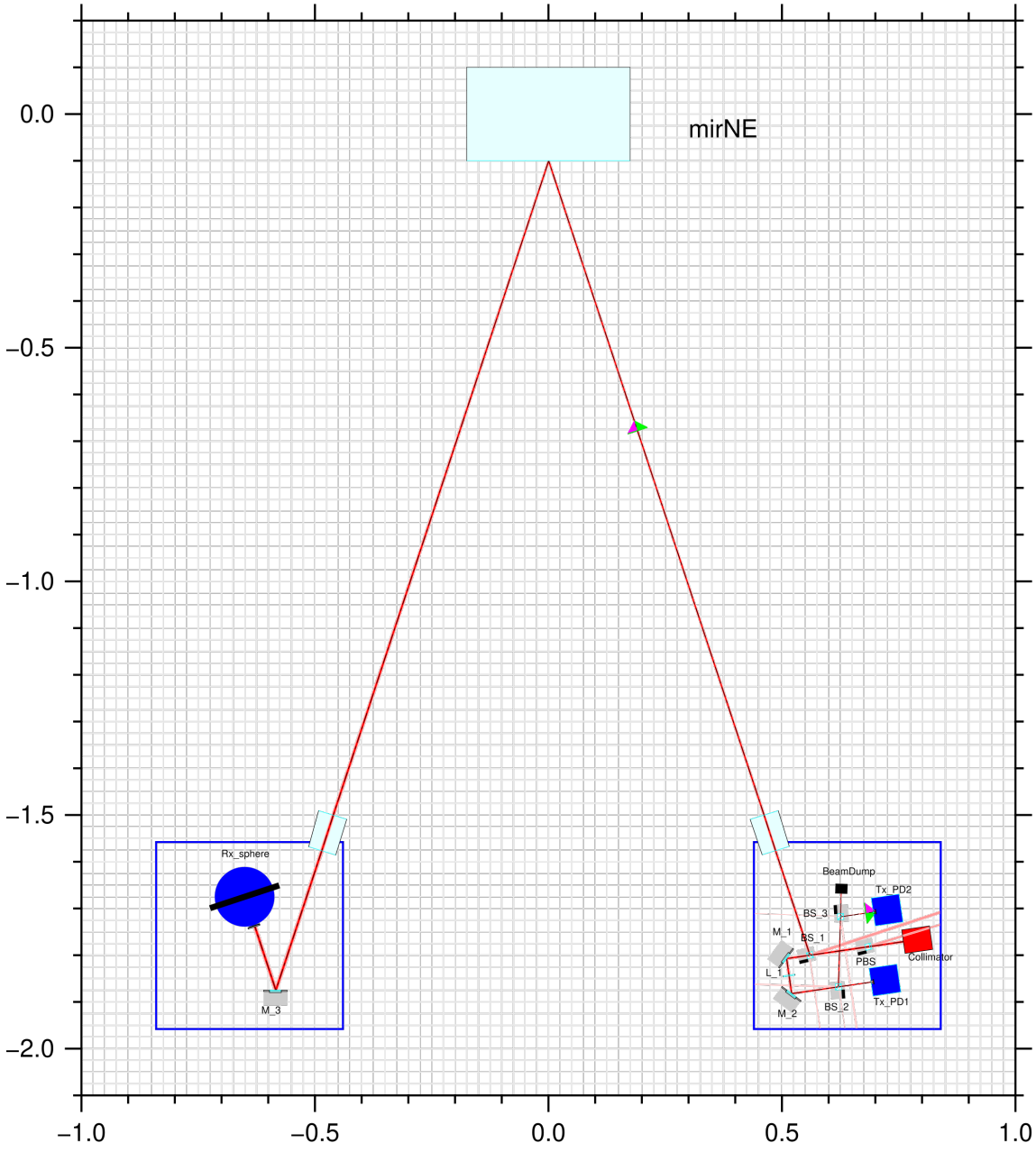

Figure 5.2: Optocad scheme of the PCal optical layout installed during the O4 run. The laser beam starts from the injection bench which at the bottom right corner of the figure. It is reflected by the end mirror at the top of the figure and goes to the reflection bench, at the bottom left corner of the figure.

5.1.2 Laser source

The laser beam is a continuous laser with a power range [0.2 W, 3 W]. It is produced by an Ytterbium fiber source made by Keopsys at the wavelength $\lambda = 1047$ nm. The power of the laser is driven remotely by a DAC. The power modulation at different frequencies is also done by the DAC, by direct modulation of the input current of the pump diode. The modulation frequency can go up to 10 kHz. The laser beam is sent from the laser source to the optical bench by a 14 m long optical fiber. The output of the laser fiber is connected to a collimator which adjusts the position of the beam waist The laser beam at the output of the fiber is polarized. Three laser drivers were used by the PCal calibration team, one for each PCal at Virgo, and a third one at LAPP to calibrate and characterize the power standards. Figure 5.3 shows a picture of the front panel of the laser driver, which is the same as the one used during O3 run.

Figure 5.3: Picture of the front panel of the laser driver.

5.1.3 Optical components

During O3, the correlation of the PCal response with the air humidity came from the variations of the reflection and transmission of the beam splitter mirrors used in the O3 design of the PCal. For the O4 run, it has been decided to replace these beam splitter mirrors by beam splitter cubes which are less sensitive to the air humidity variations. The O4 optical setup has been designed to use these cubes.

In addition, new photodiodes have been designed with better sensitivity to power noise. And a LIGO-like integrating sphere has been installed on the reflection as power calibration reference, instead of the photodiode used during O3.

PCal label	Constructor label	legend
collimator	Thorlabs CFC5-C	adjustable fiber collimator
PBS	Thorlabs PBS123	polarizing cube
BS_1	Thorlabs BS074	non polarizing cube R:90/T:10
M_1	Thorlabs BB1-E03	100 % reflectivity mirror
L_1	Thorlabs LB1391-C	lens with a focal length of 400 mm
M_2	Thorlabs BB1-E03	100 % reflectivity mirror
BS_2	Thorlabs BS062	non polarizing cube R:70/T:30
BS_3	Thorlabs BS005	non polarizing cube R:50/T:50
Tx_PD1	Laser-Components IG17x3000	photodiode
Tx_PD2	Laser-Components IG17x3000	photodiode
M_3	Samples from LMA	100 % reflectivity mirror
Rx_sphere	Labsphere + LIGO	integrating sphere
Beam Dump	Thorlabs LB1/M	beam dump

Table 5.1: List of optical components used on the PCal benches.

The laser beam is sent to the injection bench by the laser fiber. A **collimator** is connected to the fiber in order to adjust the shape of the beam. The laser beam is supposed to be s-polarized, but in order to remove further the p-polarisation, the laser beam passes trough a polarizing cube **PBS**. The beam is then splitted into two beams by a non polarizing cube **BS_1**. The beam reflected by BS_1 has a mean

power of 1.3 W and is sent to the end mirror.

The transmitted beam has a power of ∼120 mW, it is reflected by two 100% reflectivity mirrors **M_1** and **M_2**. This beam is focused by a lens **L_1** with a focal length of 400 mm in order to reduce the size of the beam on the photodiodes. The beam is then splitted by a second non polarizing cube **BS_2**. The transmitted beam has a power of ∼40 mW and is measured by the photodiode **Tx_PD1**. The reflected beam has a power of ∼80 mW and is splitted in two beams of ∼40 mW by a third non polarising cube **BS_3**. The power of the reflected beam out of this last cube is measured by the photodiode **Tx_PD2**, while the transmitted beam is dumped.

The laser beam enters the vacuum chamber of the end mirror by a viewport, coated with an anti-reflecting coating with a reflection of 0.05% per face at 1047 nm. After being reflected by the end mirror the main PCal beam passes a second viewport of the same kind and goes to the reflection bench. On the reflection bench it is reflected by a 100 % reflectivity mirror **M_3** which is a witness sample coated by the "Laboratoire des matériaux avancés" at Lyon, using the same High Reflectivity coating of the end mirrors. Then, the power of the full beam is measured by an integrating sphere **Rx_sphere**. The list of optical components is given in the table 5.1. More details about the power sensors will be given in the following section.

5.2 Power sensors

To estimate the power of the beam reflected by the end mirror, three power sensors have been installed on a PCal setup. There are two InGaAs photodiodes [17] on the injection bench, and an integrating sphere on the reflection bench. To calibrate these power sensors, a standard for power measurement is temporally installed on the PCal optical bench. The calibration process will be described later in the PhD report. Each power sensor is connected to a Data Acquisition box that reads the outputs of the sensors.

5.2.1 Data Acquisition Box

As during the O3 run, a Data Acquisition Box [3] (DAqBox) is associated to a PCal setup. The PCal DAqBox contains two ADC mezzanines, one slow DAC mezzanine which is not used anymore for O4, and one fast DAC mezzanine. The front panel of the DAqBox is shown in figure 5.4.

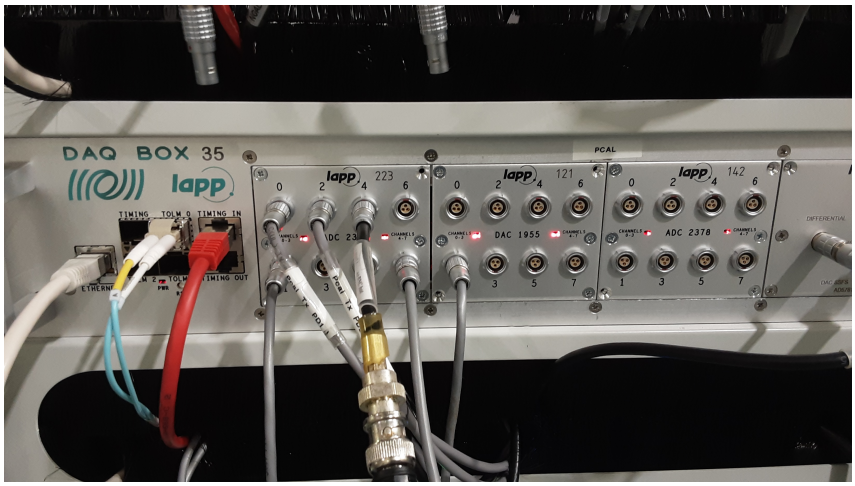

Figure 5.4: Picture of the front panel PCal DAQbox.

An ADC mezzanine reads the output voltages of the power sensors. Each of them has eight 3 pins LEMO input ports. Each port can read a differential voltage or a single-ended voltage in the range

$[-10\ \text{V}, +10\ \text{V}]$. The input impedance of the port is $\sim$2 kΩ for a differential voltage and $\sim$1.2 kΩ for a single ended voltage.

As seen in figure 5.5, the input analog signal is filtered by an analog low pass filter, which is a 5^{th} order Butterworth filter with the -3 dB cutoff frequency of 80 kHz, then it is digitized at 1 MHz. The digital signal can be down-sampled to a frequency f_S, which can be any divisor of 1 MHz. Before being down sampled, an anti-aliasing IIR filter is applied to the digital signal. This filter is a 8^{th} order Butterworth filter with a gain at the Nyquist frequency equal to $G(f_S/2) = -20$ dB. The voltage signal can be multiplied by a gain and an offset can be subtracted to get a calibrated channel. The ADC mezzanine of the PCal has two output signals, one signal sampled at 20 kHz which is sent to the data collection, and one signal sampled at 200 kHz which is used for the control loop of the laser. The 1 MHz signal can also be sent to data collection, but this is not done so as not to take up too much space in data storage.

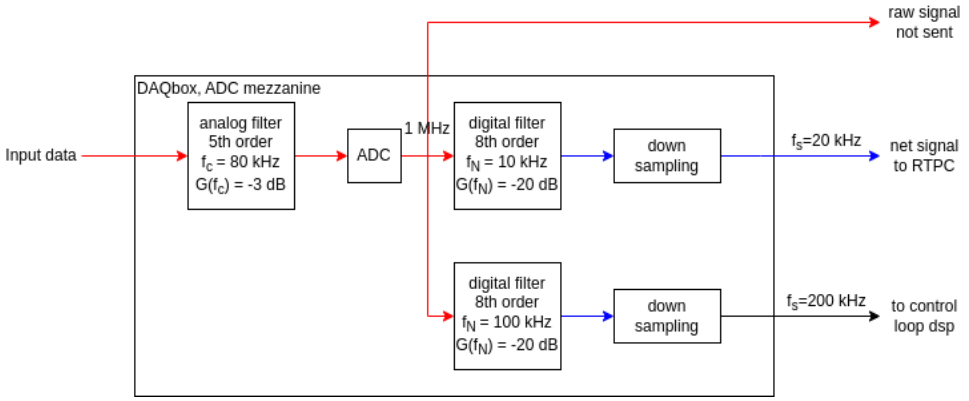

Figure 5.5: Scheme of the ADC channel

The fast DAC mezzanine generates a computer designed differential signal in the dynamic voltage range $[-10\ \text{V}, +10\ \text{V}]$. It is used to generate the command signal of the laser driver. It has only one channel with two outputs ports: a 3 pins LEMO port for differential signal, and a 2 pins coaxial LEMO port for single ended signal.

The fast DAC mezzanine contains a Digital Signal Processor (DSP) which can apply a filter to the digital signal. The value of the generated signal is updated at a frequency up to 1 MHz. On the PCal, the fast DAC generates a signal at 200 kHz to control the laser driver. It is filtered by an analog low-pass filter, which is a 2^{nd} order Butterworth filter with a cutoff frequency of 400 kHz.

5.2.2 Timing distribution

The output voltage signals of the different sensors are converted into digital signals by Analog Digital Converters (ADC). The digital signals are associated to a timestamp, and all the timestamps are synchronized with the GPS time.

As shown in figure 5.6, the timing distribution of Virgo comes from a centralized GPS receiver located in the central building of the detector AdV+. The receiver sends an IRIG-B signal to a first Time Distribution Box (TDBox) located in the central building. The TDBox distributes the IRIG-B signal to the TDboxes of the others buildings using long optical fibers. Then, the TDBox of each building distributes the IRIG-B signal to each electronic device (ADC, DAC channels, real-time PC ...) using short copper cables.

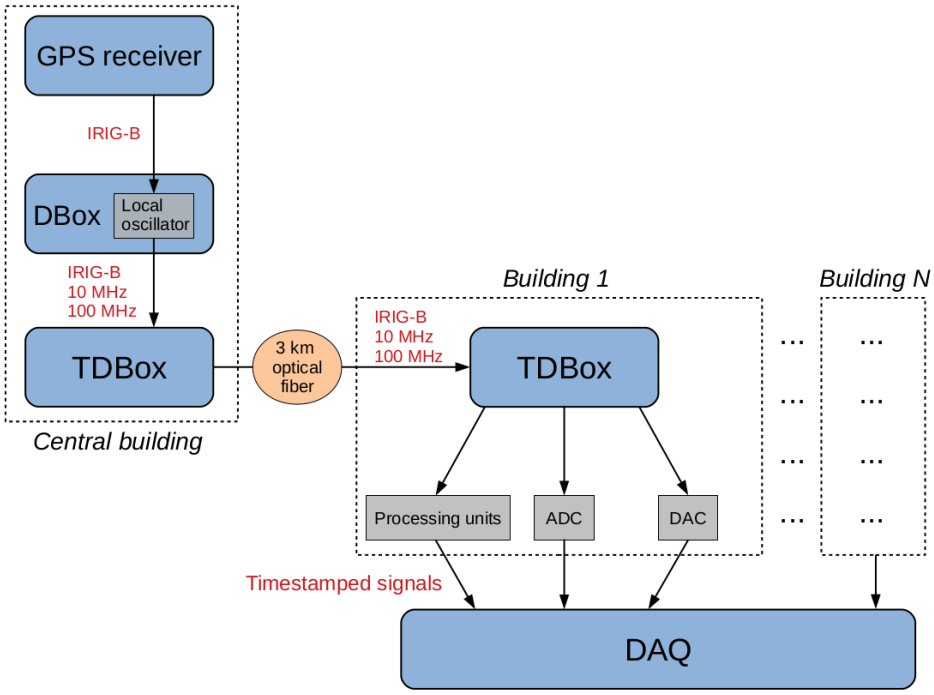

Figure 5.6: Scheme of the timing generation and distribution in AdV+.

The optical fibers that connect the TDBoxes of the end buildings are 3 km long, so the timings of the electronic devices of the end buildings are delayed by 16 µs. To have all the devices of AdV+ synchronized, a 3 km optical fiber is also used in the front-end distribution of the central building. Thus, the IRIG-B signal of the central building is also delayed by 16 µs.

5.2.3 InGaAs photodiodes

A fraction of the laser power is measured by two InGaAs photodiodes, **Tx_PD1** and **Tx_PD2**, (Laser-Components-IG17x3000). They are used to estimate the power of the laser beam reflected by the end mirror P_{ref}. Tx_PD1 is also used to control the laser power, in a digital control loop. The details of the control loop are presented in section 5.3. The characteristics of the photodiodes are given in table 5.2.

Diameter	3 mm
Typical responsivity (at $\lambda = 1047$ nm)	> 0.7 A/W
Maximum reverse voltage	10 V
Temperature dependence of the response	< 0.1 %/°C
Spectral range	850 to 1650 nm
Typical rise time	51 µs

Table 5.2: Characteristic of the InGaAs photodiode Laser-Components-IG17x3000

The photodiodes are connected to a preamplifier designed at LAPP, based on the design used for the detection system of the interferometer [17]. A picture of the photodiode on its preamplifier is shown in figure 5.7. The preamplifier has a resistive design, it has one output channel with a gain of 0.054 V/mA. The photodiode with its preamplifier has a measured gain of 41.7 V/W

The photodiodes and their preamplifiers are supplied with a differential voltage of ±13 V, generated by a Rohde & Schwartz voltage generator (figure 5.8), connected to the preamplifier with a SUBD15 connector. The output voltage of the preamplifier is connected to the ADC with a 3pins LEMO cable. The photodiode with its preamplifier accepts up to 80 mW input power, the input power on the photodiode is $\sim$ 42 mW for a reflected laser power $P_{ref} = 1.3$ W, and $\sim$ 80 mW for a reflected power $P_{ref} = 2.3$ W (maximum power of the reflected beam). The output voltage of photodiode when the laser

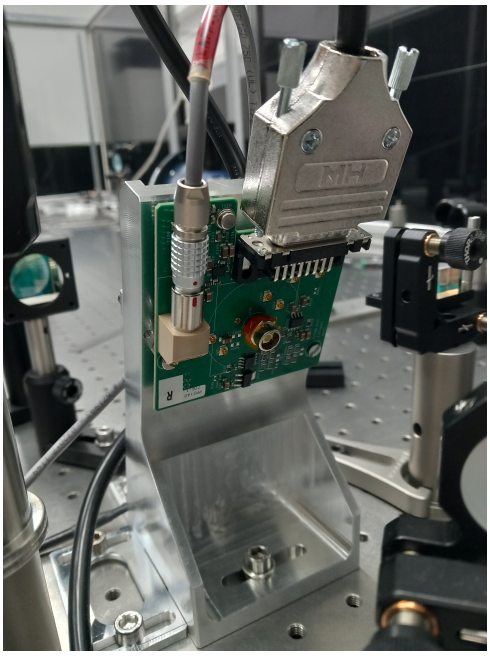

Figure 5.7: Picture of an InGaAs photodiodes on its peramplifier.

is at its maximum power is 3.4 V, which is inside the ADC input dynamics.

Figure 5.8: Picture of front panel of Rohde&Schwartz HMP4040 voltage generator.

5.2.4 Integrating spheres

For the O4 run, two kinds of integrating spheres are used: The Rx spheres which are placed on the reflection bench of the PCal, and the power standards which are used to calibrate the power sensors. The spherical shell of both kinds of spheres is the same as the one used during O3 for WSV sphere. The spheres have been mounted at LHO in May 2022, and have been shipped to the LAPP after.

The integrating sphere consists in a spherical shell with an internal diameter of 4 inches. It has an input hole with a diameter of 1 inch, and a detector hole on the top where the detector housing is connected. This housing contains a photodiode with its preamplifier. It is supplied with a $\pm$ 15 V differential voltage. A scheme of the working principle of the integrating sphere is shown in figure 5.9. The internal surface of the shell is covered with a material, named "spectralon", which scatters the laser. The input laser beam hits the back of the sphere, and the light is scattered multiple times by the spectralon, and a fraction of the scattered light passes the detector hole and is measured by the photodiode.

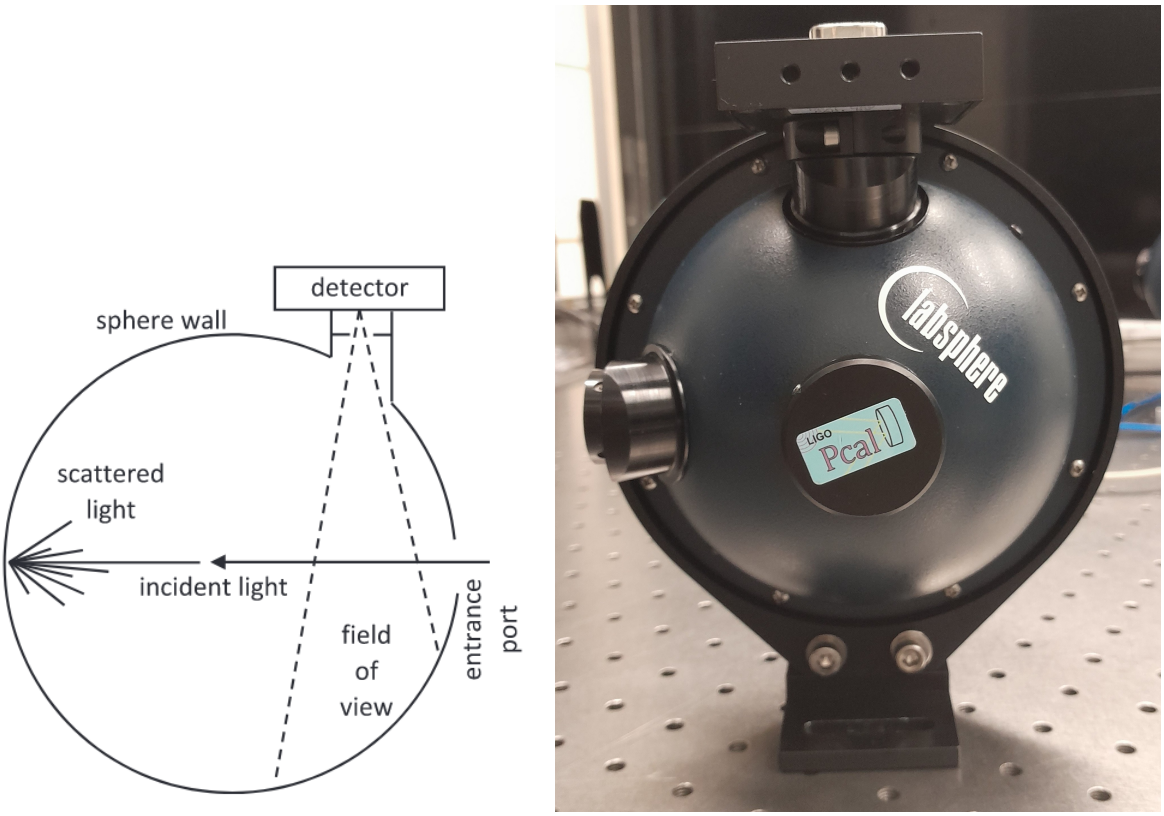

Figure 5.9: Left: Drawing of the working principle of an integrating sphere, view from the side. Right: Picture of an integrating sphere viewed from the front.

In addition to the O3 design, a spacer has been placed between the spherical shell and the photodiode housing, in order to limit the field of view of the photodiode inside the sphere, and so reduce the dependency of the response to the temperature. In theory, the measured power does not depend on the angle of incidence or the collimation of the input beam.

The sphere is supplied by a Rohde&Schwartz HMP4040 voltage generator and the output voltage is measured by an ADC channel of the DAqBox. The voltage supply and the output voltage are distributed between the sphere, the voltage generator and the DAqBox, through the blue box interface shown in figure 5.10.

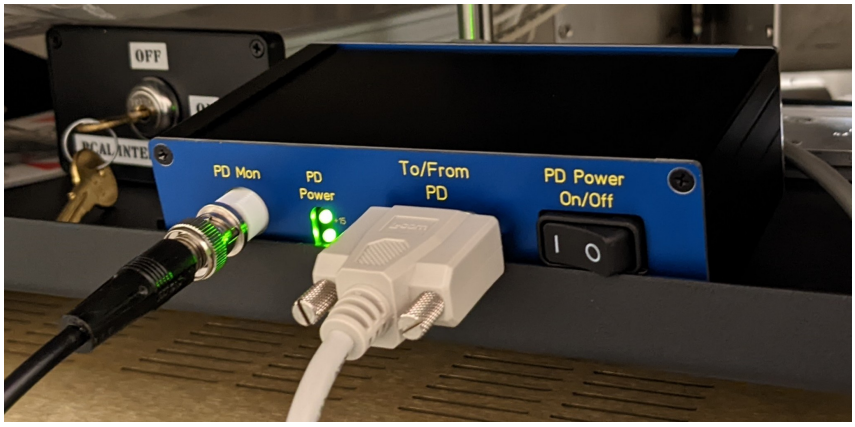

Figure 5.10: Picture of the blue box interface.

Rx integrating spheres The reflection bench contains only an integrating sphere Rx_sphere and a high reflectivity mirror M_3. This new configuration allow the Rx_sphere to measure directly the power of the reflected beam, with only the losses of the viewport and of the M_3 mirror. The Rx spheres do not have a temperature sensors. The output of the sphere is a differential voltage proportional to the incident laser power which is read by the ADC. The Rx spheres have been installed on the PCal benches in July 2022 on WE and in September 2022 on NE.

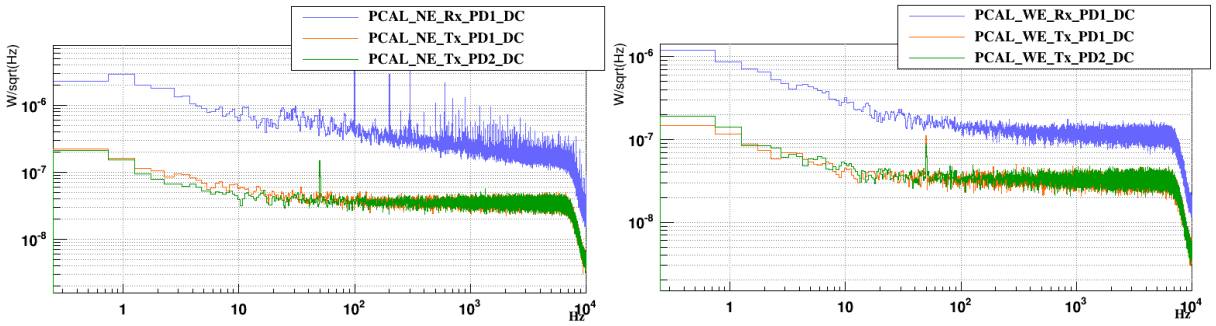

Figure 5.11: Sensing noise level of the two photodiodes and of the Rx sphere on NE (left) and on WE (right), related to the laser power. The data was taken in November 2022, after the calibration of the PCal.

Figure 5.11, shows the sensing noise level of the two photodiodes and of the Rx sphere, related to the laser power.

The sensing noise of the NE Rx sphere is higher than the sensing noise of the WE Rx sphere. The extra sensing noise of NE seems to come from the preamplifier itself and not from a cable or the ADC mezzanine.

GSV and WSV integrating spheres The PCal photodiodes and Rx_spheres are calibrated in power with respect to the power standards which are the Golden Standard Virgo (GSV) and the Working Standard Virgo (WSV). These standards are also integrating spheres. Their spherical shells are the same as Rx_sphere, their preamplifier differs from the preamplifier of the Rx sphere. The output voltage of photodiode preamplifier is single-ended, and the preamplifier contains a temperature sensor. The output voltages of the photodiode and the temperature sensor are read by the ADC. The preamplifier is also supplied with a differential $\pm$ 15 V voltage generated with a Rohde&Schwartz HMP4040 voltage generator.

The GSV sphere is kept at LAPP in order to maintain its responsivity as stable as possible, it is used as a standard for power calibration. The WSV sphere travels from LAPP to the Virgo site in order to calibrate the PCal power sensors. A first calibration of the PCal using WSV was done in November 2022, and second calibration was done in July 2023.

5.2.5 ADC impedance correction

The Virgo standards were built and calibrated in May 2022 at LHO: they are provided with an absolute calibration gain in [V/W]. The ADC mezzanine which measures the output voltage of the spheres has an input impedance of 2 kΩ [3], and the cable which connects the sphere to its blue box interface is 12 m long and has an impedance of $\sim$ 3 Ω. This caused a drop of the voltage measured by the ADC of a few tenths of percents. Thus, the measurement of the input power of the sphere was biased. This issue was found during sphere calibration measurements at LAPP, differences of about 0.2% were found between the measurements done at LHO with with a high impedance voltmeter, and the measurements done at LAPP.

In order to adapt the impedance of the ADC mezzanine, a voltage follower circuit has been designed with the LAPP electronic team in summer 2022 and added to the outputs of the sphere [18]. The output of the integrating sphere is connected via the long db9 cable to the input port of the follower circuit which has an input impedance of 100 MΩ, and the output of the circuit is connected to the DAqBox with a short cable with a negligible impedance, as shown in figure 5.12.

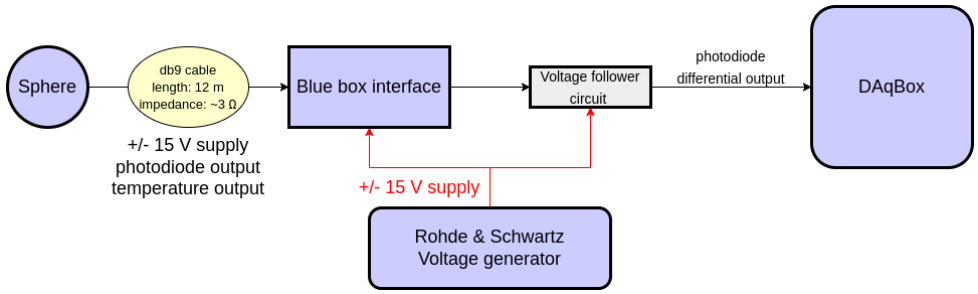

(a) Rx spheres

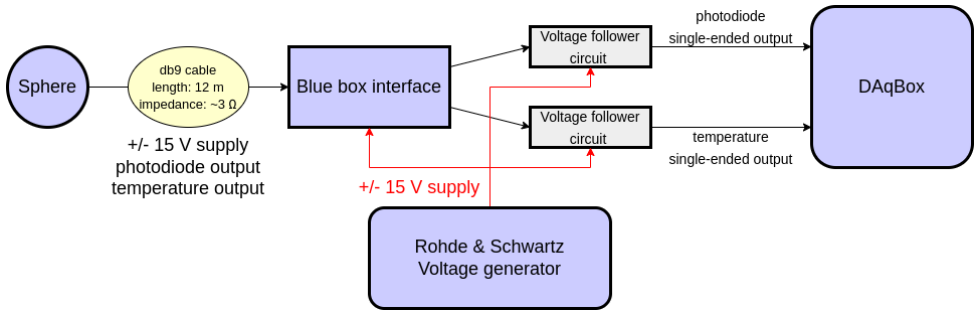

(b) WSV and GSV spheres

Figure 5.12: Schemes of the sensing chain of the two kinds of spheres

5.3 Laser control loop

The power noise of the PCal laser produces a noise in the end mirror motion signal, which is seen by the interferometer as a differential arm length signal. Thus, the power noise of the PCal contributes to the overall noise in the strain signal $h(t)$ of the interferometer. To limit the noise level of the laser, the laser command is in a control loop with one of the PCal photodiodes.

5.3.1 PCal noise constraint

The nominal sensitivity of AdV+ $h_{O4}(f)$ is defined for the O4 run. As for all technical noise, the contribution of the PCal laser power noise must be kept a factor 10 below the nominal sensitivity $\frac{\Delta L_{PCal}(f)}{L_0} < 1/10 \cdot h_{O4}(f)$. Equation (3.8) is used to convert ΔL_{PCal} into a constraint on the power noise ΔP_{ref}. Figure 5.13 shows the laser noise level when the laser power is set to 1.3 W with the laser noise constraint.

As shown in figure 5.13, the power noise produced by the PCal lasers is above the noise constraint in the frequency band 10 to 200 Hz, and thus needs to be mitigated.

5.3.2 Loop design

To mitigate the laser power noise, the PCal laser is controlled by a digital control loop running at 200 kHz on the DSP of the fast DAC mezzanine. The feedback signal of the control loop ϵ_{pre} is given by one of the photodiodes on the injection bench, in order to avoid any clipping due to the end mirror displacement. By default, the in loop photodiode is Tx_PD1 which has been calibrated so as it estimates the power reflected by the end mirror. Its output signal is sampled at 200 kHz and is directly sent to the DSP of the fast DAC. The power command P_{req} is the requested power of the beam reflected by the end mirror. A noise signal n can be added to the requested signal. The difference between the power request and the photodiode feedback gives the error signal ϵ_{post}. The error signal is filtered by the loop filter with a frequency response $F_c(f)$, then sent as a correction signal to the laser driver. A diagram of the control loop is shown in figure 5.14.

The frequency response of the PCal bench is represented by $H_{PCal}(f)$. It contains the frequency response of the laser driver and of the photodiode. The analog and digital filters for the 200 kHz channel,

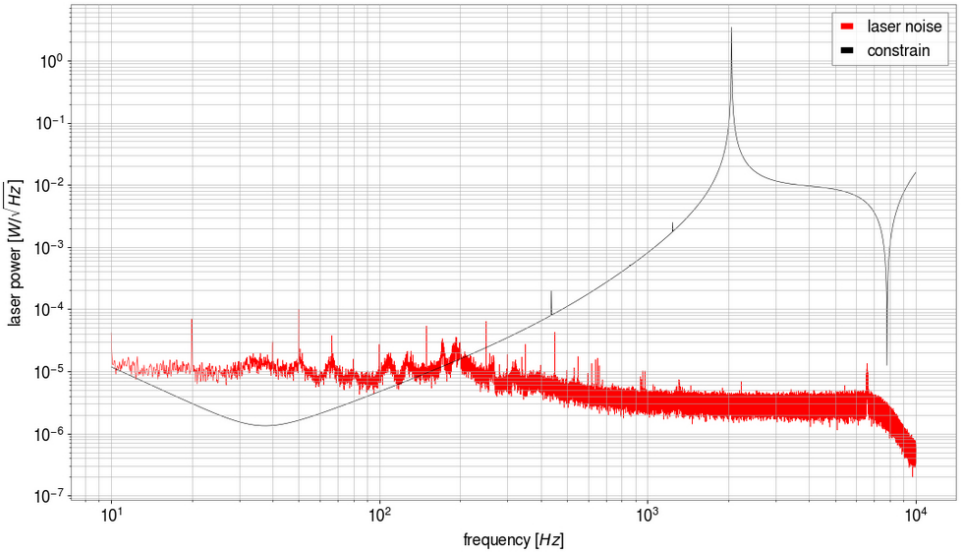

Figure 5.13: Constraint on PCal laser noise for O4 run, with power noise level of the NE PCal laser power is at 1.3 W, without control loop.

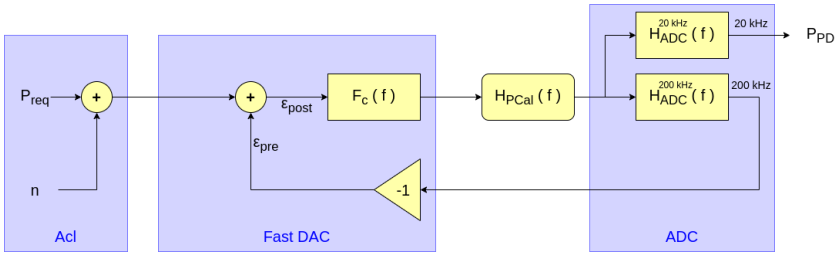

Figure 5.14: Diagram of the PCal laser control loop.

and the calibration gain of the ADC are represented by $H_{ADC}^{200kHz}(f)$.

5.3.3 Control loop filter

The loop filter $F_c(f)$ is a digital IIR filter computed by the DSP of the fast DAC mezzanine. The filtered signal is sampled at 200 kHz. This filter is defined by its frequency response $F_c(f)$, which is a product of frequency responses of poles and zeros of the 1^{st} or 2^{nd} orders. Equations (5.1a), (5.1b), (5.1c) and (5.1d) show respectively the frequency response of the 1^{st} order pole, the 2^{nd} order pole, the 1^{st} order zero and the 2^{nd} order zero, and equation (5.1e) shows the frequency response of an integrator.

$$H_{p,1}[f_p](f) = \frac{1}{1 + i\frac{f}{f_p}} \tag{5.1a}$$

$$H_{p,2}[f_p, Q](f) = \frac{1}{1 + i\frac{1}{Q}\frac{f}{f_p} - \frac{f^2}{f_p^2}} \tag{5.1b}$$

$$H_{z,1}[f_z](f) = 1 + i\frac{f}{f_z} \tag{5.1c}$$

$$H_{z,2}[f_z, Q](f) = 1 + i\frac{1}{Q}\frac{f}{f_z} - \frac{f^2}{f_z^2} \tag{5.1d}$$

$$H_{int}(f) = \frac{1}{i2\pi f} \tag{5.1e}$$

During the O3 run, the unity gain frequency (UGF) of the control loop was 3.8 kHz on NE and 4.8 kHz on WE, and associated phase margins were respectively 68° and 57° [6]. As shown in figure 5.15,

the O3 control loop did not mitigate the laser power noise enough to satisfy the noise constraint of O4 run.

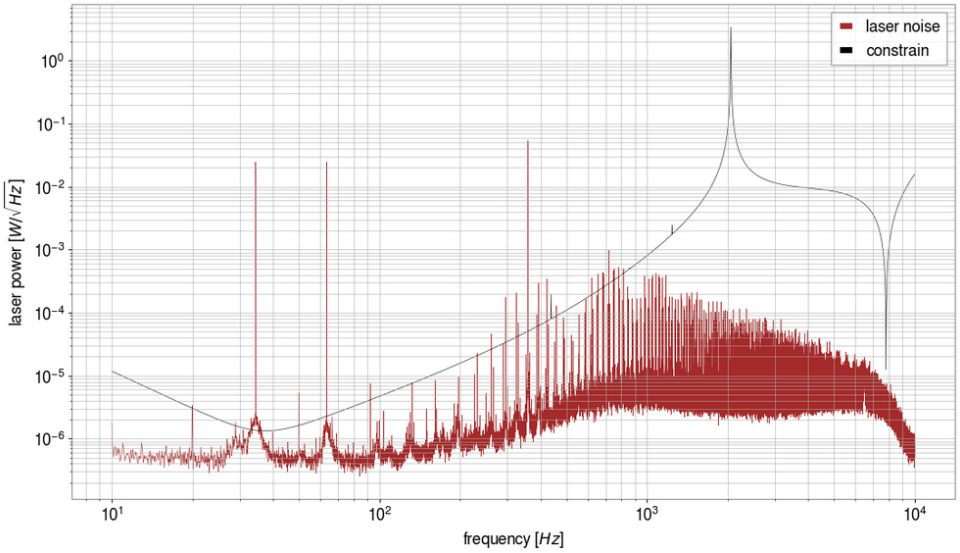

Figure 5.15: Constraint on PCal laser noise for O4 run, with power noise level of the NE PCal laser with O3 control loop, measured with Tx_PD2 photodiode. Data taken after the calibration of sensors done in November 2022.

It was needed to further lower down the laser power noise. The sensing noise level of the photodiodes is 3×10^{-8} W/$\sqrt{\text{Hz}}$ during O4 and was 3×10^{-7} W/$\sqrt{\text{Hz}}$ during O3. So it is possible to increase the gain of the control loop and to lower the laser noise. The loop filter was changed for O4 run. Asa result, the gain of the filter in the working bandwidth was increased and the UGF was higher. The new filter design is given in table 5.3, and its frequency response is given in figure 5.16.

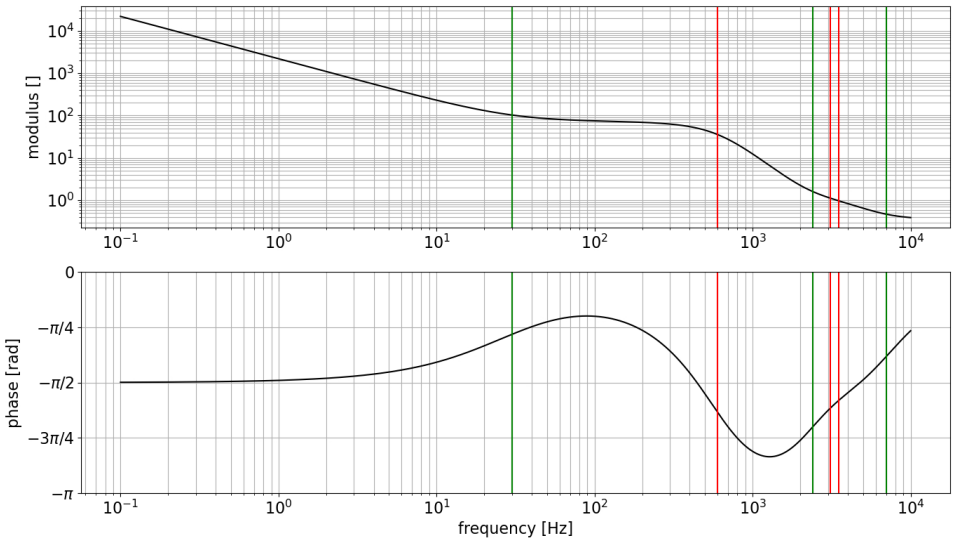

Figure 5.16: Frequency response of the O4 loop filter in the DSP. The frequency of the poles and the zeros are represented by the vertical bars.

5.3.4 Control loop characterizations

The open loop transfer function (OLTF) of the control loop characterizes its stability. To measure it, a white noise signal $n(t)$ is injected in the laser command signal. The amplitude spectral density of the noise is 1 W/$\sqrt{\text{Hz}}$. The OLTF is derived as following:

component	frequency	quality factor
integrator		
1st order zero	30 Hz	
2nd order pole	600 Hz	0.7
1st order pole	600 Hz	
2nd order zero	2400 Hz	0.7
2nd order zero	2400 Hz	0.7
1st order pole	3100 Hz	
2nd order pole	3500 Hz	0.7
2nd order zero	7000 Hz	0.7

Table 5.3: List of the poles and zeros of the O4 loop filter.

$$OLTF(f) = \frac{\epsilon_{pre}(f)}{\epsilon_{post}(f)} = -F_c(f)H_{PCal}(f)H_{ADC}(f) \tag{5.2}$$

Figures 5.17a and 5.17b show respectively the OLTF for the NE and WE PCal.

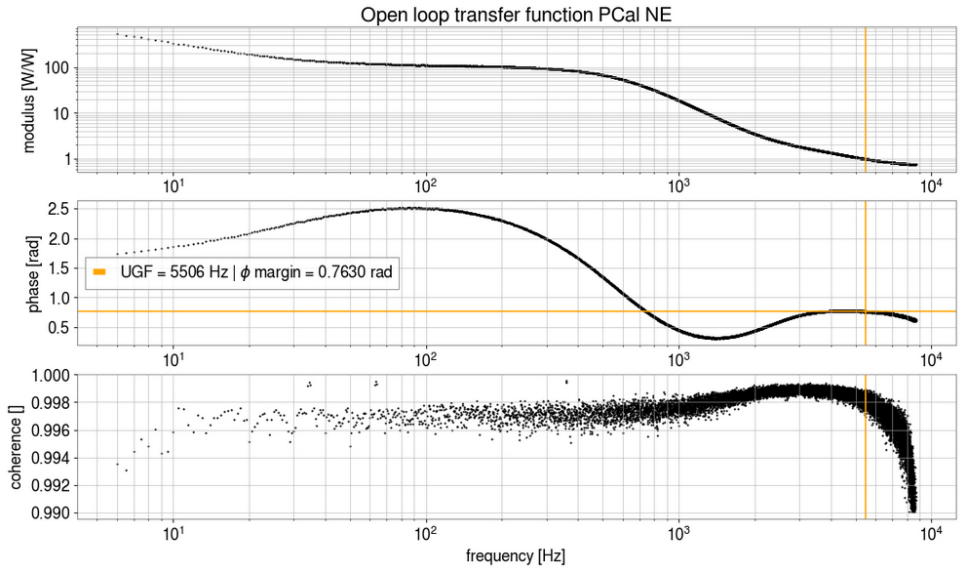

(a) PCal NE

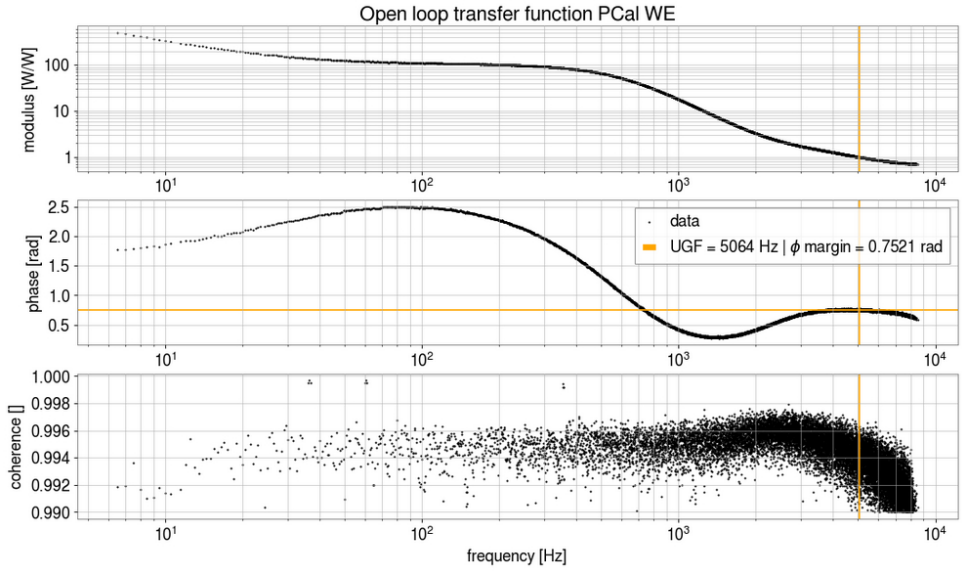

(b) PCal WE

Figure 5.17: Open loop transfer functions of the NE and WE PCals. The yellow lines represent the unity gain frequency and its phase margin. Top: Modulus of the transfer function. Middle: Phase of the transfer function. Bottom: Coherence between ϵ_{pre} and ϵ_{post} signals.

The phase margin associated with the UGF is used to characterize the stability of a control loop. Typically, a phase margin above $\frac{\pi}{6} \approx 0.52$ rad guaranty a good stability. The UGF of the control loop are 5.5 kHz on NE and 5.1 kHz on WE, and the associated phase margins are high enough, 0.76 rad on NE and 0.75 rad on WE.

The closed loop transfer function (CLTF) characterizes the amplitude of the photodiode response to a requested signal. The goal of the CLTF study is to verify if the amplitude of the photodiode response has the same order of magnitude as the requested signal. The exact value of the CLTF does not really impact the calibration data analysis, because the data analysis is done with the photodiodes outputs and not the requested power.

The CLTF is the transfer function from the requested laser power signal n to the in-loop photodiode output P_{PD}, both sampled at 20 kHz. The CLTF is derived as the following:

$$CLTF(f) = \frac{P_{PD}(f)}{n(f)} = \frac{F_c(f)H_{PCal}(f)H_{ADC}^{20kHz}(f)}{1 + F_c(f)H_{PCal}(f)H_{ADC}^{200kHz}(f)} \tag{5.3}$$

Figures 5.18a and 5.18b show respectively the measured CLTF of the NE and WE PCal.

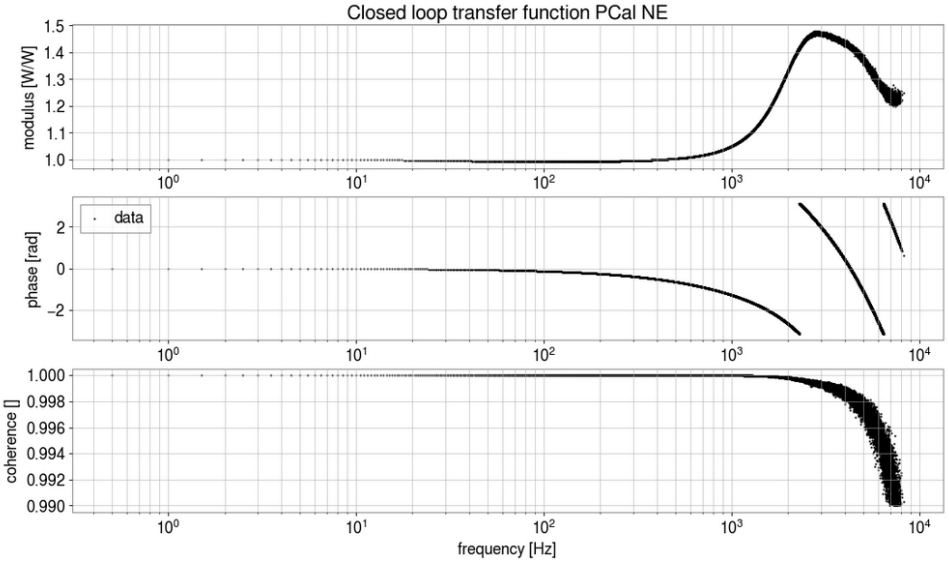

(a) PCal NE

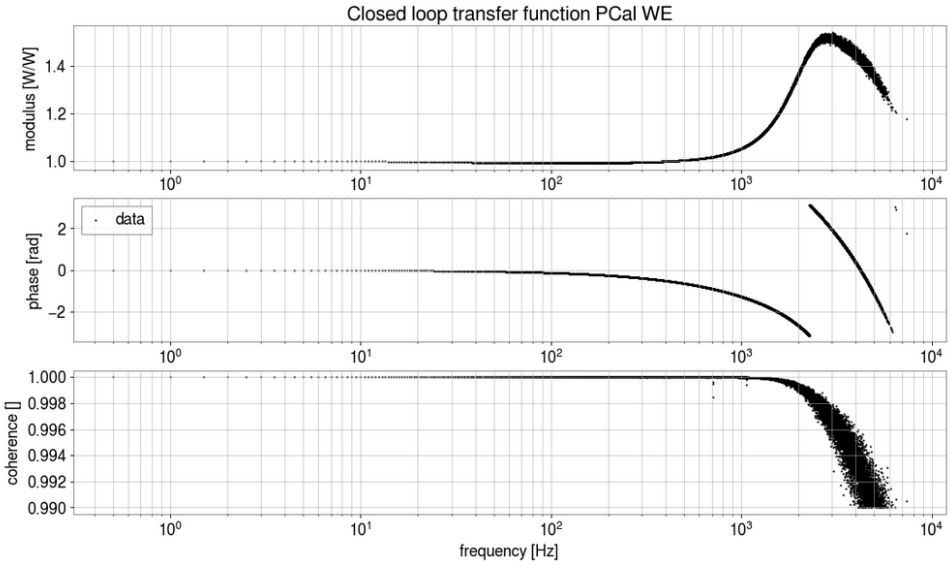

(b) PCal WE

Figure 5.18: Closed loop transfer function of the PCal. Top: Modulus of the transfer function. Middle: Phase of the transfer function. Bottom: Coherence between P_{PD} and n signals.

On both PCals, the modulus of the CLTF stays around 1, at the 5% level in the frequencies below 1 kHz, and rise to 1.5 at higher frequencies. The phase of the CLTF shows delay of 0.24 ms between the requested signal and the photodiode response. During the calibration of the interferometer, the CLTF is not taken into account. The motion of the end mirror is estimated from the power of the PCal laser measured by the power sensors, and not from the requested power signal. However, one must pay attention not to saturate the laser when requested modulation above 1 kHz.

With the new filter design and the new sensors, the PCal laser noise level is properly lower than the constraint as shown in figure 5.19. Only the calibration lines at 34.5 Hz, 63.5 Hz and 359.5 Hz on WE and at 36.5 Hz, 60.5 Hz and 355.5 Hz on NE are above the noise constraint. These lines are injected in

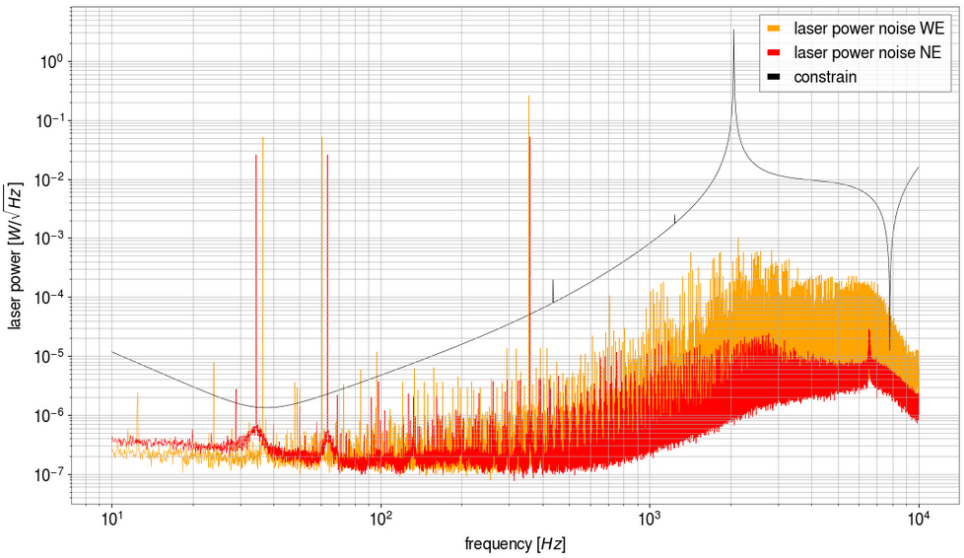

Figure 5.19: Constraint on PCal laser noise for O4 run, with power noise levels of the NE PCal and WE PCal laser with new control loop, measured with Tx_PD2 photodiode. The three lines above the constrain are requested power modulation.

order to monitor the error on the reconstructed strain signal.

Conclusion

The O3 PCal were dismounted in July 2020. Stating from October 2020 the O4 PCal setup was being designed. A PCal setup with the O4 design was built at LAPP in order to test its stability and its noise level. The injection bench of the WE PCal has been installed with the new design, in April 2021. The injection bench of NE was installed in February 2022. Since the Rx spheres were not mounted already, the reflection benches of the WE and NE PCal had the O3 design. Both PCal were calibrated with respect to the O3 WSV integrating sphere. During winter 2021-2022, work has been done to improve the control loop design, in order to the contribution of the laser power noise to the sensitivity and keep it below the O4 constraint. The Rx sphere as well as GSV and WSV were mounted at LHO in May 2022, in the LHO laboratory in collaboration with Richard L. Savage and Francisco Llamas from the LIGO collaboration. A ∼0.2% difference between the readouts of the PCal ADC and the Keithley voltmeter had been noticed, thus the follower circuits were designed be the electronic team of the LAPP during summer 2022, in order to correct the output voltage of the integrating spheres. The Rx spheres were installed on the WE reflection bench in July 2022 and on NE in September 2022 with the help of Dripta Bhattacharjee from the LIGO collaboration.

The new PCal setup has been calibrated in November 2022 and in June 2023. The calibration of the PCal photodiodes and Rx spheres is explained in chapter 7. They are calibrated with respect to the WSV and GSV integrating spheres, and the calibration of these spheres is explained in chapter 6.

Chapter 6

Calibration of the Virgo integrating spheres

Contents

Introduction

To estimate properly the mirror displacement due to the PCal, the power of the laser has to be estimated with the photodiodes Tx_PD1 and Tx_PD2, and mainly the Rx sphere. These power sensors of the PCal are calibrated with respect to the Virgo integrating spheres, WSV and GSV, themselves calibrated with respect to international standards from NIST and PTB. Each standard is provided with a responsivity ρ in [V/W]. So the measure of the absolute voltage is crucial to use this calibration gain. The goal of the calibration of the integrating spheres is to measure their responsivity.

From May 16, to June 3, 2022, I was in the United-States at the LIGO Hanford Observatory (LHO) to mount the Virgo integrating sphere and calibrate them with respect to the LIGO power standards, calibrated by NIST. Then, I built a calibration setup at LAPP which is similar to the setup used at LHO. The intercalibration of the sphere is first presented as well as the results of the measurement campaign done at LHO and then at LAPP. In the next section, I also characterized the integrating spheres in order to estimate the uncertainty on the value of the laser power measured by the sphere.

6.1 Absolute calibration of the integrating sphere LIGO-Virgo-KAGRA

The power calibration of the sensors of each PCal of each collaboration has to be common between each collaboration for a good relative calibration, and has to be done with respect to standards from the international metrology institutes foran absolute calibration. The LIGO, Virgo and KAGRA (LVK) collaborations worked with the National Institute of Science and Technology (NIST) in the United States, and the Physikalisch-Technische Bundesanstalt (PTB) in Germany, to calibrate common power standards. The goal of the calibration of the integrating spheres is to measure their responsivity ρ in V/W. Thus the measurement of the sphere output voltage is crucial for the calibration of the spheres.

6.1.1 Intercalibration procedure

For O4, the NIST has calibrated two integrating spheres named "Transfer Standard" (TSA) and (TSB). Their calibration gain is known within an uncertainty of 0.1% [27]. To prevent errors due to the differences between the different devices used for the power calibration, it has been decided to use the same kind of integrating sphere as the power standard used by the LVK collaborations. Thus, GSV and WSV are integrating spheres of the same kind as TSA and TSB. The two transfer standards are the main reference for the calibration of all the gravitational wave detectors.

Each collaboration got a Working Standard (WS) and a Gold Standard (GS). The WS is used to calibrate the sensors of the PCal, the GS is used to monitor the calibration of the WS In the case of the Virgo spheres, the GSV is kept in the optical laboratory of the LAPP, and the WSV travels back and forth between the LAPP and the Virgo site. To make sure that the calibration of the sphere keeps matching with the NIST and PTB calibration, the transfer standards (TSA/TSB) travel between the metrology institutes and the detector sites. It is planned that every two months, each transfer standard is shipped from one site to an other, the order of the locations visited by the transfer standards is shown in figure 6.1. Thus, each site will receive a transfer standard every six month.

This procedure has not started yet at the time of the writing. In this chapter, the reference calibration is a NIST-calibrated located at LHO. The sphere calibration setup and method are described in this section. The method for calibrating the spheres between each other is the same on each site, taking advantage of the developments made by LIGO in the last decade. The analysis scripts are also common between the collaborations. A gitlab repository has been created to share between the collaborations the analysis scripts and the calibration results from the transfer standards to the gold and working standards.

6.1.2 Optical bench setup at LAPP

A calibration setup has been created at LAPP, to calibrate one sphere with respect to another. The sphere to be calibrated is named "test sphere", the sphere used as a standard is named "reference sphere". The

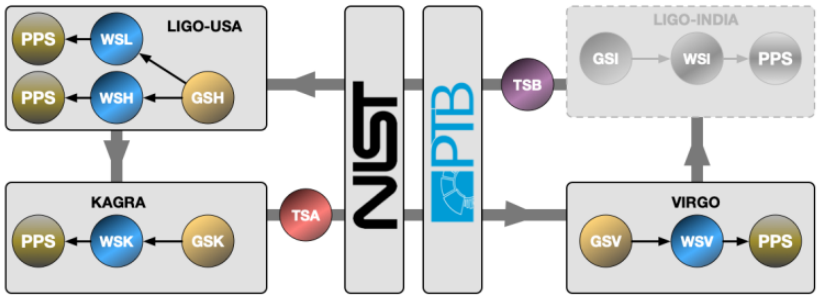

Figure 6.1: Scheme of the intercalibration procedure between LIGO, Virgo and KAGRA planned for the O4 run.

perform the sphere calibration, a laser beam with a stable power is needed. The optical setup that generates such a laser beam is named "laser module". The laser module is composed by the same optical components as the PCal injection bench described in section 5. Thus, it consists in a laser source, beam-splitters cubes, and two InGaAs photodiodes "PD1" and "PD2", but the components are arranged as shown in figure 6.2. The power of the output beam can be in a control loop with the photodiode PD1, while the photodiode PD2 monitors the laser power. The control loop is the same as the one described in section 5.3. The output beam of this laser module is used for all the measurements described in this chapter.

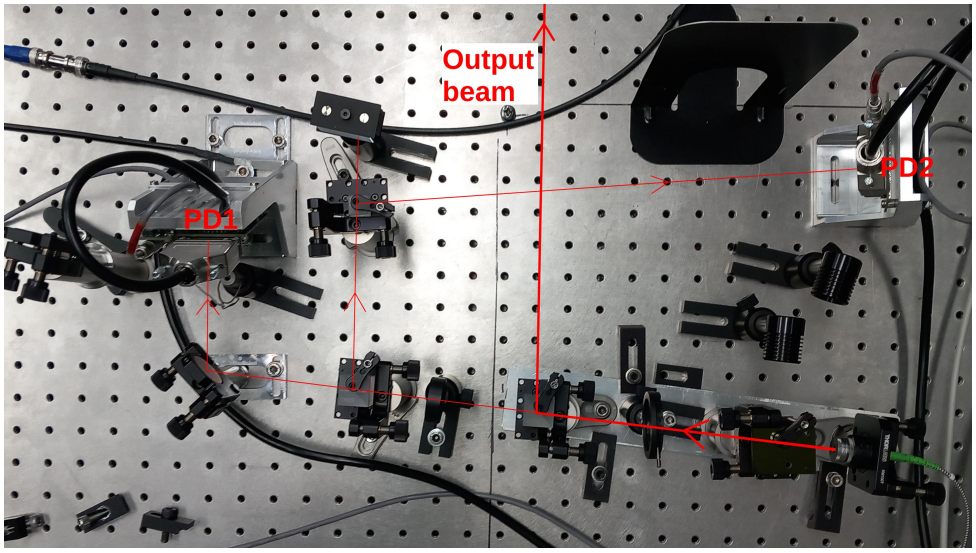

Figure 6.2: Picture of the laser module built at LAPP

The output laser beam of the laser module is splitted into two beams with a 50% transmission 50% reflection beam splitter (BS). Both the reflected beam and the transmitted beams are sent into one of the sphere. Since BS is not perfect, the powers of each beam are not exactly the same. Thus, each sphere has to measure the power of both beams. To properly calibrate the test sphere with respect to the reference sphere, the spheres have been mounted on pneumatic sliders which swap automatically the spheres. A picture of the calibration setup is shown in figure 6.3. This calibration setup was designed by LIGO and has been adapted at LAPP, in order to be able to calibrate the spheres using the same method.

6.1.3 Sphere intercalibration

The output voltages of the reference sphere and the test sphere, are named respectively $V_{ref}(P)$ and $V_{test}(P)$. It is assumed that the output voltage of the spheres is proportional to the power of the input laser beam P. The proportionality coefficient is called the responsivity of the sphere, respectively ρ_{ref} and ρ_{test}.

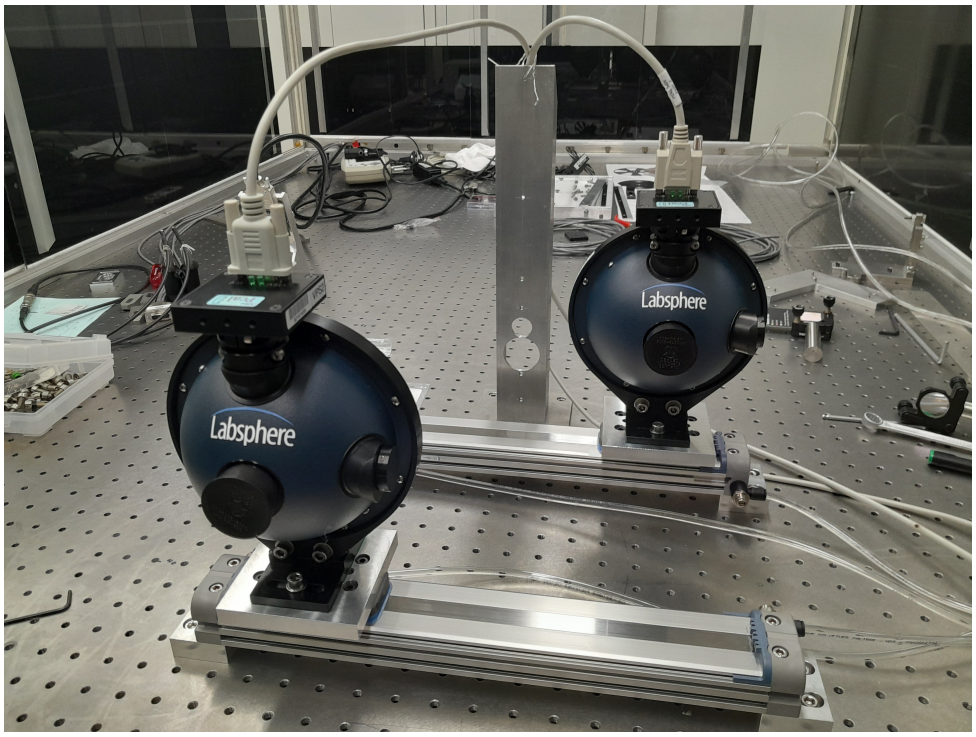

Figure 6.3: Picture of the pneumatic sliders installed at LAPP.

$$V_{ref}(P) = \rho_{ref} \cdot P \tag{6.1}$$
$$V_{test}(P) = \rho_{test} \cdot P \tag{6.2}$$

The powers of the transmitted beam P_T and the reflected beam P_R are computed with the following formula, where T is the transmission of the beam splitter, R is the reflection rate, and P_{in} is the power of the incident beam on the BS mirror.

$$P_T = T \cdot P_{in} \tag{6.3}$$
$$P_R = R \cdot P_{in} \tag{6.4}$$

Every 15 seconds, the spheres are swapped by the sliders. At each positions the output voltages of the spheres are recorded for 10 seconds, sampled at 1 Hz, and the mean of the voltage value over these 10 seconds is computed. After two successive swaps, each beam has been seen by each sphere. The responsivity ratio α between the test sphere and the reference sphere is computed as follows:

$$\alpha = \sqrt{\frac{V_{test}(T \cdot P_{in})}{V_{ref}(R \cdot P_{in})} \cdot \frac{V_{test}(R \cdot P_{in})}{V_{ref}(T \cdot P_{in})}} \tag{6.5}$$

The value of α is computed for 2 hours, which results in $n = 240$ values of α. The value taken as the responsivity ratio between the two spheres is the mean of the 240 values, and the error ϵ is the standard error assuming that the set of points is normally distributed $\epsilon = \frac{\sigma}{\sqrt{n}}$, where σ is the standard deviation.

The calibration of the sphere responsivity requires an absolute measurement of the output voltage of the sphere. At LAPP, the voltage is measured by an ADC mezzanine, so an absolute calibration of the ADC is required. In addition, the sphere emits a background voltage even if it measures no laser power, and this background voltage depends on the temperature of the sphere. The responsivity of the sphere also depends on the temperature of the sphere. To calibrate a sphere with respect to another, one needs to:

1. Calibrate the voltage of the ADC mezzanine

2. Characterize and correct the temperature dependency of the background voltage of the spheres.
3. Characterize and correct the temperature dependency of the sphere response.
4. Calibrate the responsivity of the sphere.

The characterization of those temperature dependencies and the measurement of the responsivity of GSV and WSV have been done at LHO in May 2022. The values of the temperature dependency measured at LHO are the values used to measure the responsivity at LAPP. More measurements of the temperature dependency of the background voltage and of the response has been done at LAPP, in order to update the uncertainty on the response of the spheres. These measurement are described in the following section.

6.1.4 Voltage calibration of the ADC

At Virgo and at LAPP, the power sensors are connected to an ADC mezzanine which is described in section 5.2.1: the ADC reads the value of the output voltage of the sensor. However, the value read by the ADC may be biased. Thus, the ADC needs to be calibrated. The standard voltage generator used to calibrate the ADC is the Time-Electronics 1017 shown in figure 6.4.

Figure 6.4: Standard voltage generator time electronics 1017.

The Time-Electronics 1017 generates a voltage known with an uncertainty of 0.002%. This voltage is read by the ADC. At Virgo, the average input power is 1.3 W, and the responsivity of the spheres is around -2.6 V/W, so the value of the output voltage of the spheres at Virgo is around -3.4 V. The output voltage range of the spheres is $[-4\ V, 0\ V]$, so the voltages $V_{in} \in \{-4\ V, -3\ V, -2\ V, -1\ V, 0\ V\}$ are injected for 1 min in the ADC which reads the voltages and gives the output values V_{out}. For each voltage value, the mean $\bar{V}_{out}$ and statistical error σ_{stat} on the mean of the output value over 1 min is computed. If the error is Gaussian, the statistical error is given by:

$$\sigma_{stat} = \sqrt{\frac{\frac{1}{N-1}\sum_{j=1}^{N}(V_{out,j} - \bar{V}_{out})^2}{N}} \tag{6.6}$$

The signal is sampled at 1 Hz, so there are $N = 60$ sample in 1 min of data. The linear regression between V_{in} and V_{out} is computed, where a and b are the parameters of the regression and ϵ is the residual of the regression:

$$V_{out,i} = a \cdot V_{in,i} + b + \epsilon_i \tag{6.7}$$

Figure 6.5 shows the residual between the voltage measured by the ADC and the fit. The The statistical error on the sample is not high enough to explain the residual on the fit.

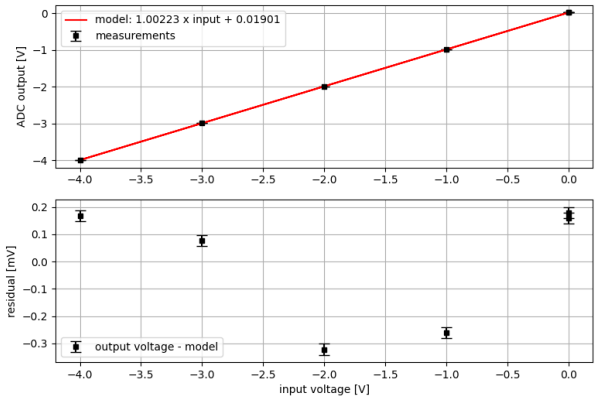

Figure 6.5: Top: ADC output voltage as function of the injected voltage, and linear fit .
Bottom: residual between the measured ADC voltage and the ADC voltage predicted with the fitted model.

In a general case, the χ^2 of the fit, and the associated p-value are expressed as follows:

$$\chi^2 = \sum_{i=1}^{N} \frac{\epsilon_i^2}{\sigma_{stat,i}^2} \tag{6.8}$$

$$\text{p-value} = \int_{\chi^2}^{\infty} \text{chi2}[dof](x)\ dx \tag{6.9}$$

Where $dof = N - 2 = 4$ is the number of degree of freedom, and $N = 6$ the number of data points. In the example in figure 6.5, the value of the χ^2 of the fit is 658, and the p-value associated is 0. The fit is considered as relevant if the p-value is higher than 0.05, which correspond to a χ^2 lower than $\chi^2_{max} = 9.488$. The uncertainty on the output voltage value is increased so that $\chi^2 = \chi^2_{max}$. Thus the new uncertainty σ_{sys} that takes into account the systematic error can be computed as:

$$\sigma_{sys} = \sqrt{\frac{\sum_{i=1}^{N} \epsilon_i^2}{\chi^2_{max}}} \tag{6.10}$$

Thus, the output voltage of the ADC is corrected by applying a gain $G = \frac{1}{a}$ and an offset $V_{off} = \frac{-b}{a}$. Using the formula above, one can compute the uncertainty on the output voltage σ_{ADC}. In the case shown in figure 6.5, the uncertainty is equal to $\sigma_{ADC} = 0.154$ mV. When the spheres are calibrated at LAPP, the input laser power is ∼0.3 W in the integrating spheres. It corresponds to an output voltage is $V_{sphere} \sim 0.78$ V, so the relative uncertainty on the output voltage is $\frac{\sigma_{ADC}}{V_{sphere}} = 0.02\%$.

The calibration was done at LAPP in March 2023, and has varied by ∼0.01% in 4 months. At Virgo, the ADC port reading the output voltage of WSV is calibrated in this way before each calibration of the photodiodes. And the ADC calibration gain varies by ∼0.01% in 6 months.

6.1.5 Measurement of the temperature dependent background

The background voltage of the spheres $V^{bg}(\mathcal{T})$ as well as their responsivity $\rho(\mathcal{T})$ depend on their temperature. The temperature of the photodiode housing of the GSV and WSV spheres is monitored. Thus, it is possible to characterize the temperature dependencies of the spheres and to correct them. The background voltage and the responsivity are corrected so as they get the value at 300.15 K. The values of the background voltage and responsivity at 300.15 K are V'^{bg} and ρ'. The dependencies of the background voltage and the response of the spheres have been characterized once at LHO in May-June 2022. This characterization is used to correct the temperature dependency of the spheres during their calibration. Then the temperature dependencies of the sphere have been characterized again at LAPP to monitor the variations and estimate the uncertainties on the output voltage of the sphere.

To characterize the temperature dependency of the background voltage, the sphere is insulated with bubble wrap, and put in a oven at about 40°C (313 K) for 30 min. Then, while it cools down to the

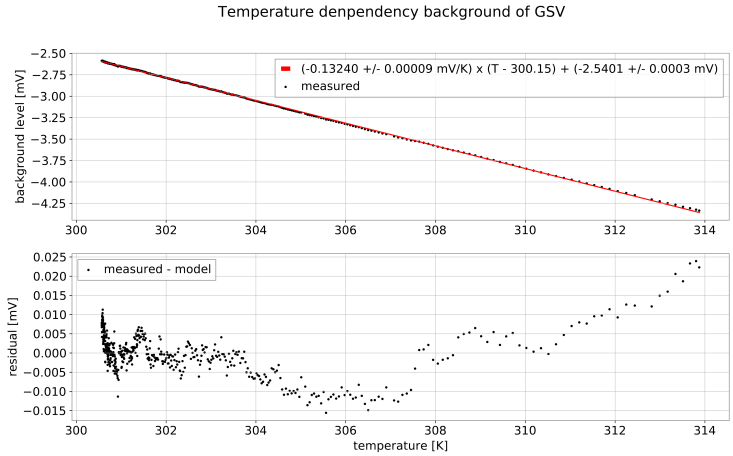

(a) GSV background voltage

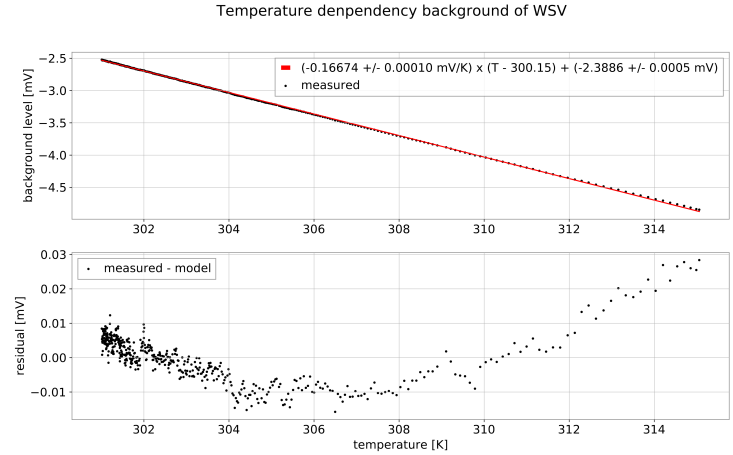

(b) WSV background voltage

Figure 6.6: Estimation of the temperature dependency of the background of Virgo spheres done in May 2022 at LHO. Top: Measured background voltage as function of the temperature of the photodiode housing of the sphere. Bottom: Residual between the measurement and the model.

room temperature, the background voltage and the temperature are recorded. The background voltage dependency to the temperature is modeled with the following formula:

$$V^{bg}(\mathcal{T}) = m \cdot (\mathcal{T} - 300.15 \text{ K}) + V'^{bg} \tag{6.11}$$

Figure 6.6 shows the background voltage as function of the temperature of the GSV and WSV spheres, the model of the temperature dependent background, and the residuals between the measurement and the model. In the same way as for the voltage calibration of the ADC, the uncertainty on the estimated background voltage is tuned so as the p-value of the χ^2 of the fit is equal to 0.05. In the case displayed in figure 6.6, the associated uncertainty on the estimated background is 7 µV. This uncertainty is negligible compared to the uncertainty on the ADC calibration.

However, the background voltage may vary with the time for other reasons than the temperature of the sphere, so the value of V'^{bg} vary from a measurement to an other, while the value of the m factor is more stable. Thus, to subtract the background during an experiment, the background is measured again without light, and a temperature dependant background voltage is computed with the measured background and the slope m. This temperature dependant background is subtracted to the voltages. The background subtraction method will be explained in details in the next section.

The value of m has been estimated once at LHO in May 2022 for each sphere, this value is the one used to correct the temperature dependency of the background. Then it has been measured three times

at LAPP to check if the value of m varies with time, and update the uncertainty on the value m, σ_m. Three measurements of the m factor have been done at LAPP, the values of the measurements of the m factor of WSV done at LHO and at LAPP are given in figure 6.7. The uncertainty on m is the standard error on the four measurements whose formula is given in appendix A. Thus the values of m are:

$$m_{WSV} = -0.1667 \pm 0.0013 \text{ mV/K} \tag{6.12}$$
$$m_{GSV} = -0.1324 \pm 0.0017 \text{ mV/K} \tag{6.13}$$

The amplitude of the temperature variations δT during the measurement of the responsivity ratio is generally lower than ∼1 K. So the uncertainty on the background due to the uncertainty on the m factor is $\sigma_{bg} = \delta T \cdot m = 1.7$ µV, which is also negligible compared to the uncertainty due the calibration of the ADC.

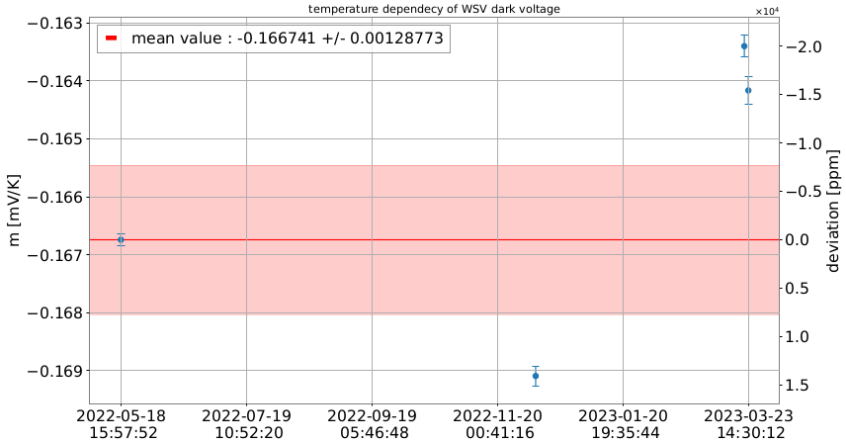

Figure 6.7: Variation of the m factor over the time. The measurement of m done at LHO is used to correct the temperature dependency of the background, the other are used to update the uncertainty on the value of m. The statistical error (in blue) is given by the formula in Appendix A.
The error on the value is increased until the p-value of model with a constant value exceed 0.05. (see appendix A). Which gives an uncertainty of $\sigma_m = 0.0013$ mV/K, so 1.0% of the average value of m.

6.1.6 Subtraction of the temperature dependent background

To estimate and subtract the background voltage from the raw output voltages of the sphere during an experiment, the background voltage and the temperature of the the sphere are measured for 30 min, before and after each experiment done with the sphere. The means of the voltage and temperature are then computed. Let's call $V_{bg,1}^{meas}$ and $V_{bg,2}^{meas}$ the background voltages measured before and after the experiment, and T_1^{meas} and T_2^{meas} the measured temperatures. The mean values of the measured background voltages and temperatures are computed as:

$$V_{bg}^{meas} = \frac{1}{2}(V_{bg,1}^{meas} + V_{bg,2}^{meas}) \tag{6.14}$$
$$\mathcal{T}^{meas} = \frac{1}{2}(T_1^{meas} + T_2^{meas}) \tag{6.15}$$

Then, the value of the background to be subtracted is computed from the temperature as:

$$V_{bg}(\mathcal{T}) = m \cdot (\mathcal{T} - \mathcal{T}^{meas}) + V_{bg}^{meas} \tag{6.16}$$

The uncertainty on the measured background value is the difference between the background values measured before and after the experiment $\delta V_{bg}^{meas} = \frac{1}{2}(V_{bg,1}^{meas} - V_{bg,2}^{meas})$. In most cases, the difference between the two mean values $\delta V_{bg}^{meas} = \frac{1}{2}(V_{bg,1}^{meas} - V_{bg,2}^{meas})$ is lower than the standard deviation of the voltages samples $\sigma_{V,bg}$ as shown in figure 6.8. In practice, the uncertainty on the measured background

voltage is the quadratic sum of the standard deviation of the data with the variation of the mean background value: $\sigma_{bg}^{meas} = \sqrt{(\sigma_{V,bg})^2 + (\delta V_{bg}^{meas})^2} = 0.019$ mV

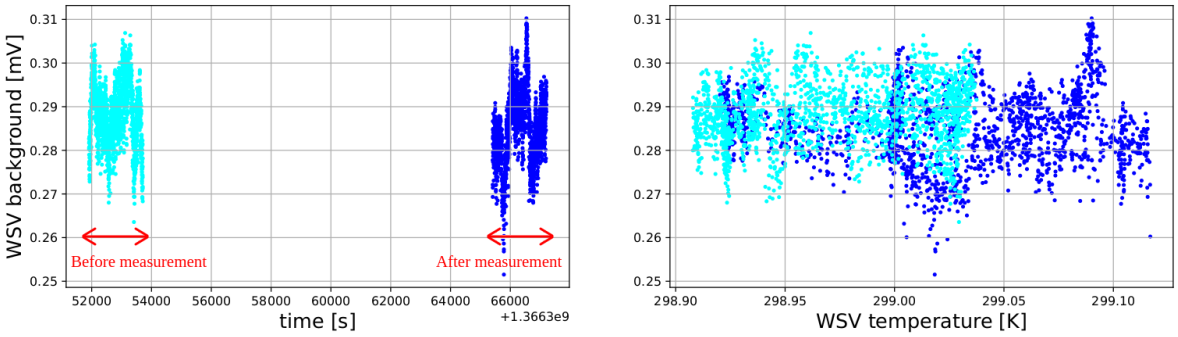

Figure 6.8: Evolution of a background voltage before and after a measurement of the responsivity ration between the sphere responses. In this case, the variation of the mean value of the background voltage is 0.01 mV, which lower than the standard deviation of the data, 0.016 mV.

The total uncertainty on the background value is a combination of the uncertainty on the background measurement during the experiment and the uncertainty on the ADC calibration. Thus, the uncertainty on the background is written as:

$$\sigma_{bg} = V_{bg}^{meas} \cdot \sqrt{\left(\frac{\sigma_{bg}^{meas}}{V_{bg}^{meas}}\right)^2 + \left(\frac{\sigma_{ADC}}{V_{bg}^{meas}}\right)^2} = \sqrt{(\sigma_{bg}^{meas})^2 + (\sigma_{ADC})^2} \tag{6.17}$$

Thus, the value of the total uncertainty on the background voltage is dominated by the uncertainty on the ADC calibration σ_{ADC}, so the uncertainty on the background voltage is $\sigma_{bg} = 0.16$ mV on both spheres. When the responsivity of the sphere is computed, the input laser power is ∼0.3 W, and the value of the responsivity of the sphere is around -2.6 V/W, so the output voltage of the spheres is around -0.78 V. Thus, the contribution of the uncertainty on the background voltage to the uncertainty on the output voltage of the sphere is 0.021%.

6.1.7 Measurement of the temperature dependent spheres responsivity

To characterize the temperature dependency of the responsivity, one needs to measure the responsivity of the sphere while its temperature is varying. Thus, the test sphere is warmed up in the oven. Then, the responsivity of the test sphere is measured with respect to reference sphere while the temperature of the test sphere is cooling down to room temperature as shown in the previous section. The value of α as function of the temperature of the test sphere is recorded. The temperature dependency of the responsivity of the test sphere is modeled as follows:

$$\rho_{test}(\mathcal{T}) = \rho'_{test} \cdot (1 + \kappa \cdot (\mathcal{T} - 300.15\text{ K})) \tag{6.18}$$

The temperature dependent background voltages of both spheres are subtracted as described in the previous section. It is assumed that the temperature dependency of the reference sphere is already known and corrected. Thus, the responsivity ratio between the test sphere and reference sphere is written as:

$$\alpha(\mathcal{T}) = \frac{\rho'_{test}}{\rho'_{ref}} \cdot (1 + \kappa \cdot (\mathcal{T} - 300.15\text{ K})) = \alpha' \cdot (1 + \kappa \cdot (\mathcal{T} - 300.15\text{ K})) \tag{6.19}$$

Where α' is the responsivity ratio at 300.15 K, ρ'_{test} and ρ'_{ref} are respectively the responsivity of the test sphere and the responsivity of the reference sphere at 300.15 K. The measurements are then down-sampled so that there is only one point every 0.5 K, then the previous function is fitted to the down-sampled points. Figures 6.9a represents the ratio $\alpha_{GSV/PS3}$ between the responses of the spheres GSV and PS3 as function of the temperature of the GSV sphere housing. And figure 6.9b represents the ratio $\alpha_{WSV/PS3}$ as function of the temperature of the WSV sphere housing. These measurements have been done at LHO in May 2022. PS3 is the LIGO standard from which the Virgo spheres have been calibrated.

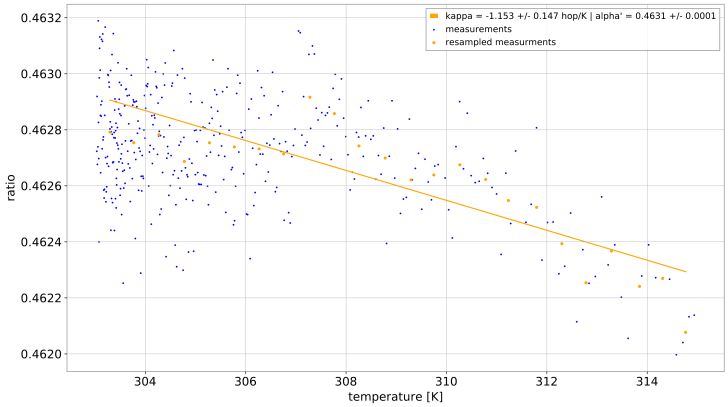

(a) GSV over PS3 response vs temperature

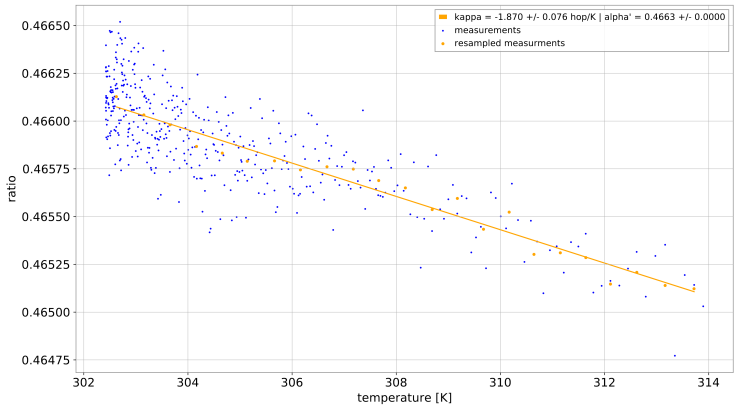

(b) WSV over PS3 response vs temperature

Figure 6.9: Ratio between the response of a Virgo spheres GSV or WSV, and the response of a sphere from LIGO called PS3 as function of the temperature of the housing of the Virgo sphere. The yellow points represent the data down sampled so as there is only one point every 0.5 K. These measurements have been done at LHO in May 2022.

The uncertainty on the responsivity ratio due to the error on the fit is tuned so that the p-value of the fit is 0.05. This gives an uncertainty value of 1.60×10^{-4} over a responsivity ratio value at 300.15 K of 0.4663 for WSV, and an uncertainty of 1.85×10^{-4} over a ratio of 0.4631 for GSV. So the error on the correction factor for the temperature dependency, because of the error on the fit, is 0.034% on WSV and 0.040% on GSV.

The value of κ estimated at LHO is the value used to correct the temperature dependency of the spheres, when their responsivity is measured. The κ factors have been estimated again at LAPP to monitor the variations and update the uncertainty on the value. Figure 6.10 shows the different values of κ of WSV.

The uncertainty on κ for the different estimations is $\sigma_\kappa = 3.08 \times 10^{-5}$ K^{-1} for GSV and $\sigma_\kappa = 2.89 \times 10^{-5}$ K^{-1} for WSV. Thus, the values of the κ factors and the associated uncertainties are:

$$\kappa_{GSV} = -115 \pm 31 \text{ ppm/K} \tag{6.20}$$

$$\kappa_{WSV} = -187 \pm 29 \text{ ppm/K} \tag{6.21}$$

On can notice the the order of magnitude of the κ factor is 0.01%/K, which is four times weaker than the integrating spheres used during O3. The temperature dependency of the O4 sphere is greatly reduced

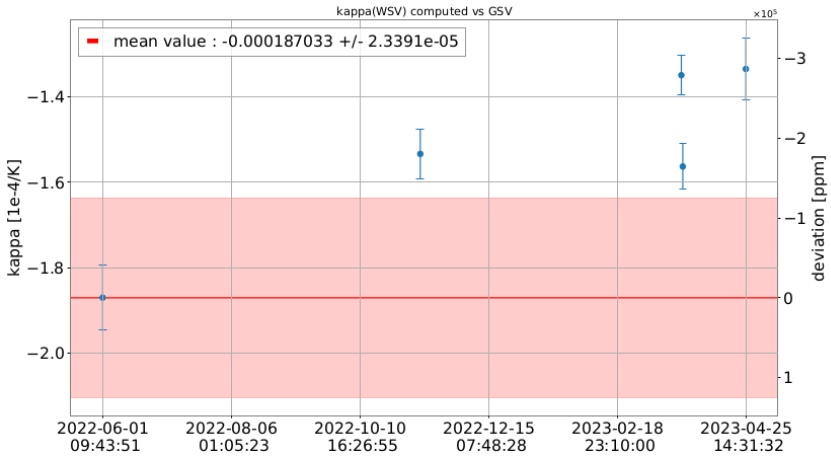

Figure 6.10: Variation of the κ factor over the time. Only the first measurement, done at LHO, is used to correct the temperature dependency of the response. This measurement was done using PS3 as reference, whereas the other measurements were done using GSV as reference. The total error on the κ factor is estimated in the same way as the error on the m factor, the error bar is increased until the p-value of model with a constant value exceeds 0.05. (see appendix A). This gives an uncertainty $\sigma_\kappa = 2.89 \times 10^{-5}$ K^{-1}, so 15% of the average value of κ.

by the spacer between the spherical shell and the photodiode housing.

The values of the uncertainty takes into account the LAPP measurements. For the characterization of the temperature of the background, we consider that the variation of the temperature of the sphere during a measurement of the responsivity is generally lower than 1 K. In this case the contribution of the uncertainty σ_κ to the uncertainty on the output voltage of the sphere does not exceed 29 ppm, which is a factor 10 lower than the error on the fit.

The temperature dependency of the responsivity is corrected by dividing the output voltage of the sphere by $(1 + \kappa \cdot (\mathcal{T} - 300.15\text{ K}))$. The corrected voltage of the sphere V^{corr} is written as:

$$V^{corr} = \frac{V^{raw} - m \cdot (\mathcal{T} - \mathcal{T}^{meas}) - V_{bg}^{meas}}{1 + \kappa \cdot (\mathcal{T} - 300.15\text{ K})} \tag{6.22}$$

6.1.8 Summary of the uncertainty on the sphere output voltage

The uncertainty on the output voltage is a combination of the uncertainty on the ADC calibration, on the background voltage estimation, and on the temperature dependency correction. The contribution of every uncertainty sources is summarized in table 6.2. The total uncertainty on the calibration of the sphere is the quadratic sum of the different contributions.

Uncertainty source	GSV	WSV
ADC voltage calibration	0.020%	
Background voltage estimation	0.021%	0.021%
Temperature dependency of the response	0.040%	0.034%
Total	**0.049%**	**0.045%**

Table 6.1: Sources of uncertainty on the sphere output voltage, and the associated relative values. The output voltage of the spheres during their calibration is ∼0.78 V, the values of the relative uncertainties are computed with respect to this voltage value.

6.1.9 Measurement of the sphere responsivity

The responsivities of the spheres WSV and GSV have been measured five times with respect to a LIGO standard named "PS3", at LHO in May and June 2022. The value of the responses of the Virgo spheres have been computed from the responsivities of PS3 and the ratio. The value of the response of PS3 sphere is $\rho_{PS3} = 5.6014 \pm 0.0060$ V/W [28]. Figure 6.11 shows the values of the five responsivity ratios α_i between WSV and PS3 and between GSV and PS3, as well as the statistical uncertainty of each measurement σ_i. The value taken to compute the responsivity ratio is the weighted mean $\bar{\alpha}$ and the associated uncertainty is the standard error σ_α, whose formula are:

$$\bar{\alpha} = \frac{\sum_{i=1}^{N} \sigma_i^{-2} \alpha_i}{\sum_{i=1}^{5} \sigma_i^{-2}} \tag{6.23}$$

$$\sigma_\alpha = \sqrt{\frac{\sum_{i=1}^{N} \sigma_i^{-2} (\alpha_i - \bar{\alpha})^2}{(N-1) \cdot \sum_{i=1}^{N} \sigma_i^{-2}}} \times t_{N-1}^{corr} \tag{6.24}$$

Where $t_4^{corr} = 1.1416$ is a correction factor that corrects the distribution of the mean error. The method to calculate it is explained in appendix A.

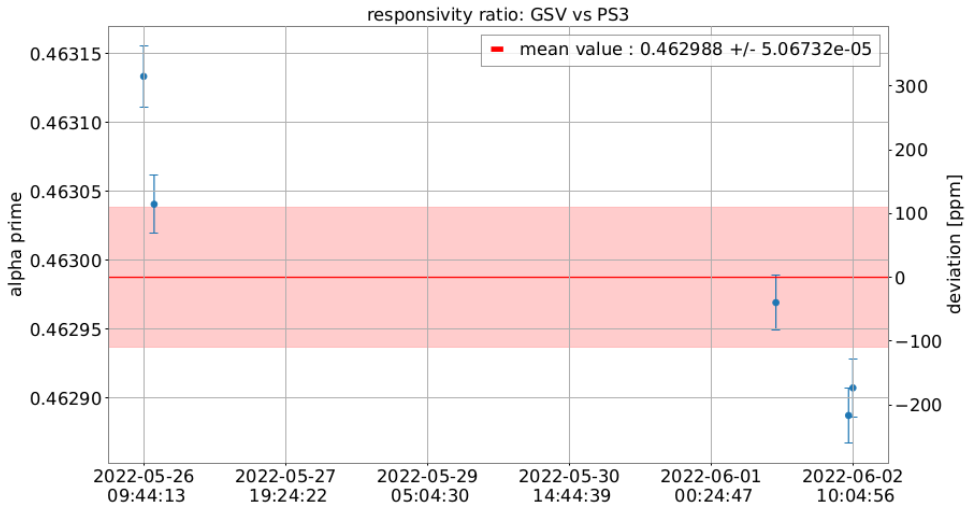

(a) ratio GSV over PS3

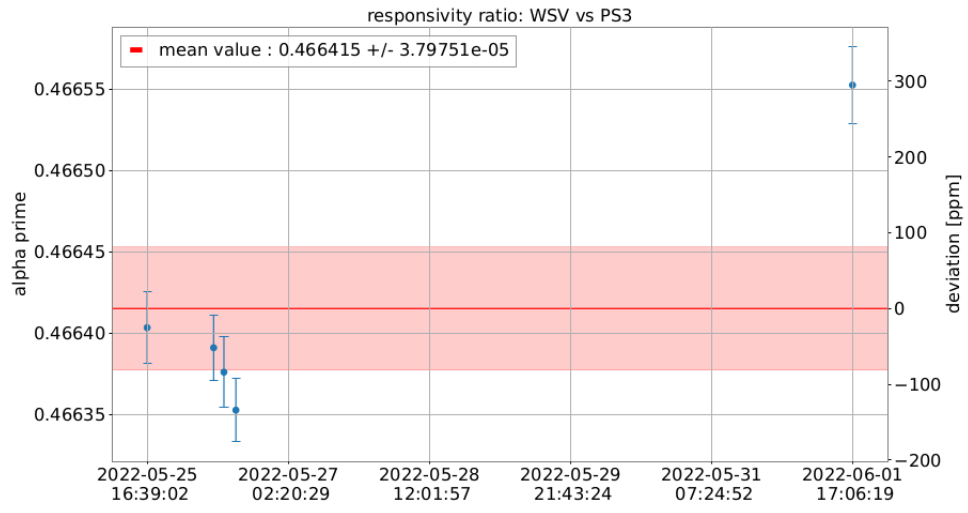

(b) ratio WSV over PS3

Figure 6.11: Measurements of the responsivity ratio between the Virgo sphere and PS3 done at LHO in May and June 2022. The mean and standard error of these measurement are represented in red.

The values of the ratio computed at LHO are:

$$\alpha'_{GSV/PS3} = 0.46299 \pm 0.00005 \text{ V/V} \tag{6.25}$$

$$\alpha'_{WSV/PS3} = 0.46642 \pm 0.00004 \text{ V/V} \tag{6.26}$$

The values of the relative uncertainty due to the measurement of the responsivity ratio measured at LHO σ_{LHO} are 0.011% on GSV and 0.008% on WSV. Thus the values of the responsivity of the spheres are computed from these ratio and the responsivity of PS3 ρ'_{PS3}:

$$\rho'_{GSV,LHO} = -2.5934 \text{ V/W} \tag{6.27}$$

$$\rho'_{WSV,LHO} = -2.6125 \text{ V/W} \tag{6.28}$$

These values are applied to the corrected output voltage signals of GSV and WSV to estimate the laser power $P = V^{corr} \cdot \rho'$ that enters the sphere. The power sensors of the PCal are then calibrated with respect to the power estimated by WSV is explained in the next chapter.

The responsivities of the spheres have been monitored at LAPP by measuring the responsivity ratio between WSV and GSV spheres, both initially calibrated with respect to PS3. Figure 6.12 shows the responsivity of WSV computed with respect to PS3 at LHO, and with respect to GSV. The value of the responsivity of WSV computed at LAPP differs by ∼0.05% from the value computed at LHO. In practice, we keep using $\rho_{WSV,LHO}$ to calibrate the PCal, but the uncertainty on this value is estimated from all the measurement done at LHO and at LAPP. A systematic error σ_{sys} is added to the standard error computed from the measurements.

The χ^2 and p-value of the constant value measured at LHO is written as follow:

$$\chi^2 = \sum_{i=1}^{N} \frac{(\rho'_i - \rho'_{LHO})^2}{\sigma_i^2 + \sigma_{sys}^2} \tag{6.29}$$

$$\text{p-value} = \int_{\chi^2}^{+\infty} \text{chi2}[N-1](x)dx \tag{6.30}$$

The systematic error is tuned so that the p-value is equal to 0.05, which gives a value $\sigma_{sys} = 0.035\%$ This systematic error is added to the LHO standard error: $\sigma_{total} = \sqrt{\sigma_{LHO}^2 + \sigma_{sys}^2}$, so the total uncertainty values are: 0.037% for GSV and 0.036% for WSV

Table 6.2 shows the uncertainty on the calibration of the WSV and GSV spheres as estimated in June 2023.

Uncertainty source	GSV	WSV
LIGO standard (PS3) response	0.107%	
Output voltage	0.049%	0.045%
Responsivity ratio	0.037%	0.036%
Total	**0.123%**	**0.122%**

Table 6.2: Uncertainty on the sphere calibration.

Starting in August 2023, the calibrations of WSV and GSV spheres will be monitored with respect to the transfer standards TSA and TSB. The Python scripts to measure the temperature dependencies and the responsivities of the spheres are common between the collaborations LIGO, Virgo and KAGRA. These scripts are shared using a common Gitlab repository that I have created. This repository is also used to share the measurements of the response of the different standards and make sure that their response is stable with time.

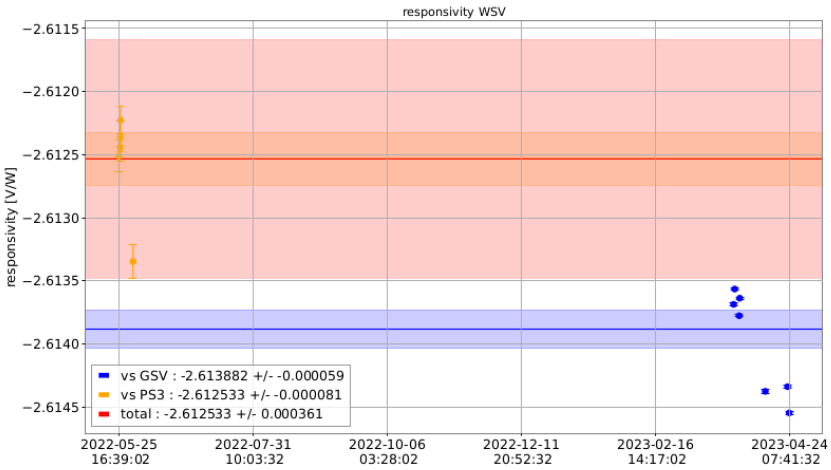

Figure 6.12: Response of WSV sphere, measured at LHO and monitored at LAPP. The red span represents the total uncertainty on the LHO value that takes into account the LAPP measurement.

6.2 Integrating spheres calibration stability characterization

Contrary to the VIS used during O3, the responsivity of the current integrating spheres should not vary with the angle of incidence of the beam in the sphere, the size of the beam, or the power of the input laser power. However, these parameters are not controlled while calibrating the integrating spheres, or calibrating the PCal sensors with the sphere. Thus, it is necessary to characterize the variations of the responsivity of the sphere with respect to these parameters in dedicated measurements that have been done at LAPP.

6.2.1 Angle of incidence and position of the laser beam

When the spheres are calibrated with respect to each other on the pneumatic rails, or when calibrating the PCal photodiodes with the WSV sphere, the laser beam enters the integrating sphere at the middle and perpendicularly to its input port. However, the angle of incidence of the beam on the sphere is not monitored and the position of the beam neither. Thus the sphere response variation with the angle of incidence and the position of the beam have been characterized at LAPP.

To characterize the responsivity of the sphere, the sphere is placed ∼50 cm after the output of the laser module with nothing between the module and the sphere. The laser power in the sphere is set to 1 W. The sphere is rotated every 60 s, and the output voltage of the sphere V_{WSV} and the power of the laser beam estimated with the photodiode PD2 P_{PD2} are recorded. Photodiode PD2 is out of the laser control loop so it monitors the laser power variations. The mean and the standard error of the ratio between the sphere and the photodiode output $\frac{V_{WSV}}{P_{PD2}}$ are computed at every angle of incidence.

In the configuration shown in figure 6.13a, the laser beam always enters the sphere by the middle of the hole and hit the bottom of the sphere at different places. As seen in figure 6.13b, the output power is not perfectly stable. However, the standard error on the output voltage is lower than 0.01% of the average value.

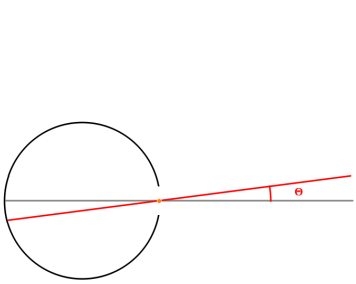

(a)

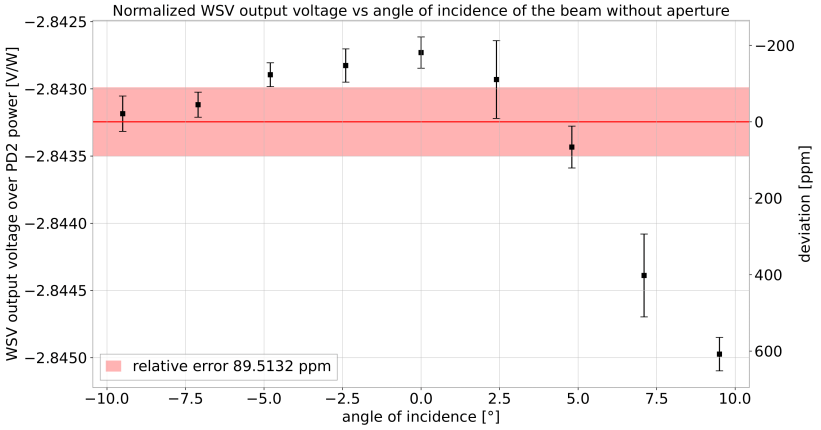

(b)

Figure 6.13: Characterization of the sphere response with the angle of incidence of the beam in the sphere, with the beam entering at the center of the hole. Left: Scheme of the laser beam position with respect to the sphere, viewed from the top. Right: WSV output voltage as function of the angle of incidence of the beam in the sphere.

In the other configuration shown in figure 6.14a, the sphere is rotated so as the beam always hit the bottom of the sphere at the middle and enters at different places of the input port. Figure 6.14b shows the output voltage of the sphere as function of the angle of incidence. It shows that the normalized output voltage varies by 9 mV/W peak to peak, so ∼4% of the maximum value. In addition, the closer the beam is from the edge of the entrance hole of the sphere, the lower is the absolute value of the voltage. It seems to indicate that the laser beam is surrounded by a halo, and this halo is clipped when the laser beam approaches the edge of the entrance of the sphere.

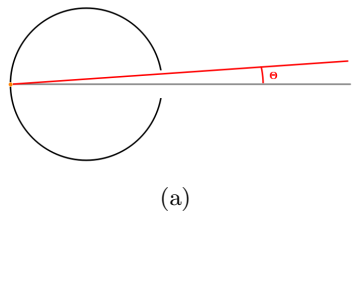

(a)

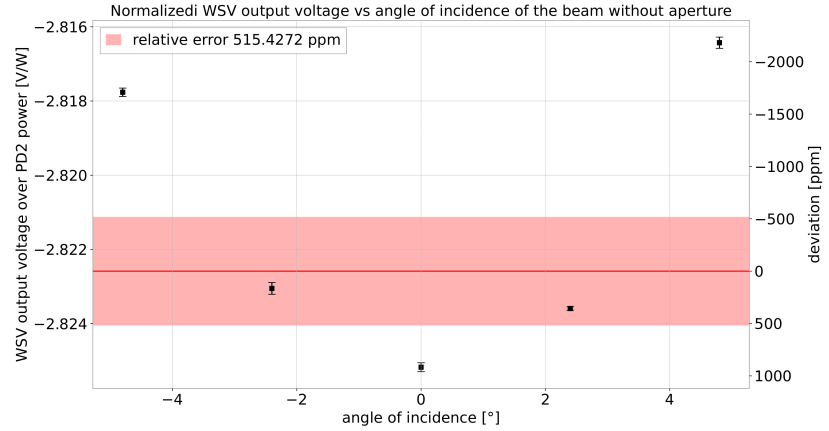

(b)

Figure 6.14: Characterization of the sphere response with the angle of incidence of the beam in the sphere, with the beam entering the sphere at different locations of the hole. Left: Scheme of the laser beam position with respect to the sphere, viewed from the top. Right: WSV output voltage as function of the angle of incidence of the beam in the sphere.

As shown in figure 6.15b, the output voltage response of the sphere varies by ∼10 mV/W peak to peak with the lateral position of the beam. And the closer the beam is from the edge of the entrance hole of the sphere, the lower is the absolute value of the voltage. The diameter of the entrance hole of the sphere is 25.4 mm. If the laser beam were a gaussian beam with a diameter of 2 mm, the amount of the power clipped when the beam is at 5 mm of the center of the hole would be less than 1 ppm. But figure 6.15b

shows that there is 542 ppm of the power that does not enter the sphere. The characterization of the sphere response with respect to the lateral shift of the beam confirms the hypothesis that there is halo around the laser beam.

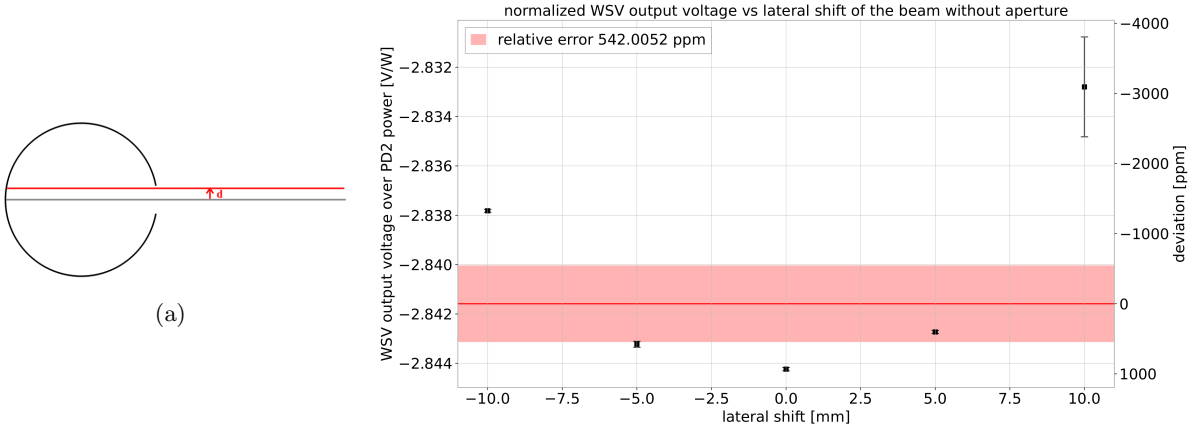

(a)

(b)

Figure 6.15: Characterization of the sphere response with the lateral shift of the beam in the sphere, with the beam entering the hole at different locations.
Left: Scheme of the laser beam position with respect to the sphere, viewed from the top.
Right: WSV output voltage as function of the lateral position of the beam in the sphere.

6.2.2 Angle of incidence and position of the laser beam with aperture

To remove the halo around the beam, an aperture has been added on the laser path. The halo may be created by one of the optical components of the laser module of from a leakage of the pump beam, but the exact origin is unknown. The halo diverges from its origin. The aperture is put at ∼50 cm of the laser module to dump most of the halo power. The sphere is put ∼50 cm further. The diameter of the aperture is ∼5 mm.

The variation of the output voltage of the sphere with the angle of incidence of the beam in the second configuration is shown in figure 6.16 and the variation of the output voltage of the sphere with the lateral position of the sphere is in figure 6.17. The standard error on the response is equal to 45 ppm of the average value between $-5°$ and $+5°$. The standard error is 55 ppm when the lateral position of the beam varies between -10 mm and 10 mm. The sphere responsivity is much more stable with respect to the angle of incidence an position when the aperture is added to clip the halo around the main beam at LAPP. In order to remove this source of systematic error, this aperture is kept at ∼50 cm after the laser module, before the BS mirror, when the sphere are calibrated. All the measurement shown in section 6.1 were done with the aperture on the laser path. So the systematic error due to the beam profile is small.

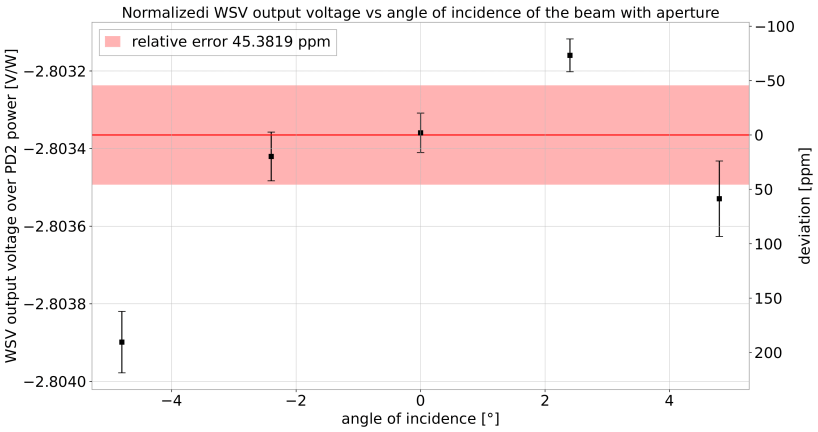

Figure 6.16: WSV output voltage as function of the angle of incidence of the beam in the sphere, with the laser beam hitting the back of the sphere at the center. The halo around the sphere has been dumped with an aperture.

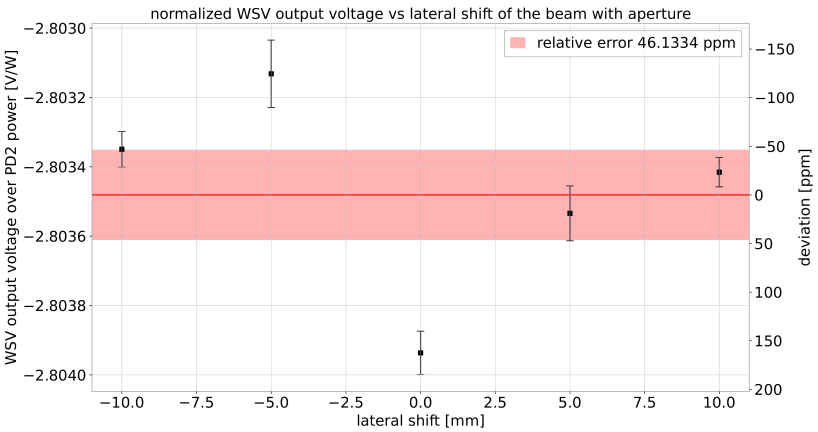

Figure 6.17: WSV output voltage as function of the lateral position of the beam in the sphere. The halo around the sphere has been dumped with an aperture.

In conclusion, the error on the sphere response due to the position of the beam on the sphere is the quadratic sum of the errors due to the angle of incidence of the laser beam (at the entrance and at the back of the sphere) and the error due to the lateral position of the beam. The value of this total uncertainty is 110 ppm.

6.2.3 Beam profile

On the PCal bench, the optical path between the sphere on the reflection bench and the laser source is around 3.6 m long. A collimator is installed on the laser source. The collimator is tuned so the waist of the beam is approximately at the end mirror position. However, the size of the beam on the reflection bench is not precisely controlled (around 3 mm on the reflection bench). Thus, the variation of the response of the sphere with the size of the beam has to be characterized.

We assume that the distribution of the light intensity of the laser beam is gaussian. The diameter of the laser beam is the diameter of the area where the light intensity is higher than the half of the maximum intensity.

The characterization is done at LAPP with the same laser module as during the calibration of the spheres, and it is done in two steps. First, the size of the beam as function of the distance from the laser module is measured with a camera and fitted with a model. Then the response of the sphere is measured as function of the distance from the laser module.

A camera is placed at 150 cm far from the laser module, in order to measure the size of the laser beam. The power of the laser beam is set to 1 W. Since the camera is designed to measure a maximum of 5 mW of laser power, two mirrors (Thorlabs BSX11) which transmit 2% of the laser power, are placed at the output port of the laser module. The aperture that removes the halo is placed after the two mirrors. The collimator is tuned so the beam at 150 cm of the mirrors has a diameter of ∼2 mm. Then the size of the beam is measured at 150, 100, 70, 45, 30 cm from the laser module and the laser profile is fitted with a hyperbolic function:

$$w[w_0, z_0, z_R](z) = w_0 \cdot \sqrt{1 + \left(\frac{z - z_0}{z_R}\right)^2} \tag{6.31}$$

Where z_0 is the position of the minimum diameter, also named wedge, w_0 is the diameter of the beam at the wedge, and z_R is the distance from the wedge at which the size of the beam is multiplied by $\sqrt{2}$. In practice, the x and y diameters w_x and w_y are fitted, figure 6.18 shows the laser beam profile.

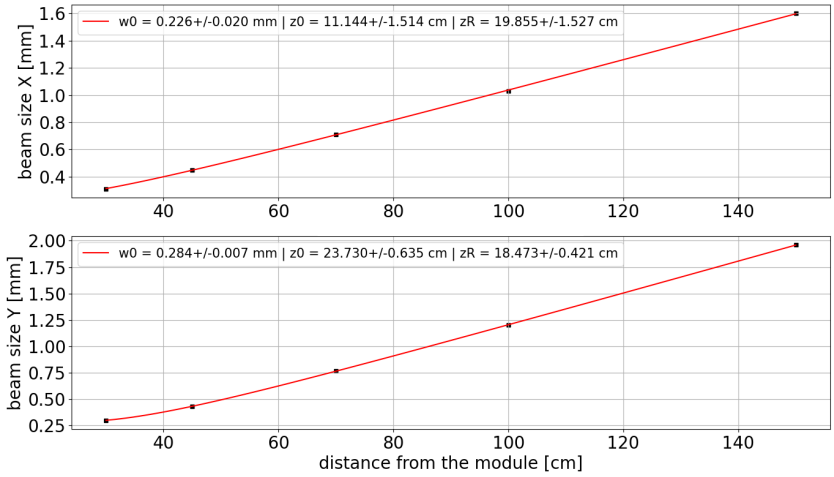

Figure 6.18: Laser beam profile: x and y diameters as function of the distance from the laser module output.

Then the BSX11 mirrors are removed from the laser module, and the sphere is placed on the optical path. The response of the sphere is measured at 50, 75, 100, 125, 150 cm from the laser module, and the size of the beam is computed using the model of the beam profile. The value of the size of the beam is the geometric average of the x and y diameters $w = \sqrt{w_x \cdot w_y}$. Figure 6.19 shows the response of the sphere as function of the size of the beam. The power measured by the sphere decreases with the distance of the sphere from the aperture, or when the beam size increases. This is probably due to a remaining halo. However, the effect is tiny and the standard error on the sphere response is 0.014% of the average value.

6.2.4 Linearity

When the spheres are calibrated with respect to each other, the input laser power of the sphere is 0.3 W, and when the PCal photodiodes are calibrated with respect to WSV integrating sphere, the input laser power of the sphere is 1.3 W. However, the response of the spheres may vary from 0.3 W to 1.3 W. Thus, the dependency to the input power of the response of WSV has been characterized at LAPP. The linearity of the response of WSV is characterized with respect to the PD2 photodiode. Since the two devices have different designs, the variations of their responses to the input power are expected to be independent.

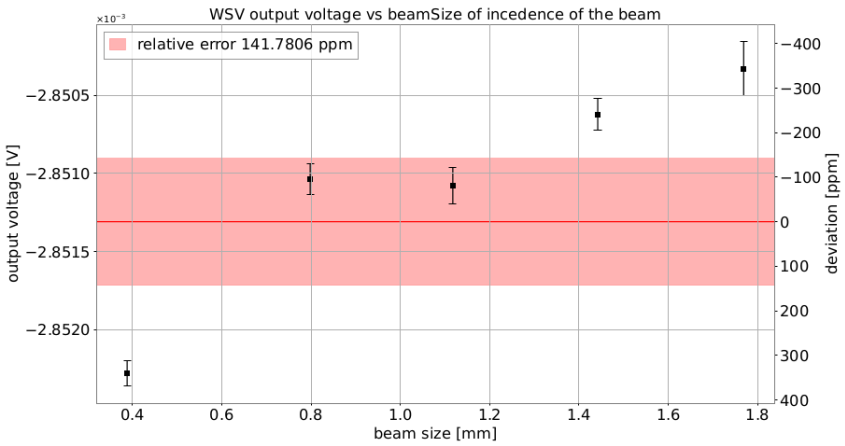

Figure 6.19: Response of the WSV sphere as function of the size of the beam. The mean value and standard error are displayed in red.

The sphere to be characterized is put at the output of the laser module. The laser power signal is a ramp signal that varies from 0.3 W to 1.3 W at the sphere entrance. The ramp duration is 500 s, slow enough for the temperature of the sensor to adapt to the power variations. The time series of the power signal is shown in figure 6.20.

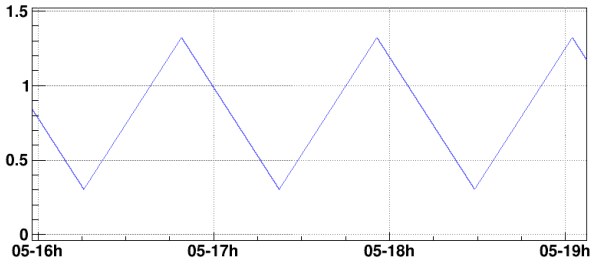

Figure 6.20: Time series of the power signal in the sphere (in W). The power varies from 0.3 W to 1.3 W with 500 s long ramps.

The temperature dependency of WSV is corrected using the formula (6.22), and the background voltage of the photodiodes measured before switching on the laser and subtracted from the measurements. The responsivity of the sphere $\rho_{WSV}(P)$ and the responsivity of the photodiode PD2 $\rho_{PD2}(P)$ may depend of the input power P. The output voltages of the WSV and of the PD2 are written as:

$$V_{WSV}(P) = \rho_{WSV}(P) \cdot P \tag{6.32}$$

$$V_{PD2}(P) = \rho_{PD2}(P) \cdot P \tag{6.33}$$

Thus, the output voltage of WSV can be written as function of the output voltage of the photodiode PD2.

$$V_{WSV}(P) = \frac{\rho_{WSV}(P)}{\rho_{PD2}(P)} \cdot V_{PD2}(P) = \alpha(P) \cdot V_{PD2}(P) \tag{6.34}$$

A linear regression without intercept is computed between the measured output voltages. The parameter α is fitted to the measurement. The residual between the measurement and the linear regression is called ϵ_i. $V_{WSV,i} = \hat{\alpha} \cdot V_{PD2,i} + \epsilon_i$, where ϵ_i is the residual between the measured WSV voltage and the model. The error on the output voltage of the sphere, due to the non-linearity of its response σ_V is computed from the χ^2 of the fit. The χ^2 and the associated p-value are expressed as follow:

$$\chi^2 = \frac{1}{\sigma_V^2} \sum_{i=1}^{N_{pts}} \epsilon_i^2 \tag{6.35}$$

$$\text{p-value} = \int_{\chi^2}^{\infty} \text{chi2}[N-2](x)dx \tag{6.36}$$

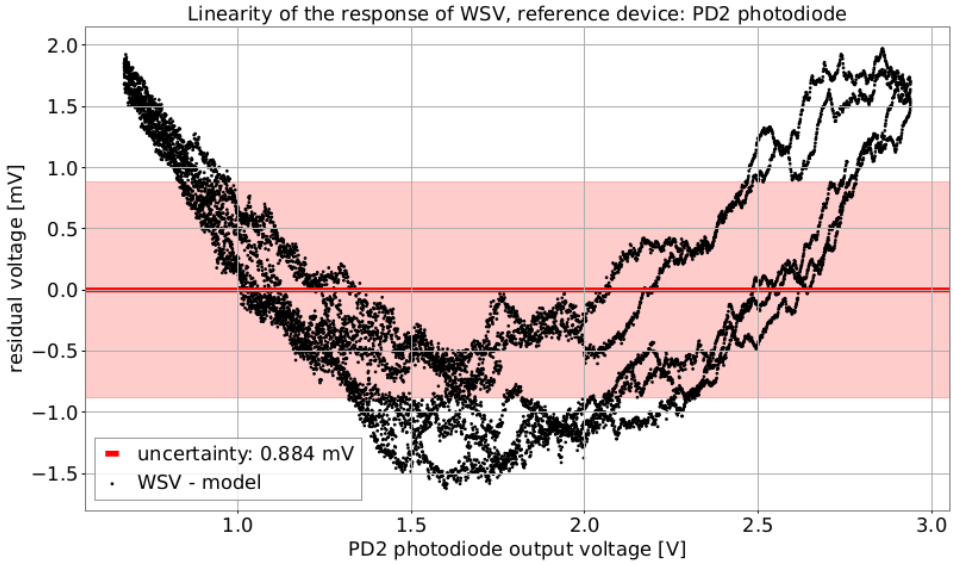

Figure 6.21: Error between the measured output voltage of WSV and the linear model as function of the output voltage of the photodiode PD2

The uncertainty σ_V is tuned so the associated p-value is equal to 0.05. Figure 6.21 shows the residual ϵ_i between the measured output voltage of WSV and model, as function of the output voltage of PD2 V_{PD2}. In the case displayed in this figure, the uncertainty on the output voltage of the sphere is $\sigma_V = 0.884$ mV. This error comes from both the WSV sphere and the photodiode and it is impossible to determine from which device the uncertainty comes from. Since the responses of WSV and PD2 vary independently with the input power, the error on the ratio can be written as a function of the errors on the response, using the following formula:

$$\left(\frac{\sigma_V}{V_{min}}\right)^2 > \left(\frac{\sigma_V}{V}\right)^2 = \left(\frac{\sigma_{\rho_{WSV}}}{\rho_{WSV}}\right)^2 + \left(\frac{\sigma_{\rho_{PD2}}}{\rho_{PD2}}\right)^2 > \left(\frac{\sigma_{\rho_{WSV}}}{\rho_{WSV}}\right)^2 \tag{6.37}$$

Thus, the relative uncertainty on the response of WSV is bounded by the relative uncertainty on the ratio. In practice, the value taken as the relative uncertainty on the WSV response is the relative uncertainty on the output voltage :

$$\frac{\sigma_{\rho_{WSV}}}{\rho_{WSV}} \sim \frac{\sigma_V}{V_{min}} \tag{6.38}$$

The values of the uncertainty on the calibration gain of WSV due to the non-linearity is 0.113%.

Conclusion

In this section, we have described the method to calibrate the integrating spheres between each other. This calibration requires to calibrate in voltage the ADC channels used to measure the output voltage of the spheres, to characterize the temperature dependency of the background voltage, the temperature dependency of the response of the sphere and to measure the responsivity ratio of the spheres. We applied this method to calibrate the Virgo integrating spheres GSV and WSV and an uncertainty on the

calibration was computed. The dependency of the responsivity of the sphere to the position of the beam on the sphere and to the size of the beam, as well as the linearity of the spheres have been characterized and the uncertainty on the sphere response due to these factors was computed. Therefore, the power measured by the integrating spheres GSV and WSV can be computed from their raw output voltage V^{raw} using the following formula:

$$P = \rho' \cdot \frac{V^{raw} - m \cdot (\mathcal{T} - \mathcal{T}^{meas}) - V_{bg}^{meas}}{1 + \kappa \cdot (\mathcal{T} - 300.15\ \mathrm{K})} \tag{6.39}$$

With ρ' the responsivity, m the temperature dependency of the background voltage and κ the temperature dependency of the responsivity. The parameter values are given in table 6.3. V_{bg}^{meas} and $\mathcal{T}^{meas}$ are respectively the background voltage and the temperature of the sphere measured before and after the measurement

Parameters	GSV	WSV
ρ' [V/W]	-2.5934	-2.6125
m [mV/K]	-0.1324	-0.1667
κ [ppm/K]	-115	-187

Table 6.3: Values of the parameters used to compute the power at the entrance of the spheres from the output voltage

The total uncertainty on the response of WSV sphere is summarized in table 6.4. The main source of uncertainty is the non-linearity of the response of the sphere. The variation of the responsivity of the sphere with the input power may come from the variation of the temperature of the spherical shell due to the variation of the laser power. A way of measuring this effect is to add a temperature sensor in the spherical shell to measure the temperature of the intern surface of the sphere and to characterize the dependency of the response to the temperature of the sphere. The response of the GSV integrating sphere has not been characterized yet, but we assume that its relative uncertainty value is the same than WSV.

Uncertainty source	WSV
LIGO standard (PS3) response	0.107%
Output voltage	0.049%
Responsivity ratio	0.037%
Angle of incidence	0.012%
Beam size	0.014%
linearity	0.113%
Total	**0.167%**

Table 6.4: Summary of the error on the response of WSV

Chapter 7

PCal calibration in preparation of O4

Contents

Introduction

The injection benches of the O4 photon calibrator was installed in April 2021 on WE and in February 2022 on NE. The PCal was calibrated roughly with respect to the O3 WSV sphere. Then the Rx spheres, GSV and WSV was mounted at LHO in May 2022, and Rx spheres was installed on WE in July 2022 and on NE in September. The photon calibrator was fully installed with the O4 design in September 2022, and calibrated with respect to the O3 WSV sphere. The first calibration with respect to the new WSV sphere was done in November 2022, and a second calibration was done in June 2023.

In order to calibrate the interferometer, the movement of the end mirror induced by the PCal has to be estimated. This estimation is done from the measurement of the laser power reflected by the end mirror and a model of the mechanical response. In this chapter, the method to calibrate the PCal is detailed, as well as the results. The calibration is divided into three steps:

- The power of the laser reflected by the end mirror is estimated by three power sensors: Two photodiodes (Tx_PD1 and Tx_PD2), and an integrating sphere (Rx_sphere). The power sensors are calibrated at DC, with respect to WSV.
- The output of the power sensors is read by an ADC mezzanine. The frequency response of the sensing chain of the PCal sensor has to be modeled.
- The motion of the end mirror induced by the PCal is computed using a model of the PCal mechanical response. This model is composed by the response of the pendulum and the response of the drum modes.

7.1 Power calibration of the PCal in DC

The movement of the end mirror induced by the PCal is deduced from the power of the PCal laser reflected by the end mirror. This power is estimated from the power sensors of the PCal. These sensors are calibrated regularly with respect to the WSV sphere. However, the power of the beam reflected by the end mirror cannot be measured directly, and the laser beam passes through a viewport before reaching the PCal reflection bench, and is reflected by the M_3 mirror before being measured by the Rx sphere. The losses of the viewport and of the M_3 mirror have to be characterized in order to estimate the power reflected in vacuum by the end mirror from the power measured on the PCal benches out of the vacuum chamber.

7.1.1 Power calibration of the power sensors

The calibration of the power sensors of the PCal is mandatory to estimate with a good accuracy the displacement of the end mass test. To calibrate the sensors, we measure their conversion gain C_{sensor} in $[W/V]$. In chapter 6, we have calibrated the integrating spheres used as standard for the power measurement. The WSV is then used to calibrate the power sensors of the PCal on the Virgo detector. The calibration of the PCal power sensors is a two-stage process: The photodiodes on the injection bench are calibrated first, then the Rx sphere is calibrated with respect to the photodiodes. To calibrate the photodiodes, the following procedure is used:

1. Replace the Rx sphere by the WSV sphere on the reflection bench.
2. Set the laser power to 1.3 W, which is the DC power value at which the PCal operates.
3. Let the WSV sphere and the Tx_PDx photodiodes measure the laser power for twelve hours.
4. Compute the new conversion factors of the photodiodes, and update them.

The conversion factor of the Tx_PDX photodiode $X \in \{1, 2\}$ is computed with respect to the responsivity of WSV ρ_{WSV}, the temperature corrected output voltage of WSV V_{WSV} computed with formula 6.22, and the output voltage of the photodiode V_{Tx_PDX} with its background voltage subtracted.

The calibrated conversion factor is the mean over the measurement duration of the ratio output voltage of the photodiode over the power measured by WSV.

$$C_{Tx\_PDX} = \text{mean}\left\{\frac{V_{WSV}}{V_{Tx\_PDX}}\right\} \cdot \rho_{WSV}^{-1} \tag{7.1}$$

The PCal sensors have been pre-calibrated in April 2022 using the O3 WSV, then calibrated with respect to the new WSV in November 2022. The calibration done in November 2022 consists in computing a correction factor α_{sensor}^{corr}, and the new calibration factors are computed as $C_{sensor}^{new} = \alpha_{sensor}^{corr} \cdot C_{sensor}^{old}$. The correction factor of the Tx_PDX photodiode is given by:

$$\alpha_{Tx\_PDX}^{corr} = \text{mean}\left\{\frac{P_{WSV}}{P_{Tx\_PDX}}\right\} = \text{mean}\left\{\frac{V_{WSV}}{V_{Tx\_PDX}}\right\} \cdot \frac{1}{\rho_{WSV} \cdot C_{Tx\_PDX}^{old}} \tag{7.2}$$

Figure 7.1 shows the evolution of the ratio between the power of the laser estimated with WSV and the pre-calibrated photodiodes, $\frac{P_{WSV}}{P_{Tx\_PD1}}$ and $\frac{P_{WSV}}{P_{Tx\_PD2}}$ through the time. The mean of this ratio gives a correction factor to the conversion factor of the photodiode. The uncertainty on the ratio is given by the standard error of the ratio over the 12 hours of measurement.

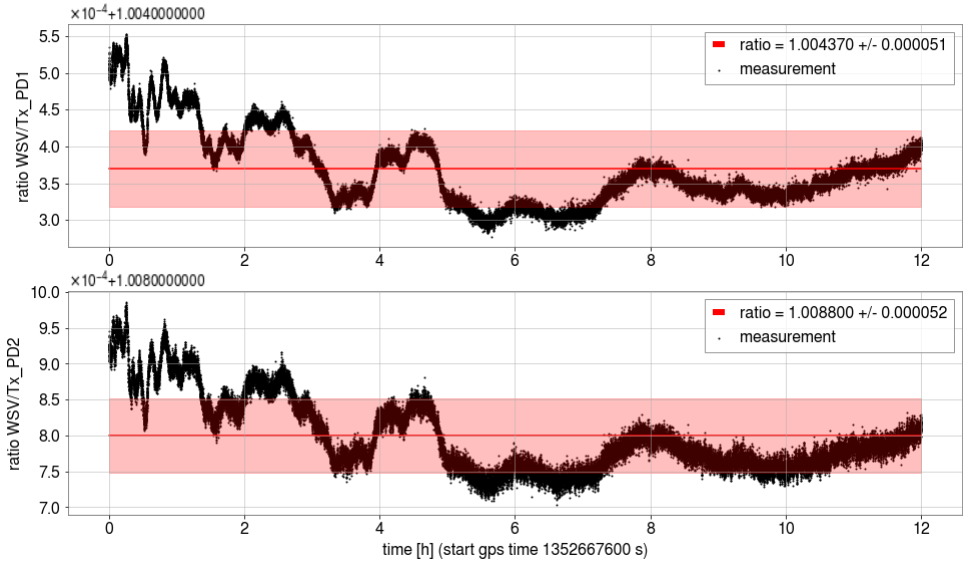

Figure 7.1: Evolution of the ratio between the power measured by the WSV sphere and the pre-calibrated photodiode of the WE PCal. The measurement was done during the calibration of the PCal in November 2022.

After the photodiodes are calibrated with respect to WSV, the Rx sphere is calibrated with respect to photodiodes using the following procedure:

1. Remove the WSV sphere from the reflection bench, and place the Rx sphere
2. Set the laser power to 1.3 W.
3. Let the Rx sphere and the Tx_PDx photodiodes measure the laser power for twelve hours.
4. Compute the new conversion factor of the Rx spheres.

As for the photodiodes, the Rx sphere was pre-calibrated in April 2022, and a correction factor α_{Rx}^{corr} to the conversion factor in of the sphere is computed. The correction factor to the calibration gain is given by the ratio between the power estimated by Tx_PD1 calibrated with respect to WSV in November P_{Tx_PD1}, and the power estimated by Rx_sphere calibrated in April 2022 P_{Rx}. The correction factor of the Rx_sphere is computed as:

$$\alpha_{Rx}^{corr} = \text{mean}\left\{\frac{P_{Tx\_PD1}}{P_{Rx}}\right\} = \text{mean}\left\{\frac{V_{Tx\_PD1}\cdot}{V_{Rx}}\right\} \cdot \frac{C_{Tx\_PD1}^{new}}{C_{Rx}^{old}} \tag{7.3}$$

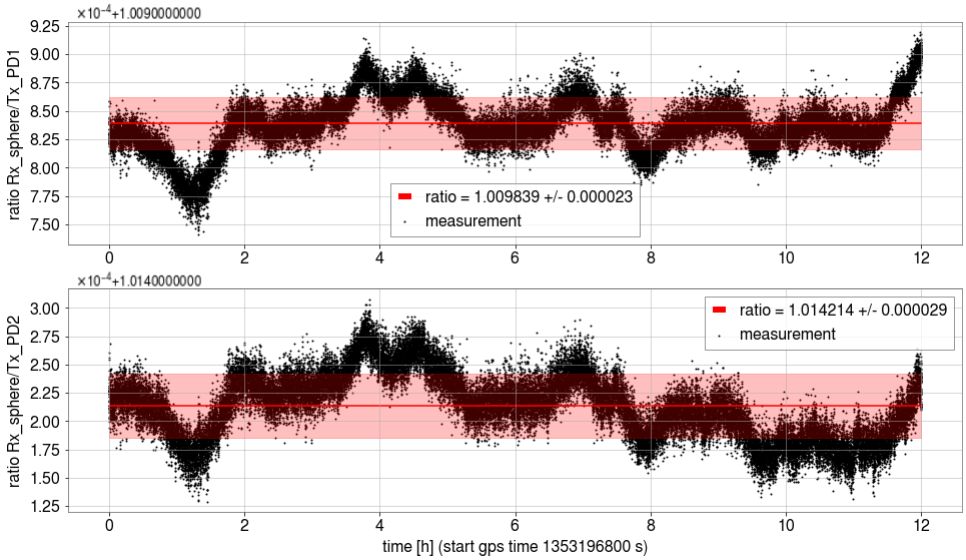

Figure 7.2: Evolution of the ratio between the power measured by the photodiode calibrated and the Rx sphere on the WE PCal. The measurement is done during the calibration of the PCal in November 2022.

The evolution of this ratio is shown by Figure 7.2.

The calibration gain of the PCal power sensors computed in November 2022 are given in table 7.1, as well as the relative error on the correction factor computed during the measurement of the ratio.

PCal	NE			WE		
Power sensor	Tx_PD1	Tx_PD2	Rx_sphere	Tx_PD1	Tx_PD2	Rx_sphere
Conversion factor [W/V]	-0.81018	-0.80918	0.73318	-0.73761	-0.78404	0.69058
Relative error on the ratio [ppm]	145	94	148	51	52	56

Table 7.1: Value of the calibration gain of each PCal sensors calibrated in November 2022, with the associated uncertainty on the ratio between the reference sensor and the calibrated sensors outputs.

7.1.2 Stability of the calibration

All the power sensors of both NE and WE PCal were recalibrated in June 2023. This calibration was done with respect to WSV integrating sphere, using the same method as the one described in the previous section. The new calibration gains are given in table 7.2.

PCal	NE			WE		
Power sensor	Tx_PD1	Tx_PD2	Rx_sphere	Tx_PD1	Tx_PD2	Rx_sphere
Conversion factor [W/V]	-0.777962	-0.860066	0.731686	-0.74093	-0.78515	0.692039
Relative error on the ratio [ppm]	90	73	69	48	58	49
Variation since November [%]	+3.99	-6.30	-0.20	-0.45	-0.14	+0.20

Table 7.2: Value of the calibration gain of each PCal sensors calibrated in June 2023, with the associated uncertainty on the ratio between the reference sensor output and the calibrated sensors output.

One can notice that the calibration gains of the NE PCal photodiodes have changed by more than 1%. This is because the laser beam on the NE PCal injection bench has been realigned with the photodiodes. The main power sensors of the PCal are the Rx spheres because their calibration is more stable than the photodiodes. So the stability of their conversion factor is more crucial than the stability of the conversion factor of the photodiodes. The calibration gains of the Rx spheres have varied by -0.20% and +0.20% respectively on NE and WE. However, as we have seen in chapter 6, the response of the integrating spheres is stable within 0.167%. Therefore, the variation of the gain of the Rx sphere is due to a bias on the calibration of the Rx sphere of the photodiode Tx_PD1.

To estimate the bias of the calibration of Rx b_{Rx}, the ratio between the Rx sphere output over the Tx_PD1 output is computed the day after the update of conversion factor of the Rx spheres for 24 hours. The bias of Rx is computed using equation (7.4). The calibration of the Tx_PD1 also may be biased when the Rx sphere is calibrated. The bias of the photodiode b_{PD} is computed from the ratio between the outputs of the two photodiodes using equation (7.5). The maximum bias $b_{Rx,max}$ of the calibration of the Rx sphere is the sum of the absolute value of the two biases.

$$b_{Rx} = \text{mean}\left\{\frac{Rx}{Tx\_PD1}\right\} - 1 \tag{7.4}$$

$$b_{PD} = \text{mean}\left\{\frac{Tx\_PD2}{Tx\_PD1}\right\} - 1 \tag{7.5}$$

$$b_{Rx,max} = |b_{Rx}| + |b_{PD}| \tag{7.6}$$

Figure 7.3 shows the ratios after the calibrations of November 2022 and after the calibration of June 2023. The maximum bias values of the Rx spheres calibration are given in table 7.3.

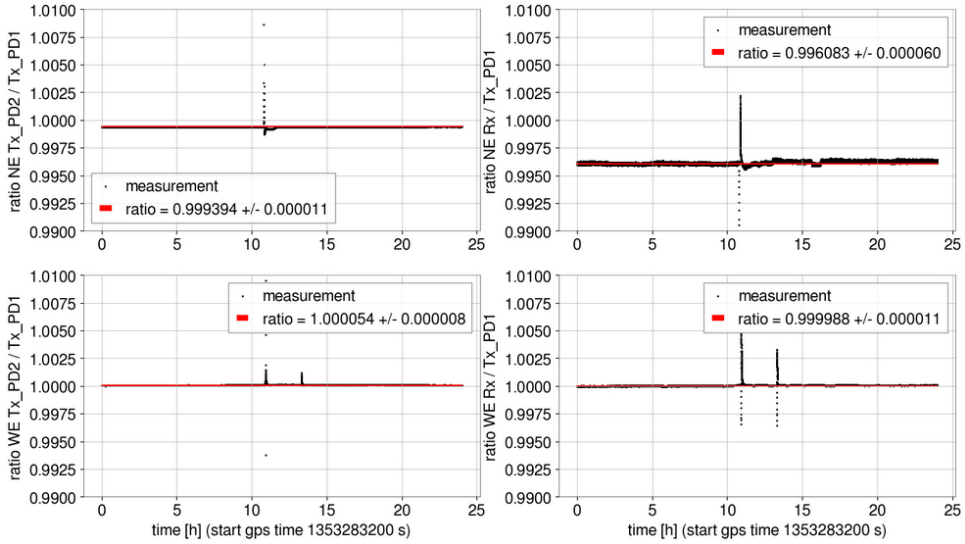

(a) November 24, 2022

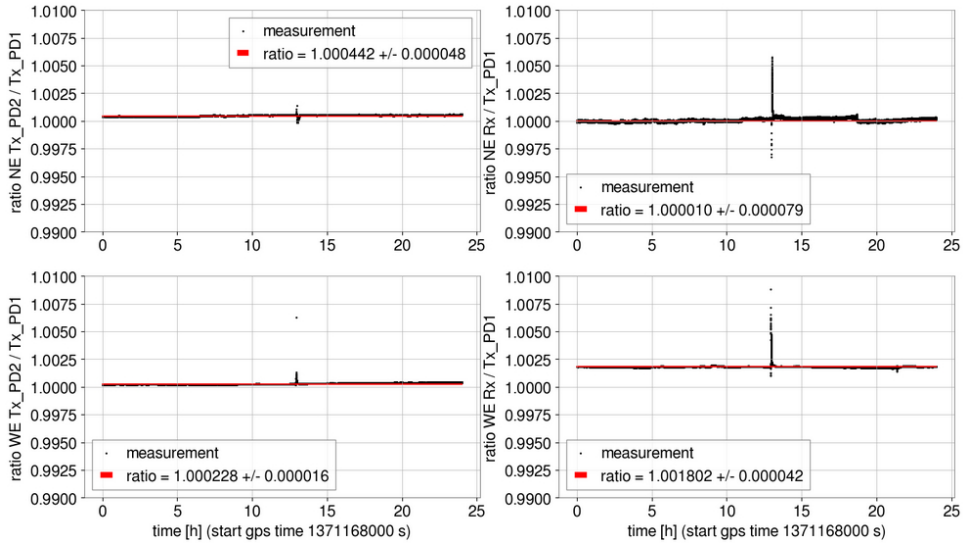

(b) June 06, 2023

Figure 7.3: Ratios Tx_PD2 over Tx_PD1 and Rx sphere over Tx_PD1 done after the calibrations done in November 2022 and in June 2023. The outlier samples are not taken into account in the mean.

These bias values indicate that a mistake has been made during the calibration of the power sensors but it is impossible to determine which sensor is biases from these measurement. The bias in the calibration can explain the variation of the Rx sphere calibration gain between November 2022 and June 2023.

The calibration of the power sensors of the NE PCal in November 2022 has been done using only 2 hours of data instead of 12. Which may explain why the bias of the NE Rx sphere is higher than the bias on WE. So the 0.449% bias on the calibration of NE Rx sphere computed in November 2022 is not taken as the uncertainty on the calibration. The value taken as the uncertainty on the calibration is 0.201%, which the bias on the calibration of the WE Rx sphere computed in June 2023. This bias is probably due to the calibration method, this method of the power sensors has to be improved for the O5 run in order to reduce the uncertainty.

7.1.3 Losses due to the viewport and M_3 mirror

When the power sensors of the PCal are calibrated with respect to WSV, the WSV sphere is installed on the reflection bench of the PCal, at the place of the Rx sphere. Thus the power sensors estimate

PCal	NE Rx sphere	WE Rx sphere
November 2022	0.449%	0.008%
June 2023	0.044%	0.201%

Table 7.3: Maximum bias of the calibration of the Rx sphere computed in November 2022 and June 2023.

the power of the laser on the reflection bench. However, the end mirror moves as function of the power reflected by it, and the laser beam passes through a viewport and is reflected by the M_3 mirror on the reflection bench, before reaching the integrating sphere. This viewport is tilted vertically with respect to the optical bench by $2.4° \pm 0.5°$ downward and the laser beam arrives on the M_3 mirror with an angle of incidence of $18.2° \pm 1°$. The losses of the viewports and of the M_3 mirror have been characterized at LAPP, then measured on the optical bench.

The loss of a viewport similar to the ones on the PCal bench has been characterized at LAPP. An optical setup similar to the one presented in chapter 6 is used. The laser power is set to 1 W, in loop with the photodiode PD1. The power of the output laser beam is measured by the sphere WSV. A first measurement of the output laser power is done without the viewport, the power value is called P_{ref}. Then, the viewport is placed on the laser beam between the laser module and the WSV sphere, and the value of the transmitted power $P_{trans}(\theta)$ is measured, with the viewport tilted vertically at different angles θ. The losses of the viewport are computed with the following formula:

$$l_{vp}(\theta) = 1 - \frac{P_{trans}(\theta)}{P_{ref}} \tag{7.7}$$

Figure 7.4 shows the losses of the viewport as function of the tilt angle of the viewport. The losses are measured for an angle between 0 and 4°, and the measurements are fitted with a second order polynomial function. $l_{vp}(\theta) = A \cdot \theta^2 + B \cdot \theta + C$. The parameters of the fit are $A = -0.085\ \% \cdot (°)^{-2}$, $B = 0.313\ \% \cdot (°)^{-1}$ and $C = 0.337\ \%$. At 2.4°, the losses of the viewport are $l_{vp} = 0.600\% \pm 0.095\%$. The uncertainty on the losses is computed using the method described in appendix A.

Figure 7.4: Losses of the viewport as function of the angle of incidence of the beam on the viewport. And a 2^{nd} order polynomial model is fitted to the measurement.

The losses of the M_3 mirror have been characterized at LAPP in a similar way. A measurement of the output laser power P_{ref} is measured with WSV. Then the M_3 mirror is put on the optical bench, and the reflected power $P_{ref}(\theta)$ is measured with WSV, with the laser power arriving on the mirror at different horizontal angles of incidence. Figure 7.5 shows the losses of the M_3 mirror as function of the angle of incidence of the laser beam on the mirror.

Figure 7.5: Losses of the M_3 mirror as function of the angle of incidence of the beam on the mirror. A 2^{nd} order polynomial model is fitted to the measurement.

The losses of the mirror as function of the angle of incidence is fitted with a second order polynomial function $l_{M\_3}(\theta) = A{\cdot}\theta^2 + B{\cdot}\theta + C$. The parameters are $A = 2.93{\times}10^{-4}$ %$\cdot(^\circ)^{-2}$, $B = -4.68{\times}10^{-3}$ %$\cdot(^\circ)^{-1}$ and $C = 9.47 \times 10^{-2}$ %. The angle of incidence of the beam on the M_3 mirror on the PCal reflection bench is 18.2°. By using the polynomial model, we found that the power losses of the mirror are $l_{M\_3} = 0.107\% \pm 0.012\%$.

The value of the laser power measured by the Rx sphere has to be multiplied by a factor $\frac{1}{(1-l_{vp})\cdot(1-l_{M\_3})} = 1.0071$, and this correction add an uncertainty of $\sqrt{(0.095\%)^2 + (0.012\%)^2} = 0.096\%$ on the value of the laser power.

7.2 Calibration of the sensing chain of the PCal power sensors

The calibration of the power sensors is done in DC, however the sensors will measure power variations up to 10 kHz when the PCal is used to calibrate the interferometer. So the frequency response of the sensing chain has to be known. The output voltage of the photodiode is read by the ADC mezzanine. The frequency response of the ADC mezzanine is not flat due to the anti-aliasing filters, so it is measured in order to be corrected while measuring the laser power of the PCal.

During O3, the sensing was measured using the raw channel of the ADC mezzanine, sampled at 1 MHz, and the frequency response of the ADC mezzanine was modeled as a simple delay. For the O4 run, we want to avoid using the raw channel which takes a large amount of memory in the RTPC. In addition, the sensing channel of the ADC mezzanine is modeled using the same filters as those in the ADC mezzanine. In this section, the method to measure the frequency response of the sensing channel of the ADC mezzanine $S_{ADC}(f)$ is explained.

7.2.1 Description of the sensing chain of the PCal power sensors

As seen in section 5.2.1, the output voltages of the power sensors are read by the ADC mezzanine and converted into a digital signal sampled at $f_{net} = 20$ kHz. To do so, the voltage signal is filtered by an analog anti-aliasing filter which is a 5^{th} order Butterworth filter whose cutoff frequency is 80 kHz. The voltage signal is then digitized at $f_{raw} = 1$ MHz by an ADC chip, the resulting digital signal is named "raw signal". The raw signal is filtered by a IIR anti-aliasing filter named "digital filter". The digital filter is a 8^{th} order Butterworth filter whose cutoff frequency is 7503.65 Hz, it has been designed so as the gain at 10 kHz is -20 dB. The signal is then down-sampled to 20 kHz. The last sample of each frame of 50 samples of the 1 MHz signal is kept to form the 20 kHz signal. Thus, the frequency response of

the down sampling is equivalent to an advance of 49 µs. The down sampling method is shown in figure 7.6.

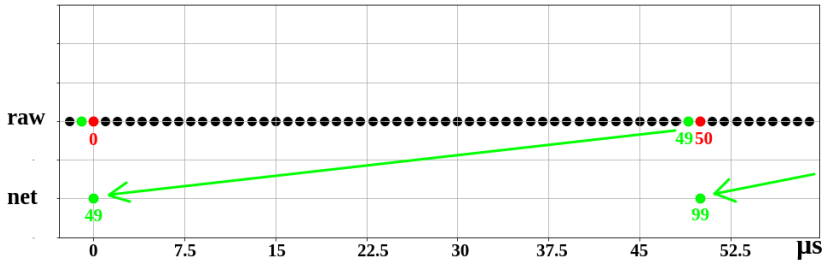

Figure 7.6: Time stamps of a 1 MHz signal, to be down sampled at 20 kHz. Only the last sample of each frame of 50 µs is kept in the net signal, and stored in the Virgo data frame at the position 49 µs earlier.

The resulting signal is named the "net signal". On the PCal benches, only the net signal is sent to the RTPCs to be saved. A scheme of the sensing channel of the PCal power sensor is given in figure 7.7.

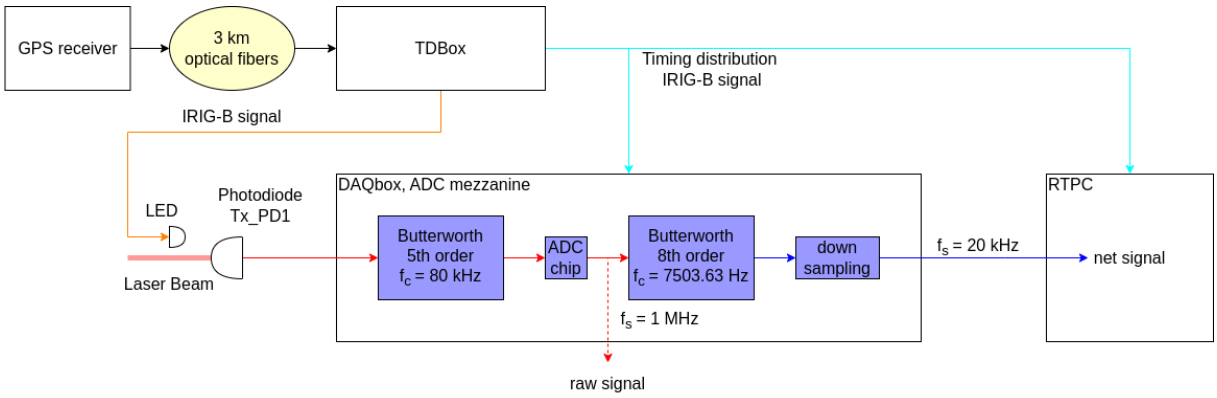

Figure 7.7: Scheme of the sensing chain of the PCal photodiode

The time stamps of the signals are synchronized with the global timing of the interferometer. The timing distribution is synchronized by a main GPS receiver located in the central building of AdV+, the receiver provides an IRIG-B signal which is distributed to the different buildings with 3 km longs optical fibers, the propagation duration of the signal through the fiber is $\tau_{fiber} = 16$ µs. A Timing Distribution Box (TDBox) is located in every building, it distributes the timing signal to every electronic device (DAQBox, RTPCs, DSP boards ...) with short copper cable of a few meters. Thus, the internal clocks of every devices are synchronized with the GPS time.

To measure the frequency response of the sensing chain, a LED has been placed in front of the Tx_PD1 photodiode of each PCal bench. The LED is connected to the same TDBox that distributes the timing to the DAqBox. Thus, the LED can generate a signal which is synchronized with the internal clock of the DAqBox.

7.2.2 Tests of the method at LAPP

A similar setup has been installed in the optical lab at LAPP, in order to test the method to measure the frequency response of the sensing chain. In order to study each part of the sensing chain independently, the IRIG-B signal is measured directly by the ADC mezzanine, as well as the photodiode output. The channels are respectively called "TDBox" and "photodiode". Both the raw and net signal of the TDBox and of the photodiode are send to the RTPC. A scheme of the LAPP setup is shown in figure 7.8.

The sensing chain is composed by the photodiode, and the ADC mezzanine. The ADC mezzanine can be divided into two parts, the analog processing and the digital processing.

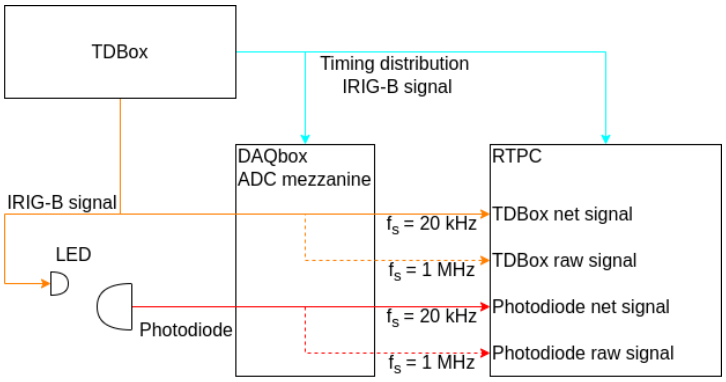

Figure 7.8: Scheme setup to test the method of measurement of the photodiode sensing chain.

The frequency response of the photodiode is measured by measuring the transfer function from the net signal of the TDBox to the net signal of the photodiode. All the transfer functions are a mean of $N_{TF} = 20$ transfer functions computed over Hann windows with a length of 1 s. Only the points with a coherence γ above 0.9999 are kept. The formula (7.8) and (7.9) give us the value of the statistical uncertainty on the modulus and on the phase. The values of the statistical uncertainties are $\frac{\sigma_\rho}{\rho} = 0.19\%$ on the modulus and $\sigma_\phi = 2.0$ mrad on the phase.

$$\frac{\sigma_\rho}{\rho} = 0.85 \cdot \sqrt{\frac{1-\gamma}{\gamma \cdot N_{TF}}} \tag{7.8}$$

$$\sigma_\phi = 0.89 \cdot \sqrt{\frac{1-\gamma}{\gamma \cdot N_{TF}}} \tag{7.9}$$

As shown in figure 7.9 the standard variation of the modulus of the frequency response is 0.18% and standard variation of the phase is 2 mrad, the variations are explainable by statistical uncertainty. The frequency response of the photodiode is flat and with a negligible delay of 74 ± 7 ns.

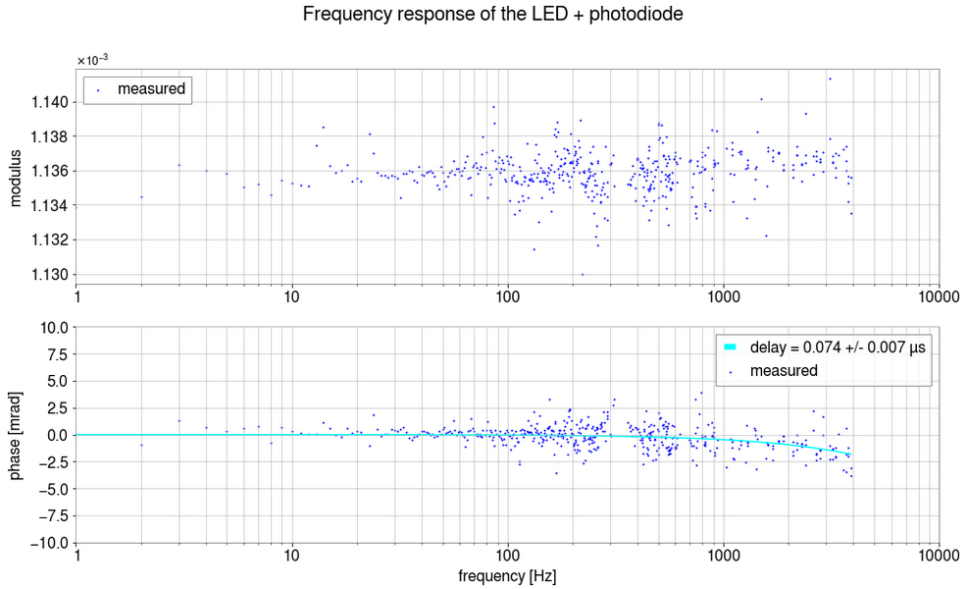

Figure 7.9: Transfer function from the TDBox net signal to the photodiode net signal. Only the points with a coherence above 0.9999 are displayed.

The analog process is composed by the analog filter and the ADC chip. It is measured by computing the frequency response from the IRIG-B signal to the TDBox raw signal. The frequency response of the ADC chip is flat, so the frequency response of the analog process is equal to the frequency response of

the analog filter. The analog filter is modeled with an IIR filter. Figure 7.10 shows the measurement and model of the frequency response of the analog process, and the residual between them.

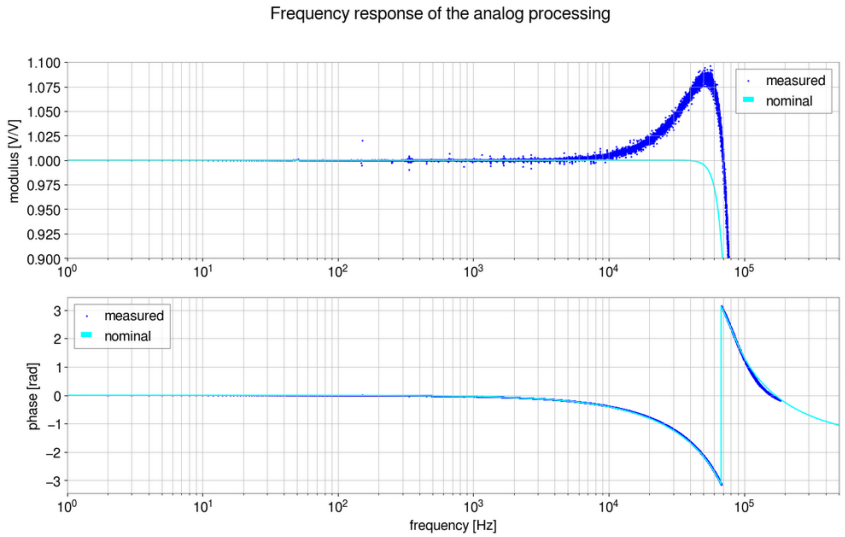

(a) frequency response

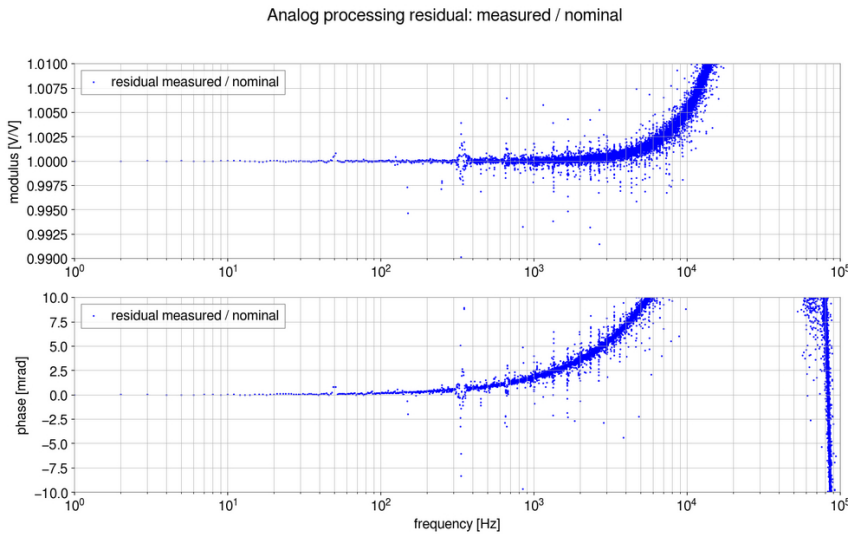

(b) residual

Figure 7.10: Frequency response of the analog processing with the IRIG-B signal injected in the ADC.

The modulus of the residual between the measured frequency response and the model is 0.5% at 10 kHz. Below 5 kHz, the modulus of the residual is flat at 1, with only statistical noise, and the phase has an advance of 0.3 µs. The modulus of the residual may be caused by an aliasing of the signal or by a difference between the physical analog filter and its model. However, the advance in the phase may be caused by a difference between the responses of the ADC analog filter and of the IIR filter used to modeled it.

The digital processing is composed by the digital filter and the down sampling, and it is modeled with the same digital filter as the one defined in the DSP of the ADC, and an advance of 49 µs. The frequency response of the digital processing is measured by computing the transfer function from the raw signal to the net signal of the TDBox. The measurement of the frequency response and the model of the frequency response is shown in figure 7.11. Below 4 kHz, the modulus of the residual is flat within 0.1 % and 1 mrad on the phase, but vary at higher frequencies. Despite the anti-aliasing filters, the residual between the frequency response and the model of the digital processing highlight an aliasing of the frequency response at frequencies above 4 kHz.

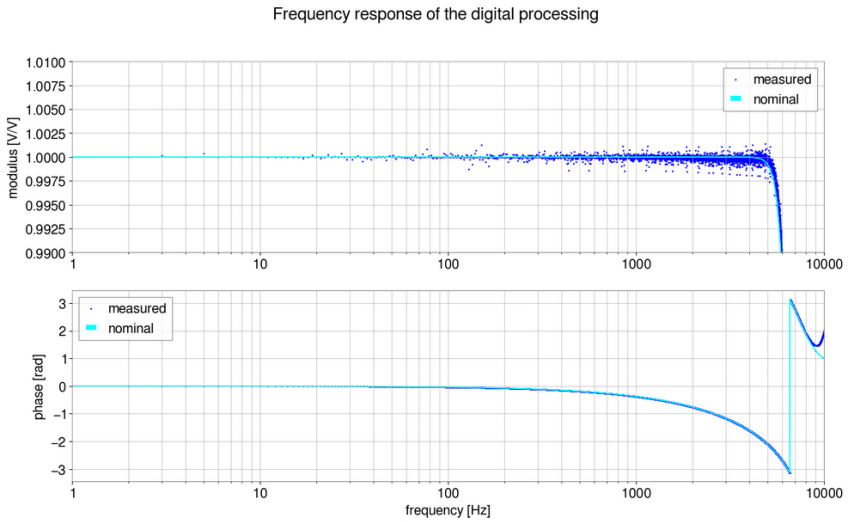

(a) frequency response

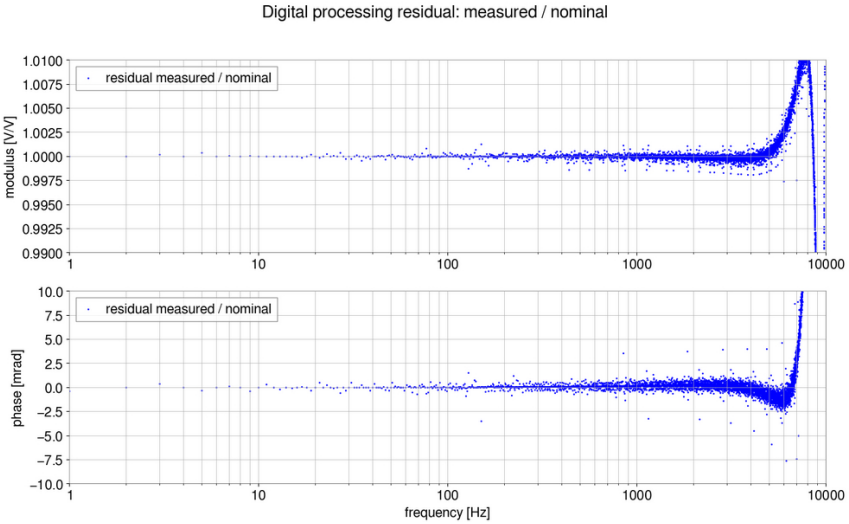

(b) residual

Figure 7.11: Frequency response of the digital processing with the IRIG-B signal injected in the ADC.

However, if we stop injecting the IRIG-B signal in the ADC mezzanine, the output signals contain only the electronic noise of the ADC. The transfer function from the raw signal to the net signal in that case is shown in figure 7.12. With only the ADC noise in the signal, the residual between the measurement and the model of the frequency response has the statistical noise level.

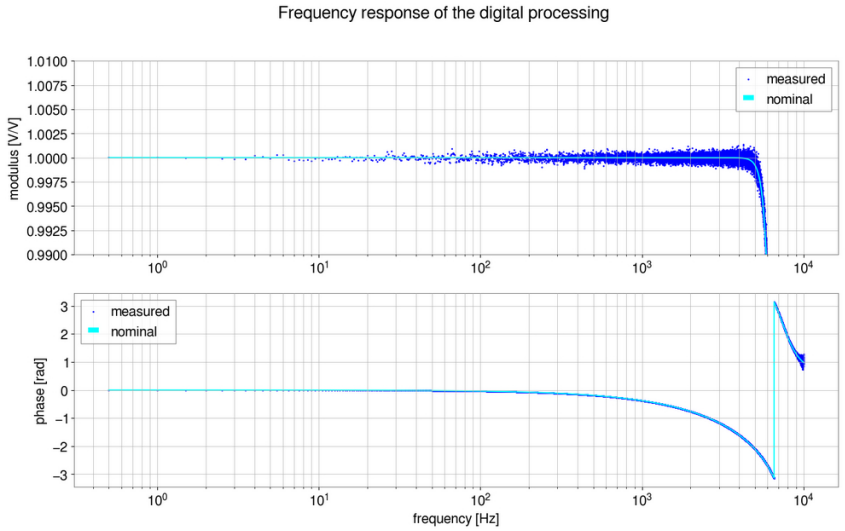

(a) frequency response

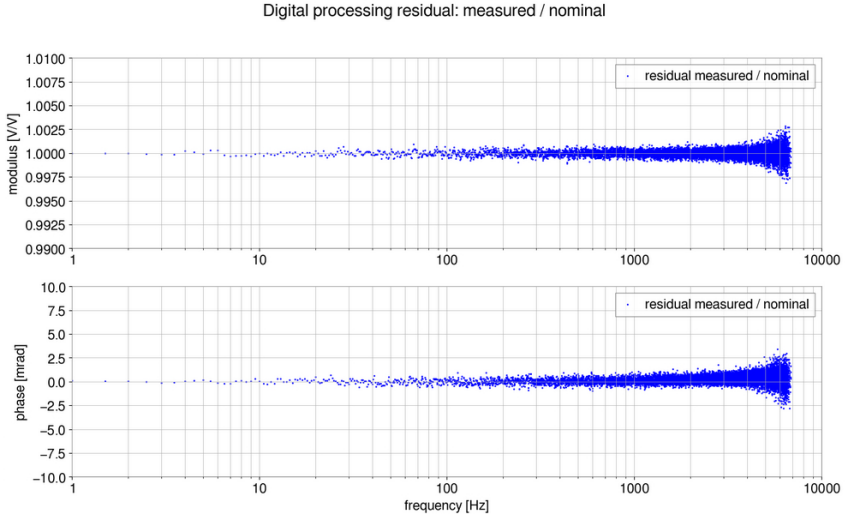

(b) residual

Figure 7.12: Frequency response of the digital processing without any signal injected in the ADC.

When we measure the sensing chain of the power sensors, we inject an IRIG-B signal with the LED, so the aliasing effect is visible on the photodiode response above 4 kHz. Thus the measurement of the sensing chain of the power sensors is done by fitting the model to the measurement in the frequencies below 4 kHz, and only on the points with a coherence γ above 0.9999. However, the effect of the aliasing are no longer visible when the IRIG-B signal is not injected, so this model is relevant in the frequency bandwidth [1 Hz, 10 kHz]. The uncertainty is dominated by the statistical uncertainty, which is 0.19% on the modulus and 2.0 mrad on the phase.

7.2.3 Measurement of the sensing chain on the PCal

In this section, the method to measure the frequency response of the sensing chain of the PCal power sensors is described. To measure the frequency response of the sensing chain, a LED has been placed in front of the Tx_PD1 photodiode of each PCal bench. To measure the frequency response of this photodiode, the laser of the PCal is switched off and the LED flashes the IRIG-B signal in the photodiode, and the transfer function from the IRIG-B signal to the photodiode output is computed. An example of frequency response measurement with the fitted model is shown in figure 7.13.

The frequency responses of the Tx_PD2 photodiode and the Rx_sphere are measured with respect to the Tx_PD1 photodiode. They are measured by injecting a white noise in the laser power signal, which

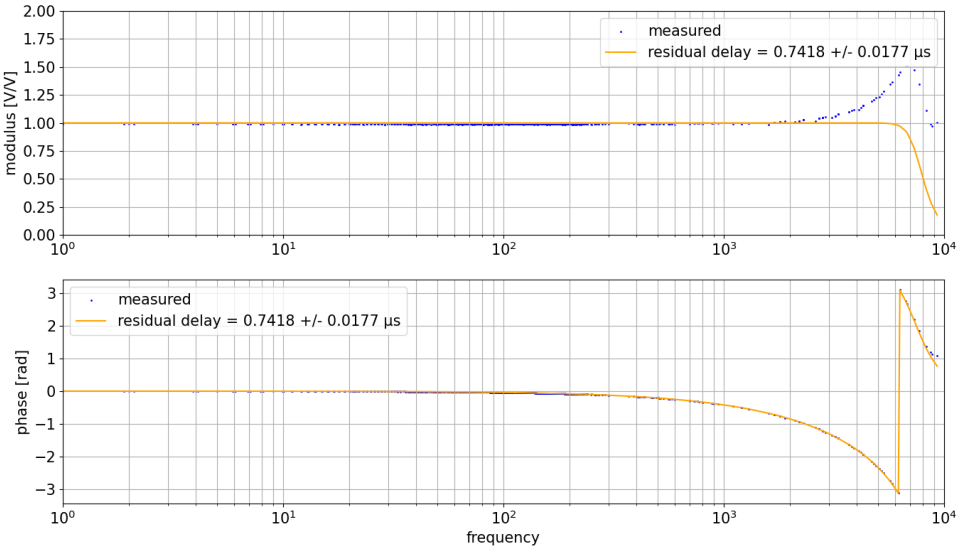

Figure 7.13: Transfer function from the IRIG-B signal to the output signal of the Tx_PD1 photodiode, with the model fitted to the data.

increase the coherence between the Tx_PD1 output signal and the output signals of the other sensors. The transfer functions from Tx_PD1 to Tx_PD2 outputs and from Tx_PD1 to Rx_sphere outputs are computed. The phase of these transfer functions is fitted with a simple delay. An example of transfer functions from Tx_PD1 to Tx_PD2 is given in figure 7.14

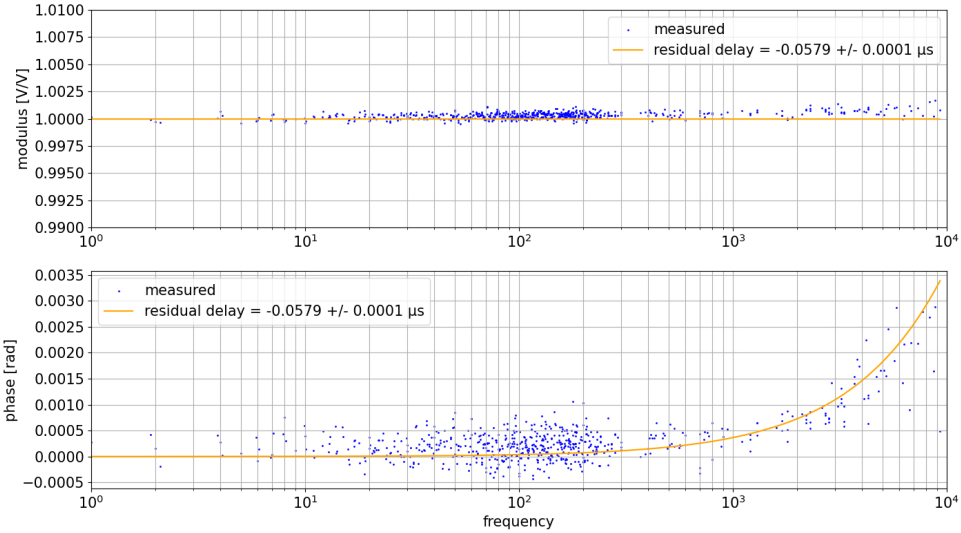

Figure 7.14: Transfer function from the Tx_PD1 photodiode output to the Tx_PD2 photodiode output, with the delay fitted to the transfer function.

A 16 µs delay has to be added to the frequency response of the power sensors, due to the propagation of the IRIG-B signal from the central building to the end buildings in the optical fibers.

The procedure to measure the frequency response of the sensing chain is automatized so the frequency response of the sensing chain has been measured several times in March 2023. Table 7.4 summarizes the model of the sensing chain and shows the values of the residual delay between the measured and modeled frequency responses.

If the coherence γ between the signals is higher than 0.9999 and for $N_{TF} = 20$, the uncertainty on the modulus of the frequency response is $\frac{\sigma_\rho}{\rho} = 0.190\%$ and $\sigma_\phi = 2.0$ mrad.

PCal	NE			WE		
Sensor	Tx_PD1	Tx_PD2	Rx_sphere	Tx_PD1	Tx_PD2	Rx_sphere
Analog filter	5^{th} order Butterworth filter $f_c = 80$ kHz					
Digital filter	8^{th} order Butterworth filter $f_c = 7503.65$ Hz					
Down sampling delay	-49 µs					
Residual delay	0.62 µs	0.54 µs	1.45 µs	0.72 µs	0.66 µs	1.38 µs

Table 7.4: Model of the frequency response of the sensing chain.

The sensing model of the sensing chain of all power sensor is validated by the measurements done at LAPP and at Virgo. The residual delays measured at Virgo are below 1 µs, they are due to the difference between the real analog filter and its model. The inverse of the frequency response is applied to the readout channel in order to get the power unbiased in frequency and synchronized with GPS time.

7.3 Mechanical response from the PCal laser power to the mirror motion

We can now estimate the reflected laser power signal from the PCal sensors calibrated in power and corrected for their responsivity and delay. In order to estimate the mirror motion ΔL_{PCal} induced by the PCal, the mechanical response of the PCal have to be estimated.

The end mirror displacement is estimated from the measurement of the reflected laser power and a model of the mechanical response of the mirror to the PCal. This mechanical response is composed by the frequency response of the pendulum, and the response of the drum modes. The parameters of the model of the frequency response of the pendulum model are measured individually, whereas the parameters of the drum modes response are fitted to a measurement of the mechanical response at high frequency. In this section, we will estimate the parameters of the model of the frequency response of the pendulum model. Then we will measure the drum modes response and fit a model of the mechanical response to the measurement.

7.3.1 Calibration of the PCal geometric parameters

The pendulum response describes the mirror motion induced by the PCal power reflected by the mirror. As seen in chapter 3, for $f >> 0.6\ Hz$, the frequency response of the pendulum is modeled as:

$$\Delta L_{PCal}(f) = H_{pend}(f) \cdot P_{ref}(f) = \frac{-2 \cdot \cos(\theta)}{M \cdot c \cdot (2\pi f)^2} \cdot P_{ref}(f) \tag{7.10}$$

The parameters of the frequency response of the pendulum are:

- The mass of the end mirror M.
- The angle of incidence of the PCal laser beam on the end mirror θ.

However, it is assumed in this formula (7.10) that the main beam of the interferometer and the PCal laser beam are centered on the end mirror. In the case that the interferometer laser beam hits the end mirror at the position $\vec{a}$ with respect to the center of the mirror and that the PCal beam hits the mirror at a position $\vec{b}$, equation (7.10) becomes:

$$\Delta L_{Pcal}(f) = H_{pend}(f) \cdot \left(1 + \frac{M \cdot \vec{a} \cdot \vec{b}}{I}\right) \cdot P_{ref}(f) \tag{7.11}$$

Where $I = \frac{Ml^2}{12} + \frac{Mr^2}{4}$ is the moment of inertia of the mirror, $r = 0.175$ m is its radius and $l = 0.200$ m is its thickness. The position of the PCal beam on the mirror $\vec{b}$ is also a parameter of the pendulum

response. Thus, the list of parameters of the pendulum frequency response also called "the geometric parameters" is:

- The mass of the end mirror M.
- The angle of incidence of the PCal laser beam on the end mirror θ.
- The position of the PCal laser beam on the mirror $\vec{b}$.

In this section, we will determine the uncertainty on the parameters and the contribution of the uncertainty on the mirror displacement.

The mass of the end mirror is $M = 42.30 \pm 0.02$ kg [24]. The uncertainty on the end mirror mass represents 0.05% of the value. Since the mirror displacement is inversely proportional to the mirror mass, the contribution of the uncertainty on the mirror mass to the mirror displacement error is also 0.05%.

Since we cannot access the vacuum chamber, we cannot measure directly the angle of incidence θ and the position $\vec{b}$ of the PCal beam on the end mirror. Instead, the angle of incidence and the position are computed from the position of the PCal laser beam on the viewports of the injection bench $\vec{x}_{inj}$ and of the reflection bench $\vec{x}_{ref}$.

A base $\mathcal{B} = (O, \hat{x}, \hat{y}, \hat{z})$ is associated to the chamber. The origin of the base O is the center of the end mirror, z is the normal to the mirror surface, x is the vertical axis and y is the horizontal axis. The center of the PCal viewports are located at $z_{inj} = z_{ref} = 1430 \pm 10$ mm from the surface of the end mirror along the optical axis, and the $y_{inj} = -y_{ref} = 478 \pm 10$ mm, they are aligned vertically with center of the end mirror $x_{inj} = x_{ref} = 0 \pm 10$ mm. The viewports have a diameter of 63 mm, the laser beam has been centered within better than ± 10 mm. The angle of incidence of the PCal laser beam on the end mirror θ is computed from the position as:

$$\theta = \arctan\left(\frac{y}{z}\right) = 18.5^\circ \tag{7.12}$$

The uncertainty on the angle of incidence σ_θ is computed form the uncertainty on the beam position on the viewport $\sigma_y = 10$ mm with the formula:

$$\sigma_\theta = \frac{\partial \theta}{\partial y} \cdot \sigma_y = \frac{1}{1 + \left(\frac{y}{z}\right)^2} \cdot \frac{\sigma_y}{z} = 0.36^\circ \tag{7.13}$$

And the uncertainty on the mirror displacement σ_L due to the angle of incidence is computed as:

$$\frac{\sigma_L}{\Delta L_{PCal}} = \frac{\partial(\Delta L_{PCal})}{\partial \theta} \cdot \frac{1}{\Delta L_{PCal}} \cdot \sigma_\theta \tag{7.14}$$

Because the mirror displacement is proportional to $\cos(\theta)$, $\frac{\partial \Delta L}{\partial \theta} \propto \sin(\theta)$. Thus, the uncertainty on the mirror displacement is written as:

$$\frac{\sigma_L}{\Delta L_{PCal}} = \tan(\theta) \cdot \sigma_\theta = 0.207\% \tag{7.15}$$

The position of the PCal laser beam on the end mirror $\vec{b}$ is given by the following formula:

$$\vec{b} = \begin{cases} b_x = (x_{inj} + x_{ref})/2 \\ b_y = (y_{inj} + y_{ref})/2 \\ b_z = 0 \end{cases} \tag{7.16}$$

The uncertainty on the beam position on the mirror σ_b is written as function of the uncertainty on the beam position on the viewport $\sigma_x = \sigma_y = 10$ mm on both viewport, with formula:

$$\sigma_b = \frac{1}{2}\sqrt{2 \cdot \sigma_x^2} = \frac{1}{\sqrt{2}} \cdot \sigma_x = 7.07 \text{ mm} \tag{7.17}$$

The interferometer beam is centered with an accuracy of ± 0.5 mm. If we consider the worst case where the positions of the two beams on the end mirror $\vec{a}$ and $\vec{b}$ are collinear and at the maximum of

amplitude. The value of the factor $\frac{M \cdot \vec{a} \cdot \vec{b}}{I}$ is 0.032%. The table 7.5 summarizes the contribution of the geometrical parameters to the uncertainty on the mirror displacement. This uncertainty is frequency independent. This simple pendulum model is valid from 10 Hz to a few hundred Hertz. At higher frequency, the internal modes of the mirror start to contribute to the PCal response is explained in the following section.

Mass of the end mirror	0.047%
Angle of incidence	0.207%
Beam position	0.032%
Total	0.215%

Table 7.5: List of uncertainty on the mirror displacement du to the geometrical parameters.

7.3.2 Measurement of the mechanical response at high frequency

In this section, a model of the frequency response of the drum modes is defined. As seen in chapter 3, the mechanical response of the PCal $H_{PCal}(f)$ is the sum of the response of the pendulum $H_{pend}(f)$ and the response of the drum modes $H_{drum,i}(f)$.

$$H_{PCal}(f) = H_{pend}(f) + \sum_n H_{drum,n}(f) = \frac{G_p}{1 + \frac{i}{Q_p}\frac{f}{f_p} - \left(\frac{f}{f_p}\right)^2} + \sum_n \frac{G_{d,n}}{1 + \frac{i}{Q_{d,n}}\frac{f}{f_{d,n}} - \left(\frac{f}{f_{d,n}}\right)^2} \tag{7.18}$$

Where G_p and $G_{d,i}$, are the gains of the response of the pendulum and of the drum modes, f_p and $f_{d,n}$ are their resonant frequencies and Q_p and $Q_{d,n}$ their quality factors. The gain of the pendulum is $G_p = 1.69 \times 10^{-3}\text{kg}^{-1}\text{s}^2$, the resonant frequency is $f_p = 0.6\ Hz$ and the quality factor is $Q_p = 1000$, as seen section 3.1. In practice the value of the gain is normalized by the length of the interferometer arms $L_0 = 3$ km, so the used value is $G_p = 3.5115 \times 10^{-15}$h/W. During the O3 run, only the first drum mode was taken into account in the model of the mechanical response. The resonant frequency of the first drum mode was estimated to be 7812.8 Hz on WE and 7813.2 Hz on NE. Around 2 kHz, the response of the pendulum and the response of the drum mode compensate each other, which create a notch in the mechanical response. The frequency of the notch was 2042 Hz on WE and 2055 Hz on NE. The gain of the first drum mode $G_{d,1}$ is tuned so as the response of the drum mode compensates the response of the pendulum at the notch frequency.

Also during O3, a more accurate model of the mechanical response on WE has been computed using three drum modes plus a frequency independent gain to take into account the higher drum modes, instead of one drum mode. The parameters of the drums modes are given in table 7.6. We called this model the accurate model of the mechanical response of the PCal H^{acc}_{PCal}, the model using only one drum mode is called the O3 model H^{O3}_{PCal}.

Resonant frequency [Hz]	Amplitude [h/W]	Quality factor
7812.8	$(4.24 \pm 0.06) \times 10^{-23}$	10^6
10120	$(9.28 \pm 3.28) \times 10^{-23}$	10^6
12905	$(-1.45 \pm 0.85) \times 10^{-22}$	10^5
-	$(3.08 \pm 0.54) \times 10^{-22}$	-

Table 7.6: List of the drum modes excited by the PCal laser on WE, with their resonant frequencies, amplitudes and quality factors in the "accurate model".

Figure 7.15 shows the frequency responses of the accurate and the O3 models in the frequency bandwidth [1 kHz, 15 kHz], and the residual between the two models. One can notice that there is no visible phase shift between the two models below 8 kHz, but the gains differ by 2% at 1 kHz and by 6% at 2 kHz. For the O4 run, a new model of the PCal mechanical response response has been defined. The O4 model takes into account the first drum mode, and assumes that the contribution o the higher model is flat in frequency. Thus they are model by a frequency independent gain G_c. The formula of the new mechanical response of the PCal is written as follow:

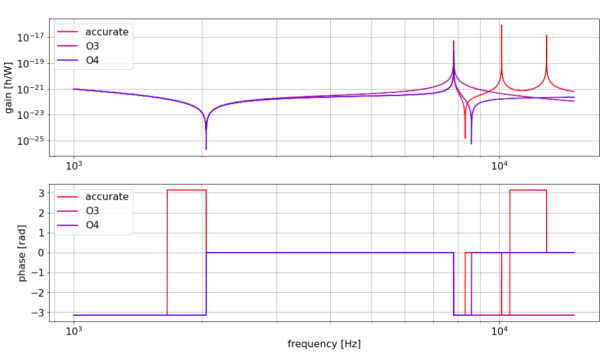

(a) Frequency response

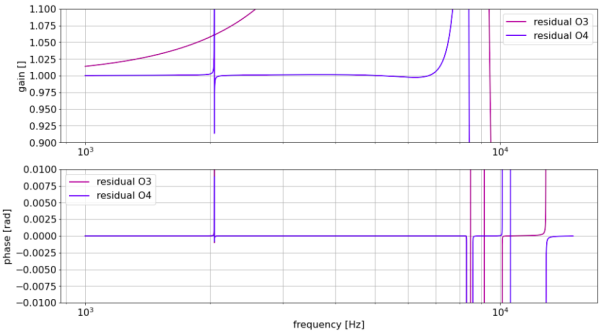

(b) Residual between the 3 drum modes model and the others models.

Figure 7.15: Model of the mechanical response of the WE PCal. Model using the 3 drum modes. Model using only 1 drum mode model With one drum mode and a frequency independent gain.

$$H_{PCal}^{O4}(f) = \frac{G_p}{1 + \frac{i}{Q_p}\frac{f}{f_p} - \left(\frac{f}{f_p}\right)^2} + \frac{G_d}{1 + \frac{i}{Q_d}\frac{f}{f_d} - \left(\frac{f}{f_d}\right)^2} + G_c \tag{7.19}$$

If the frequency of the drum mode f_d is fixed at 7812.8 Hz, and if the parameters G_d and G_c are tuned so as the O4 model fit the accurate model in the frequency bandwidth [1 kHz, 7 kHz], the modulus of the O4 model differs from the accurate model by 0.2% in the bandwidth [1 kHz, 7 kHz]. The O4 model fitted to the accurate model is also plotted in figure 7.15.

Since the NE mirror has been replaced in June 2023, the parameters of the drum modes may have changed. So the mechanical response of the mirror is measured and the O4 model is fitted to the measurement. To measure the mechanical response, a sinusoidal motion at the frequency f is given to the mirror using the PCal, and the transfer function from the PCal laser power measured by the photodiode Tx_PD2 to the output signal of the interferometer $DARM$. At high frequency (f>1 kHz), the transfer function can be written as:

$$\left(\frac{DARM}{P_{Tx\_PD2}}\right)(f) = O_{mir}(f) \cdot G_{OR} \cdot H_{PCal}(f) \tag{7.20}$$

The gain of the optical response is called G_{OR}. The optical response of the interferometer $O_{mir}(f)$ to a displacement of the mirror mir is modeled as a simple pole:

$$O_{mir}(f) = \frac{1}{1 + i\frac{f}{f_{OR}}} \tag{7.21}$$

Where f_{OR} is the resonant frequency of the pole cavity, fixed at $f_{OR} \sim 400\ Hz$. The optical response $O_{mir}(f)$ is used to normalize the transfer function $\left(\frac{DARM}{P_{Tx\_PD2}}\right)$. The gain of the optical response G_{OR} is unknown, so the measured optical response to be fitted is can be written as:

$$\left(\frac{DARM}{P_{Tx\_PD2}}\right)(f) \cdot O_{mir}^{-1}(f) = H_{PCal}(f) \cdot G_{OR} \tag{7.22}$$

The model of the mechanical response is fitted in two steps:

1. Measure the resonant frequency of the drum mode by injecting lines in the frequency bandwidth [7810 Hz, 7820 Hz]. Since the quality factor if the drum mode is high ($Q_d = 10^6$), the phase of the mechanical response jump by π at the resonant frequency.

2. Once the resonant frequency is known, the mechanical response of the PCal is fitted to the measured mechanical response in the bandwidth [1 kHz, 7 kHz]. In the bandwidth, the response of the pendulum is approximated with the high frequency approximation:

$$H_{pend}(f) \sim -G_p \cdot \left(\frac{f_p}{f}\right)^2 \tag{7.23}$$

Because the value of the quality factor of the drum mode is high $Q_d = 10^6$, the response of the drum mode is approximated with:

$$H_{drum}(f) \sim \frac{G_d}{1 - \left(\frac{f}{f_d}\right)^2} \tag{7.24}$$

Thus, the model of the PCal mechanical response to be fitted is written as:

$$H_{PCal}(f) \cdot G_{OR} = (H_{pend}(f) + H_{drum}(f) + G_c) \cdot G_{OR} = -G_p \cdot G_{OR} \cdot \left(\frac{f_p}{f}\right)^2 + \frac{G_d \cdot G_{OR}}{1 - \left(\frac{f}{f_d}\right)^2} + G_c \cdot G_{OR} \tag{7.25}$$

In practice, an equivalent function is fitted to the measurement. This function uses the following parameters:

- f_n the notch frequency which satisfy $H_{pend}(f_n) = H_{drum}(f_n) + G_c$
- $\Gamma_p = -H_{pend}(f_n) \cdot G_{OR}$ the modulus of the pendulum at the notch frequency
- $\Gamma_d = H_{drum}(f_n) \cdot G_{OR}$ the modulus of the drum mode at the notch frequency.

The fitted function is written as:

$$H_{PCal}(f) \cdot G_{OR} = -\Gamma_p \cdot \left(\frac{f_n^2}{f^2}\right) + \Gamma_d \cdot \left(\frac{1 - \left(\frac{f_n}{f_d}\right)^2}{1 - \left(\frac{f}{f_d}\right)^2}\right) + (\Gamma_p - \Gamma_d) \tag{7.26}$$

3. The gain of the pendulum response G_p is given by equation (7.10). So the gain of the optical response G_{OR} can be computed from it with the following formula:

$$G_{OR} = \frac{\Gamma_p}{G_p} \left(\frac{f_n}{f_p}\right)^2 \tag{7.27}$$

Thus the gains of the drum mode G_d and the frequency independent gain G_c are computed as:

$$G_d = \frac{\Gamma_d}{G_{OR}} \cdot \left(1 - \left(\frac{f_n}{f_d}\right)^2\right) \tag{7.28}$$

$$G_c = \frac{\Gamma_p - \Gamma_d}{G_{OR}} \tag{7.29}$$

In June 2023, the NE mirror has been replaced, and the interferometer is still recovering from this intervention in July 2023, so the mechanical response cannot be measured as described above. However, a measurement of the notch frequency has been done in April 2023.

The resonant frequency of the drum modes are not measured with the PCal, be it is visible in the amplitude spectral density (ASD) of the output signal of the interferometer as shown in figure 7.16.

The exact resonant frequency of the drum modes may vary a bit due to the temperature of the mirror. But they are expected to be above 7810 Hz, and the resonant frequency of NE is expected to be above the resonant frequency of WE. The quality factor of the NE drum mode is lower than the quality factor of WE, so the NE peak in the ASD of B1 is larger and lower than the WE peak. The values of the resonant frequencies are 7811.4 Hz on NE and 7810.5 Hz on WE. Sinusoidal lines are injected successively with

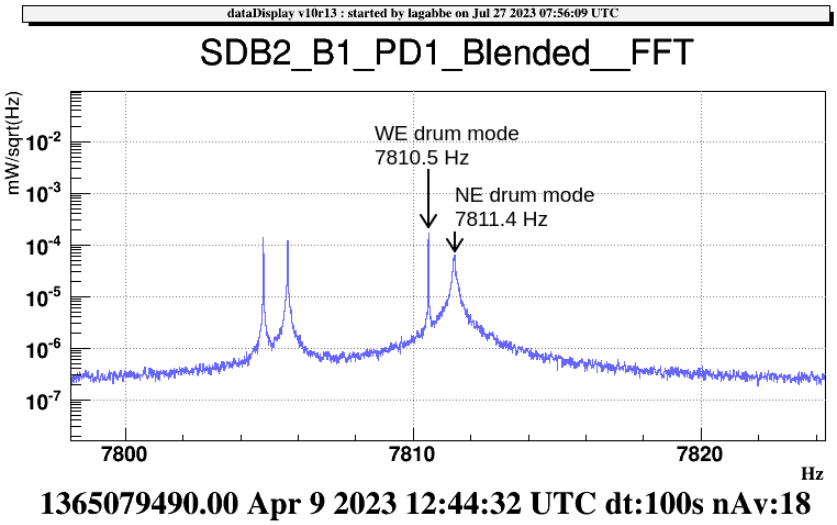

Figure 7.16: Amplitude spectral density of the output signal of the B1 photodiode around 7800 Hz, measured in April 9, 2023.

NE	1069.53	1139.53	1279.53	1409.53	1529.53	1689.53
	1839.53	2139.53	2309.53	2599.53	3249.53	3559.53
WE	1073.53	1133.53	1273.53	1403.53	1523.53	1683.53
	1833.53	2133.53	2303.53	2593.53	3243.53	3553.53

Table 7.7: List of frequencies injected by the PCal to measure the mechanical response at high frequency.

both PCal at frequencies written in table 7.7:

The transfer function from the power of the PCal laser $P_{Tx\_PD2,mir}$, with $mir \in \{NE, WE\}$ to the $DARM$ signal is computed. The transfer function is a mean of 18 transfer functions computed with 100 s long Hann windows, overlapping by 50 s. The signal $H_{PCal,mir}(f)$ is computed at each frequency for each PCal using formula (7.22), and the modulus is fitted with the O4 model expressed in formula (7.26). In order to compare the O4 model with the O3 model, the measurement of the mechanical response is also fitted with the O3 model expressed in formula (7.30).

$$H_{PCal}(f) \cdot G_{OR} = -\Gamma \cdot \left(\frac{f_n^2}{f^2}\right) + \Gamma \cdot \left(\frac{1 - \left(\frac{f_n}{f_d}\right)^2}{1 - \left(\frac{f}{f_d}\right)^2}\right) \tag{7.30}$$

The measurement of the mechanical response and the fitted functions are displayed in figure 7.17.

The fitted parameters of each model are given in tables 7.8 and 7.9:

Mirror	G_p [h/W]	G_d [h/W]	G_c [h/W]
NE	$3.5115 \pm 0.0075 \times 10^{-15}$	$-1.3 \pm 2.1 \times 10^{-22}$	$4.4 \pm 2.3 \times 10^{-22}$
WE	$3.5115 \pm 0.0075 \times 10^{-15}$	$-1.0 \pm 1.1 \times 10^{-22}$	$4.2 \pm 1.2 \times 10^{-22}$

Table 7.8: Fitted parameters of the O4 model of the mechanical response.

One can notice that the gain of the drum mode G_d in the O4 model of the mechanical response is negative. However, the uncertainty on the gain is higher than the absolute value of the gain $\sigma_{G_d} > |G_d|$. The values of the drum mode gain G_d and of the frequency independent gain G_c of the O4 model cannot be determined precisely by the measurement of the mechanical response in the bandwidth [1 kHz, 3 kHz]. So the measurement of the mechanical response has to be done again, and at frequencies higher than 3 kHz.

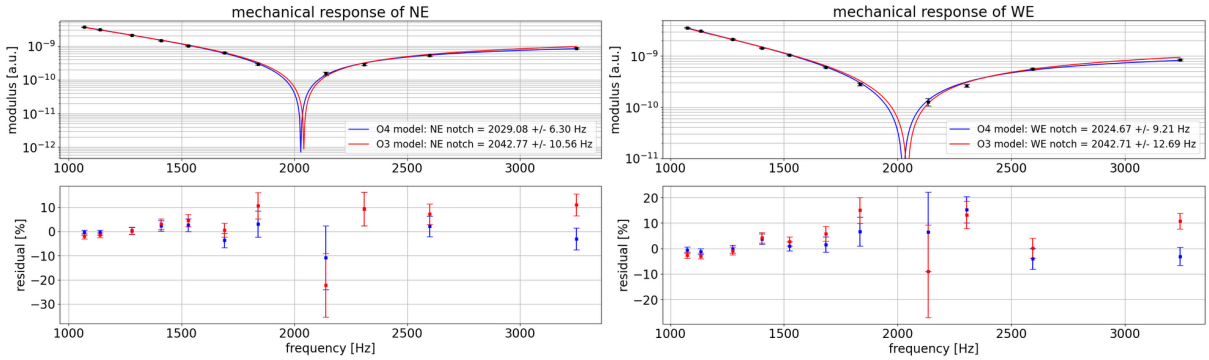

(a) NE (b) WE

Figure 7.17: Measurement of the mechanical response of the PCal NE and WE, fitted with the O3 model and with the O4 model .

Mirror	G_p [h/W]	G_d [h/W]
NE	$3.5115 \pm 0.0075 \times 10^{-15}$	$2.822 \pm 0.032 \times 10^{-22}$
WE	$3.5115 \pm 0.0075 \times 10^{-15}$	$2.834 \pm 0.045 \times 10^{-22}$

Table 7.9: Fitted parameters of the O3 model of the mechanical response.

Figure 7.18 shows the O3 and O4 models of the mechanical response of the WE PCal in the bandwidth [0.1 kHz, 10 kHz] and the frequency dependent uncertainty on the model.

The frequency dependent uncertainty is computed assuming the gain of the pendulum G_p known within $\frac{\sigma_{G_p}}{G_p} = 0.215\%$ uncertainty due to the geometrical parameters. The fitting algorithm returns a parameter vector $X = (f_n, \Gamma_p, \Gamma_d)$ and a covariance matrix $\mathbf{\Sigma^{fit}}$ of the fitted parameters. The pendulum gain G_p is added to the parameter vector so $X = (f_n, \Gamma_p, \Gamma_d, G_p)$, and the covariance matrix is written as:

$$\mathbf{\Sigma^X} = \left(\begin{array}{ccc|c} & \mathbf{\Sigma^{fit}} & & \begin{matrix}0\\0\\0\end{matrix} \\ \hline 0 & 0 & 0 & \sigma^2_{G_p} \end{array}\right) \tag{7.31}$$

The frequency dependant uncertainty is computed from the covariance matrix $\mathbf{\Sigma^X}$ and the Jacobian matrix of the mechanical response $\boldsymbol{J_H}(f) = \left(\frac{\partial H_{PCal}}{\partial X}(f)\right)_{X \in (f_n, \Gamma_p, \Gamma_d, G_p)}$ using the following equation:

$$\sigma_H(f) = \sqrt{\boldsymbol{J_H}(f) \cdot \mathbf{\Sigma^X} \cdot \boldsymbol{J_H}^T(f)} \tag{7.32}$$

The uncertainty on the O4 model for frequencies above 3 kHz is higher than the uncertainty on the O3 model, since the parameters G_d and G_c of the O4 model are not well known. However, the O3 model is biased at high frequency.

The uncertainty on the O4 model can be improved by measuring the mechanical response for frequency above 3 kHz. However, this cannot be done in July 2023 because the NE mirror has just been replaced and the interferometer is in a recovery state. Since the NE mirror has been changed, the resonant frequency of the drum mode also has changed. It has been measured at 7795 Hz in July 2023 after the replacement of NE. Thus the resonant frequency of the drum mode of both mirrors has to be measured again. Then the mechanical responses of the PCals have to be measured in the bandwidth [1 kHz, 7 kHz].

7.4 Total frequency response of the PCal

The mirror displacement induced by the PCal is computed from the measurement of the PCal laser power ΔP by the sensors. In this section, the reconstructed mirror displacement ΔL_{PCal} is defined, and the uncertainty on the mirror displacement is computed.

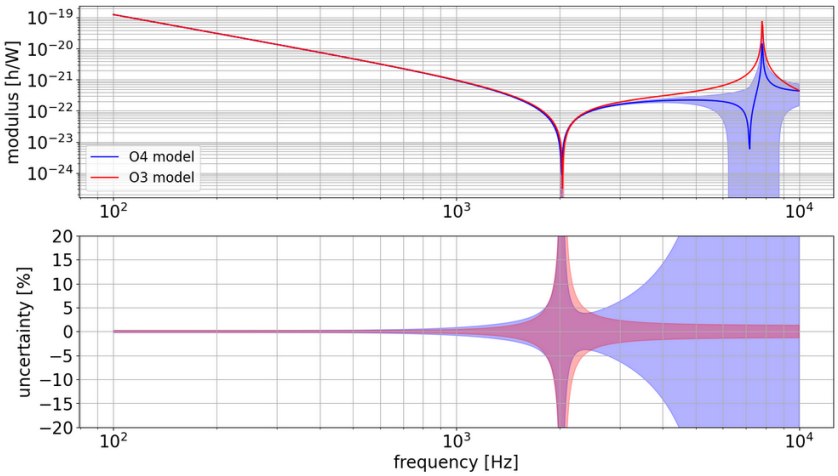

Figure 7.18: Top: Frequency responses of the O3 model and with the O4 model of the WE PCal mechanical response. Bottom: 1σ uncertainty envelope of the two models.

7.4.1 Definition of the model of the frequency response

The mirror displacement is estimated from the laser power reflected by the end mirror P_{ref}. The reflected beam passes through the viewport and is reflected by the M_3 mirror on the reflection bench of the PCal before being measured by the Rx sphere. The losses of the viewport and the M_3 mirror are called respectively $l_{vp} = 0.60\%$ and $l_{M\_3} = 0.11\%$. So the real power measured by the Rx sphere is written as:

$$P_{bench} = (1 - l_{vp}) \cdot (1 - l_{M\_3}) \cdot P_{ref} \tag{7.33}$$

The PCal power sensors (Tx_PD1, Tx_PD2 and Rx sphere) estimate the power P_{bench}, the output of each power sensors are called respectively P_{Tx_PD1}, P_{Tx_PD2} and P_{Rx}. The calibration of the Rx sphere is more stable than the calibration of the photodiodes. However the sensing noise of the photodiodes is lower than the Rx sphere. Since Tx_PD1 is used for the control loop of the PCal laser, P_{bench} is estimated from P_{Tx_PD2}. A correction factor C is applied to P_{Tx_PD2} so the average level of $C \cdot P_{Tx\_PD2}$ is the same as the average power level of the P_{Rx}. The correction factor is the mean over the ratio $C = \text{mean}\left(\frac{P_{Rx}}{P_{Tx\_PD2}}\right)$.

The frequency response of the photodiode sensing chain is corrected, using a model of the sensing chain $S_{PCal}(f)$ computed in section 7.2, in order to reconstruct the reflected power signal. The characteristics of the sensing chain response are given in table 7.4. Thus, the reflected power P_{ref} is estimated from the following formula:

$$P_{ref}(f) = (1 - l_{vp}) \cdot (1 - l_{M\_3}) \cdot P_{Tx\_PD2}(f) \cdot \text{mean}\left(\frac{P_{Rx}}{P_{Tx\_PD2}}\right) \cdot S^{-1}_{PCal}(f) \tag{7.34}$$

The mirror displacement ΔL_{PCal} induced by the PCal is computed from the reflected power using the the mechanical response $H^{O4}_{PCal}(f)$ computed as:

$$H^{O4}_{PCal}(f) = \frac{G_p}{1 + \frac{i}{Q_p}\frac{f}{f_p} - \left(\frac{f}{f_p}\right)^2} + \frac{G_d}{1 + \frac{i}{Q_d}\frac{f}{f_d} - \left(\frac{f}{f_d}\right)^2} + G_c \tag{7.35}$$

The values of the parameters of the mechanical response measured in April 2023 are given in table:

Mirror	G_p [h/W]	f_p [Hz]	Q_p [ ]	G_d [h/W]	f_d [Hz]	Q_d [ ]	G_c [h/W]
NE	3.5115×10^{-15}	0.6	10^3	-1.3×10^{-22}	7811.4	10^6	4.4×10^{-22}
WE	3.5115×10^{-15}	0.6	10^3	-1.0×10^{-22}	7810.5	10^6	4.2×10^{-22}

Table 7.10: Parameters of the mechanical response of the PCal fitted with the measurement done in April 9, 2023

Thus, the mirror displacement induced by the mirror is computed as:

$$\Delta L_{PCal}(f) = H_{PCal}(f) \cdot \Delta P_{ref}(f) \tag{7.36}$$

The power signal read by the PCal sensors are delayed by 16 µs with respect to the absolute GPS time due to the propagation time of the timing signals in the optical fibers as explained in chapter 5.2.2. This model does not correct this delay, thus the mirror displacement is also delayed by 16 µs.

7.4.2 Calibration uncertainty budget

In this chapter, we have stated all the contributions to the uncertainty on the mirror displacement ΔL_{PCal} caused by NE and WE PCals in preparation for the O4 run. The different contributions are independent from each other, so total uncertainty on the mirror displacement is computed as $\sigma_{tot} = \sqrt{\sum_i \sigma_i^2}$. Table 7.11 summarizes the frequency independent uncertainties on the estimation of the reflected power of the PCal laser by the end mirror $\sigma_{P,ref}$.

Variable	1σ uncertainty value [%]
Response of WSV	0.167
Calibration of Rx sphere	0.201
ADC sensing chain	0.190
Losses of the viewport	0.095
Losses of the M_3 mirror	0.012
Total $\frac{\sigma_{P,ref}}{P_{ref}}$	0.337

Table 7.11: List of the contribution to the uncertainty on the estimation of the reflected power of the PCal laser by the end mirror.

The uncertainty on the mirror displacement $\sigma_{\Delta L}(f)$ is estimated from the uncertainty on the reflected power $\sigma_{P,ref}$ and the frequency dependant uncertainty on the mechanical response $\sigma_H(f)$.

$$\frac{\sigma_{\Delta L}}{\Delta L_{PCal}}(f) = \sqrt{\left(\frac{\sigma_{P,ref}}{\Delta P_{ref}}\right)^2 + \left(\frac{\sigma_H}{H_{PCal}}(f)\right)^2} \tag{7.37}$$

Figure 7.19 shows the frequency dependent relative uncertainty on the mirror displacement, using the O3 and O4 models of the mechanical response. At low frequency, the value of the relative uncertainty on the mirror displacement is 0.4%. The uncertainty on the mirror displacement could be improved by doing further measurements of the mechanical response.

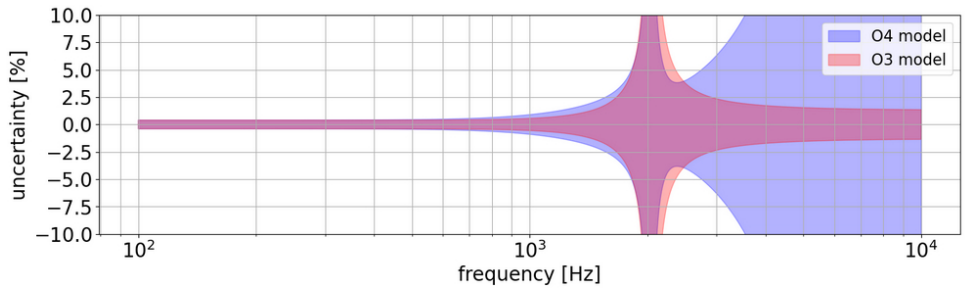

Figure 7.19: Frequency dependent relative uncertainty on the mirror displacement. The uncertainty on the mechanical response is computed using either the O3 model of the mechanical response or the O4 model .

Once the PCal optical bench are fully installed in September 2022, the PCals have been calibrated in DC with respect to the new power standard WSV in November 2022 and a second time in June 2023. The response of the sensing chain has been measured and modeled and the power losses of the viewport and of the M_3 mirror are characterized. Thus the power sensors of the PCal estimate the power of the PCal laser beam reflected by the end mirror.

The mirror displacement induced by the PCal is computed from the value of the reflected power with a model of the mechanical response. A first measurement of the mechanical response in the bandwidth [1 kHz, 3 kHz] has been done in April 2023, and a new model has been defined and fitted on this measurement. However, this model is not accurate at frequency above 3 kHz. The NE mirror has been replaced in June 2023, so the mechanical response of the NE PCal has changed, and has to be measured again.

Starting from April 2023, the electromagnetic actuators of the mirrors are calibrated using the photon calibrators. And the computation of the mirror displacement induced by the PCal is crucial for the calibration of the actuators.

Chapter 8

Actuator calibration using PCal

Contents

Introduction

In chapter 4, we have seen that the frequency responses of the electromagnetic actuators of the mirrors and marionettes are needed to reconstruct the strain signal of the interferometer. Each actuator is calibrated using an other calibrator as reference, and the photon calibrator is the main reference for the calibration. The actuators of the end mirrors and marionettes as well as the actuators of the input mirrors and marionettes are calibrated with respect to the PCal. Then, the actuator of the BS and PR mirrors are calibrated with respect to the WI mirror and the actuator of SR mirror is calibrated with respect to the NI mirror.

In this chapter, the method to calibrate the electromagnetic actuators of each mirror will be explained and the results of the calibration for the O4 run will be detailed. In this chapter, the index m represents the mirror of the interferometer $m \in \{NE, WE, NI, WI, BS, PR, SR\}$, and the index l represents the actuator level $l \in \{mirror, marionette\}$.

8.1 Overview of the electromagnetic actuators

8.1.1 Calibration response vs Reconstruction response

We have seen in section 2.3 that the electromagnetic actuators receive a correction signal Sc from the control loops of the mirror in order to keep the interferometer locked. To calibrate the electromagnetic actuators of the mirror m at the level l, a calibration signal $CAL_{m,l}$ is sent to the actuator. This calibration signal is sum to the correction signal $ctrl$ and filtered by a DSP filter, then send to the actuator. The sum of the calibration signal and correction signal is also monitored. It is filtered by an anti aliasing, the result is called $Sc_{m,l}(f)$. This signal is equal to the command signal sent to the actuator. A scheme of the electromagnetic actuators is given in figure 8.1.

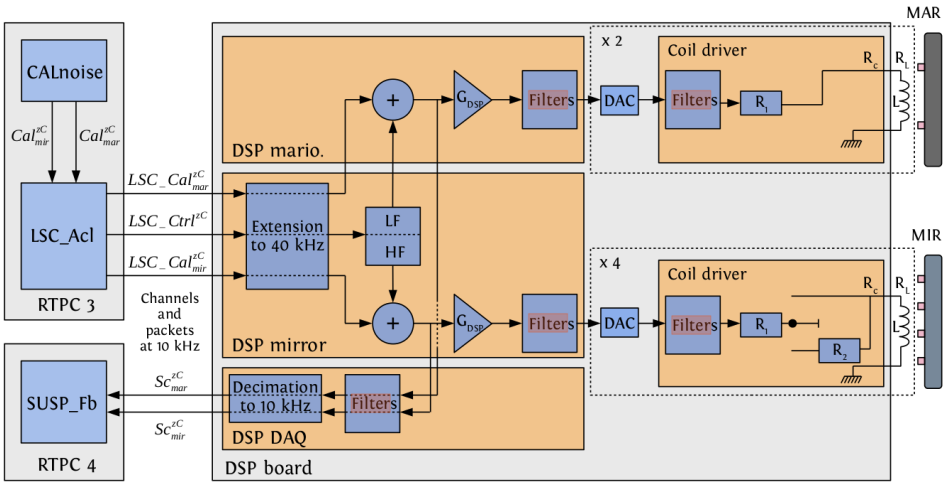

Figure 8.1: Scheme of the electronic chain of the EM actuator of the marionette and the mirror.

The frequency response $A^{CAL}_{m,l}$ is called the "Calibration response", it represents the mirror motion response ΔL_m to a calibration signal $CAL_{m,l}$ in m/V. However, as shown in chapter 4, the actuator response needed for the reconstruction is the response to a command signal $Sc_{m,l}$. We call this response the "Reconstruction response" of the actuator $A^{Sc}_{m,l}$.

$$A^{CAL}_{m,l}(f) = \left(\frac{\Delta L_m}{CAL_{m,l}}\right)(f) \tag{8.1}$$

$$A^{Sc}_{m,l}(f) = \left(\frac{\Delta L_m}{Sc_{m,l}}\right)(f) \tag{8.2}$$

The response $A^{Sc}_{m,l}$ can be written as $A^{Sc}_{m,l}(f) = A^{CAL}_{m,l}(f) \cdot TF^{CALtoSc}_{m,l}(f)$. In the bandwidth [10 Hz, 2 kHz],

$TF_{m,l}^{CALtoSc}(f)$ is modeled by a double pole the the frequency f_p^{DSP} with a simple delay τ^{DSP}.

The pole frequency f_p^{DSP} and the delay τ^{DSP} is measured by injecting a noise signal in the CAL channel, when the interferometer is unlocked, so there is no *ctrl* signal to be sum to the calibration signal. The transfer function from the CAL signal to the Sc signal is computed and fitted with the following model.

$$\left(\frac{Sc_{m,l}}{CAL_{m,l}}\right)(f) = \frac{\exp\left(-i2\pi\tau_{m,l}^{DSP} f\right)}{\left(1 + i\frac{f}{f_p^{DSP}}\right)^2} = TF_{m,l}^{CALtoSc}(f) \tag{8.3}$$

Figure 8.2 shows an example of a CAL to Sc transfer function measured on June 16 2023. The pole frequency of all the actuators is $f_p^{DSP} = 8174$ Hz and table 8.1 lists the values of each measured delay.

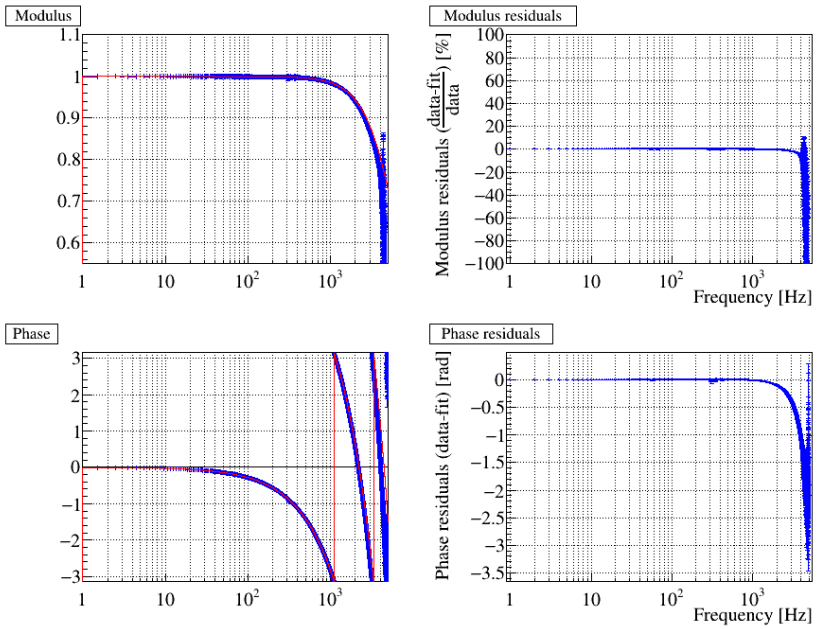

Figure 8.2: Transfer function from CAL to Sc signal of the WE mirror actuator, measured on June 16 2023

Actuator	measured delay [µs]	expected delay [µs]
NE mirror	412	412
WE mirror	412	412
NI mirror	420	412
WI mirror	421	412
BS mirror	413	412
PR mirror	420	412
SR mirror	413	412
NE marionette	470	470
WE marionette	470	470
NI marionette	470	470
WI marionette	470	470
BS marionette	472	470

Table 8.1: Value of the delay between CAL ans Sc signals measured on June 16 2023

8.1.2 Calibration method

The strain signal $h(t)$ is reconstructed in the frequency bandwidth [10 Hz, 10 kHz], from the output signal of the interferometer and from the control signals Sc of the mirror and marionette actuators. However, the mirror actuators are efficient mainly at frequency $f < 1$ kHz, because of the attenuation in f^{-2} due to the simple pendulum response. So the mirrors actuators are calibrated in the frequency bandwidth $\Delta f_{mir} = [10\text{ Hz},\ 1\text{ kHz}]$. The response of the marionette actuators are attenuated in f^{-4} due to the double pendulum response. So they are efficient at frequency $f < 100$ Hz. The calibration bandwidth of the marionette actuators is $\Delta f_{mar} = [10\text{ Hz},\ 100\text{ Hz}]$.

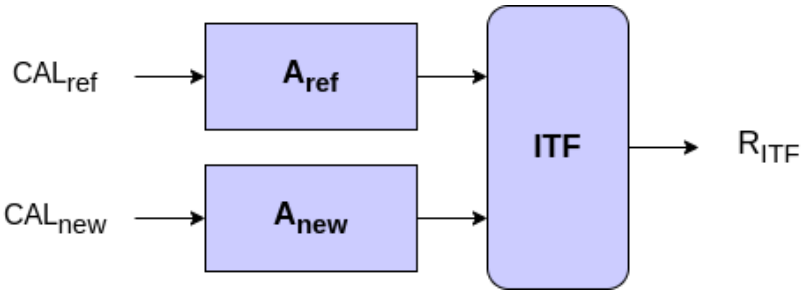

Figure 8.3: Principle diagram of the calibration transfer from one actuator to another.

Each actuator is calibrated with respect to a reference actuator, the principle diagram of the calibration transfer from the reference actuator to the actuator to be calibrated is shown in figure 8.3. To calibrate an actuator, calibration lines CAL_{new} are injected in the actuator to be calibrated and the transfer function from the calibration signal to the response of the interferometer R_{new} is computed.

The same lines CAL_{ref} are injected in the reference actuator and the transfer function from the calibration signal to the response of the interferometer R_{ref} is computed. The two transfer functions can be written as:

$$\left(\frac{R_{new}}{CAL_{new}}\right)(f) = A^{CAL}_{new}(f) \cdot O_{new}(f) \cdot \frac{1}{1 + OLTF(f)} \tag{8.4}$$

$$\left(\frac{R_{ref}}{CAL_{ref}}\right)(f) = A^{CAL}_{ref}(f) \cdot O_{ref}(f) \cdot \frac{1}{1 + OLTF(f)} \tag{8.5}$$

Where $A^{CAL}(f)$ are the frequency responses of the actuators, $O(f)$ are the optical responses of the interferometer to the mirror displacement, and $OLTF(f)$ is the open loop transfer function of the interferometer control loop. Thus, the response of the actuator can be written.

$$A^{CAL}_{new}(f) = \left(\frac{R_{new}}{CAL_{new}}\right)(f) \cdot \left(\frac{R_{ref}}{CAL_{ref}}\right)^{-1}(f) \cdot A^{CAL}_{ref}(f) \cdot \frac{O_{ref}(f)}{O_{new}(f)} \tag{8.6}$$

This response is the calibration response of the actuator $A^{CAL}_{new}(f)$. However, the reconstruction of the strain signal uses the reconstruction response of the actuator $A^{Sc}_{new}(f)$ of the actuator. The reconstruction response is computed using the CAL to Sc transfer function $TF^{CALtoSc}_{new}$ computed in the previous section.

$$A^{Sc}_{new}(f) = \left(\frac{R_{new}}{CAL_{new}}\right)(f) \cdot \left(\frac{R_{ref}}{CAL_{ref}}\right)^{-1}(f) \cdot A^{CAL}_{ref}(f) \cdot \frac{O_{ref}(f)}{O_{new}(f)} \cdot \left(TF^{CALtoSc}_{new}(f)\right)^{-1} \tag{8.7}$$

In practice, the state of the interferometer depends on the actuator to be calibrated. So, the channel used as interferometer response R, the optical responses $O(f)$ and the open transfer function of the interferometer $OLTF(f)$ differs from one state of the interferometer to another. The calibration of the each mirror will be detailed.

As seen in section 2.3, the response of the electromagnetic actuator can be divided into two parts, the contribution of the actuator itself, called the "electronic response" A^{elec}, and the contribution of the suspension system of the mirror called the "normalized mechanical response" H^{mech}. The deviations of the electromagnetic response are small compare to the $\propto f^{-2}$ attenuation of the mechanical response. Therefore, the measured frequency response of the actuator is divided by the normalized mechanical response of the mirror actuator $H^{mech}_{mir}(f)$ or the marionette actuator $H^{mech}_{mar}(f)$, with a quality factor $Q_p = 10^3$ and a resonant frequency $f_p = 0.6$ Hz.

$$H^{mech}_{mir}(f) = \frac{1}{1 + \frac{i}{Q_p}\frac{f}{f_p} - \frac{f^2}{f_p^2}} \tag{8.8}$$

$$H^{mech}_{mar}(f) = \frac{1}{\left(1 + \frac{i}{Q_p}\frac{f}{f_p} - \frac{f^2}{f_p^2}\right)^2} \tag{8.9}$$

The residual $A^{elec}_{m,l}$ is the electronic response of the actuator, it is fitted with a model which differs from an actuator to another. The reconstruction responses of the actuators $A^{Sc}_{m,l}(f)$ of the mirror m at the level $l \in \{mir, mar\}$, is the product of the mechanical response by the electronic response of the actuator:

$$A^{Sc}_{m,l}(f) = A^{elec}_{m,l} \cdot H^{mech}_{l}(f) \tag{8.10}$$

8.2 Calibration of the mirror actuators in "observation mode"

Starting from the end of April 2023, the lock of the interferometer with the end mirror actuators in LN2 mode was achieved. The first successful measurement of the frequency response of the end mirror actuator in LN2 mode was done on April 28, 2023. A second measurement has been done on May 5. The calibration of the end and input marionette actuators in LN mode was done the same days than the calibration of the end mirror actuators.

The EM actuators are calibrated in the same configuration as if the interferometer were in observing mode. When the interferometer is in observing mode, the EM actuators of the end mirrors are in the LN2 mode and their marionette are in the LN mode. However, the input mirror EM actuators are in the open mode be cause they produces a lot of noise while activated. In this configuration, the EM actuators of the input mirrors cannot be moved and the calibration of the input mirrors cannot be done at the same time as the end mirrors are calibrated. However, the EM actuators of the end mirrors and marionettes, as well as the EM actuators of the input marionettes can be calibrated. The PCals are used as reference actuators for the calibration of the end mirror and marionette actuators and for the input marionette actuators. The method to calibrate the EM actuators of the end mirror and marionette and the EM actuators of marionettes of the input mirrors with respect to to the PCals, while the interferometer is in observation mode is described in the section.

8.2.1 Method

When the interferometer is in observation mode, the channel taken as the response of the interferometer is the output signal of the B1 photodiodes. This channel monitor the differential arm length (DARM) of the interferometer, thus it is called $DARM$[1]. Lines are injected in the excitation signal $CAL_{m,l}$ of the actuators of the mirror m at level l. The transfer function from the excitation signal of the actuators $CAL_{m,l}$ to the $DARM$ signal can be written as:

$$\left(\frac{DARM}{CAL_{m,l}}\right)(f) = A^{Sc}_{m,l}(f) \cdot TF^{CALtoSc}_{m,l}(f) \cdot O_m(f) \cdot \frac{S(f)}{1 + OLTF(f)} \tag{8.11}$$

Where $O_m(f)$ is the optical response of the interferometer to the m mirror displacement, $S(f)$ is the sensing function of the B1 photodiodes and $OLTF(f)$ is the open loop transfer function of the DARM control loop.

[1] channel name: LSC_DARM

Then the same lines are injected with the PCal, and the transfer function from the power the the PCal laser $P_{PCal,m}$ to the $DARM$ signal can be written as:

$$\left(\frac{DARM}{P_{PCal,m}}\right)(f) = H_{PCal,m}(f) \cdot O_m(f) \cdot \frac{S(f)}{1 + OLTF(f)} \tag{8.12}$$

The response of the PCal $H_{PCal,m}(f)$ has been computed in section 3.1. The actuators of the end mirror and marionette are calibrated with respect to the corresponding PCal. Thus, the frequency response of the actuators of the end mirrors and marionettes $A^{CAL}_{NE,l}(f)$ and $A^{CAL}_{WE,l}(f)$ can be computed from the equation 8.7, assuming that the optical response O_m does not vary from one injection to another:

$$A^{Sc}_{NE,l}(f) = \left(\frac{DARM}{CAL_{NE,l}}\right)(f) \cdot \left(\frac{DARM}{P_{PCal,NE}}\right)^{-1}(f) \cdot H_{PCal,NE}(f) \cdot \left(TF^{CALtoSc}_{m,l}(f)\right)^{-1} \tag{8.13}$$

$$A^{Sc}_{WE,l}(f) = \left(\frac{DARM}{CAL_{WE,l}}\right)(f) \cdot \left(\frac{DARM}{P_{PCal,WE}}\right)^{-1}(f) \cdot H_{PCal,WE}(f) \cdot \left(TF^{CALtoSc}_{m,l}(f)\right)^{-1} \tag{8.14}$$

The WI marionette actuator is calibrated with respect to the WE PCal, and the NI marionette actuator is calibrated with respect to the NE PCal:

$$A^{Sc}_{NI,mar}(f) = \left(\frac{DARM}{CAL_{NI,mar}}\right)(f) \cdot \left(\frac{DARM}{P_{PCal,NE}}\right)^{-1}(f) \cdot H_{PCal,NE}(f) \cdot \left(TF^{CALtoSc}_{m,l}(f)\right)^{-1} \cdot \frac{O_{NE}(f)}{O_{NI}(f)} \tag{8.15}$$

$$A^{Sc}_{WI,mar}(f) = \left(\frac{DARM}{CAL_{WI,mar}}\right)(f) \cdot \left(\frac{DARM}{P_{PCal,WE}}\right)^{-1}(f) \cdot H_{PCal,WE}(f) \cdot \left(TF^{CALtoSc}_{m,l}(f)\right)^{-1} \cdot \frac{O_{WE}(f)}{O_{WI}(f)} \tag{8.16}$$

The response of the EM actuators of the end mirrors and marionettes, and the EM actuators of the input marionette have been measured on April 28, 2023.

8.2.2 WE and NE mirrors actuators response calibration

The frequency responses of the electromagnetic actuators of the end mirrors has been measured in the frequency bandwidth [10 Hz, 1 kHz]. Figures 8.4a and 8.4b show the measured responses of the NE and WE mirrors EM actuators $A^{Sc}_{mir}(f)$, divided by the mechanical response $H^{mech}_{mir}(f)$. The injected calibration lines are not all injected at the same time but they are injected bunch after bunch in a sequence. The optical response of the interferometer to a mirror displacement may vary from one bunch to another, which can affect the measurement of the response of the actuator.

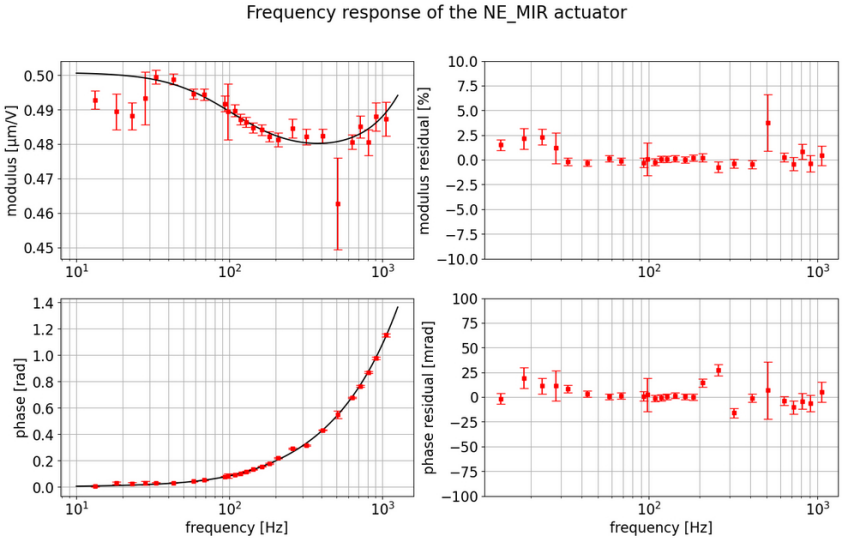

(a) NE

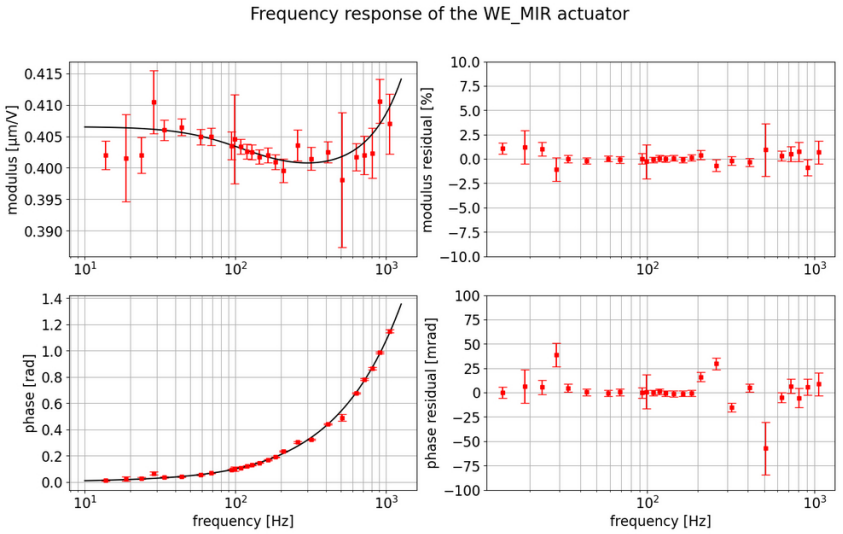

(b) WE

Figure 8.4: Electronic response of the end mirror actuator, measured on May 5 2023

The electronic response of the actuator is fitted with a model with two first order zeros, one pole and a delay:

$$A^{elec}_{NE/WE,mir}(f) = G \cdot \frac{1 + i\frac{f}{f^{elec}_{z1}}}{1 + i\frac{f}{f^{elec}_{p}}} \cdot \left(1 + i\frac{f}{f^{elec}_{z2}}\right) \cdot \exp(-2i\pi\tau^{elec} f) \tag{8.17}$$

The residual between the measured frequency response of May 5, and the model fitted on it up to ∼2%. The total actuator response of the actuator is computed by multiplying the electronic response by the mechanical response of the mirror $H^{mech}_{mir}(f)$:

$$A^{Sc}_{NE,mir}(f) = A^{elec}_{NE,mir}(f) \cdot \frac{1}{1 + \frac{i}{Q_p}\frac{f}{f_p} - \frac{f^2}{f_p^2}} \tag{8.18}$$

$$A^{Sc}_{WE,mir}(f) = A^{elec}_{WE,mir}(f) \cdot \frac{1}{1 + \frac{i}{Q_p}\frac{f}{f_p} - \frac{f^2}{f_p^2}} \tag{8.19}$$

In section 2.3, the nominal value of the mirror actuator response has been computed from the parameters of the electronic components of the actuators. The nominal and measured values of the modulus of

Measurement data	Actuator	G µm/V	f_p^{elec} Hz	f_{z1}^{elec} Hz	f_{z1}^{elec} Hz	τ^{elec} µs
April 28	NE mir	0.506 ± 0.001	117 ± 13	127 ± 14	1945 ± 229	-98 ± 9
	WE mir	0.412 ± 0.003	49 ± 11	51 ± 11	1893 ± 169	-111 ± 7
May 5	NE mir	0.5009 ± 0.0007	100 ± 8	105 ± 8	3410 ± 348	-151 ± 4
	WE mir	0.4065 ± 0.0003	112 ± 16	114 ± 16	3356 ± 316	-148 ± 4

Table 8.2: List of the parameters of the electronic response of the NE and WE mirror actuators.

the response at 100 Hz are given in table 8.3. The measured WE mirror actuator response differs by 0.7% from the nominal value whereas the measured NE mirror actuator response differs by 20%. However, the responses measured on May 5, differ by 1.7% from the response measured during O3 on NE, and 3.7% on WE. The EM actuators have not been modified between O3 and the measurements of May 5. This difference can be explained by an error on the measurement. The pole frequency at 42.3 kHz cannot be measured below 2 kHz.

Actuator	nominal	measured on May 5,	measured during O3 [6]
NE mir	1.46×10^{-5}	$1.76 \pm 0.02 \times 10^{-5}$	$1.697 \pm 0.002 \times 10^{-5}$
WE mir	1.46×10^{-5}	$1.45 \pm 0.02 \times 10^{-5}$	$1.426 \pm 0.002 \times 10^{-5}$

Table 8.3: Values of the modulus of the responses $A^{Sc}_{NE,mir}$(100 Hz) and $A^{Sc}_{WE,mir}$(100 Hz) in [µm/V] of the NE and WE mirror actuator responses, in LN2 mode, at 100 Hz.

The χ^2 associated to the fits done on April 28 are 275 on NE and 250 on WE, and the χ^2 associated to the fits done on May 5 are 138 on NE and 112 on WE. The optical responses of the NE and WE mirror were more stable during the measurements done on May 5, than during the measurement of April 28. The model fitted on the measurement of May 5, 2023 would have been used to reconstruct the strain signal. However, the NE mirror has been replaced on June 2023, so the NE mirror and marionette actuator responses measured on May 5, are no longer valid and have to be done again.

8.2.3 WE and NE marionette actuators response calibration

The actuators of the marionettes are efficient only at low frequency (<100 Hz), due to the attenuation of their mechanical response in $\propto f^{-4}$. The measurement of the electronic response of the marionette EM actuators of the end mirrors is done using the same method as for the measurement of the electronic response of the mirror EM actuators. The measured frequency response of the electronic part of the EM actuator is shown in figure 8.5.

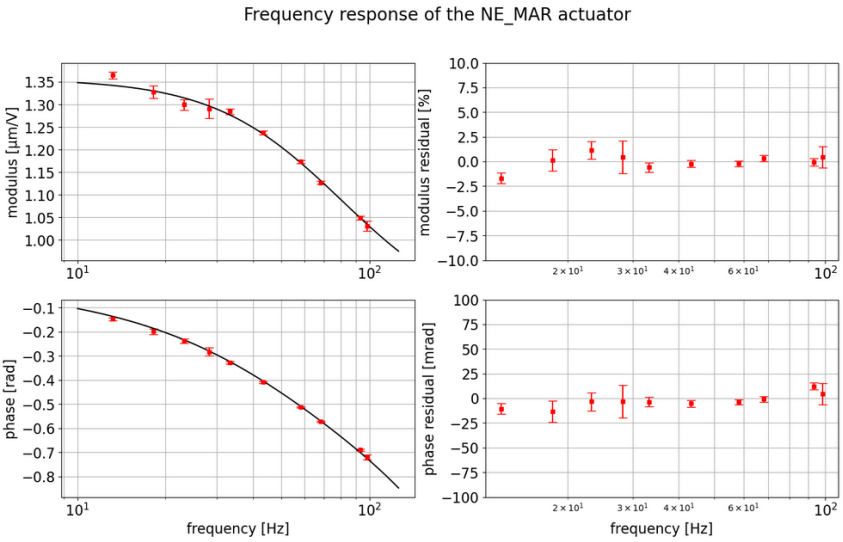

(a) NE

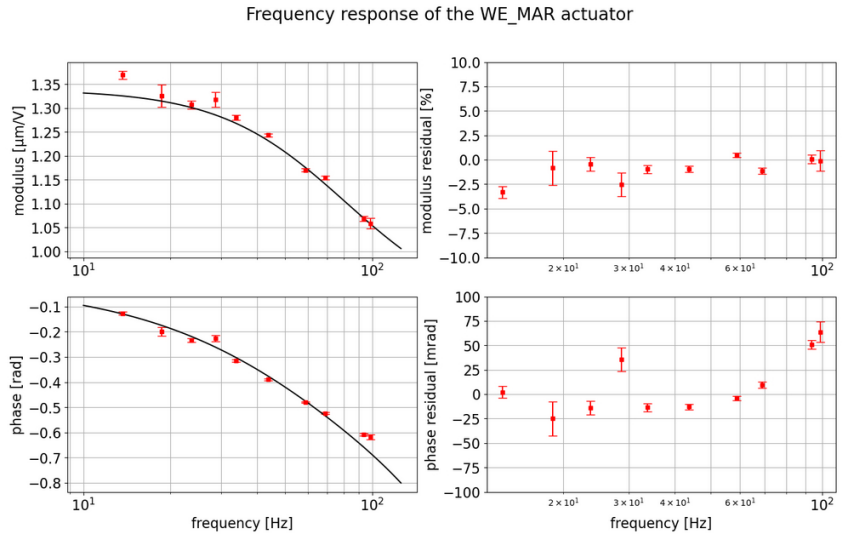

(b) WE

Figure 8.5: Electronic response of the end marionettes actuator, measured on May 5 2023

The response of the marionette is modeled with the response of a pole at the frequency f_p^{elec} with a zero at f_z^{elec} and a delay τ^{elec}:

$$A_{NE/WE,mar}^{elec}(f) = G \cdot \frac{1 + i\frac{f}{f_z^{elec}}}{1 + i\frac{f}{f_p^{elec}}} \exp(-i2\pi\tau^{elec} f) \tag{8.20}$$

The response of the marionette is measured below 100 Hz, so the value of the delay τ^{elec} cannot by fitted precisely because this parameter affects the phase of the frequency response mainly at high frequency. Since the actuator of the marionette is efficient mainly at low frequency, the value of the delay is not important. The total actuator response of the actuator is computed by multiplying the electronic response by the mechanical response of the mirror $H_{mar}^{mech}(f)$:

$$A_{NE,mar}^{Sc}(f) = A_{NE,mar}^{elec}(f) \cdot \frac{1}{\left(1 + \frac{i}{Q_p}\frac{f}{f_p} - \frac{f^2}{f_p^2}\right)^2} \tag{8.21}$$

$$A_{WE,mar}^{Sc}(f) = A_{WE,mar}^{elec}(f) \cdot \frac{1}{\left(1 + \frac{i}{Q_p}\frac{f}{f_p} - \frac{f^2}{f_p^2}\right)^2} \tag{8.22}$$

Measurement date	Actuator	G [µm/V]	f_p^{elec} [Hz]	f_z^{elec} [Hz]	τ^{elec}
April 28	NE mar	1.49 ± 0.05	45 ± 12	76 ± 18	708 ± 307
	WE mar	1.42 ± 0.05	53 ± 5	83 ± 9	687 ± 947
May 5	NE mar	1.36 ± 0.02	71 ± 7	118 ± 13	769 ± 369
	WE mar	1.37 ± 0.01	66 ± 4	103 ± 7	668 ± 358

Table 8.4: List of the parameters of the electronic response of the NE and WE marionette actuators.

As for the actuator of the mirrors, the variation of the optical response during the measurement of the response of the actuator affect the measurement. During the replacement of the NE mirror on June 2023, the actuator of the marionette has not been modified. However, the response of the marionette actuator may have been affected by the replacement of the mirror, so it has to be measured again.

8.2.4 WI and NI marionette actuators response calibration

The input marionette actuators in LN mode can also be calibrated with respect to the PCals while the interferometer is in observation mode. However, the PCals are located in front of the end mirrors, and the optical responses of the input mirrors and of the end mirrors are slightly different. As seen in section 2, the optical response of the end mirror are delayed by 10 µs due to the propagation time of the EM field across the arms. And the optical response of the input mirrors also takes into account the response of the small Michelson made with the input mirrors and the BS mirror. The ratio between the optical responses of the end mirrors over the input mirror can be written as:

$$\frac{O_{end}(f)}{O_{input}(f)} = \exp(-i2\pi\tau_{FP}f) \cdot \frac{g_0 O^{FP}(f)}{1 - g_0 O^{FP}(f)} \tag{8.23}$$

With $\tau_{FP} = 10$ µs the propagation time of the photon across the arm cavity, $g_0 \sim 288$ the arm cavity gain, and $O^{FP}(f)$ the frequency response of the arm cavity, written as:

$$O^{FP} = \frac{1}{1 + i\frac{f}{f_p}} \exp(-i2\pi\tau_p f) \tag{8.24}$$

With f_p the pole cavity to be measured in section 9, its value is around $f_p \sim 400$ Hz, and $\tau_p = -10$ µs. The frequency responses of the ratios $\frac{O_{NE}(f)}{O_{NI}(f)}$ and $\frac{O_{WE}(f)}{O_{WI}(f)}$ are plotted in figure 8.6. This ratio is estimated from the model of the optical response defined in chapter 2.1, and taken into account when the actuator of the input mirror are calibrated.

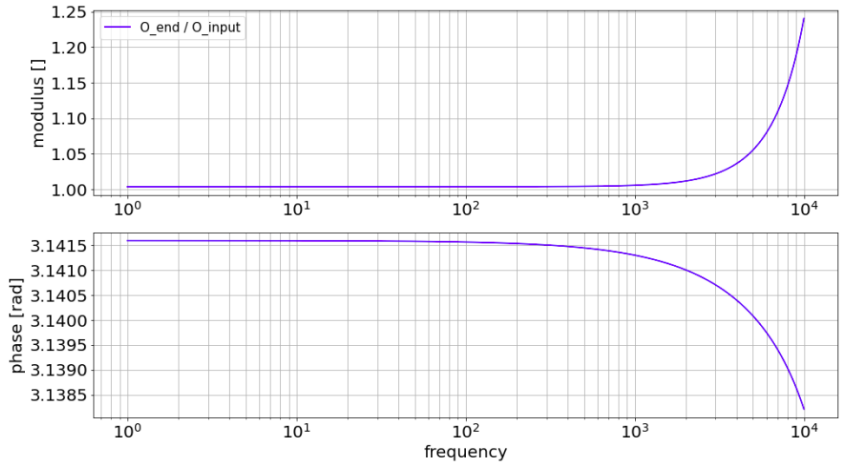

Figure 8.6: Ratio between the optical responses of NE over the optical response of NI, the modulus of the ratio at low frequency is equal to 1.0035

The factor $\frac{O_{end}(f)}{O_{input}(f)}$ is corrected in the measurement of the actuators response of the input marionette. Figure 8.7 shows the measured electronic response of the input marionette actuator done on May 5, 2023.

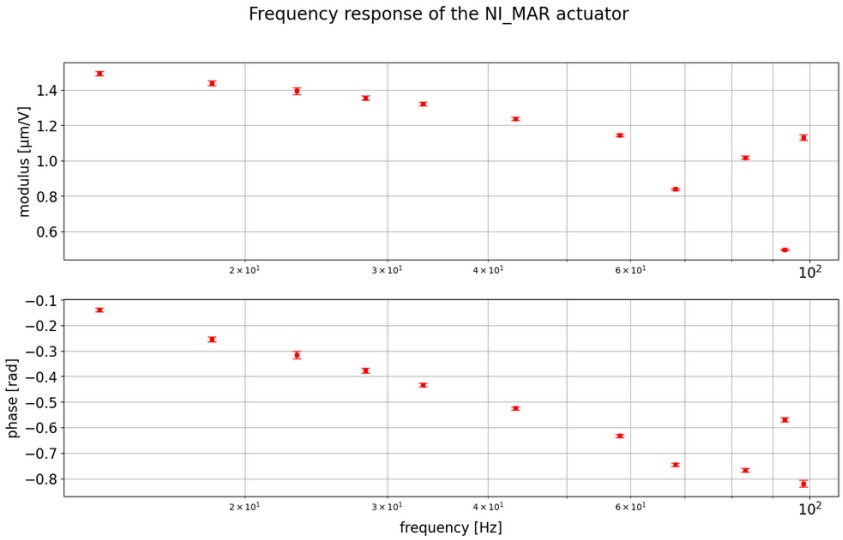

(a) NI marionette

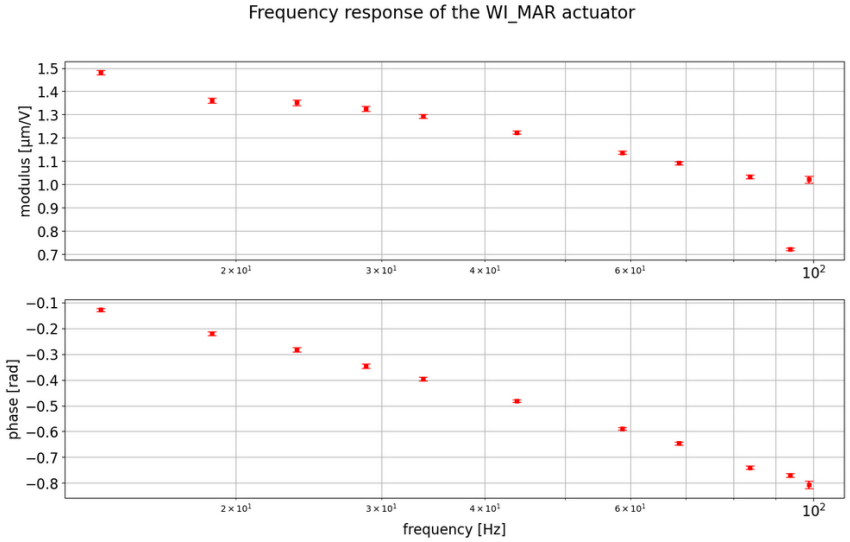

(b) WI marionette

Figure 8.7: Electronic response of the input marionettes actuator, measured on May 5 2023

Because of the high variation of the response in the frequency bandwidth [60 Hz, 100 Hz], no model has been fitted on these measurement, and further investigations will be needed if this is confirmed by future measurements. The response if the input marionette actuator is not used neither in the reconstruction of the strain signal nor in the measurement of the optical responses nor in the verification of the strain signal. The response of the input marionette actuator will be measured again after the replacement of the NE mirror.

8.3 Input mirrors calibration

If the interferometer is in observation mode, the actuators of the input mirror are open because they produce too much noise in the interferometer output signal when they are in HP mode. However, their calibration is required to calibrate the BS, PR and SR mirrors. To calibrate the input mirrors actuators, their actuators is set in HP. The observed output signal is still $DARM$. The actuators of the input mirror are calibrated with respect to the PCal. When the actuators of the input mirror are in HP mode, the actuators of the end mirrors cannot be calibrated in LN2 mode because the effect of the end mirror displacement on the $DARM$ signal is too low compared to the $DARM$ noise produced by the input mirror actuators.

8.3.1 Method

The method to calibrate the input mirrors actuators with respect to the PCal is similar to the method to calibrate the input marionette actuators. Lines are injected to the actuators of the input mirrors, the transfer function from the excitation signal $CAL_{m,mir}$, of the mirror $m \in \{NI, WI\}$ to the $DARM$ signal is written as:

$$\left(\frac{DARM}{CAL_{m,mir}}\right)(f) = A^{CAL}_{m,mir}(f) \cdot O_m(f) \cdot \frac{S(f)}{1 + OLTF(f)} \tag{8.25}$$

Then, the same lines are injected in the corresponding PCal, the transfer function from the PCal laser power $P_{PCal,m}$ to the $DARM$ signal.

$$\left(\frac{DARM}{P_{PCal,m}}\right)(f) = H_{PCal,m}(f) \cdot O_m(f) \cdot \frac{S(f)}{1 + OLTF(f)} \tag{8.26}$$

Thus, the frequency response of the input mirror actuators can be written as:

$$A^{Sc}_{NI,mir}(f) = \left(\frac{DARM}{CAL_{NI,mir}}\right)(f) \cdot \left(\frac{DARM}{P_{PCal,NE}}\right)^{-1}(f) \cdot \left(TF^{CALtoSc}_{m,l}(f)\right)^{-1} \cdot H_{PCal,NE}(f) \cdot \frac{O_{NE}(f)}{O_{NI}(f)} \tag{8.27}$$

$$A^{Sc}_{WI,mir}(f) = \left(\frac{DARM}{CAL_{WI,mir}}\right)(f) \cdot \left(\frac{DARM}{P_{PCal,WE}}\right)^{-1}(f) \cdot \left(TF^{CALtoSc}_{m,l}(f)\right)^{-1} \cdot H_{PCal,WE}(f) \cdot \frac{O_{WE}(f)}{O_{WI}(f)} \tag{8.28}$$

As for the calibration of the input marionette actuator the ratio between the optical responses of the end mirrors and input mirrors $\frac{O_{NE}(f)}{O_{NI}(f)}$ and $\frac{O_{WE}(f)}{O_{WI}(f)}$ have to be corrected. The correction fact is the same as for the input marionette actuator.

8.3.2 WI and NI mirror actuators response calibration

In May 2023, the lock of the interferometer became stable enough to use the input mirror actuator in HP mode without unlocking the interferometer. The first calibration of the input mirror actuator was done on May 11, and another calibration has been don on June 1. As for the calibration of the EM actuators of the end mirror, the input mirror actuators are calibrated with respect to the PCal, in the frequency bandwidth [10 Hz, 1 kHz]. The actuators are calibrated over the whole bandwidth in one injection, a sequence of injections is defined to calibrate the actuator. The electronic response of the actuator is shown in figure 8.8.

The electronic responses of the input mirror actuators are fitted using the following model:

$$A^{elec}_{NI/WI,mir}(f) = G \cdot \frac{1}{1 + i\frac{f}{f^{elec}_p}} \cdot \exp(-2i\pi\tau^{elec} f) \tag{8.29}$$

The values of the fitted parameters are given in table 8.5.

Measurement date	Actuator	G µm/V	f^{elec}_p Hz	τ^{elec} µs
May 11,	NI mir	0.486 ± 0.001	317 ± 1	-184 ± 1
	WI mir	0.473 ± 0.001	322 ± 2	-220 ± 2
June 1,	NI mir	0.482 ± 0.001	324 ± 2	-210 ± 1
	WI mir	0.451 ± 0.001	334 ± 2	-220 ± 1

Table 8.5: List of the parameters of the electronic response of the NI and WI mirror actuators.

The model of the input mirror actuator are not used to reconstruct h_{rec}. However, the WI mirror is used as a reference actuator for the calibration of the BS and PR mirrors actuators, and the NI mirror is used as a reference actuator for the calibration of the SR mirror. The models of the frequency response of the input mirror actuator measured on June 1 are used in the calibration of the BS, PR and SR mirror

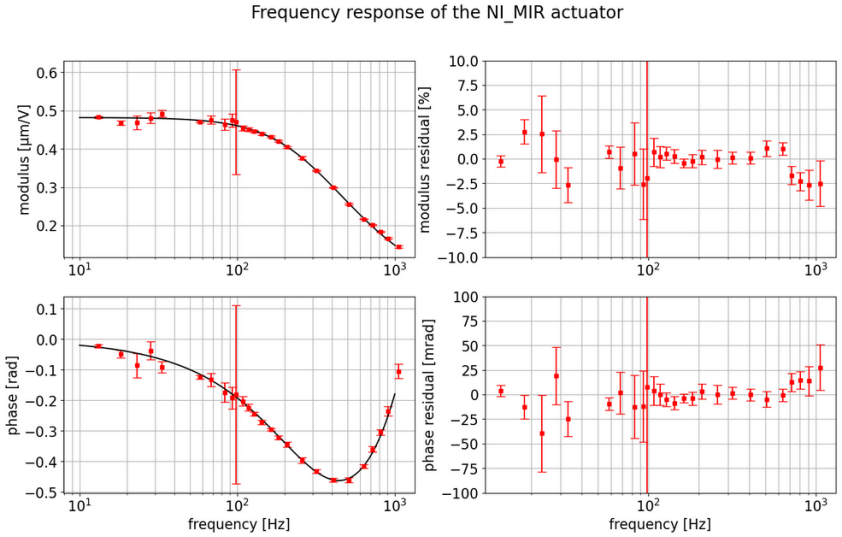

(a) NI mirror

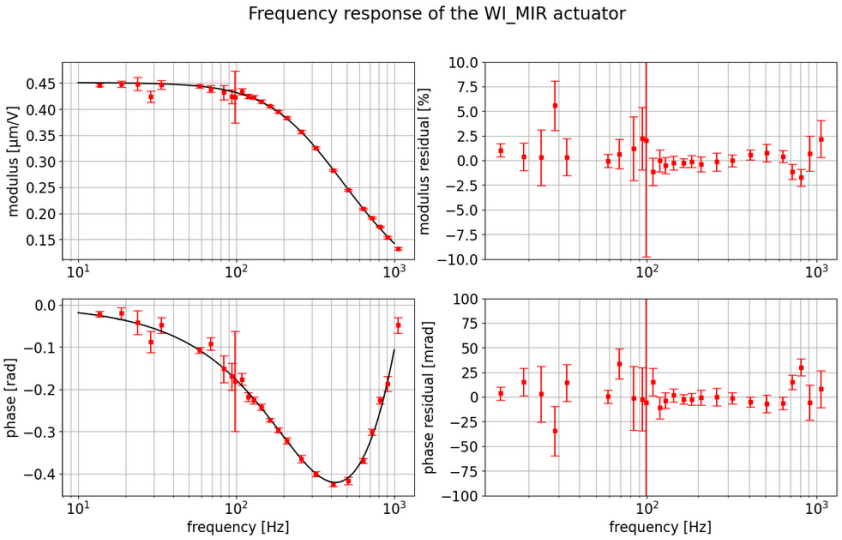

(b) WI mirror

Figure 8.8: Electronic responses of the input mirror actuators, measured on June 1 2023

actuators. The simple pole at ∼320 Hz is expected to be the simple pole of the RL circuit of the actuator in HP mode computed in section 2.3. The nominal pole frequency is 287.8 Hz. The total frequency response of the input mirror actuator is computed as:

$$A^{Sc}_{NI,mir}(f) = A^{elec}_{NI,mir}(f) \cdot \frac{1}{1 + \frac{i}{Q_p}\frac{f}{f_p} - \frac{f^2}{f_p^2}} \tag{8.30}$$

$$A^{Sc}_{WI,mir}(f) = A^{elec}_{WI,mir}(f) \cdot \frac{1}{1 + \frac{i}{Q_p}\frac{f}{f_p} - \frac{f^2}{f_p^2}} \tag{8.31}$$

The frequency response of the input mirror at 100 Hz are computed from the formula above. Their values are given in table 8.6. The values of the NI mirror actuator responses at 100 Hz differs by 19% from its nominal value, and the WI mirror actuator response differs by 14%. The values are the approximately same as the values measured during O3, the differences are contained within the uncertainties.

The χ^2 associated to the fits done on May 11, 2023 are 72 on NE and 217 on WE, and the χ^2 associated to the fits done on June 1, 2023 are 52 on NE and 58 on WE. The model fitted on the measurements of June 1, 2023 is more accurate than the model fitted on May 11, 2023, thus the model if June 1, 2023 will

Actuator	nominal	measured on June 1,	measured during O3 [6]
NI mir	1.34×10^{-5}	$1.66 \pm 0.03 \times 10^{-5}$	$1.622 \pm 0.002 \times 10^{-5}$
WI mir	1.34×10^{-5}	$1.55 \pm 0.03 \times 10^{-5}$	$1.567 \pm 0.002 \times 10^{-5}$

Table 8.6: Values of the modulus of the responses $A^{Sc}_{NI,mir}(100\text{ Hz})$ and $A^{Sc}_{WI,mir}(100\text{ Hz})$ in [µm/V] of the NI and WI mirror actuator responses, in HP mode, at 100 Hz.

be used to calibrate the BS, PR and SR mirror actuators.

8.4 BS and PR calibration

The optical responses of the BS and PR mirrors are too different from the optical response of the end mirrors to be calibrated with respect to them with the interferometer in science mode. The BS and PR mirror actuators are calibrated with respect to the WI mirror. The cavities of the interferometer are unlocked and misaligned, and only the PR cavity is locked. The PR cavity is made of the mirrors WI, BS and PR, with the actuators of the WI and PR mirrors in HP mode, and with BS in LN mode.

8.4.1 Method

Once the input mirrors actuators have been calibrated, the BS and PR mirror actuators can be calibrated with respect to the WI mirror actuator. During the calibration, the interferometer is unlocked and all the mirrors are misaligned but the BS, PR and WI mirrors, this configuration is called "PRWI". The PR cavity is locked and its length is monitored by the B4 photodiodes[2]. The output signal of the B4 photodiode is called $PRCL$. A scheme of the PR cavity in PRWI configuration is shown in figure 8.9.

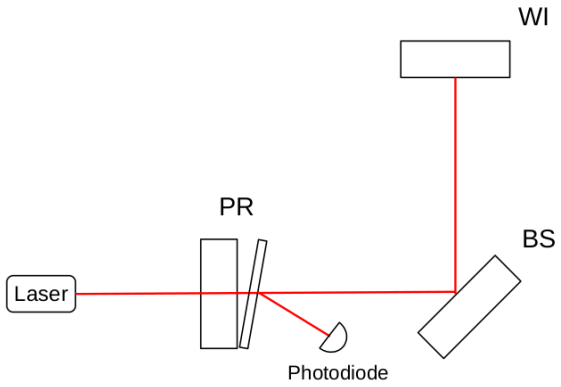

Figure 8.9: Scheme of the PR cavity in PRWI configuration used to transfer the calibration from the WI mirror to the BS and PR mirror actuators.

The transfer functions from the BS, PR and WI command signals (respectively $CAL_{BS,mir}$, $CAL_{PR,mir}$ and $CAL_{WI,mir}$) to the $PRCL$ signal are written as:

$$\left(\frac{PRCL}{CAL_{BS,mir}}\right)(f) = A^{Sc}_{BS}(f) \cdot TF^{CALtoSc}_{BS,mir}(f) \cdot O_{BS}(f) \cdot \frac{S^{B4}(f)}{1 + OLTF(f)} \tag{8.32}$$

$$\left(\frac{PRCL}{CAL_{PR,mir}}\right)(f) = A^{Sc}_{PR}(f) \cdot TF^{CALtoSc}_{PR,mir}(f) \cdot O_{PR}(f) \cdot \frac{S^{B4}(f)}{1 + OLTF(f)} \tag{8.33}$$

$$\left(\frac{PRCL}{CAL_{WI,mir}}\right)(f) = A^{Sc}_{WI}(f) \cdot TF^{CALtoSc}_{WI,mir}(f) \cdot O_{WI}(f) \cdot \frac{S^{B4}(f)}{1 + OLTF(f)} \tag{8.34}$$

[2]In practice the B4 photodiode monitor the sideband at 12 MHz.

Where $OLTF$ is the open loop transfer function of the PR cavity, O_{BS}, O_{PR} and O_{WI} are the optical responses of the cavity to a motion of the mirrors BS, PR or WI. And S^{B4} is the sensing of the B4 photodiodes. The frequency responses of the BS and PR mirrors $A^{Sc}_{BS}(f)$ and $A^{Sc}_{PR}(f)$ can be written as function of the response of the mirror actuator of WI $A^{Sc}_{WI}(f)$ which has been modeled in section 8.3.

$$A^{Sc}_{BS}(f) = \left(\frac{PRCL}{CAL_{BS,mir}}\right)(f) \cdot \left(\frac{PRCL}{CAL_{WI,mir}}\right)^{-1}(f) \cdot \frac{TF^{CALtoSc}_{WI,mir}(f)}{TF^{CALtoSc}_{BS,mir}(f)} \cdot \frac{O_{WI}(f)}{O_{BS}(f)} \cdot A^{Sc}_{WI}(f) \tag{8.35}$$

$$A^{Sc}_{PR}(f) = \left(\frac{PRCL}{CAL_{PR,mir}}\right)(f) \cdot \left(\frac{PRCL}{CAL_{WI,mir}}\right)^{-1}(f) \cdot \frac{TF^{CALtoSc}_{WI,mir}(f)}{TF^{CALtoSc}_{PR,mir}(f)} \cdot \frac{O_{WI}(f)}{O_{PR}(f)} \cdot A^{Sc}_{WI}(f) \tag{8.36}$$

The optical response of BS, PR and WI are expected to be flat in frequency, and with the same gain, so their ratios are equal to 1.

8.4.2 BS and PR mirror actuator calibration

The BS and PR mirror have been calibrated on April 17, 2023. They have been calibrated before the actuator of the end mirrors and input mirror because the PRWI configuration is easier to achieve than the full lock of the interferometer. However, the data analysis could not be done since the actuator of the WI mirror, which is the reference actuator, was not calibrated yet. In this section, the model of the WI mirror actuator response is the model computed on June 1, in section 8.3. The measured electronic responses of the BS and PR mirrors are shown in figure 8.10.

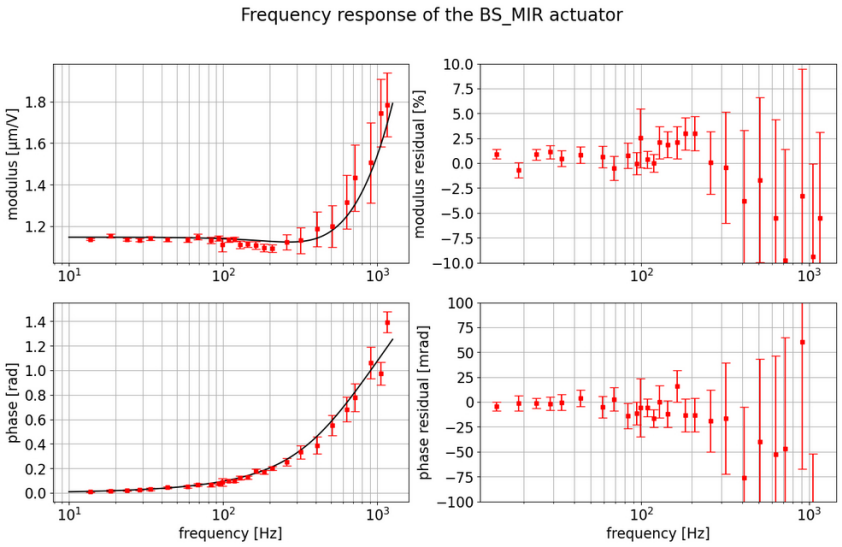

(a) BS mirror

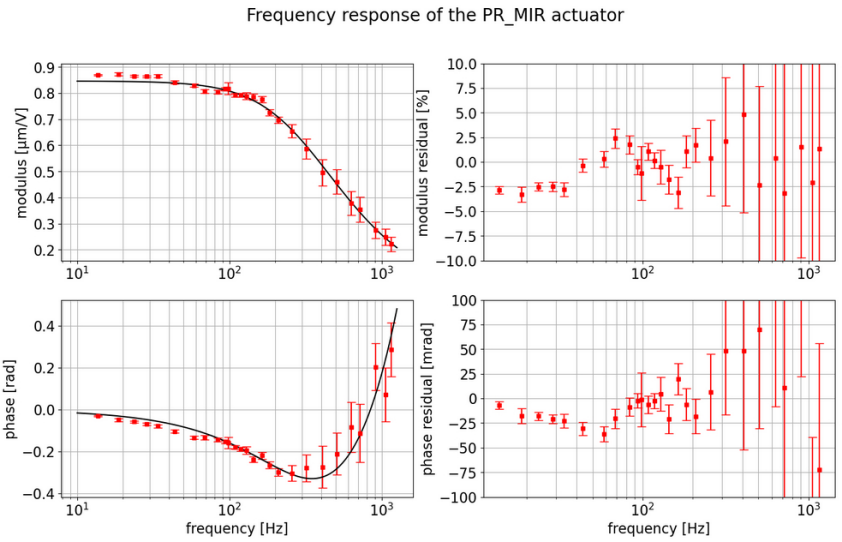

(b) PR mirror

Figure 8.10: Electronic responses of the BS and PR mirror actuators measured on April 17

The electronic responses of the BS and PR mirror actuators are modeled as:

$$A^{elec}_{BS,mir}(f) = G \cdot \frac{\left(1 + i\frac{f}{f_z^{elec}}\right)^2}{1 + i\frac{f}{f_p^{elec}}} \cdot \exp(-2i\pi\tau^{elec} f) \tag{8.37}$$

$$A^{elec}_{PR,mir}(f) = G \cdot \frac{1}{1 + i\frac{f}{f_p^{elec}}} \cdot \exp(-2i\pi\tau^{elec} f) \tag{8.38}$$

The optimal parameters are of the given in table 8.7. The pole in the electronic response of PR is expected at 267.8 Hz in section 2.3, and is measured at 319 Hz.

The models of the BS and PR actuator responses $A^{Sc}_{BS,mir}(f)$ and $A^{Sc}_{BS,mir}(f)$ are computed be multiplying the electronic responses by the mechanical response of the simple pendulum $H^{mech}_{mir}(f)$.

Actuators	G µm/V	f_p^{elec} Hz	f_z^{elec} Hz	τ^{elec} µs
BS mir	1.15 ± 0.01	379 ± 51	599 ± 55	-35 ± 7
PR mir	0.785 ± 0.007	332 ± 4	-	-228 ± 4

Table 8.7: List of the parameters of the electronic response of the BS and PR mirror actuators, fitted with the measurement of April 17.

$$A^{Sc}_{BS,mir}(f) = A^{elec}_{BS,mir}(f) \cdot \frac{1}{1 + \frac{i}{Q_p}\frac{f}{f_p} - \frac{f^2}{f_p^2}} \tag{8.39}$$

$$A^{Sc}_{PR,mir}(f) = A^{elec}_{PR,mir}(f) \cdot \frac{1}{1 + \frac{i}{Q_p}\frac{f}{f_p} - \frac{f^2}{f_p^2}} \tag{8.40}$$

These models of the actuator responses are used in the strain reconstruction algorithm and to measure the optical response of the interferometer of the BS and PR mirrors. The modulus of the actuator response at 100 Hz expected from the electronic circuits of the BS and PR mirror actuators are shown in table 8.8, with the measured value of April 17, 2023, and the values measured during O3. The modulus of the BS mirror actuator response at 100 Hz measured on April 2023, differs from its O3 value by 2%, but the two measured values differ by more than 100% from the nominal value. And the modulus of the PR mirror actuator response at 100 Hz measured on April 2023 differs from its O3 value by 3%, and differs from its nominal value by 32%. The nominal values of the BS and PR actuator responses may be not estimated properly.

Actuator	nominal	measured on April 17,	measured during O3 [6]
BS mir	1.35×10^{-5}	$3.82 \pm 0.10 \times 10^{-5}$	$3.737 \pm 0.002 \times 10^{-5}$
PR mir	5.15×10^{-5}	$2.91 \pm 0.09 \times 10^{-5}$	$2.826 \pm 0.002 \times 10^{-5}$

Table 8.8: Values of the modulus of the responses $A^{Sc}_{BS,mir}(100\text{ Hz})$ and $A^{Sc}_{PR,mir}(100\text{ Hz})$ in [µm/V] of the BS mirror actuator response in LN mode and PR mirror actuator responses in HP mode, at 100 Hz.

8.5 SR mirror calibration

The SR mirror has been added to the interferometer after the O3 run. It forms the SR cavity with the input mirrors. The SR mirror actuator also contributes to the $DARM$ signal and it is taken into account in the reconstruction of h_{rec} signal. As for the PR and BS mirror, the SR mirror actuator is calibrated using a special state of the interferometer. The SR mirror actuator is calibrated with respect to the NI mirror actuator with the interferometer.

8.5.1 Method

The SR mirror actuator is calibrated with respect to the NI mirror actuator. As for the calibration of BS and PR mirror actuators, the interferometer is set in a special configuration called "SRNI". In this configuration only the SR cavity is locked and the other mirror are misaligned. The length of the SR cavity is monitored by the photodiode B1p[3]. The output signal of the photodiode is called $SRCL$. Figure 8.11 shows the SR cavity in SRNI configuration.

The transfer functions from the BS, PR and WI command signals (respectively $CAL_{BS,mir}$, $CAL_{PR,mir}$ and $CAL_{WI,mir}$) to the $PRCL$ signal are written as:

$$\left(\frac{SRCL}{CAL_{PR,mir}}\right)(f) = A^{Sc}_{SR}(f) \cdot TF^{CALtoSc}_{SR,mir}(f) \cdot O_{SR}(f) \cdot \frac{S^{B1p}(f)}{1 + OLTF(f)} \tag{8.41}$$

$$\left(\frac{SRCL}{CAL_{WI,mir}}\right)(f) = A^{Sc}_{NI}(f) \cdot TF^{CALtoSc}_{NI,mir}(f) \cdot O_{NI}(f) \cdot \frac{S^{B1p}(f)}{1 + OLTF(f)} \tag{8.42}$$

[3]The length of the SR cavity is monitored by the DC signal.

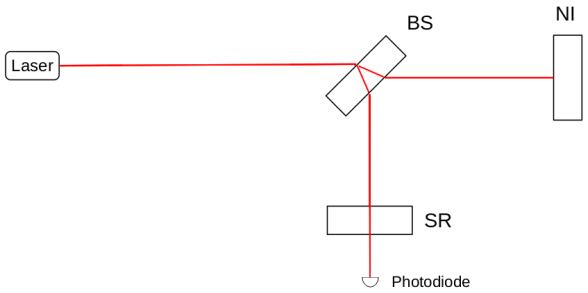

Figure 8.11: Scheme of the SR cavity in SRWI configuration used to transfer the calibration from the NI mirror to the SR mirror actuator.

With $O_{SR}(f)$ and $O_{NI}(f)$ the optical responses of SR cavity to a motion of SR and NI, $S^{B1p}(f)$ the sensing of the B1p photodiode, and $OLTF(f)$ the open loop transfer function of the SR cavity. Thus the SR mirror actuator response can be written as:

$$A^{Sc}_{SR}(f) = \left(\frac{SRCL}{CAL_{SR,mir}}\right)(f) \cdot \left(\frac{SRCL}{CAL_{NI,mir}}\right)^{-1}(f) \cdot \frac{TF^{CALtoSc}_{NI,mir}(f)}{TF^{CALtoSc}_{SR,mir}(f)} \cdot \frac{O_{WI}(f)}{O_{SR}(f)} \cdot A^{Sc}_{NI}(f) \tag{8.43}$$

The optical responses of SR and NI are the same, so the ratio $\frac{O_{WI}(f)}{O_{SR}(f)}$ is equal to 1.

8.5.2 SR mirror actuator calibration

The calibration of the SR mirror actuator has been done the same day as the calibration of the BS and PR mirror actuators. Its calibration requires the calibration of the NI mirror actuator. The measured electronic responses of the BS and PR mirrors are shown in figure 8.12.

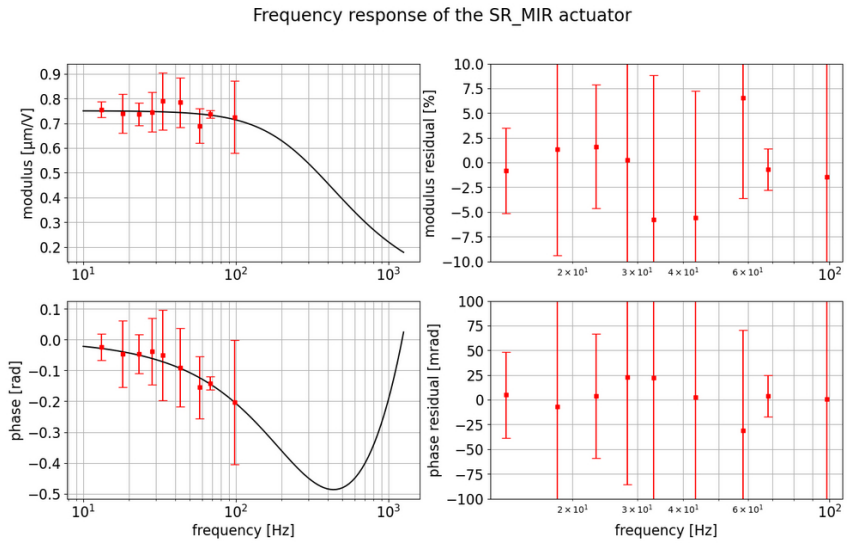

Figure 8.12: Electronic response of the SR mirror actuator, measured on April 17.

During the measurement, the injected signals and the output signal $SRCL$ were not very coherent due to a high noise level. So the error bars on the measurement are tall, and it is difficult to fit a model on it. The measurement of the SR mirror actuator response has to be done again by injecting lines with a higher SNR. The model of the response of the actuator is written as a simple pole as it is expected in HP mode.

$$A^{elec}_{SR,MIR}(f) = G \cdot \frac{1}{1 + i\frac{f}{f_p^{elec}}} \tag{8.44}$$

This model does not contain a delay The value of the parameters fitted to the measurement are given in table 8.9:

Actuator	G µm/V	f_p^{elec} Hz
SR mir	0.738 ± 0.007	517 ± 71

Table 8.9: List of the parameters of the electronic response of the SR mirror actuator, fitted with the measurement of April 17.

The SR mirror actuator model is written as the product of the electronic response by the mechanical response H^{mech}_{mir} of the mirror:

$$A^{Sc}_{SR,mir}(f) = A^{elec}_{SR,mir}(f) \cdot \frac{1}{1 + \frac{i}{Q_p}\frac{f}{f_p} - \frac{f^2}{f_p^2}} \tag{8.45}$$

The model of the SR mirror actuator responses is used in the strain reconstruction algorithm and to measure the optical response of the interferometer of the SR mirror. Table 8.10 shows the values of the response modulus computed at 100 Hz with the measured model and with the nominal model. The measured actuator response modulus differs from its nominal value by 25%. Which is above the uncertainty on the measurement, so the nominal value may be biased.

Actuator	nominal	measured on April 17
SR mir	3.50×10^{-5}	$2.61 \pm 0.21 \times 10^{-5}$

Table 8.10: Values of the modulus of the response $A^{Sc}_{SR,mir}(100\text{ Hz})$ in [µm/V] of the SR mirror actuator response in HP mode, at 100 Hz.

Conclusion

In spring 2023, the lock of the interferometers became easier to achieve and lasted for longer periods. Starting from April 2023, the lock of the interferometer became stable enough to start calibrating the actuators. The first actuators that were calibrated are the BS, PR and SR mirror actuators because their calibration does not require a full interferometer lock. By the end of April, the full lock of the interferometer was achieved and the mirror and marionette actuators of the end mirrors and input mirrors were calibrated with respect to the PCal. Due to interferometer response variations, the measured frequency response of the end mirror and marionettes actuators is distorted. Also the errors on the measurements are high due to the noise on the $DARM$ signal. The measurements of the actuator responses have to be done again when the interferometer is more stable.

However, one or two successful measurements have been done for each configuration The actuators are calibrated with respect to the photon calibrator which has been calibrated in power. As seen in chapter 7, the time series of the mirror displacement induced by the PCal is delayed by 16 µs due to the propagation time of the timing signal in the fibers, so the mirror displacement compute from the model of the EM actuators are also delayed by 16 µs. This delay has to be corrected when the strain signal is reconstructed, but the calibration of the optical response can be done without correcting this delay.

In June 2023, the NE mirror has been replaced in order to reduce a thermal noise measured in the interferometer. The replacement of the NE mirror may have changed the response of the NE mirror actuator so the NE mirror actuator needs to be calibrated again.

The calibration of the actuators needs to be repeated several times in order to monitor its stability, and to compute averages of the responses to be used in the reconstruction in prevision of the Virgo O4 run.

Chapter 9

Measuring the interferometer optical response

Contents

Introduction

In chapter 8, we have shown how the different electromagnetic actuators have been calibrated from the PCal. The other models needed in the reconstruction of the strain signal are the optical responses of the interferometer to the motion of the mirrors. As seen in chapter 4, the optical responses to a displacement of the mirrors NE, WE, BS, PR and SR are needed to reconstruct the interferometer strain signal. We have built the theoretical models of the optical response in section 2.1. However, these models are made with the strong assumption that the mirrors of the interferometer are perfectly aligned and that the different optical cavities are at their resonant points. In practice, a slight misalignment of the mirrors can change drastically the optical responses of the interferometer. Thus, the optical responses are measured, and modeled.

In the chapter, the methods to compute the optical response of each mirror will be described as well as the model fitted to the measurements.

9.1 Optical response measurement method

9.1.1 DARM control loop

The optical response is the variation of the laser power at the output port of the interferometer as function of the displacement of the mirror. The longitudinal positions of the end mirrors are controlled to keep the interferometer in dark fringe mode (+ DARM offset). This control loop is named "DARM control loop", and it is schematized in figure 9.1.

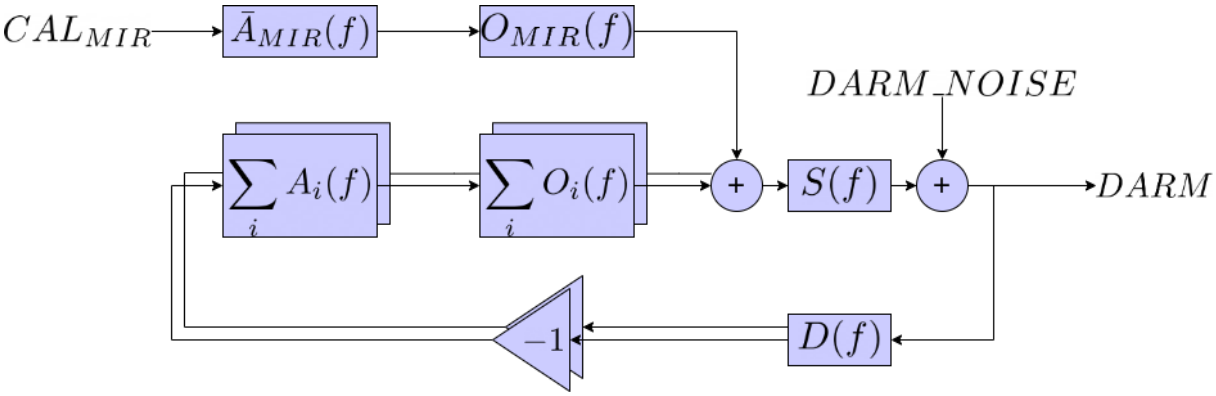

Figure 9.1: Scheme of the DARM control loop.

When an excitation signal CAL_{mir} is applied on the actuator of the mirror mir, the mirror is moved by $\Delta L_{mir} = A_{mir} \cdot CAL_{mir}$ where A_{mir} is the response of the actuator of the mirror. The variation of the output laser power is seen by the B1 photodiodes with a sensing function $S_{DARM}(f)$. The output signal of the photodiodes is used to compute the $DARM$ signal. The $DARM$ signal is taken as the error signal of the DARM control loop. The $DARM$ signal is filtered by a digital filter $D(f)$ and sent to the end mirror and marionette actuators $A_i(f)$, with $i \in \{NE, WE\}$. The optical responses to the end mirrors displacement are called $O_i(f)$.

A signal can be injected directly in the DARM control loop with the $DARM\_NOISE$ channel. This channel is added to the output signal of the B1 detector, the sum of the $DARM\_NOISE$ with the output signal of the B1 photodiode is the $DARM$ signal.

9.1.2 Method

The measurement of the optical response $O_{mir}(f)$ of the interferometer to a mirror mir displacement is done in 2 steps.

In the first step, a command signal CAL_{mir} is injected to the mirror actuator. This command signal can be either a sum of sinusoidal signals or a noise signal. The transfer function from the command signal to the $DARM$ signal is computed. The transfer function is the mean over $N_{TF} = 24$ transfer functions computed using Hann windows 10 s long, overlapping over 5 s. Only the samples with a coherence over 0.9999 are kept. This transfer function is the closed loop function of the DARM control loop, and it is written as:

$$\left(\frac{DARM}{CAL_{mir}}\right)(f) = \frac{A_{mir}(f) \cdot O_{mir}(f) \cdot S_{DARM}(f)}{1 + OLTF(f)} \tag{9.1}$$

Where $OLTF(f)$ is the open loop transfer function of the DARM loop, it is written as:

$$OLTF(f) = D(f) \cdot \sum_{i \in \{NE,WE\}} \left(A_i^{mir}(f) + A_i^{mar}(f)\right) \cdot O_i(f) \cdot S_{DARM}(f) \tag{9.2}$$

In the second step, the open loop transfer function is measured by injecting the same signal directly on the DARM loop. The command signal is named $DARM\_NOISE$. The transfer function from $DARM\_NOISE$ to $DARM$ gives us the open loop transfer function.

$$\left(\frac{DARM}{DARM\_NOISE}\right)(f) = \frac{1}{1 + OLTF(f)} \tag{9.3}$$

Thus, the optical response can be computed from these two transfer functions using the following formula:

$$O_{mir}(f) = \left(\frac{DARM}{CAL_{mir}}\right)(f) \cdot \left(\frac{DARM}{DARM\_NOISE}\right)^{-1}(f) \cdot A_{mir}^{-1}(f) \cdot S_{DARM}^{-1}(f) \tag{9.4}$$

The responses of the mirror actuator $A_{mir}(f)$ and of the B1 photodiode sensing $S_{DARM}(f)$ have to be known to compute the optical response. The model of the actuator response computed in chapter 8 is used, and the photodiode sensing is modeled as a simple delay of 245 µs as shown in the following section.

9.1.3 Sensing of the B1 photodiodes

The $DARM$ signal is computed from the output signals of the B1 photodiodes, which are connected to a DAqBox. To model the optical responses, the frequency response of the sensing chain of the photodiodes has to be computed as well as the transfer function from the B1 photodiodes output to the $DARM$ signal. The combination of these two frequency responses is called $S_{DARM}(f)$.

The B1 power is estimated by two photodiodes "B1_PD1" and "B1_PD2", and each photodiodes has three output signals named DC, $Audio$ and RF. The DC signal has a bandwidth from DC to 100 kHz, the $Audio$ signal is from 5 kHz to 100 kHz and is less noisy than the DC signal, and the RF signal is from 1 MHz to 100 MHz, but it is not used in the $DARM$ signal. The two signals DC and $Audio$ are read by a "Service mezzanine" of a DAqBox [3]. The sensing chain of the service mezzanine is composed by:

- The analog filter
  - For the DC channel: a 3^{rd} order Butterworth analog filter with a cut-off at 20 kHz.
  - For the $Audio$ channel: a 5^{th} order Butterworth analog filter with a cut-off at 80 kHz.
- The ADC chip which samples the signal at 1 MHz.
- A 8^{th} order Butterworth digital filter with a cut-off at 37.5 kHz (-20 dB at 50 kHz).
- The decimation to 100 kHz, which advance the signal of 9 µs

The output signal of the DAqBox is sent to the RTPC by packets at 10 kHz, which cause a delay of ∼100 µs. The signals *DC* to *Audio* are filtered and decimated to 20 kHz, and are blended together to create the "*Blended* signal". A scheme of the chain is shown in figure 9.2. The timing of the *Blended* signal has been measured at 130 ± 6 µs

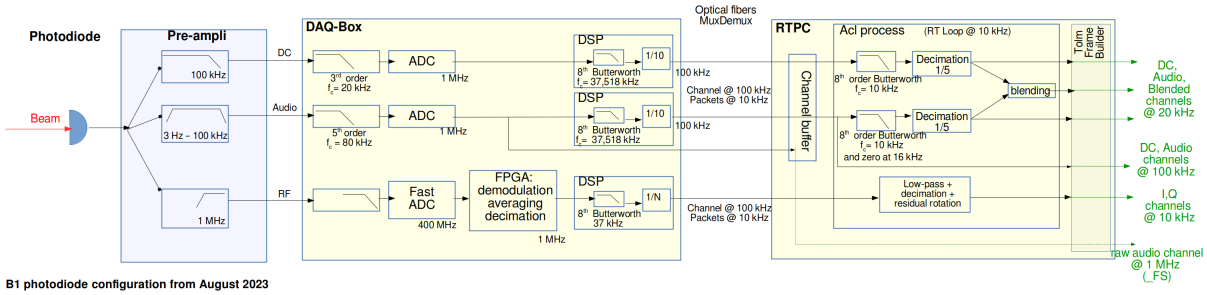

Figure 9.2: Scheme of the sensing chain of the B1 photodiodes

The *Blended* signals of both photodiodes are summed and the result is send in the DARM control loop in another RTPC, where this signal is called *DARM*. The transfer function from the *Blended* signals of each photodiode to the *DARM* signal is shown in figure 9.3. The timing measured between the *Blended* signal and the *DARM* signal is 115 ± 2 µs. The gain of the transfer functions $G_s = 0.970 \pm 0.002$ W/W.

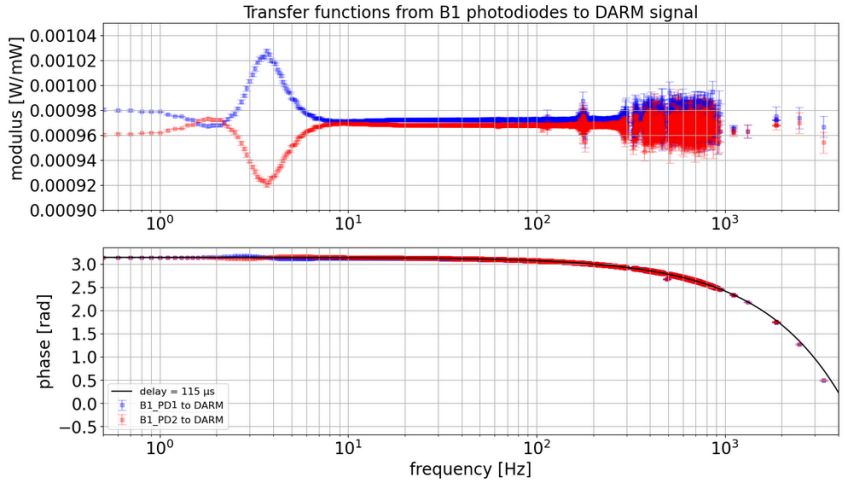

Figure 9.3: Transfer functions of the *blended* signals of the B1 photodiodes to the DARM signal.

The total sensing chain of the *DARM* signal can be modeled as a simple delay $\tau_s = 245 \pm 6$ µs with a gain $G_s = 0.970$. This model is used to compute the optical response of the interferometer to a mirror displacement.

$$S_{DARM}(f) = G_s \cdot \exp(-2\pi \cdot \tau_s \cdot f) \tag{9.5}$$

9.2 Results of the optical response measurements

9.2.1 Response to the motions of NE, WE and BS mirrors

The optical responses of the NE, WE and BS mirrors have been measured during calibration shifts on May-June 2023. The measured optical response of the NE, WE and BS mirror are written as:

$$O_{NE}^{(meas)}(f) = \left(\frac{DARM}{CAL_{NE}}\right)(f) \cdot \left(\frac{DARM}{DARM\_NOISE}\right)^{-1}(f) \cdot A_{NE}^{-1}(f) \cdot S_{DARM}^{-1}(f) \tag{9.6}$$

$$O_{WE}^{(meas)}(f) = \left(\frac{DARM}{CAL_{WE}}\right)(f) \cdot \left(\frac{DARM}{DARM\_NOISE}\right)^{-1}(f) \cdot A_{WE}^{-1}(f) \cdot S_{DARM}^{-1}(f) \tag{9.7}$$

$$O_{BS}^{(meas)}(f) = \left(\frac{DARM}{CAL_{BS}}\right)(f) \cdot \left(\frac{DARM}{DARM\_NOISE}\right)^{-1}(f) \cdot A_{BS}^{-1}(f) \cdot S_{DARM}^{-1}(f) \tag{9.8}$$

The transfer functions are computed using 10 s long Hann windows, overlapping over 5 s. The mean over 60 s of the transfer functions is computed to measure the optical responses, and only the samples where the coherence of the transfer function is above 0.9 are kept for the measurement. Figures 9.4, 9.5 and 9.6 show the measured optical responses of NE, WE and BS and the fitted models, the parameters of the fit are given in table 9.1.

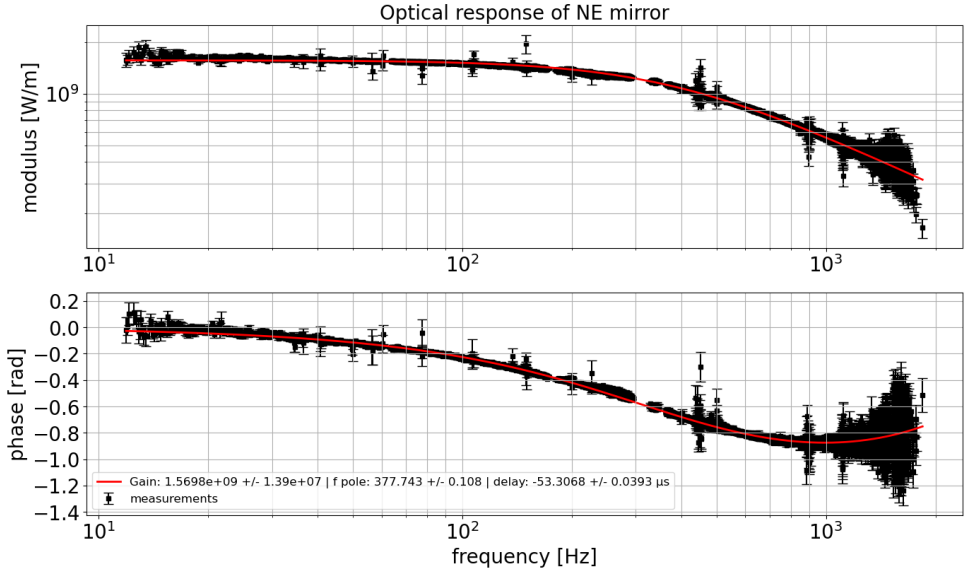

Figure 9.4: Measurement of the optical response of the NE done on June 1 (1^{st} measurement), 2023.

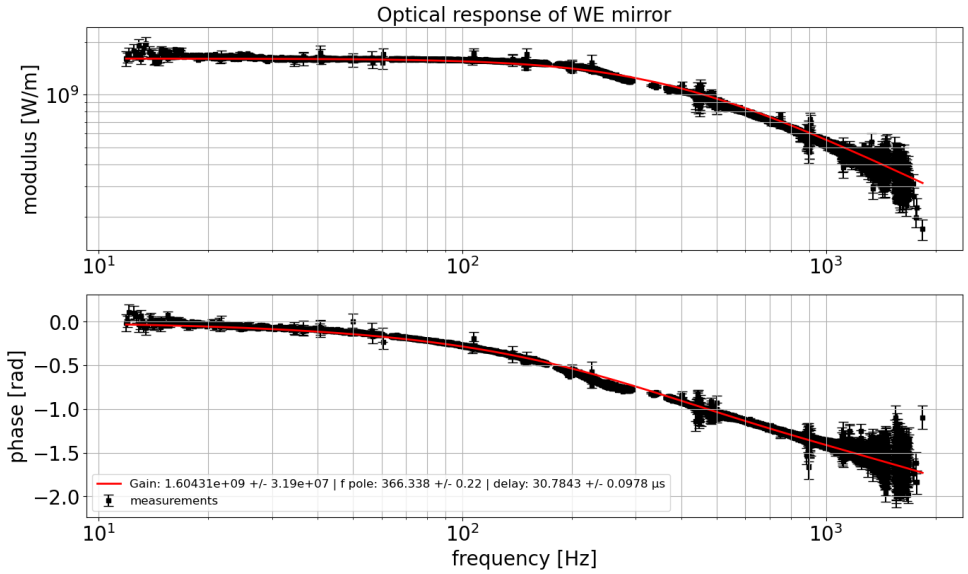

Figure 9.5: Measurement of the optical response of the WE done on June 1 (1^{st} measurement), 2023.

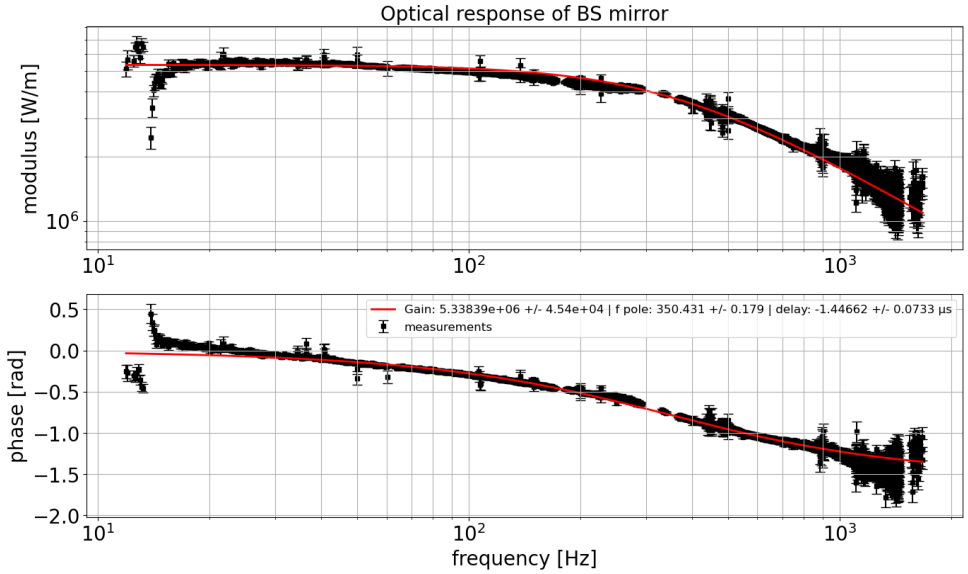

Figure 9.6: Measurement of the optical response of the BS done on June 1 (1^{st} measurement), 2023.

The transfer functions are coherent in the bandwidth [10 Hz, 2 kHz]. As seen in chapter 2.1, the optical responses of NE, WE and BS can be approximated with a simple pole response in the frequency bandwidth. The model used to fit the optical response cavity is written as follow:

$$O_{mir}^{(model)}(f) = \frac{G_{mir}}{1 + i\frac{f}{f_p}} \cdot \exp(-2\pi \cdot \tau \cdot f) \tag{9.9}$$

The parameters to be fitted are the gain G_{mir}, the pole frequency f_p and the delay τ. The values of the fitted parameters are given in table 9.1.

Measurement	Mirror	G_{mir}	f_p	τ
June 1, 2023: 1^{st} measurement	NE	$1.57 \pm 0.01 \times 10^9$ W/m	378 ± 1 Hz	-53 ± 1 µs
	WE	$1.60 \pm 0.03 \times 10^9$ W/m	366 ± 1 Hz	31 ± 1 µs
	BS	$5.34 \pm 0.05 \times 10^6$ W/m	350 ± 1 Hz	-1 ± 1 µs
June 1, 2023: 2^{nd} measurement	NE	$1.55 \pm 0.02 \times 10^9$ W/m	389 ± 1 Hz	-48 ± 1 µs
	WE	$1.54 \pm 0.01 \times 10^9$ W/m	386 ± 1 Hz	23 ± 1 µs
	BS	$5.11 \pm 0.04 \times 10^6$ W/m	375 ± 1 Hz	8 ± 1 µs

Table 9.1: Values of the parameters fitted to the measurements of the optical response done on June 1, 2023

The gain of the optical response of BS is ∼300 times lower the the gain of the optical response of NE and WE, which is expected because the gain of the NE and WE optical responses is amplified by the arm cavities as shown in section 2.1. The pole frequency of the three optical response is the same within 30 Hz of uncertainty. Figure 9.7 shows the evolution of the pole frequencies of the responses of NE, WE and BS during the measurement of June 1, computed by the reconstruction algorithm as explained in section 4.1.3. The values of the poles of the optical responses measured with the noise injection are compatible with the values computed by the reconstruction algorithm which were varying between 350 and 400 Hz during the measurement.

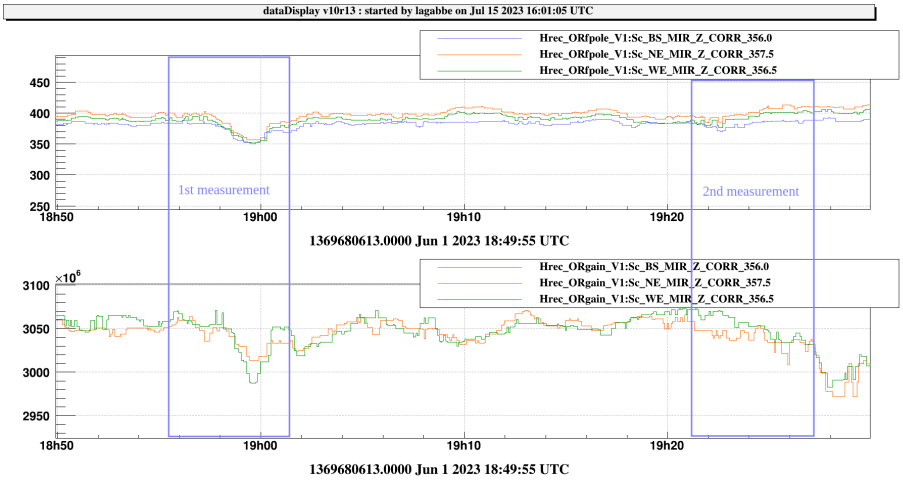

Figure 9.7: Pole frequency and gain of the optical response estimated by the optical response monitoring algorithm of the reconstruction pipeline. There is a factor $2 \times G_s = 1.94$ on the gain because the $DARM$ signal is the mean of the two photodiodes at B1, whereas the h_{rec} is computed from the sum of the two photodiodes.

The fitted delays are different on each mirror (∼-50 µs on NE, ∼20 µs on WE and ∼0 on BS). A delay of 10 µs is expected in the optical response of the end mirrors due to the propagation of the electromagnetic wave in the arm cavity. This delay is not present in the optical response of BS. The difference between the expected and the measured delay in the optical response of the end mirror may be due to a bad estimation of the $\left(\frac{Sc}{CAL}\right)$ transfer function of the end mirrors. During the next measurement of the optical response, the transfer function $\left(\frac{Sc}{CAL}\right)$ has to be measured more precisely.

9.2.2 Response to the motions of the SR mirror

The SR mirror has been added to the interferometer after the end of the O3 run. So its optical response has never been measured before. The measurement method is the same as for the measurement of the optical responses of the NE, WE and BS mirrors. However, the contribution of the SR mirror motions to the $DARM$ signal is expected to be weak. So the amplitudes of the SR mirror motions have to be high enough to make its contribution visible in the output signal of the interferometer. In order not to unlock the interferometer, the optical responses are measured by injecting lines instead of a broadband noise. The optical responses of SR has been measured on May 11, June 1 and on July 21 2023. The measured optical response of SR is computed from formula 9.4, it is expressed as:

$$O_{SR}^{(meas)}(f) = \left(\frac{DARM}{CAL_{SR}}\right)(f) \cdot \left(\frac{DARM}{DARM\_NOISE}\right)^{-1}(f) \cdot A_{SR}^{-1}(f) \cdot S_{DARM}^{-1}(f) \tag{9.10}$$

The three measurements of the optical response of SR are shown in figure 9.8.

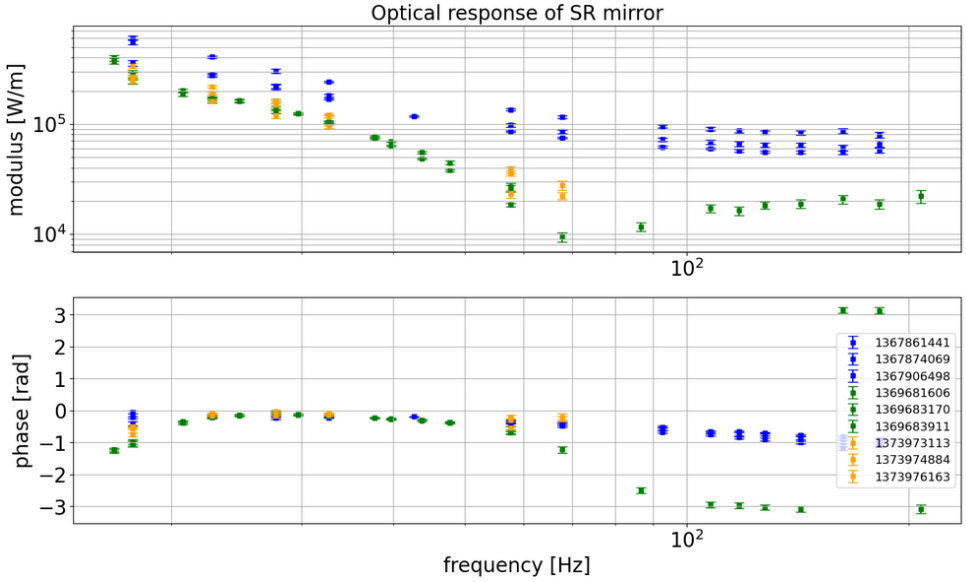

Figure 9.8: Measurement of the optical responses of SR. The three measurements were done on May 11, 2023 on June 1, 2023 and on July 21, 2023

The optical response of SR is too unstable to be modeled properly. However, as shown in [29], SR contributes to the $DARM$ signal mainly in the bandwidth [10 Hz, 80 Hz], so the optical response model has to be accurate only in this bandwidth. Figure 9.9 shows simulations of the optical responses of SR.

In this simulation, the optical response of SR decreases as $\propto f^{-2}$ at low frequency, and this seems to be confirmed in the measurements. So the optical response of SR is modeled as a double integrator with a delay. The model can be written as:

$$H_{SR}^{(model)}(f) = \frac{G_{SR}}{(i2\pi f)^2} \cdot \exp(-i2\pi\tau f) \tag{9.11}$$

Where G_{SR} is the gain and τ is the delay. The parameters of the model will be continuously monitored in h_{rec} by injecting a permanent line at 62.0 Hz on SR.

9.2.3 Response to the motion of PR mirror

During the O3 run, the optical response of PR mirror was subtracted modeling the optical response by a simple pole response. In reality, the optical responses of PR is more complex. In section 2.1, we have seen that the output power of the interferometer does not depend on the position of the PR mirror. However, in section 2.1, the coupling between the PR cavity and the arm cavities are neglected. In practice, the PR cavity is coupled with the arm cavity and a motion of the PR mirror induces a variation of the output power of the interferometers. The contribution of the PR and SR mirrors to the $DARM$ signal are faint

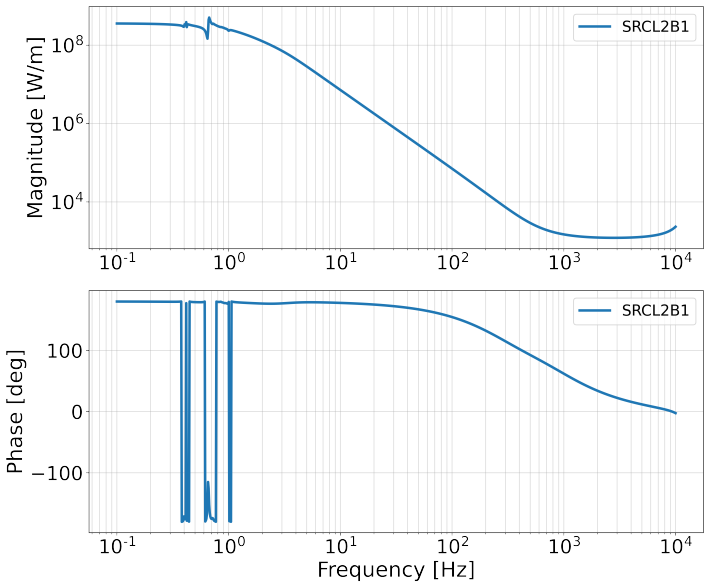

Figure 9.9: Simulation of the optical responses of the SR mirror.
Source [29]

compared to NE, WE and BS. So the precision of the optical responses of PR and SR is not as crucial as the optical responses of the other mirrors. The measured optical response of the PR mirror is written as:

$$O_{PR}^{(meas)}(f) = \left(\frac{DARM}{CAL_{PR}}\right)(f) \cdot \left(\frac{DARM}{DARM\_NOISE}\right)^{-1}(f) \cdot A_{PR}^{-1}(f) \cdot S_{DARM}^{-1}(f) \tag{9.12}$$

The optical response of PR was measured during the same shifts as the optical response of SR. As for the SR optical response, the PR optical response is measured by injecting lines. Figure 9.10 shows the measurements of the PR optical response.

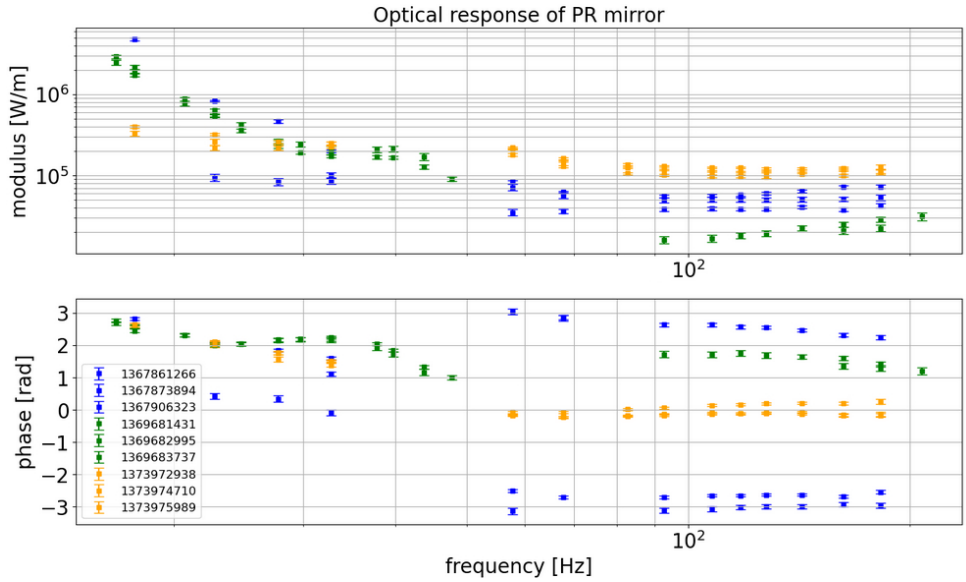

Figure 9.10: Measurements of the optical response of the PR. The three measurements were done on May 11, 2023 on June 1, 2023 and on July 21, 2023

The optical response of PR has also been simulated in [29]. The simulation is shown in figure 9.11. The simulated optical response does not seem to match with any of the measured optical response. The

optical response of PR is not yet well understood.

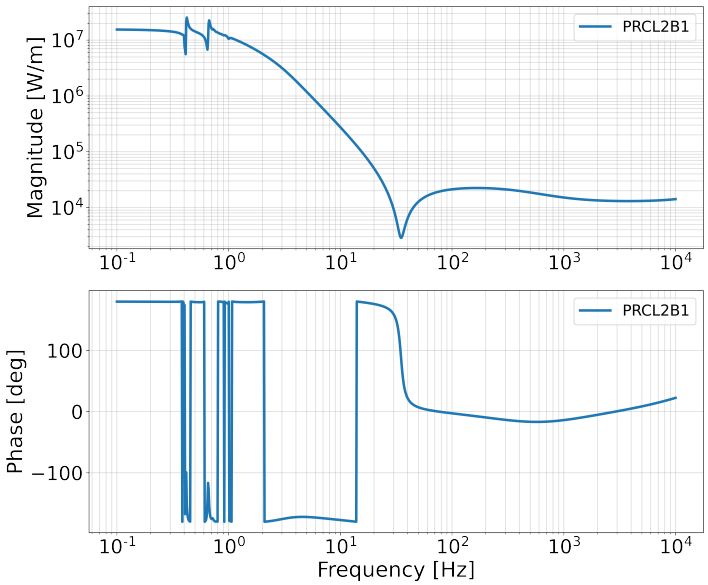

Figure 9.11: Simulation of the PR optical response.
Source: [29]

Between the measurements of May 11 and June 1, two magnets of the EM actuators of the WI mirror were removed, and between the measurements of June 1, and July 21, the NE mirror has been replaced. The measurements have been done after partial recovery of the ITF lock but with probably not the same tuning. Which might explain the different optical response measured. More measurements have to be done in order to understand the behaviour of PR. These measurements can be done by injecting more lines in the bandwidth [10 Hz, 80 Hz], or by injecting a noise in this bandwidth. If the optical response of PR still varies from one measurement to another, it may be better not to subtract the contribution of PR in h_{rec} than to subtract a contribution badly estimated. Investigations will be needed in this direction.

Conclusion

The measurements of the optical responses have begun on May 2023, and the measured optical responses of NE, WE and BS match with their models defined in chapter 2. The optical responses of PR and SR are not yet well understood. The replacement of the NE mirror has prevented us from measuring the optical responses as often as we wanted on June-July 2023. After the mirror replacement, only one measurement has been done and the lock of the interferometer was not stable enough to allow further measurements. The optical response measurement procedure is automatized so it can be applied weekly during the O4 run.

Chapter 10

Prospects

Contents

Introduction

This chapter shows the improvements of the PCal of Advanced Virgo+ Phase II, in prevision of the O5 run. The AdV+ Phase II configuration is similar to the Phase I, but with heavier test masses. The design BNS range of the phase II is between 150 and 200 Mpc.

The new test masses add new constraints on the PCal, so a new PCal optical bench will be designed, its characteristics are shown in [26]. This chapter shows the main constrains on the PCal due to the change of the end test masses, and the O5 design PCal bench. The methods to calibrate the PCal in DC power and to measure the frequency response of the power sensor are also shown in this chapter. The intercalibration procedure has not started yet, so the possible deficiencies of the procedure are not known yet. Unless strong variations of the sphere responsivity are found during the O4 run, it is not planned to change the intercalibration procedure between LIGO Virgo and KAGRA for the O5 run.

Due to difficulties to achieve a stable lock of the interferometer, only a few measurements of the actuator responses and optical response could have been done so far. More measurements of these response will be done during summer 2023, in preparation of the O4 run. This section gives some general ideas to improve the precision of the models of the actuator responses and of the optical responses.

10.1 Changes of the PCal

10.1.1 New end mirrors characteristics and their consequences on the PCal

During the O3 and O4 runs, the end mirrors are as described in section 2.1, their diameter is $\sim$ 350 mm, their thickness is $\sim$ 200 mm and their mass is $\sim$ 42.3 kg. For the O5 run, the end mirrors will be replaced by bigger mirrors. Their diameter will be $\sim$ 550 mm and their mass will be $\sim$ 104 kg. The other characteristics of the mirrors are given in table 10.1.

Diameter	550 $\pm$ 0.5 mm
Thickness	200 $\pm$ 0.5 mm
Mass	104 $\pm$ 1 kg
Roc, of the HR surface	1969 $\pm$ 10 m
Roc, of the AR surface	5.0 $\pm$ 0.03 m
Transmission of the HR coating (λ = 1047 nm)	3.2 $\pm$ 1 ppm
Transmission of the AR coating (λ = 1047 nm)	1 - (60 ppm)
Losses of the substrate (λ = 1047 nm)	2 ppm/cm

Table 10.1: Characteristics of the end mirrors designed for the O5 run.

The new characteristics of the mirrors have consequences on the mechanical response of the PCal. The amplitude of the pendulum response is proportional to the inverse of the mirror mass, so it will decrease. In addition, the resonant frequency of the drum mode will vary from $\sim$ 7.8 kHz to $\sim$ 4 kHz, and its amplitude will increase due the the larger diameter of the mirror. Thus, the notch frequency where the pendulum and the drum modes cancel each other is expected to be below 1 kHz. The frequency region around the notch frequency will be a blind region around which the calibration of the interferometer will be impossible.

In order to not excite the drum modes of the mirror, the O5 design of the PCal will use two laser beams to push the end mirror. The two beams will hit the mirrors 200 mm above and below the center of the mirror. Such PCal design is already used by LIGO for the O3 and O4 run, but the laser beams are sent to 111 mm above and below the center of mirror. The drawback of this method is that the PCal response will no longer be amplified by the drum mode, but it is still damped in $\propto f^{-2}$ by the pendulum, so the response of the PCal is too faint at high frequency. One solution is to add a third laser beam the hit the center of the mirror and excites the drum modes. Thus, the upper and lower beams will be used to calibrate the interferometer at low frequency, and the middle beam will be used to calibrate the interferometer at high frequency.

During the O3/O4 runs, the PCal laser beam is hitting the HR surface, from the Fabry-Perot cavity side. However, splitting the laser beam into three beams requires a larger optical bench for the PCal with several levels, and there is not enough room around the Fabry-Perot cavity. Thus, the new PCal benches will be installed at the back side of the tower and will push the end mirror by the back. Figure 10.1 shows a simplified scheme of the PCal.

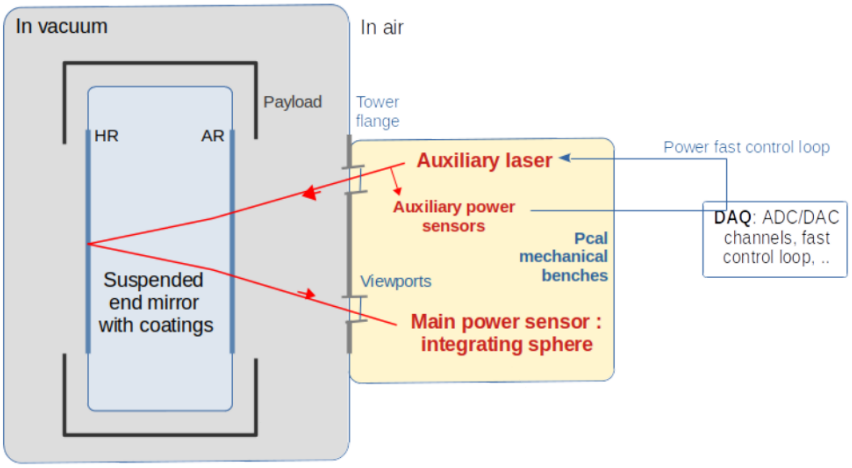

Figure 10.1: Concept scheme of the chamber of the end mirror, with the PCal bench.

The PCal beams are reflected by the HR surface of the end mirror, so the laser beams must pass twice through the AR coating and the substrate of the mirror. If we combine the losses of the substrate, the reflection of the AR coating, and the transmission of the HR coating, the total losses of the end mirror would be around 200 ppm (0.02%).

As for O4, the PCal benches will be on air, so the PCal laser beams will have to pass through viewports, each beam passes through a viewport at the injection bench and another at the reflection bench, so the new PCal requires the installation of six viewports on the back flange. The radius of curvature of the AR surface is set to$\sim$ 5 m, which has consequences on the location of the PCal viewports. In order to hit the HR surface 200 mm above or below the mirror center, the upper and lower laser beams must reach the AR surface with a vertical angle of incidence of 1.04° upward. Since the rear flange is located 1.5 m behind the center of the tower, where the mirror is located, the upper and lower viewports have to be located 174 mm above and below the level of the mirror center. The viewports of the middle beam are located at the same height as the center of the mirrors. A scheme of the rear flange of the end tower is shown in figure 10.2.

The injection and reflection viewports of the upper and lower beams are distant by 680 mm horizontally, and the injection and reflection viewports of the middle beam are distant by 800 mm horizontally. So the angle of incidence of the upper and lower beam on the AR surface of the end mirror is 12.8° and the angle of incidence of the middle beam is 14.5°. Finite element method simulations of the system have started to better define the optimal position of the two beams on the mirror and hence the position of the viewport. Figure 10.3 shows a simulation of the PCal upper beam propagation.

10.1.2 New setup of the PCal optical bench

As said in the previous section, the O5 PCal setup must be able to send two laser beams on the top and bottom of the end mirror to calibrate the interferometer at low frequency. It also must be able to send a third beam at the center of the end mirror to excite the drum modes and calibrate the interferometer at high frequency. The PCal bench will be located at the rear flange of the end mirror. Like during the other runs, the power of each beam has to be stable in time and its value must be known precisely.

Thus, the PCal optical benches will be divided into three levels called the upper, the middle and the lower levels. The laser source will be on the lower level, periscopes will be installed in order to send the

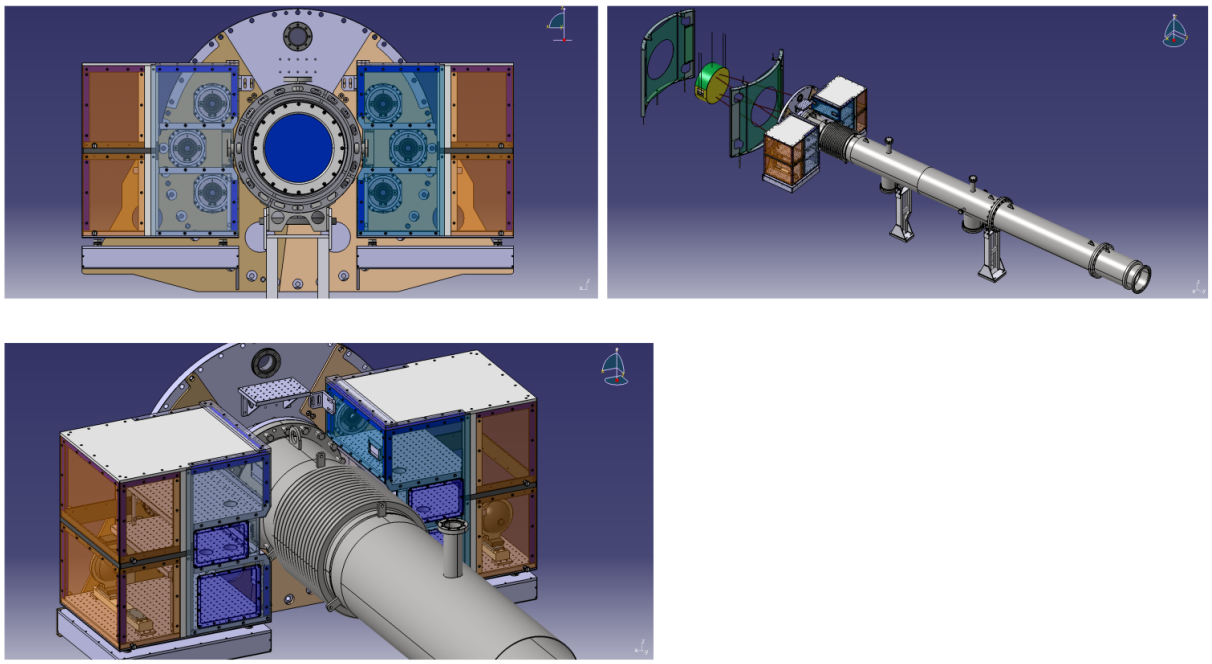

Figure 10.2: CAD scheme of the rear flange of the tower with the preliminary O5 design of the PCal bench.

laser beam to the other levels. The periscope of the middle level is placed on a flipper mount in order to be able to switch between the two beams configuration and the one beam configuration. The pick-off of the beam used for power control is done before the periscopes. So the pick-off beam can be aligned with the photodiodes without moving the beams going toward the end mirror. A scheme of the future PCal optical bench is available in figure 10.4.

The power balance of upper and lower beams, and their positions on the end mirror have to be controlled. So the deflecting mirrors in font of the viewport on the injection bench will be mounted on picomotors.

The reflections and transmissions of the beam splitter mirrors and of the periscopes have to be known and stable with time, and must not vary with the air humidity rate. So the coating of the different mirror will be done by ion beam sputtering, by the Laboratoire des Matiériaux Avancées, at Lyon, or by private company.

Another issue encountered during the preparation of the O4 run was the high sensing noise level of the Rx spheres. The sensing noise causes an uncertainty on the PCal power noise signal, and the laser power noise estimated by the Rx spheres are overestimated. In addition, this is a source of uncertainty for estimating the Rx sphere's frequency response. Thus, new preamplifiers will be designed in collaboration with the LIGO and KAGRA team in order to reduce the Rx sphere sensing noise.

10.2 Calibration of the PCal

10.2.1 Calibration in power of the PCal sensors

During the calibration of the PCal bench done in prevision of the O4 run, two problems have been encountered. As seen in section 7.1.2, the calibration of the Rx sphere was biased by $\sim$0.2%, which has not been explained. And it was difficult to measure the losses of the viewports directly on the optical bench, due to the light scattered by the optical components.

In order to determine what causes the bias on the power calibration of the PCal sensors, the calibration has to be done more regularly. Thus, the WSV and GSV integrating spheres will be stored on the

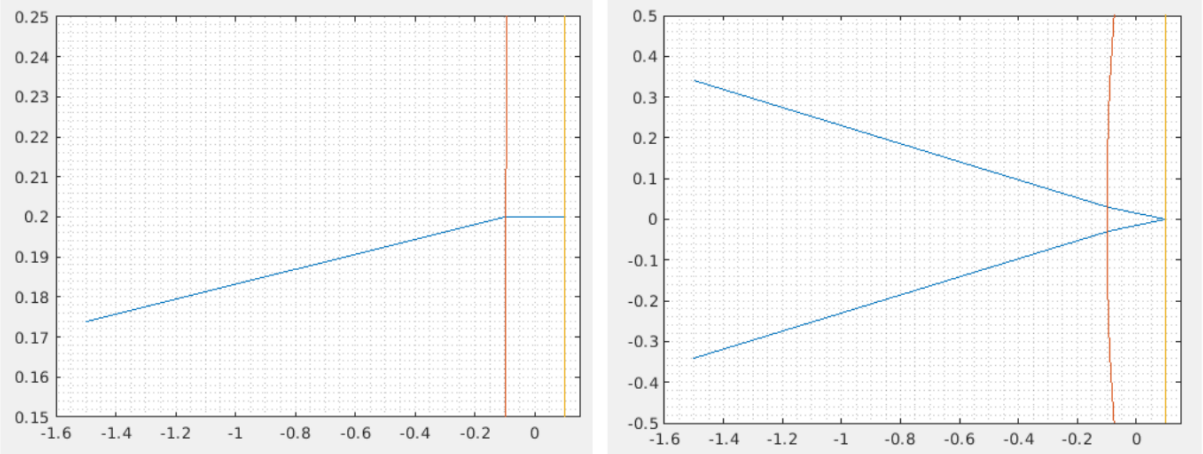

Figure 10.3: Simulation of the propagation of the upper PCal beam. The scale of the X and Y axis is in meters. Left: viewed from the side, Right: viewed from the top.

Virgo site instead of the LAPP. This will require a new dedicated optical laboratory with a compressed air supply, in order to build the sphere calibration setup at Virgo. This will also require a team working on the calibration on site.

One way to avoid the bias is to install a sphere calibration setup directly on the PCal optical bench, and to calibrate the Rx sphere with respect to the WSV sphere without transferring via the photodiodes. This will require a beam splitter mirror on a flipper mount in order to switch the PCal from the actuation mode to the calibration mode and the pneumatic sliders. This is possible only if the optical bench is big enough to hold the sphere calibration setup, and if a compressed air supply is available.

One of the major issue during the PCal calibration in prevision of the O4 run was the estimation of the power losses due to the viewports. It was impossible to measure directly the losses from the PCal benches because the WSV sphere used to estimate the scattered light was too close from the beam splitter BS_1 of the O4 PCal, and the light scattered by the beam splitter BS_1, entered the integrating sphere, and falsified the measurement of the laser power. In order to be able to measure the losses of the viewport of each level, the O5 PCal will be designed with an empty space of ∼30 cm between the viewport and the deflecting mirror, so an integrating sphere can be put at this place. There will be more than 10 cm if free space in front of the sphere entrance in order to limit the scattered light entering the sphere.

10.2.2 Calibration of the sensing chain frequency response of the power sensors

During my thesis, the estimation of the sensing chain frequency response of the photodiode was not measured in frequencies above 4 kHz due to the aliasing of the signal, despite the anti-aliasing filters of the ADC mezzanine. In addition, the sensing noise of the Rx spheres limits the precision of the sensing chain frequency response of the Rx sphere.

During the O5 run, the timing calibration of the power sensors will be based on a LED flashing the IRIG-B signal in front of one of the photodiodes, as during O3/O4. One solution to attenuate the aliasing is to filter the input voltage (current?) signal of the LED by a low-pass filter whose frequency response is precisely known. If the sensing noise of the sphere preamplifier is lowered, it will be possible to measure the frequency response of the Rx sphere from the photodiodes, by injecting a broadband power signal in the sensors and computing the transfer function from the photodiode to the sphere responses.

In addition, the frequency response of each power sensors will be characterized at LAPP on a dedicated setup, before being installed. This characterization will be done using either a chopper disk or a LED with a controlled illumination. The solution using the LED with a controlled illumination can also be installed on the PCal benches. More particularly, the calibration of the sensors frequency response

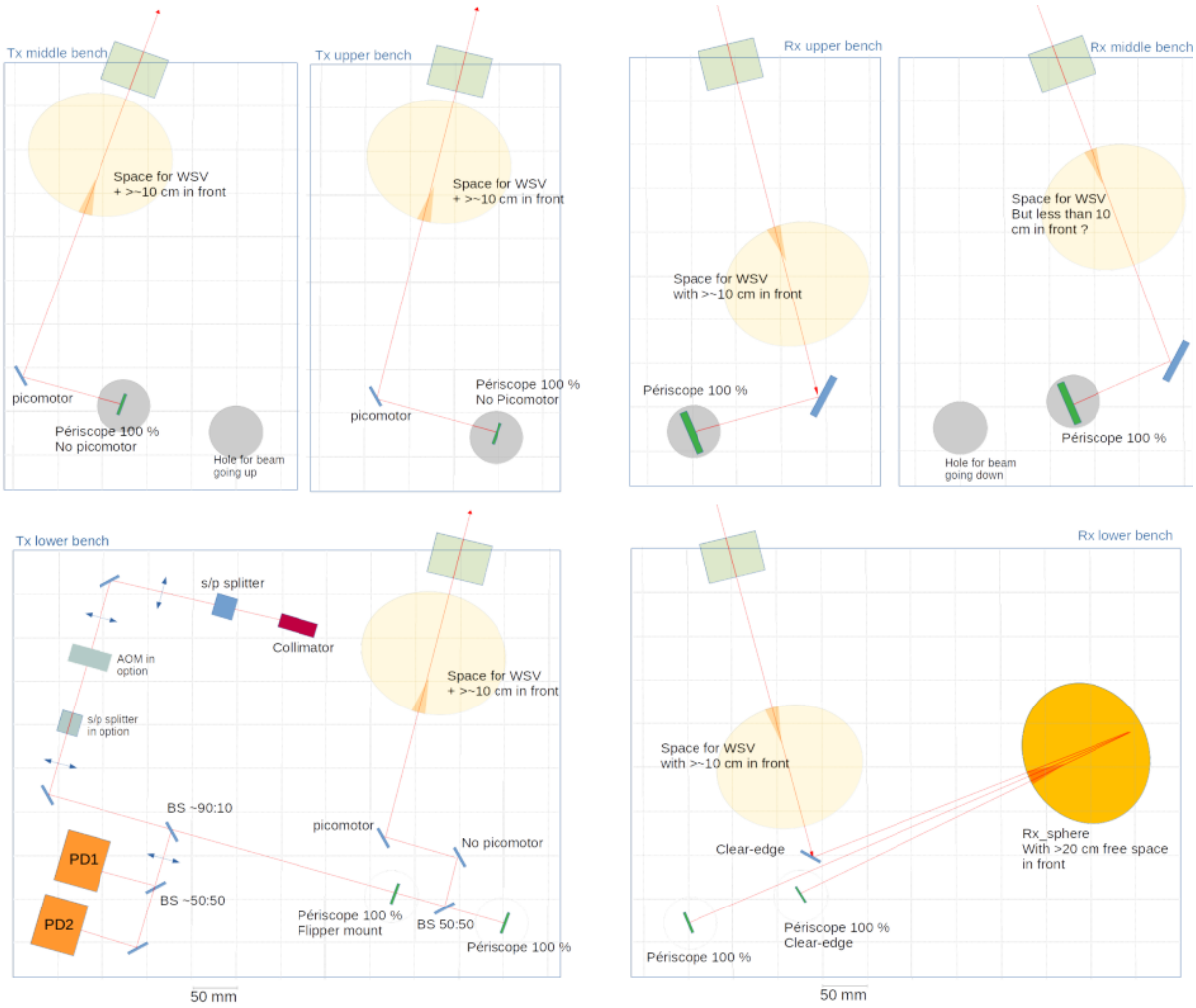

Figure 10.4: Conceptual design of the PCal optical benches.
Source: [26]

from DC to ∼10 Hz is important to check that their DC gain is still valid in all the Virgo frequency bandwidth

10.3 Calibration of the interferometer

The calibration of the interferometer in prevision of the O4 run started in spring 2023. Due to difficulties to lock the interferometer, the calibration of the interferometer couldn't be done as regularly as expected. The final models of the AdV+ responses are not yet defined but some problems has been highlighted during the measurements of the different responses.

10.3.1 Calibration of the electromagnetic actuators.

The measurement of the electromagnetic actuator frequency responses is the most crucial since their models are used to calibrate the optical responses of the interferometer. One of the major issue during the measurement of the actuator responses was the instability of the optical response of the interferometer during the measurement. To tackle this issue, the actuator response are measured weekly for several month, the mean over these months is computed, and the model is fitted over this mean response. This assume that the actuator response does not vary though time, and that the variations of the optical responses of the interferometer is random.

Another solution would be to monitor the optical response variations using the permanent lines as explained in section 4.1.3, and to correct them during the measurement of the actuator response. However, the monitoring of the optical response is not very accurate, and the method require models of the actuator responses. One solution would be to compute of the actuator response, use the new actuator model to correct the optical responses and compute again the actuator responses, and reiterate until the actuator response converge.

The model fitted to the measurement can also be improved. A machine-learning model, such as a gaussian process regression, can also be used to fit the measurement, as it is done in [9]. However, the measurement of the actuator response is highly sensitive to optical response variations. A machine-learning model fitted on only one measurement would be over-fitted. But the machine learning model can be used to fit the mean of the measured actuator response if enough data is taken.

Until now, the responses of some digital processes such as the $TF^{CalToSc}$ functions in the actuator response, and the sensing function of the $DARM$ signal, were measured. In section 7.2, we have seen that the nominal model of the PCal photodiode sensing response fit the measured sensing function. Thus, using a nominal function to model a digital process is a good approximation. The $TF^{CalToSc}$ functions, and the sensing function of the $DARM$ signal can be modeled with a nominal function.

10.3.2 Calibration of the optical responses of the interferometer

As seen in chapter 9, the models of the optical responses of NE, WE and BS fit the optical measurement, within a few percent of uncertainty. Which indicates that the single pole approximation is a good one. However, slight differences can be seen between the measured optical response and the model. These differences can be due to the variation of the optical response during the injection period. Indeed, the values of the cavity pole frequency and of the gain measured by the $h(t)$ reconstruction algorithm varies through time.

In addition, the method used by the reconstruction algorithm to measure the optical response, seen in section 4.1.3, differs from the method used during calibration shifts seen in chapter 9. Further investigations are needed to determine whether a bias is possible between the two methods. More particularly, an uncertainty value on the optical response measured by the $h(t)$ reconstruction algorithm must be computed.

The precision of the optical response model is less crucial than the actuator response model because the optical response model is used only in the reconstruction algorithm so far. In addition, the bias on $h(t)$ due to the discrepancies between the physical optical responses and their models can be corrected after the reconstruction as explained in section 4.2.

10.3.3 Other calibration methods

The NCal response is expected to be precise within 0.3% of uncertainty [1] for the O4 run. Whereas the PCal response is precise within 0.4% of uncertainty as seen in chapter 7. During the O3 run, the NCal and PCal agreed within 3% of discrepancy [6]. The intercalibration between PCal and NCal has not been done yet for the O4 run. If the two calibrators disagree, further investigations has to be done in order to determine the origin of the disagreement. The stability through the time of the PCal and NCal has to by characterized. If the NCal response is more stable over time than the PCal response, the NCal response will be used to correct the DC response of the PCal. The frequency response of the NCal has to be characterized in the bandwidth [10 Hz, 100 Hz]. If the NCal frequency response is more accurate than the PCal frequency response, the NCal will be used as reference for the interferometer calibration in the bandwidth [10 Hz, 100 Hz], and the PCal will be used to extend the calibration to 2 kHz. For the O5 run, the NCal rotors will be designed to turn faster in order to calibrate the interferometer at higher frequency.

The free swinging Michelson method was biased by 3% with respect to the PCal during O3 as seen in section 3.3.3. Therefore, this method will no longer be used to calibrate AdV+ during O4.

Conclusion

During the O3 run, photon calibrators were already installed in front of the end mirrors and were used as reference for the calibration of the mirror actuators of and the optical response of Advanced Virgo. The relative uncertainty on the estimation of the end mirror displacement was 1.36%. The two main sources of uncertainty were the calibration of the power sensors and the stability of the calibration through the time. The most of the uncertainty on the calibration comes from the use of the Virgo Integrating Sphere made by Newport. The correlation between air humidity rate with the transmission and reflection of the beam-splitter mirror used on the PCal benches during O3, makes the response of the PCal vary through the O3 run. For the O4 run, these issues have been solved. In addition, the design sensitivity of AdV+ for the O4 run increases the constraint on the precision of the PCal response, and the constraint on the laser power noise.
During my thesis, I improved the PCal setup by using beam-splitter cubes which are less sensitive to the air humidity variation than the mirrors used during O3. The laser power of the PCal is measured by a LIGO-like integrating sphere with a more stable responsivity than the Virgo Integrating sphere. The laser power is monitored with a new kind of photodiodes with a lower sensing noise, which allowed us to lower the laser power noise. The digital filter of the laser control loop has been modified, which reduced the laser power noise to a lower level and on a wider bandwidth.
To calibrate in DC the power sensors of the PCal, the new GSV and WSV integrating spheres have been mounted and calibrated with respect to the LIGO stardards at LHO, then shipped to the LAPP. Their calibration stability has been characterized at LAPP, and their response relative uncertainty is estimated at 0.167%. A sphere calibration setup, inspired from the LIGO calibration setup, has been designed at LAPP, in order to be able to intercalibrate the integrating spheres with respect to each other. This setup will be used in the new intercalibration procedure between LIGO, Virgo and KAGRA, which will start in August 2023.
The WSV integrating sphere has been used to calibrate the power sensors of the Virgo PCal several times, in order to estimate the calibration variation after several months. In order to compensate the sensing of the power sensors, the frequency response of the sensing chain has been measured and modeled using the frequency responses of the ADC mezzanine filters. A new model of the PCal mechanical response has been defined and fitted to a preliminary measurement in the bandwidth [1 kHz, 3 kHz]. A measurement of the mechanical response in a wider bandwidth [1 kHz, 7 kHz] is required to fit the model more precisely at high frequency. At low frequency [10 Hz, 0.5 kHz], the estimation of the mirror displacement induced by the PCal is accurate within an uncertainty of 0.4%.
During the preparation of O4 at Virgo, it was difficult to acquire the lock of the interferometer and to keep the lock stabilize it, probably due to the addition of the signal recycling mirror with marginally stable optical cavities. Because of this situation, the calibration of AdV+ could start only during spring 2023, and Virgo did not start the O4 run in May 24 with LIGO and KAGRA. On the last months of my thesis, I worked on the calibration of the Virgo detector to provide a reliable strain signal $h(t)$ for the commissioning, and in prevision of the O4 run.
One or two measurements of the response of all mirror actuators have been done using the O4 PCal calibrated with respect to the new power standards, in the bandwidth [10 Hz, 1 kHz]. Due to the instability of the interferometer response, the measurements were not precise. However, it was possible to fit a model to the measurements. The model fitted on these measurements agrees with the O3 models within 3%, which is expected since the electromagnetic actuators have not been modified. The new models have been temporarily used by the strain reconstruction algorithm. They are also used to measure the optical response of the interferometer. But the actuator responses have to be measured more precisely as soon as the interferometer response is more stable. Two magnets of the WI mirror actuators has been removed in May 2023 and the NE mirror has been replaced in June 2023, which may modify the frequency response of their actuators. Thus, the actuator response models of these mirrors are no longer

valid and have to be measured again.
Unlike what has been done during O3, different optical response models have been defined for each mirror in the reconstruction. The strain signal reconstruction algorithm has been updated to use different models of optical response for each mirror. The optical responses have also been measured preliminarily in the bandwidth [10 Hz, 1 kHz], and models have been fitted the measurements. The measurement procedure have been automatized in order to be repeated regularly before and during the O4 run when the optical response of the interferometer is more stable. The calibration models are being used in the $h(t)$ signal reconstruction during the commissioning period, in order to search for the limiting sources of noises.
For the O5 run, larger end mirrors will be installed, the internal modes are expected to resonate at lower frequency. In order not to excite the surface modes, the PCal beam will be splitted in two. Eventually, a third laser beam will be added to the PCal in order to actuate the mirror at high frequency. These features require a bigger PCal optical benches. Due to space constraint, the PCal benches will be installed at rear of the end tower and will push the mirror from behind. A sphere calibration setup will be installed on the PCal in order to calibrate directly the Rx sphere with respect to the WSV sphere without using the photodiodes on the injection bench, and reduce the uncertainty on the calibration. The optical components will be coated in laboratory in order to control their characteristics, and will be mounted on picomotors to control remotely their orientation.
The intercalibration procedure between LIGO, Virgo, KAGRA, NIST and PTB is just being started. Unless large biases on the Virgo sphere calibration with respect to the TS sphere are measured during the intercalibration procedure, it has not been planned to change the intercalibration procedure for the O5 run. Also, a comparison between the calibrations with PCal and the NCal will be of utmost importance to reduce the calibration error in the future.

Bibliography

[1] Virgo calibration team. Calibration status: hrec, pcal, ncal. https://tds.virgo-gw.eu/ql/?c=19506.

[2] The Virgo Collaboration. Advanced virgo plus phase i design report. https://tds.virgo-gw.eu/ql/?c=14430.

[3] A. Dalmaz, N. Letendre, A. Masserot, B. Mours, E. Pacaud, S. Petit, and L. Rolland. Daqbox and mezzanines user manual. https://tds.virgo-gw.eu/ql/?c=14584.

[4] A. Einstein. Die grundlage der allgemeinen relativitätstheorie. *Annalen Der Physik*, 49, 1916.

[5] D Estevez, B Mours, and T Pradier. Newtonian calibrator tests during the virgo o3 data taking. *Classical and Quantum Gravity*, 38(7):075012, mar 2021.

[6] Dimitri Estevez. *Upgrade of Advanced Virgo photon calibrators and first intercalibration of Virgo and LIGO detectors for the observing run O3*. PhD thesis, École Doctorale de Physique de Grenoble, 2020.

[7] B. P. Abbott et. al. First narrow-band search for continuous gravitational waves from known pulsars in advanced detector data. *Physical Review D*, 96(12), dec 2017.

[8] D Estevez et. al. The advanced virgo photon calibrators. *Classical and Quantum Gravity*, 38(7):075007, feb 2021.

[9] D Tuyenbayev et. al. Improving LIGO calibration accuracy by tracking and compensating for slow temporal variations. *Classical and Quantum Gravity*, 34(1):015002, dec 2016.

[10] Derek Davis et. al. Improving the sensitivity of advanced LIGO using noise subtraction. *Classical and Quantum Gravity*, 36(5):055011, feb 2019.

[11] F Acernese et. al. Calibration of advanced virgo and reconstruction of the detector strain h(t) during the observing run o3. *Classical and Quantum Gravity*, 39(4):045006, jan 2022.

[12] F Antonucci et. al. From laboratory experiments to LISA pathfinder: achieving LISA geodesic motion. *Classical and Quantum Gravity*, 28(9):094002, apr 2011.

[13] M Maggiore et. al. Science case for the einstein telescope. *Journal of Cosmology and Astroparticle Physics*, 2020(03):050–050, mar 2020.

[14] Matthew Evans et. al. A horizon study for cosmic explorer. https://dcc.cosmicexplorer.org/public/0163/P2100003/007/ce-horizon-study.pdf.

[15] Pau Amaro-Seoane et. al. Low-frequency gravitational-wave science with eLISA/NGO. *Classical and Quantum Gravity*, 29(12):124016, jun 2012.

[16] T Accadia et. al. Calibration and sensitivity of the virgo detector during its second science run. *Classical and Quantum Gravity*, jan 2011.

[17] F. Frappez. Low noise preamplifier for dc readout photodiodes. https://tds.virgo-gw.eu/?content=3&r=19538.

[18] F. Frappez, L. Rolland, and P. Lagabbe. Design of impedance matching boards to be used before adc channels (and use case for photon calibrators). https://tds.virgo-gw.eu/ql/?c=18861.

[19] Francesca Badaracco Lucia Trozzo. Seismic and newtonian noise in the gw detectors. https://tds.virgo-gw.eu/ql/?c=17640.

[20] Michele Maiorano, Francesco De Paolis, and Achille A. Nucita. Principles of gravitational-wave detection with pulsar timing arrays. *Symmetry*, 13(12):2418, dec 2021.

[21] Kara Merfeld. Search for gravitational-wave transients associated with magnetar bursts during the third advanced ligo and advanced virgo observing run, 2022.

[22] Alexander H. Nitz, Sumit Kumar, Yi-Fan Wang, Shilpa Kastha, Shichao Wu, Marlin Schäfer, Rahul Dhurkunde, and Collin D. Capano. 4-ogc: Catalog of gravitational waves from compact-binary mergers, 2021.

[23] L. Pinard. Ni characteristic. https://tds.virgo-gw.eu/ql/?c=10649.

[24] P. Puppo. Evaluation of the quality factors of the mirrors in advanced virgo. https://tds.virgo-gw.eu/ql/?c=12425.

[25] T Regimbau and V Mandic. Astrophysical sources of a stochastic gravitational-wave background. *Classical and Quantum Gravity*, 25(18):184018, sep 2008.

[26] L. Rolland. Advanced virgo + phase ii cal.04 review document. https://tds.virgo-gw.eu/ql/?c=18806.

[27] D Bhattacharjee S Karki and R Savage. Toward calibration of the global network of gravitational wave detectors with sub-percent absolute and relative accuracy. *Galaxies*, Jan 2022.

[28] R. Savage, D Bhattacharjee, F Llamas, and S. Karki. Characterization of pcal o4 power sensors.

[29] E. Tapia, D. Bersanetti, and M. Mantovani. Lsc sensing noise projections for o4 v2. https://tds.virgo-gw.eu/ql/?c=17369.

Appendix A

Statistical formula

A.1 Uncertainty on the measurement of a parameter.

Let $\{x_1, x_2, ..., x_N\}$ be N measurement of a Parameter X, associated with an uncertainty $\{u_1, u_2, ..., u_N\}$. The measurements are distributed along a normal distribution law $x_i \rightsquigarrow \mathcal{N}(X, \sigma^2)$.

The estimator of the parameter X is the weighted mean of the measurements.:

$$\bar{x} = \frac{\sum_{i=1}^{N} u_i^{-2} \cdot x_i}{\sum_{i=1}^{N} u_i^{-2}} \tag{A.1}$$

The standard error on the mean is written as:

$$s^2 = \frac{\sum_{i=1}^{N} u_i^{-2} \cdot (x_i - \bar{x})^2}{(N-1) \cdot \sum_{i=1}^{N} u_i^{-2}} \cdot (t^{corr})^2 \tag{A.2}$$

Since the random variable $\frac{\bar{x}-X}{s} \cdot \sqrt{N}$ is distributed along a t-Student distribution law $\mathcal{T}(0, 1, N-1)$, a factor t^{corr} is applied to the standard error. The t^{corr} correction factor is compute so as:

$$\mathcal{T}.\text{cdf}(t^{corr}, N-1) = \mathcal{N}.\text{cdf}(1) \tag{A.3}$$

A.2 Propagation of the uncertainty

Let $\mathcal{F}$ be a function of the parameter vector $X = (X_i)_{i\in[1,n]}$, and $Y = \mathcal{F}(X)$ the result vector of the function $\mathcal{F}$. Let $\mathbf{\Sigma^X}$ the covariance matrix of the vector X with $\Sigma^X_{i,j} = \text{cov}(X_i, X_j)$, and $\mathbf{\Sigma^Y}$ the covariance matrix of the Y with $\Sigma^Y_{i,j} = \text{cov}(Y_i, Y_j)$. The covariance Σ^Y can be written as:

$$\mathbf{\Sigma^Y} = \boldsymbol{J_{\mathcal{F}}} \cdot \mathbf{\Sigma^Y} \cdot \boldsymbol{J_{\mathcal{F}}^T} \tag{A.4}$$

Where $J\mathcal{F}$ is the jacobian of the function $\mathcal{F}$. In the case the result vector Y contains only one parameter, and the parameters X_i are independents, the covariance matrix $\mathbf{\Sigma^X}$ is a diagonal matrix containing the variances of the parameters X_i. And the variance of the parameter Σ^Y is written as:

$$\Sigma^Y = \sum_{i=1}^{N} \left(\frac{\partial \mathcal{F}}{\partial X_i} \right)^2 \cdot \Sigma^X_{i,i} \tag{A.5}$$